Resolving Zn Metal Anode Degradation Mechanisms by in-situ Liquid Cell Electron Microscopy



Yi. Yuan

Mansfield College

Department of Materials, University of Oxford

A thesis submitted for the degree of

Doctor of Philosophy

October 2024

Declaration

I hereby confirm that this thesis is my own work and that it has not been submitted for a degree at this or any other university. This thesis complies with the word limit of 40000 words. All information derived from other sources has been clearly indicated, and all collaborative efforts contributing to this research have been duly acknowledged within the thesis.

Yi Yuan



Acknowledgements

First, I offer my sincerest thanks to my supervisors, Dr. Alex W. Robertson and Sir Prof. Peter G. Bruce, for their unwavering support and invaluable guidance throughout my DPhil studies. I feel incredibly fortunate to have enjoyed such an excellent experimental environment and the freedom to pursue my research passions.

I am thankful to all the members of our research group for always being supportive. I would like to thank those who helped me survive the tough times at the beginning of my DPhil journey; the days and nights we spent together, and the meals we cooked and shared, will always hold a special place in my heart. I am also grateful to Xiaran and Yihui for their encouragement during a period of deep depression in my first year, chatting with me and listening to my complaints whenever I needed. Without the company of all of you, I cannot imagine how I would have managed through those tough and challenging times.

Finally, I owe my deepest gratitude to my family, especially my parents, JJ, and Yu. Thank you for your selfless love and support, for always being by my side, for allowing me to be myself.

Abstract

This thesis investigates the degradation mechanisms of Zn metal anodes in mild aqueous electrolytes and evaluates various strategies to mitigate these degradation processes using in situ electrochemical liquid cell transmission electron microscopy (TEM). Key issues are studied such as corrosion, dendrite growth, and hydrogen evolution, which are critical factors in determining the shelf life and cycling performance of the Zn metal anode.

In Chapter 1, the recent advancements in rechargeable batteries, especially Li-ion batteries, were briefly outlined. This chapter discussed the challenges and limitations associated with the use of Li, prompting the investigation into alternative battery systems. Aqueous Zn-based batteries have emerged as a promising alternative, attracting significant research interest due to their enhanced safety and lower cost. The history, types, and properties of Zn-based batteries were summarised, with a comparative analysis of the Zn metal anode in various electrolyte environments.

In Chapter 2, the focus was first shifted to the Zn metal anode in the Zn-ion batteries using mildly acidic electrolytes. This chapter has delved deeper into the challenges associated with the Zn metal anode, and previous work on additive engineering to enhance its performance via different mechanisms was categorized and reviewed. Additionally, representative studies on the application of in situ liquid cell TEM in advanced battery research were presented, particularly in Zn batteries.

In Chapter 3, the theoretical foundations and operational principles of various electrochemical tests and characterisations were explained, with particular emphasis on the in situ electrochemical liquid cell TEM. The configuration of and critical considerations for operating the in situ liquid cell TEM were also discussed.

Content from these three chapters was partially adapted from my previously published review paper, titled ‘The Application of In Situ Liquid Cell TEM in Advanced Battery Research’ in ***Energy Materials***,

and a book chapter entitled ‘Corrosion and Degradation in Aqueous Zn-based Batteries’, in the publication ***Corrosion and Degradation in Fuel Cells, Supercapacitors, and Batteries***.

In Chapter 4, the corrosion process of Zn in the $ZnSO_4$ aqueous electrolyte was studied. The dissolution process of Zn metal during battery rest (that is, when not being electrically cycled) was observed using the in situ liquid cell TEM, which has usually been neglected in mild Zn electrolytes. It was found that the initial pH value of the electrolyte was one of the key factors leading to such Zn dissolution process. By adjusting the pH value of $ZnSO_4$ electrolyte using zinc acetate, the dissolution of Zn was suppressed, which was verified by in situ liquid cell experiments.

In Chapter 5, the suppression mechanism of Zn dendrite via the electrostatic shielding mechanism was revealed via in situ liquid cell TEM, contrasting with that applicable to Li dendrites. The Zn nucleation and growth behaviours under different electrolyte compositions were directly observed. It was determined that the electrostatic shielding additive suppresses dendrites by inhibiting secondary zinc nucleation along the (100) edges of existing primary deposits and encouraging preferential deposition on the (002) faces, leading to a dense and block-like zinc morphology. This chapter was based on my published paper, ‘Diagnosing the electrostatic shielding mechanism for dendrite suppression in aqueous zinc batteries’, in ***Advanced Materials***.

In Chapter 6, the effects of a series of organic additives in Zn aqueous electrolytes are systematically examined for their ability to direct uniform Zn deposition morphologies and reduce side reactions. The impacts of these additives on solvation structures, the electric double layer, solid electrolyte interphase formation, and nucleation behaviours are assessed and compared through a series of characterisation methods.

List of Publications

Publications within the scope of the thesis

1. **Y. Yuan**, et al., Diagnosing the electrostatic shielding mechanism for dendrite suppression in aqueous zinc batteries. ***Advanced Materials***, 2024, 36, 2307708.

2. **Y. Yuan**, et al., Corrosion and degradation in aqueous Zn-based batteries. ***Corrosion and degradation in fuel cells, supercapacitors and batteries***, 2024. (Book chapter)

3. **Y. Yuan**, et al., The application of in situ liquid cell TEM in advanced battery research, ***Energy Materials***, 2023, 3, 300032.

Other publications as joint lead author and co-author

I contributed to these papers by conducting experimental characterisations and data analysis.

1. Z. Li, **Y. Yuan**, et al., Achieving planar Zn electroplating in aqueous zinc batteries with cathode-compatible current densities by cycling under pressure. ***Advanced Materials***, 2024, 2401576.

2. Y. Quan, D. Ji, **Y. Yuan**, et al., Mg-rich disordered rocksalt oxide cathodes for Mg-ion batteries. ***Journal of Materials Chemistry A***, 2024.

4. C. Gong†, S. Pu†, S. Zhang†, **Y. Yuan**†, et al., The role of an elastic interphase in suppressing gas evolution and promoting uniform electroplating in sodium metal anodes. ***Energy & Environmental Science***, 2023, 16, 535-545.

5. S. Pu†, B. Hu†, Z. Li†, **Y. Yuan**, et al., Decoupling, quantifying, and restoring aging-induced Zn-anode losses in rechargeable aqueous zinc batteries. ***Joule***, 2023, 7, 366-379.

6. S. Ahn, M. Lagnoni, **Y. Yuan**, et al., Chemical origins of a fast-charge performance in disordered carbon anodes. ***ACS Applied Energy Materials***, 2023, 6, 8455-8465.

7. S. Pu†, C. Gong†, Y. T. Tang, Z. Ning, J. Liu, S. Zhang, **Y. Yuan**, et al., Achieving ultrahigh-rate planar and dendrite-free zinc electroplating for aqueous zinc battery anodes. ***Advanced Materials***, 2022, 34, 2202552.

List of Abbreviations

AFM	Atomic Force Microscopy	**LP**	Linear Polarization
CV	Cyclic Voltammetry	**LSV**	Linear Sweep Voltammetry
DEC	Diethyl Carbonate	**NMC**	$LiNi_{1-X-Y}Mn_xCo_yO_2$
DFT	Density Functional Theory	**NMP**	N-Methyl-2-Pyrrolidone
DMSO	Dimethyl Sulfoxide	**NMR**	Nuclear Magnetic Resonance
DMC	Dimethyl Carbonate	**PC**	Propylene Carbonate
DOE	1,4-Dioxane	**PEO**	Polyethylene Oxide
EC	Ethylene Carbonate	**RTC**	Relative Texture Coefficients
EDL	Electric Double Layer	**SEI**	Solid Electrolyte Interphase
EDX	Energy Dispersive X-Ray	**SEM**	Scanning Electron Microscopy
EIS	Electrochemical Impedance Spectroscopy	**SFL**	Sulfolane
EMC	Ethyl Methyl Carbonate	**SHE**	Standard Hydrogen Electrode
EXAFS	Extended X-Ray Absorption Fine Structure	**STEM**	Scanning Transmission Electron Microscopy
FEC	Fluoroethylene Carbonate	**TEM**	Transmission Electron Microscopy
FTIR	Fourier Transformed Infrared	**TC**	Texture Coefficients
GLC	Graphene Liquid Cell	**XAFS**	X-Ray Absorption Fine Structure
H-bond	Hydrogen Bonding	**XANES**	X-Ray Absorption Near-Edge Structure
HAADF	High Angle Annular Dark Field	**XPS**	X-Ray Photoelectron Spectroscopy
HCP	Hexagonal Closed-Packed	**ZHS**	Zinc Hydroxide Sulphate
HER	Hydrogen Evolution Reaction	**XRD**	X-Ray Diffraction
ICP-OES	Inductively Coupled Plasma-Optical Emission Spectrometry		

Table of Contents

CHAPTER 1 INTRODUCTION

1.1 Current state-of-the-art rechargeable battery systems ..... - 1 -

1.1.1 Rechargeable Li-ion batteries ..... - 2 -

1.1.2 Li metal anodes ..... - 6 -

1.1.3 Issues and shortcomings of Li-based batteries ..... - 8 -

1.1.4 Advanced rechargeable battery systems: Beyond Li ..... - 9 -

1.2 Overview of aqueous Zn-based batteries ..... - 10 -

1.2.1 History and development of Zn-based batteries ..... - 11 -

1.2.2 Types of rechargeable Zn-based batteries ..... - 12 -

1.2.3 Properties of Zn metal anodes ..... - 15 -

1.2.3.1 Zn metal anode in alkaline electrolytes ..... - 16 -

1.2.3.2 Zn metal anode in neutral/mildly acidic electrolytes ..... - 17 -

1.2.4 Summary and outlook ..... - 19 -

CHAPTER 2 LITERATURE REVIEW

2.1 Tackling issues of the Zn metal anode by electrolyte additives ..... - 21 -

2.1.1 Challenges of the Zn metal anode in Zn-ion batteries ..... - 21 -

2.1.1.1 Dendrite formation ..... - 22 -

2.1.1.2 HER ..... - 24 -

2.1.1.3 Corrosion ..... - 26 -

2.1.2 Electrolyte additives for stabilizing Zn metal anodes ..... - 28 -

2.1.2.1 Electrostatic shielding additives ..... - 28 -

2.1.2.2 Solvation structure and water activity adjustment additives ..... - 30 -

2.1.2.3 In situ SEI formation additives ..... - 34 -

2.1.2.4 Electrode surface adsorption additives ..... - 37 -

2.1.2.5 Texture regulation additives ..... - 38 -

2.1.3 Summary and outlook ..... - 40 -

2.2 The application of in situ liquid cell TEM in advanced battery research ..... - 41 -

2.2.1 Application of in situ liquid cell TEM in Li batteries ..... - 44 -

2.2.2 Application of in situ liquid cell TEM in aqueous Zn batteries ..... - 48 -

2.2.3 Application of in situ liquid cell TEM in other advanced battery systems ..... - 51 -

2.2.4 Summary and outlook ..... - 53 -

CHAPTER 3 METHODOLOGY

3.1 Electrochemical tests ..... - 56 -

3.1.1 Galvanostatic cycling ..... - 56 -

3.1.2 Linear sweep voltammetry (LSV) and cyclic voltammetry (CV) ..... - 57 -

3.1.3 Linear polarization (LP) ..... - 58 -
3.1.4 Chronoamperometry ..... - 58 -
3.1.5 Electrochemical impedance spectroscopy (EIS) ..... - 59 -
3.2 In situ electrochemical liquid cell transmission electron microscopy (TEM) ..... - 61 -
3.2.1 Basic working principles of TEM ..... - 61 -
3.2.2 Configuration of the in situ electrochemical liquid cell TEM holder ..... - 63 -
3.2.3 Experimental setup for in situ liquid cell TEM ..... - 65 -
3.3 Scanning electron microscopy (SEM) and energy dispersive X-ray (EDX) analysis ..... - 68 -
3.4 X-ray diffraction (XRD) ..... - 69 -
3.5 X-ray photoelectron spectroscopy (XPS) ..... - 70 -
3.6 Atomic force microscopy (AFM) ..... - 72 -
3.7 Inductively coupled plasma-optical emission spectrometry (ICP-OES) ..... - 73 -
3.8 X-ray absorption fine structure spectroscopy (XAFS) ..... - 74 -
3.9 Raman spectroscopy ..... - 75 -

CHAPTER 4 UNVEILING THE ANODE CORROSION PROCESS IN ZN-ION BATTERIES

4.1 Introduction ..... - 77 -
4.2 Experimental ..... - 78 -
4.2.1 Chemicals and materials ..... - 78 -
4.2.2 Setup for in situ TEM characterisation ..... - 79 -
4.2.3 Electrochemical tests ..... - 79 -
4.2.4 Characterisations ..... - 80 -
4.3 Results and discussion ..... - 80 -
4.3.1 ZHS formation on the Zn metal anode during rest under different conditions ..... - 80 -
4.3.2 Self-corrosion property of the Zn metal anode in Zn-ion batteries ..... - 82 -
4.3.3 Investigation of the ZHS formation via ex situ liquid cell experiments ..... - 84 -
4.3.4 Decrease in the coulombic efficiency during rest via in situ liquid cell experiments ..... - 88 -
4.3.5 Dissolution behaviour of Zn during rest in the $ZnSO_4$ electrolyte ..... - 93 -
4.3.6 Mitigation of Zn dissolution behaviour by initial pH adjustment of the electrolyte ..... - 97 -
4.3.7 In situ monitoring of pH change near the Zn metal anode surface during rest ..... - 100 -
4.3.8 Influence of the pH adjustment on the corrosion process ..... - 102 -
4.3.9 Comparison of electrochemical performances ..... - 106 -
4.4 Conclusion ..... - 110 -

CHAPTER 5 DIAGNOSING THE ELECTROSTATIC SHIELDING MECHANISM FOR ZN DENDRITE SUPPRESSION

5.1 Introduction ..... - 113 -
5.2 Experimental ..... - 117 -
5.2.1 Chemicals and materials ..... - 117 -

5.2.2 Setup for in situ TEM characterisation ..... - 117 -
5.2.3 Electrochemical tests ..... - 118 -
5.2.4 Characterisations ..... - 119 -
5.2.5 Density functional theory (DFT) calculation ..... - 119 -
5.3 Results and discussion ..... - 121 -
5.3.1 Electrodeposition behaviour in the $ZnSO_4$ electrolyte ..... - 121 -
5.3.2 Electrodeposition behaviour in the $ZnSO_4$ electrolyte with LiCl ..... - 125 -
5.3.3 Illustration of different nucleation and growth processes ..... - 127 -
5.3.4 Computational modelling results of binding energies ..... - 129 -
5.3.5 Ex situ structural and morphological characterisations of electrodes after cycling ..... - 132 -
5.3.6 Influences of the additive concentration ..... - 137 -
5.3.7 Comparison of cycling performances ..... - 139 -
5.3.8 Other potential influencing factors ..... - 146 -
5.3.9 Studies of other additive analogues ..... - 148 -
5.3.10 Comparison of the 'Electrostatic shielding' mechanism in different battery systems ..... - 151 -
5.4 Conclusion ..... - 153 -

CHAPTER 6 EXPLORING ROLES OF ORGANIC ADDITIVES IN ALLEVIATING ZN DENDRITES AND SIDE REACTIONS: A COMPARATIVE RESEARCH

6.1 Introduction ..... - 155 -
6.2 Experimental ..... - 156 -
6.2.1 Chemicals and materials ..... - 156 -
6.2.2 Electrochemical tests ..... - 156 -
6.2.3 Characterisations ..... - 157 -
6.3 Results and discussion ..... - 157 -
6.3.1 Effects on the bulk solvation structure of electrolytes ..... - 158 -
6.3.2 Effects on the EDL adsorption at electrode/electrolyte interfaces ..... - 161 -
6.3.3 Implications on the nucleation and growth behaviours ..... - 162 -
6.3.4 Comparison of compositional distribution over the Zn metal anode ..... - 166 -
6.3.5 Contributions to the suppression of HER and corrosion ..... - 169 -
6.3.6 Further concerns of organic additive in overall performance of Zn-ion batteries ..... - 170 -
6.4 Conclusion ..... - 171 -

CHAPTER 7 CONCLUSION AND FUTURE WORK ..... - 174 -

APPENDIX ..... - 177 -

REFERENCES ..... - 181 -

Chapter 1 Introduction

1.1 Current state-of-the-art rechargeable battery systems

The energy issue is one of the most concerning challenges facing society. Researchers have paid great effort to finding alternative options to help us move beyond our heavy dependence on fossil fuels [1,2]. Renewable energy sources are essential, and batteries are considered one of the most promising solutions to the intermittency problem associated with them. Batteries have been rapidly developed to satisfy the fast-growing demands for electric vehicles, portable electrical devices, and other energy storage equipment in daily life [3,4].

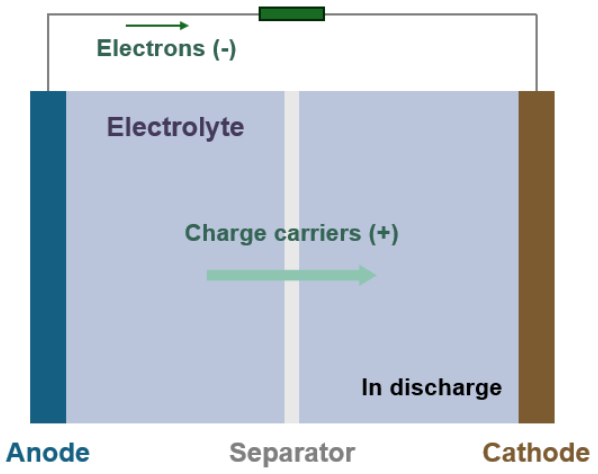


Figure 1.1 Schematic diagram of the discharging process in a typical battery.

The term 'battery' initially referred to a series of interconnected single cells, but now has evolved to encompass a broader definition [5]. A conventional battery comprises two electrochemically active components, namely the anode and the cathode, which are partitioned by an ion-conductive yet electron-insulating medium, known as the electrolyte. A separator permeable to the electrolyte is also commonly used to keep two electrodes from contacting with each other within the cell. During discharge, the working ions and electrons transfer from the anode to the cathode via the electrolyte inside the cell and the external circuit, respectively, as is shown in

Figure 1.1. Such chemical reaction between the anode and the cathode cannot be readily reversed in primary batteries, while for rechargeable batteries, also named as secondary batteries, it can be reversible, or recharged, by an applied electric field.

The following discussion in this thesis focuses solely on rechargeable battery systems. Numerous rechargeable battery systems have been developed to cater to diverse requirements across a series of applications, each tailored to address specific demands and constraints inherent to their respective domains [3,6,7]. These battery systems vary in chemistry, material, design, performance characteristics, and operating condition, ranging from lead/acid (Pb/acid) batteries predominant in stationary energy storage [8], nickel/metal hydride (Ni/MH) batteries currently utilised in hybrid electric vehicles [9,10], to ubiquitous lithium-ion (Li-ion) batteries favoured in portable electronics and electric vehicles [11–13], and other emerging technologies such as all-solid-state Li batteries [14,15], sodium-ion (Na-ion) batteries [16–18], etc.

1.1.1 Rechargeable Li-ion batteries

The inception of the alkali-ion (Li and Na) battery can be traced back to the late 1960s, when rapid Na ion conductivity was discovered within the ceramic Na β-alumina, thus stimulating the idea of using framework structures as crystalline matrices for mobile alkali ions [3]. The extensive research interest in rechargeable alkali-ion batteries was further enhanced by the oil crisis in the 1970s, during which researchers endeavoured to explore fossil fuel-independent alternative energy sources [19]. Based on the previous exploration of reversible insertion of lithium into the layered sulphides [20], Dr M. Stanley Whittingham first demonstrated the success of using titanium disulfide (TiS_2) as an intercalation cathode material, culminating in the development of rechargeable "rocking chair" batteries [21]. Such Li-TiS_2 batteries were then commercialised by Exxon-Mobile. Nonetheless, safety concerns surrounding the use of metallic lithium as the anode

prompted subsequent research efforts. In the following decade, Professor John B. Goodenough's theoretical insights advocated for the utilisation of layered metal oxides, particularly lithium cobalt oxide ($LiCoO_2$) and lithium nickel oxide ($LiNiO_2$), as cathode materials, thereby enhancing battery voltage potentials [22]. Building upon these advancements, Professor Akira Yoshino's pioneering work substituted metallic lithium with petroleum coke as an anode material, resulting in the fabrication of the first commercially viable Li-ion battery prototype in 1985, with Goodenough's cathode as the foundation [23]. Sony's commercialisation of Li-ion batteries based on graphite and $LiCoO_2$ in 1991 marked a seminal milestone. Since then, subsequent research on rechargeable batteries has predominantly focused on Li-ion batteries, catalysing a transformative shift towards sustainable energy systems, ushering in an era of wireless and fossil fuel-independent technologies [24–26]. The pioneering contributions of John B. Goodenough, M. Stanley Whittingham, and Akira Yoshino to Li-ion battery technology were acknowledged through the conferral of the 2019 Nobel Prize in Chemistry, affirming their vital role in advancing this field.

The performance of Li-ion batteries, which includes capacity, energy density, durability, safety, and environmental sustainability, depends largely on the characteristics of the electrode materials and the electrolytes. The capacity indicates the total charge that the cell can store, which is usually expressed in ampere-hours (Ah) or milliampere-hours (mAh). It can be further quantified as specific capacity, relative to the mass of the active material in the electrode (mAh/g), or areal capacity, relative to the area of the active electrode surface (mAh/cm^2). Energy density refers to the amount of energy stored per unit volume or mass of a battery, typically measured in watt-hours per litre (Wh/L) or watt-hours per kilogram (Wh/kg). Traditionally, graphite has long been the dominant anode material used in Li-ion batteries due to its ideal ability to intercalate lithium ions, of which the market share has reached 98% since it was developed [12]. Current research on modifying the graphite anode is mainly focused on

optimising the solid electrolyte interphase (SEI) by advanced coating technique or electrolyte engineering, to enhance its stability and safety [27–30]. However, its capacity limits under high-performance scenarios have driven research into alternative materials. To surpass the limitations of graphite, materials such as silicon, lithium metal, and various alloys are being explored. Silicon, for example, offers a theoretical capacity ten times that of graphite, and has emerged as a most promising anode material [31,32]. Challenges related to its volume expansion during lithiation and irreversible capacity loss due to the unstable SEI, which can lead to structural failure and rapid degradation, are the focus of current research [33,34]. Efforts are underway to engineer nanostructured silicon and silicon composites with carbon to overcome such limitations [35–38]. Transition metal oxides, such as titanium dioxide (TiO_2), are also promising anode materials due to their low cost, high reversible capacity and good safety, but they face challenges like low conductivity and significant volume expansion during cycling [39–41]. Despite progress in the nano-design and structure/composite modification, commercial scalability remains a significant challenge [42–44].

The landscape of Li-ion battery cathode materials is diverse, with each type offering unique advantages and trade-offs [45–50]. Common cathode materials used in Li-ion batteries include: (i) Layered transition metal oxides, such as $LiCoO_2$, lithium manganese oxide ($LiMnO_2$), lithium nickel manganese cobalt oxide ($LiNi_{1-x-y}Mn_xCo_yO_2$, NMC), lithium nickel cobalt aluminium oxide ($LiNi_{1-x-y}Co_xAl_yO_2$); (ii) Spinel Mn-based transition metal oxides, such as $LiMn_2O_4$, $LiNi_{0.5}Mn_{1.5}O_4$; (iii) Polyanion compounds, such as olivine lithium iron phosphate ($LiFePO_4$). The choice of cathode material depends on the specific requirements of the application, including energy density, power output, safety, cost, and environmental impact. For example, as one of the first commercial cathode materials, $LiCoO_2$ is still widely used in consumer electronics like smartphones and laptops due to its high energy density [51]. However, its use in larger scale applications is limited due to safety concerns and the high cost of cobalt. NMC is a versatile

cathode material that balances performance, safety, and cost. The ability to fine-tune the ratio of Ni, Mn and Co allows manufacturers to tailor NMC materials for different requirements of electric vehicles and energy storage systems, making it one of the most promising cathodes today [48,52–54]. $LiFePO_4$ cathodes are renowned for their superior thermal and chemical stability, making them one of the safest cathode materials available [55,56]. Despite the lower energy density compared to $LiCoO_2$ and NMC, the abundance and low cost of iron and phosphate make $LiFePO_4$ particularly advantageous for applications requiring durability and safety, such as electric buses and stationary energy storage [57,58].

The electrolyte in Li-ion batteries is responsible for the conductance of lithium ions between the cathode and anode during cycling, which plays a crucial role in the overall stability, performance, and safety [59]. Traditional liquid electrolytes comprise lithium salts in organic solvents [60]. Lithium salts are critical component of the electrolyte, providing the lithium ions for battery operation. The most commonly used lithium salt is lithium hexafluorophosphate ($LiPF_6$) for its good ionic conductivity and chemical stability within a moderate voltage window [61,62]. However, $LiPF_6$ is sensitive to moisture and can decompose under high temperatures or in the presence of water, producing hydrofluoric acid, which is detrimental to both battery performance and safety [63,64]. Alternative salts, such as lithium tetrafluoroborate ($LiBF_4$) and lithium bis(trifluoromethanesulfonyl)imide (LiTFSI), have been explored to address these issues [65–70]. The solvents facilitate the mobility of lithium ions; common solvents include ethylene carbonate (EC), dimethyl carbonate (DMC), ethyl methyl carbonate (EMC), and diethyl carbonate (DEC) [71,72]. Each solvent has its characteristics that influence the battery's performance parameters, such as ionic conductivity, viscosity, and dielectric constant [73–78]. For instance, EC is valued for its high dielectric constant, which enhances the solubility of lithium salts and the stability of the electrolyte, whereas DMC offers lower viscosity, which can improve ionic mobility [73,78–80]. Nowadays, the $LiPF_6$ salt and mixtures of EC and DMC, EC and DEC, or EC and EMC solvent, have

been the most widely used components in electrolytes [81–83]. Additives are also usually used to improve the performance of liquid electrolytes. Common additives include vinylene carbonate and fluoroethylene carbonate, which can facilitate the formation of a robust SEI layer and enhance the stability of electrolytes [84–88].

1.1.2 Li metal anodes

The first generation of Li-ion batteries based on lithium transition metal oxide cathode and graphite anode only possessed an energy density below 100 Wh/kg, while the energy density of current commercial Li-ion batteries can reach to 300 Wh/kg, with a growth rate of 7-8% per year [11,89]. However, improvements in the energy density still have hardly caught up with the increased demands of portable electronic devices and electric vehicles, as they have nearly reached the energy density limit of current Li-ion batteries (e.g., approximately 380 Wh/kg for graphite||$LiFePO_4$ in theory), which is due to the capacity limitation of the cathode and anode materials caused by the intrinsic intercalation reaction [90,91]. The intercalation reactions always need host materials to reversibly store and release Li ions, thus the capacities of these materials can never reach a very high level. Furthermore, fast charging is crucial for developing next-generation batteries, particularly for accelerating the adoption of electric vehicles [92]. However, graphite anodes with their intercalation mechanism cannot support fast charging as high current densities can cause significant polarization leading to limited capacity utilisation and safety risks [93]. Therefore, it is urgent to develop “beyond intercalation reaction” systems with a high energy density, thus making the Li metal anode of interest.

The Li metal anode, also known as the “Holy Grail” among all anode materials, offers the lowest electrochemical potential (-3.04 V) and an exceptionally high theoretical specific capacity 3860 mAh/g, which is almost 10 times of traditional graphite anode (372 mAh/g) [94,95]. When

replacing graphite with metallic Li, the energy density of $LiMnO_2$ type battery can be significantly improved to 440 Wh/kg [96]. In addition, for the lithium-sulphur (Li-S) and lithium-air (Li-O_2) battery systems, their specific energy can reach even up to 650 Wh/kg and 950 Wh/kg [97–99].

The implementation of Li metal anodes in commercial applications still faces significant challenges [100–102]: (i) The high chemical and electrochemical reactivity of Li metal leads to reactions with almost all electrolytes, resulting in corrosion and a low utilisation rate of the Li metal; (ii) Uneven Li deposition caused by irregular Li ion flux distribution near the electrode surface leads to dramatic growth of Li dendrites, which can easily pierce the separator and cause serious safety issues such as internal short circuits, thermal runaway, fire, and explosion; (iii) Dendritic Li metal can easily lose electrical connection with the bulk Li anode or current collector, subsequently forming "dead Li," which results in severe capacity loss; (iv) The Li metal anode experiences significant volume expansion and contraction during the plating/stripping process, leading to continuous reconfiguration of the SEI layer, which consumes Li and thus reduces coulombic efficiency and cycle life. Coulombic efficiency and cycle life are two key factors that describe the performance of batteries, indicating the reversibility of charge carriers and the battery's ability to maintain capacity over repeated cycling, respectively.

To address the aforementioned challenges, various strategies have been developed to stabilize Li metal anodes. One approach involves engineering artificial SEI layers with suitable flexibility and mechanical strength on the Li anode surface, effectively suppressing Li dendrite formation and enhancing electrochemical performance [103–105]. Using three-dimensional (3D) structured current collectors has been widely reported to mitigate volume changes, while modified separators can inhibit Li dendrite penetration [106–108]. And, optimising electrolytes by incorporating additives and utilising high-concentration formulations can improve overall stability and performance [109–111]. Advancements are also being made in transitioning from

traditional solvent-salt mixtures to more advanced formulations, including ionic liquid and solid-state electrolytes [112,113]. Li metal anodes are particularly advantageous in solid-state batteries, as they can potentially eliminate many safety issues associated with liquid electrolytes, such as leakage and flammability. Solid-state electrolytes also offer superior mechanical stability, reducing the possibility of dendritic growth and thereby enhancing the safety and longevity of Li metal anodes [14,114]. Although these methods successfully enhance stability of Li metal anodes and mitigate degradation, their practical adoption is still limited by production requirement, environmental concerns, and high manufacturing costs [15,115,116].

1.1.3 Issues and shortcomings of Li-based batteries

Despite their widespread use and significant advantages, all Li-based batteries are beset by several critical issues and shortcomings that impede their performance and broader adoption. One of the most critical challenges facing lithium batteries is safety concerns. The high reactivity of Li element can lead to dangerous scenarios, particularly under conditions of overcharging, short-circuiting, or exposure to high temperatures [117,118]. Li dendrite formation during repeated charge-discharge cycles poses a significant risk. These dendrites can penetrate the separator and cause internal short circuits, leading to thermal runaway, potentially causing fires or explosions [119,120]. The flammability of organic electrolytes even further exacerbates these safety risks [81,121]. Secondly, high manufacturing costs of Li batteries remain a substantial barrier, particularly in cost-sensitive applications like the large-scale energy storage. The production of high-purity lithium salts, sophisticated electrode materials, and precise cell assembly processes are inherently expensive [122]. Besides, essential raw materials like lithium, cobalt and nickel are relatively scarce, and the extraction and processing of these elements, which are often sourced from geopolitically unstable regions, are resource-intensive, further complicating supply chains and driving up costs [123]. The environmental impact of Li battery production and disposal is

another significant issue [124]. Mining activities can lead to habitat destruction, water depletion, and pollution. Additionally, the end-of-life disposal of Li batteries also poses environmental hazards due to the potential release of toxic substances [125,126]. Therefore, developing alternative battery systems is essential, especially for large-scale applications, due to the challenges in safety, cost, material limitations, environmental impact, and scalability associated with Li battery technology.

1.1.4 Advanced rechargeable battery systems: Beyond Li

As mentioned above, one possible solution to solve the challenges of Li is to explore alternative charge carrier ions. Various ions have been previously identified from the periodic table, with their prices per kilogram and theoretical charge capacities summarised in *Figure 1.2* [18].

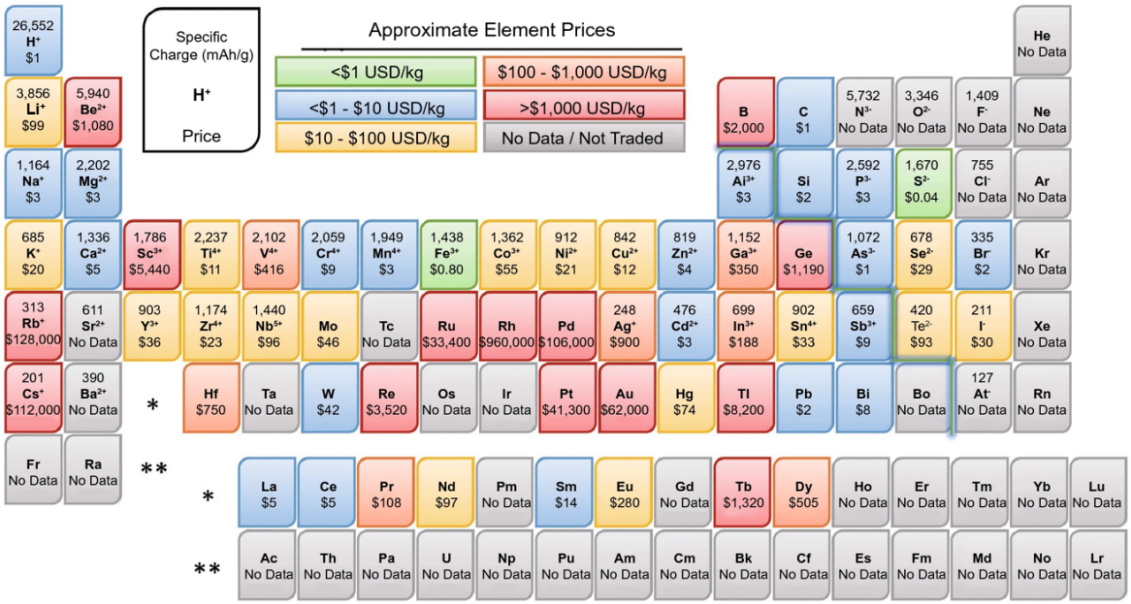


Figure 1.2 Periodic table of elements with price and charge capacity of each element [18]. **Reprinted by permission, copyright 2022 Springer Nature.**

Other alkali-ion battery systems, including Na-ion and potassium-ion (K-ion) batteries, are emerging as promising alternatives to solve the resource and cost issues of Li-ion batteries

[17,127,128]. Similar to Li-ion in operation, these alkali-ion batteries involve the shuttling of alkali metal ions between the cathode and anode through an electrolyte, of which the properties closely resemble those of Li-ion batteries, yet at a significantly lower cost [129]. These alternative batteries leverage abundant and widely distributed Na and K resources, which could substantially reduce material costs and mitigate the geopolitical risks tied to Li supply. Additionally, the ability to use inexpensive species such as Mn and Fe, instead of Co and Ni, in layered Na and K cathodes, is expected to further reduce the cost [130–133]. Divalent alkaline-earth metal ions, such as magnesium (Mg) and calcium (Ca), as well as trivalent aluminium (Al) ions, have gained research attention due to their outstanding theoretical energy densities [134–136]. However, the development of these multivalent-ion batteries is hindered by the limited selection of electrolytes that provide both high ionic conductivity and compatibility with metal anodes, as well as cathode materials that can reversibly intercalate these ions [137–139]. Compared to multivalent-ion batteries that require organic environments, zinc-ion (Zn-ion) batteries are closer to commercialisation [140]. Despite its relatively low energy density, the Zn metal anode has a less negative standard reduction potential, allowing it to be stable in aqueous electrolytes, which brings benefits of lower cost and enhanced safety [141]. While the theoretical understandings of these alternative ions beyond Li have been advanced significantly, there are still complex challenges encountered by these novel battery systems, including issues with electrodes, electrolytes, and scale-up manufacturing processes [16,142]. Moreover, merely substituting the active ions might not yield substantial cost savings. It is crucial to explore advanced cost-effective electrolytes and cathode materials as well [143].

1.2 Overview of aqueous Zn-based batteries

As the demand for efficient, cost-effective, and environmentally friendly energy storage technologies continues to grow, researchers and scientists have been exploring novel materials

and chemistries to overcome the limitations of traditional Li-ion batteries. One such emerging technology is the aqueous Zn-based battery, which has garnered significant attention in recent years due to its potential for providing safe, sustainable, and high-performance energy storage solutions [144].

1.2.1 History and development of Zn-based batteries

The exploration of zinc as a potential battery material can date back to more than two centuries ago (*Figure 1.3*) [145]. In 1799, Alessandro Volta developed the first true electrochemical cell, known as the Voltaic pile, which used zinc and copper plates separated by an electrolyte-soaked cardboard to generate an electrical current [146]. This invention laid the foundation for modern battery technology. Later, in 1860s, Georges Leclanché invented a battery that consisted of Zn and manganese dioxide (MnO_2), using ammonium chloride (NH_4Cl) as the electrolyte solution [147]. The first rechargeable Zn battery was invented at the end of the nineteenth century, based on an aqueous solution of zinc bromide [148]. Soon after, in 1901, Thomas Edison was awarded one of the first patents on the rechargeable alkaline Ni-Zn battery system, using potassium hydroxide (KOH) as the electrolyte [149]. Inspired by Edison's work, Lewis Urry developed the modern primary alkaline Zn-MnO_2 batteries in the 1950s, which became commercially successful and dominated the primary battery market segment even until now [150]. There were also several other types of Zn-based batteries, including the Zn-air battery and Zn-silver oxide (Ag_2O) battery in the meantime, which were also successfully commercialised [151–153].

However, the utilisation of alkaline electrolytes makes Zn batteries suffer from severe dendrite growth and irreversible side reactions, leading to rapid battery degradation and hindering its further development [154]. In 1986, a type of mild zinc sulphate ($ZnSO_4$) aqueous electrolyte was developed by Yamamoto and co-workers, where the rechargeable Zn-MnO_2 battery was

operated with high cycle stability and coulombic efficiency [155]. The underlying mechanism of this novel battery system was not clearly understood until 2011 when Kang and co-workers revealed the operation mechanism of reversible Zn^{2+} insertion/extraction into/from the MnO_2 cathode using $ZnSO_4$ and zinc nitrate ($Zn(NO_3)_2$) aqueous electrolytes [156]. This is similar to how Li-ion batteries work and the concept of the "Zn-ion battery" was then proposed for the first time. Investigation interests in Zn-ion batteries have surged since then as researchers are seeking cost-effective and safe alternatives to Li-ion batteries.

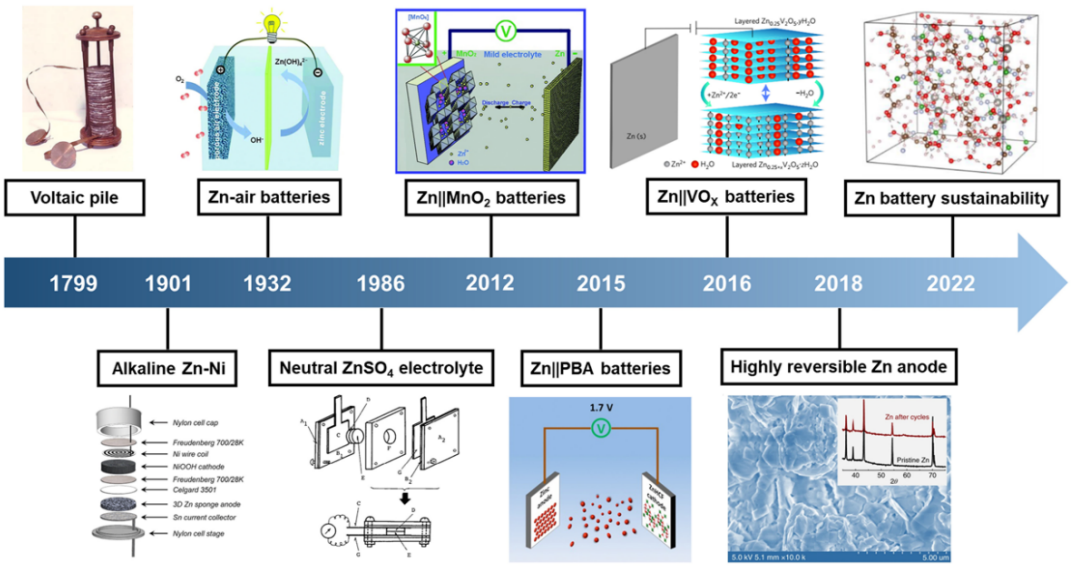


Figure 1.3 A timeline for the development of Zn-based batteries [145]**. Reproduced with permission, copyright 2023 Elsevier.**

1.2.2 Types of rechargeable Zn-based batteries

Generally, all Zn-based batteries utilise Zn metal as the anode. However, there are significant differences in terms of operating mechanisms and chemistry due to the utilisation of different electrolytes and cathode materials. Typical types of Zn-based batteries are compared in *Figure 1.4*, which includes Zn-air batteries, Zn-metal batteries, Zn-ion batteries, and systems using other conversion-type cathodes [157].

A typical Zn-air battery consists of the Zn metal anode, alkaline electrolyte, and air cathode integrated with oxygen electrocatalysts, which operates through the electrochemical reaction between the Zn metal and oxygen in the alkaline electrolyte. The output voltage of Zn-air batteries stands at about 1.4 V, and their energy density is significantly higher due to the use of oxygen as the cathode reactant (can be up to 440 Wh/kg). However, their short lifespan, poor kinetics and reliance on expensive catalysts can introduce problems [152,153].

Zn-metal batteries refer to a series of systems, mainly including Zn-Ag, Zn-Ni, Zn-Ni/Co, which have been commercially accessible and in use for long time [158]. Despite the high output voltage and relatively high energy density (e.g., 1.6 V and 140 Wh/kg for Zn-Ni batteries), severe side reactions and the rapid degradation in capacity still limit their further development.

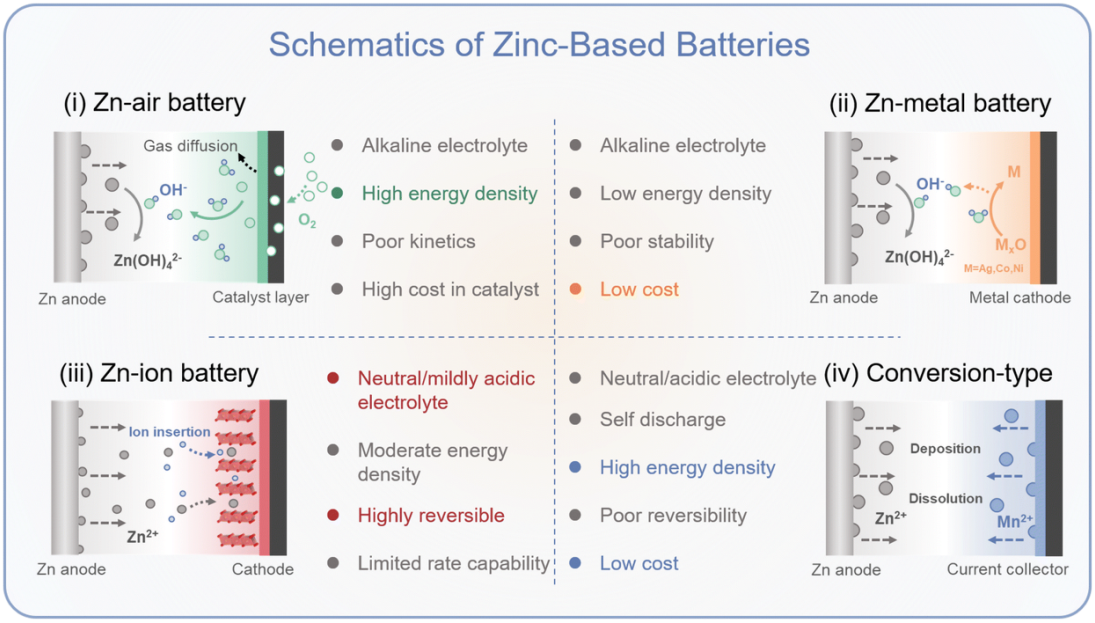


Figure 1.4 Comparison of the four main types of Zn-based batteries [157]. Reproduced with permission, copyright 2022 Royal Society of Chemistry.

Zn-ion batteries are a relatively new concept and have attracted intensive research interest in the last few years, composed of intercalation-type cathodes and neutral/mildly acidic electrolytes, where issues related to the utilisation of tradition alkaline electrolytes can be alleviated [140,159]. The performance of Zn-ion batteries with different cathodes varies significantly, depending heavily on the properties of the cathode materials, as summarised in *Figure 1.5*.

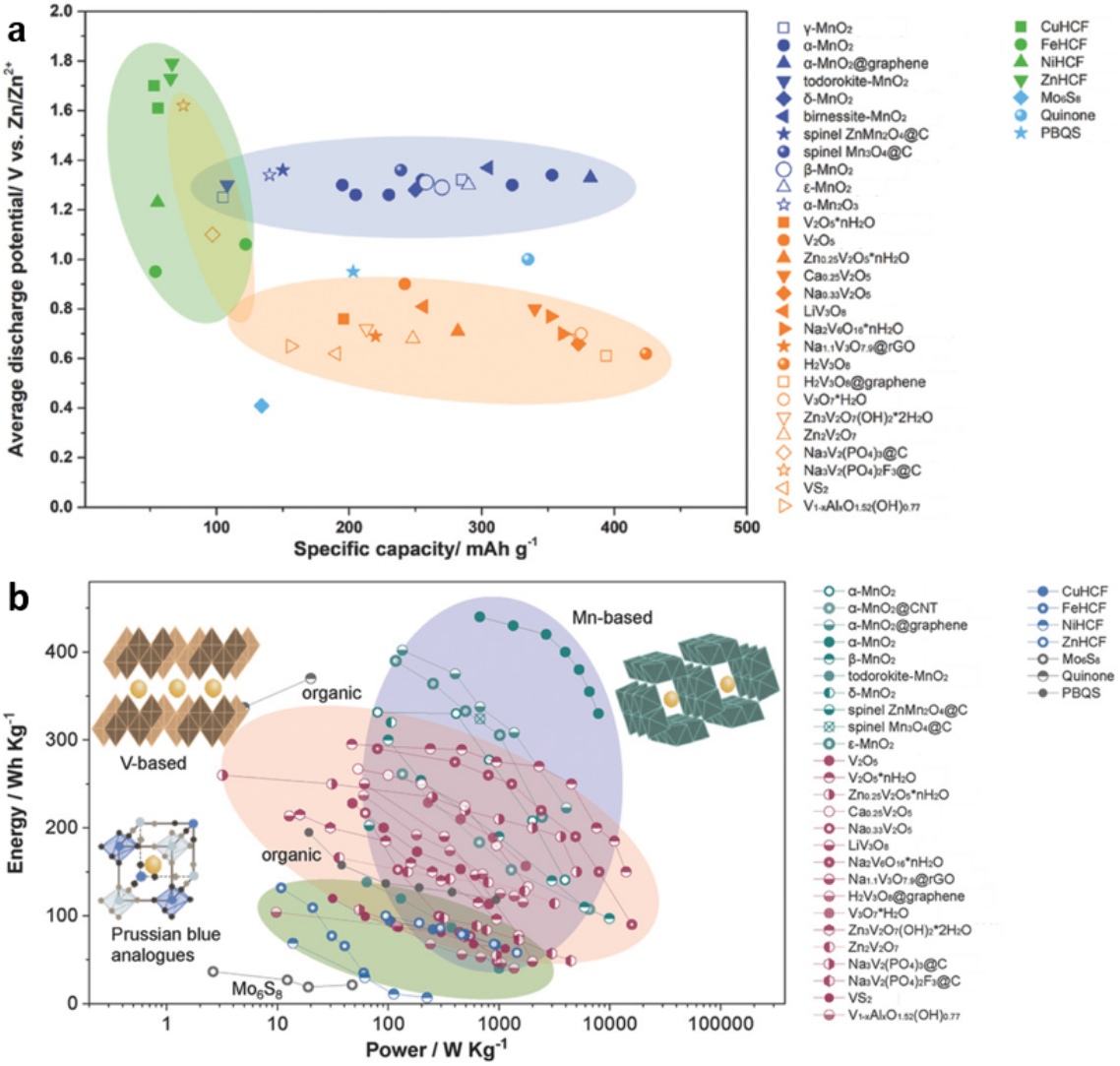


Figure 1.5 (a) Specific capacities, average discharge potentials, and (b) specific energy densities of representative cathode materials in Zn-ion batteries [140]. Reproduced with permission, copyright 2018 Wiley-VCH.

Except for the types of Zn-based batteries mentioned above, there are also innovative systems based on other conversion chemistries emerging as promising candidates, such as Zn-iodine (I_2) batteries [160], Zn-bromine (Br_2) batteries [148,161], Zn-chlorine (Cl_2) batteries [162], and electrolytic Zn-MnO_2 batteries [163,164].

1.2.3 Properties of Zn metal anodes

In theory, during the discharging process of the Zn battery, electrons are generated from the oxidation of zinc metal and move to the cathode side through the external circuit. While in practise, this process is always accompanied by various side reactions, such as the decomposition of water and the formation of byproducts, leading to the degradation of cycling performance [145,165].

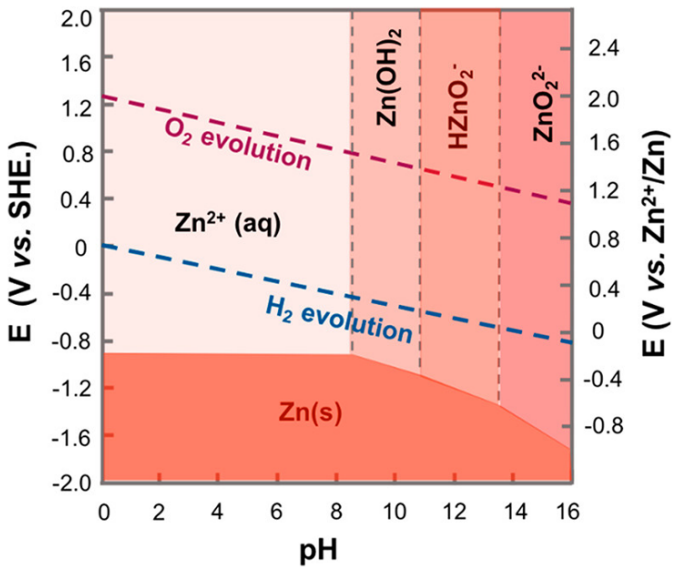


Figure 1.6 Pourbaix diagram of Zn/H_2O system [166]. Reproduced with permission, copyright 2020 American Chemical Society.

To comprehend the fundamental electrochemical processes and factors that limit performance of the Zn electrode, it is imperative to analyse the potential-pH equilibrium diagram (Pourbaix

diagram) of Zn within an aqueous environment [166]. As is shown in *Figure 1.6*, this diagram illustrates the potential equilibrium phases achievable across different pH ranges and equilibrium conditions. In the diagram, the region between the lines referring to hydrogen evolution reaction (HER) and oxygen evolution reaction represents the electrochemical window of water. It is evident from the diagram that Zn is thermodynamically unstable in aqueous solutions, making it susceptible to dissolution along with the evolution of H_2 gas across the entire pH spectrum, while the stable states vary. Under acidic conditions, Zn metal facilely dissolves and exists in the form of Zn^{2+} ions. Slightly alkaline solutions, where the pH resides between 8.0 and 10.5, foster the insoluble product $Zn(OH)_2$, which can cover the Zn metal surface and inhibit further dissolution of Zn. In strong alkaline environments, the solubility of Zn increases as the hydroxyl ions (OH^-) can complex with Zn^{2+} ions to form zincate ions, which can decompose to form ZnO. Therefore, due to different solutes and pH values in the working environments, Zn metal anodes in Zn-based batteries experience different chemical reaction behaviours in alkaline and mild/acidic aqueous electrolytes. This brings about a series of differences in terms of the reaction mechanism, redox potential and issues faced by the Zn electrode in different electrolyte types [165,167].

1.2.3.1 Zn metal anode in alkaline electrolytes

For the alkaline Zn electrolytes, LiOH, NaOH and KOH hydroxide compounds are usually used as the solutes in the electrolytes to create a strong alkaline environment, among which KOH is the most used due to its relatively higher ionic conductivity compared with others [154,165].

During storage, Zn metal can spontaneously react with OH^- in alkaline electrolytes (Equation 1.1) [168]. When being discharged, the Zn metal anode is oxidized and reacts with OH^- ions to yield $Zn(OH)_4^{2-}$, while when being charged the $Zn(OH)_4^{2-}$ ions are reduced to Zn, which is the deposition process. However, $Zn(OH)_4^{2-}$, resulted from both the self-corrosion and discharge process, will

easily decompose and generate insulating ZnO on the electrode surface, which is viewed as the passivation process, resulting in the inactivity of the Zn electrode and degradation of the whole battery [154,168]. The formation of ZnO also initiates a variety of problems concerning the morphology change of the Zn electrode, including the electrode surface roughening and exacerbation of dendrite growth [165,169]. These reactions can be demonstrated by equations as follows:

Self-corrosion process: $Zn + 2OH^- + 2H_2O \rightarrow Zn(OH)_4^{2-} + H_2$ (Equation 1.1)

Discharge process: $Zn + 4OH^- - 2e^- \rightarrow Zn(OH)_4^{2-}$ (Equation 1.2)

Charge process: $Zn(OH)_4^{2-} + 2e^- \rightarrow Zn + 4OH^-$ (Equation 1.3)

Passivation process: $Zn(OH)_4^{2-} \rightarrow ZnO + 2OH^- + H_2O$ (Equation 1.4)

At pH 14, the redox potential of the overall Zn/ZnO reaction above is -1.26 V vs. standard hydrogen electrode (SHE), below the standard potential of the HER in alkali media ($E = -0.059 \cdot pH$, -0.83 V vs. SHE at pH = 14), which leads to the thermodynamic favourability of the HER in alkaline Zn electrolytes during Zn deposition [165]. Therefore, in alkaline electrolytes, Zn metal electrode undergoes the reaction with water to produce ZnO and H_2:

HER: $2H_2O + 2e^- \rightarrow H_2 + 2OH^-$ (Equation 1.5)

1.2.3.2 Zn metal anode in neutral/mildly acidic electrolytes

In mild or acidic Zn systems, most electrolytes consist of soluble Zn salts, such as $ZnSO_4$, $Zn(NO_3)_2$, zinc chloride ($ZnCl_2$), zinc acetate ($Zn(CH_3COO)_2$), zinc trifluoromethanesulfonate ($Zn(OTf)_2$), and

zinc di[bis(trifluoromethylsulfonyl)imide] ($Zn(TFSI)_2$). Among these candidates, $ZnSO_4$ and $Zn(OTf)_2$ are most widely used due to their wide electrochemical window, good reversibility and relatively low price, while some anions of Zn salts, such as Cl^- and NO_3^-, can result in poor cycling performances [165,170,171].

The concept of Zn-ion batteries was first proposed when the $ZnSO_4$ aqueous electrolyte was developed, because the working mechanism of Zn metal anode in mild or acidic electrolytes is similar with that of a Li anode, where only Zn-ions are involved as the charge carrier [156]. Zn metal undergoes very slow corrosion in a completely neutral solution, but in practice most Zn salts present as mildly acidic, which will speed up self-corrosion during battery resting (that is, when the battery is not being actively cycled) [172,173]. During the charge and discharge process, Zn^{2+} ions are reversibly plated/stripped on/from the Zn metal anode surface with the reduction potential of -0.76 V vs. SHE. This process is also inevitably accompanied by the HER due to the higher redox H^+/H potential (E = -0.059 · pH, -0.41 V vs. SHE at pH = 7) [165]. The reaction equations are as follow:

Self-corrosion process: $Zn + 2H^+ \rightarrow Zn^{2+} + H_2$ (Equation 1.6)

Discharge process: $Zn - 2e^- \rightarrow Zn^{2+}$ (Equation 1.7)

Charge process: $Zn^{2+} + 2e^- \rightarrow Zn$ (Equation 1.8)

HER: $2H^+ + 2e^- \rightarrow H_2$ (Equation 1.9)

Despite no dense ZnO layer forming during battery operation, the Zn electrode in the mild and acidic environment will generate other insoluble byproducts by reacting with electrolytes [145,165].

For example, in the most widely used $ZnSO_4$ electrolyte, it has been reported that Zn metal suffers from corrosion by involvement of the Zn salt, thus forming a Zn-based basic salt byproduct with a hexagonal structure, zinc hydroxide sulphate $Zn_4(OH)_6SO_4{\cdot}xH_2O$ (ZHS) [174]. This as-produced byproduct layer usually has a loose and porous structure, and so does not function like the continuous SEI layer in Li batteries that blocks further side reactions, thus leading to continuing consumption of electrolytes and degradation of Zn batteries [175]. The reaction mechanism can be expressed as follow:

Byproducts: $4Zn^{2+} + SO_4^{2-} + 6OH^- + xH_2O \rightarrow Zn_4(OH)_6SO_4{\cdot}xH_2O$ (Equation 1.10)

It is worth noting that OH^- ions are involved in the formation of ZHS, despite the acidic chemical environment of electrolytes. This is related to both the chemical and electrochemical H_2 evolution during battery rest and cycling, which leads to the generation of OH^- and local pH increase near the electrode surface [174].

1.2.4 Summary and outlook

In summary, aqueous Zn-based batteries are promising alternatives to Li-ion batteries, particularly in the realms of stationary energy storage and biocompatible devices [157,176]. Although Zn metal is a most promising anode material for aqueous Zn-based batteries due to its safety, high abundance, nontoxicity, low price, and superior theoretical capacity, it is still facing a series of problems that hinder its practical use [177]. One of the main obstacles that impedes the further development of Zn-based batteries is the lack of suitable cathode materials. For instance, current cathode materials in Zn-ion batteries, such as Mn-based oxides, are still encountering sluggish diffusion kinetics of Zn ions during insertion/extraction. Furthermore, their underlying working and degradation mechanisms are still not fully understood. Therefore,

despite intensive studies have been conducted to clarify and mitigate these problems, strategies should be further developed to ease these challenges for more advanced Zn-based batteries.

From the anode side, despite the advantages of Zn metal, it still suffers from instability and poor reversibility. Zn metal anodes face different challenges in different electrolytes. In alkaline systems, this is mainly dendrite growth, HER, dissolution, shape change (due to partial surface densification by ZnO) and passivation. In mildly acidic electrolytes, issues of passivation and shape change can be avoided, while the dendrite issue and HER remain, and the formation of byproducts continuously consumes electrolyte species and Zn. These issues associated with the Zn metal anode in mildly acidic electrolytes of Zn-ion batteries, along with corresponding mitigation strategies, will be discussed in detail in Chapter 2.1. The underlying mechanisms will be further investigated in subsequent chapters.

Chapter 2 Literature review

2.1 Tackling issues of the Zn metal anode by electrolyte additives

2.1.1 Challenges of the Zn metal anode in Zn-ion batteries

Extensive efforts have been devoted to the development of novel cathode materials for Zn-ion battery systems since the concept was proposed, including various Mn-based compounds [178,179], vanadium-based compounds [180,181], Prussian blue analogues [182,183], and organic materials [184,185]. Compared with the intensive interest in developing cathode materials, research on the anode side for Zn batteries has attracted less attention until recently [141]. This is mainly because there has been little incentive to find new anode materials to replace metallic Zn anode, which has been widely considered to be the golden standard.

Despite their advantages, Zn metal anodes are still facing many challenges and are far from satisfactory [145,186]. As mentioned in the previous chapter, water stability of the Zn metal anode is only relative but not absolute. This intrinsic thermodynamic instability of Zn metal anodes in Zn-ion batteries with mildly acidic electrolytes can trigger spontaneous interfacial corrosion during storage [145,172]. Moreover, the dendrite formation and HER are inevitable issues during cycling, which are closely related to the electroplating process of Zn, as illustrated in *Figure 2.1*. First, Zn ions migrate from the bulk electrolyte to the electrode surface. Then, Zn ions coordinated with water molecules, $[Zn(H_2O)_6]^{2+}$, take off the solvation sheath, which is known as the de-solvation process, and are reduced to adatoms by accepting electrons from the electrode. At this stage, water molecules can also accept electrons from the electrode, making HER a competitive reaction of the Zn reduction. After that, Zn adatoms diffuse along the electrode surface to form Zn clusters, which can further form Zn dendrites. These issues during

both storage and cycling finally result in poor irreversibility and low coulombic efficiency of the Zn metal anode [145,186,187].

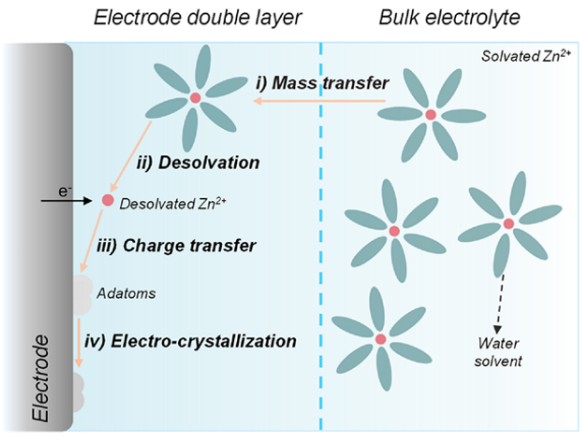


Figure 2.1 Schematic illustration of the Zn electrodeposition process [172]. Reproduced with permission, copyright 2022 Wiley-VCH.

2.1.1.1 Dendrite formation

Similar to other metal anodes, the Zn metal anode also suffers from the issue of dendrite formation during cycling [188]. As a hcp metal, Zn has an anisotropic lattice structure, and its electrodeposited morphology follows this intrinsic crystal symmetry. According to the Wulff construction method, which indicates the equilibrium crystalline shapes that exhibit minimum surface energies, the preferred crystal planes for Zn are (002), (100) and (101). Thus, Zn deposits usually show an intrinsic hexagonal flake shape (*Figure 2.2 a*). The higher hardness of Zn metal and the sharp edges of Zn flakes make it easier for Zn dendrites to penetrate separators, leading to internal short-circuits [189]. Additionally, the loose structure of Zn dendrites increases the risk of detachment of active Zn from the electrode surface, resulting in 'dead Zn' and capacity loss [190]. Therefore, a uniform and compact deposition layer (*Figure 2.2 b*) is essential for achieving high coulombic efficiency and long lifespan (> 200 h) of Zn-ion batteries [190].

The nucleation process of Zn on the electrode surface is shown in *Figure 2.2 c*. Following the reduction of Zn ions, the Zn atoms first undergo a 2D diffusion process, during which the Zn atoms diffuse along the electrode surface to accumulate and form initial nuclei at energetically favoured sites, such as protrusions, lattice defects, impurities, and boundaries [89,191]. These inhomogeneous nuclei further evolve into Zn tips or protrusions, which in turn cause an uneven distribution of the electric field. Consequently, subsequent ions are inclined to be deposited on the existing tips, eventually leading to the formation of dendrites. This 'tip effect' is therefore a self-amplifying process, with sharp protrusions continuing to grow once formed [165,192]. Moreover, Zn deposits usually adopt a hexagonal flake shape, and the random orientation of these Zn flakes, especially the vertical growth, further aggravates dendrite formation, resulting in dead Zn and short-circuits (*Figure 2.2 d*).

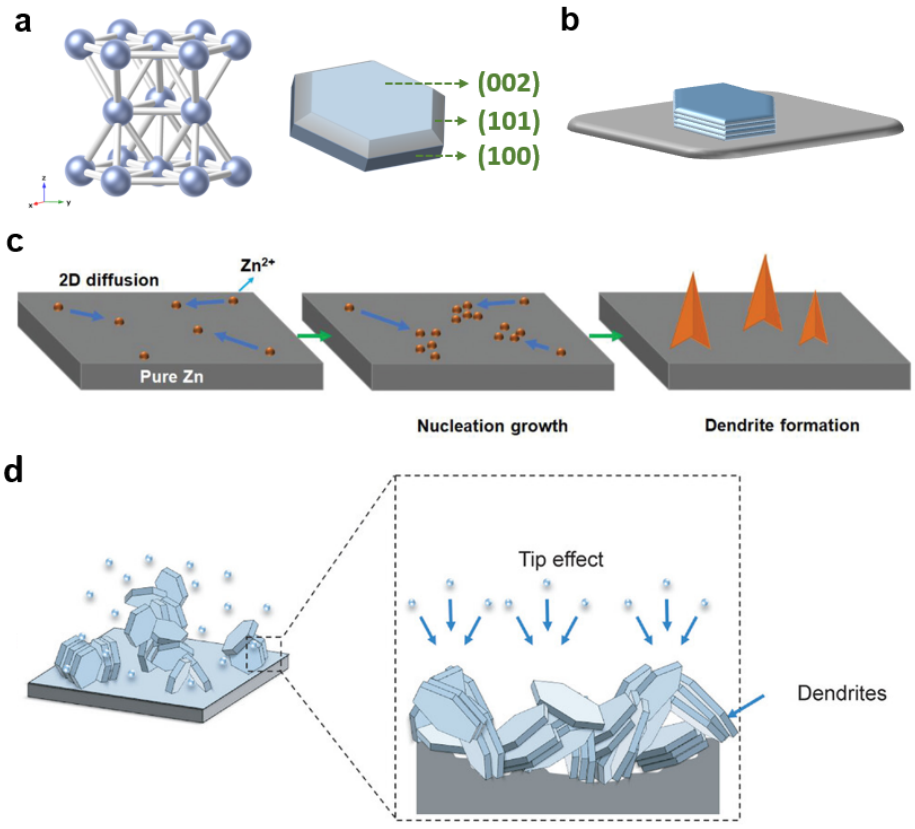


Figure 2.2 (a) The crystal structure and Wulff plot of the equilibrium shape of Zn metal, with facets indicated. (b) Schematic illustration of the uniform and compact Zn deposition layer. (c) Schematic

illustration of the Zn dendrite formation due to 2D diffusion [193]**. Reproduced with permission, copyright 2022 Wiley-VCH. (d) Schematic illustrating the random orientation of Zn flakes with loose structures** [194]**. Reproduced with permission, copyright 2024 Wiley-VCH.**

In general, the formation of Zn dendrites is determined by the unrestricted 2D diffusion and uneven electric field distribution. Other influencing factors such as the morphology of the Zn metal anode [195], the electrolyte formulation [196], current density [189,197], temperature [198,199], overpotential [200], and internal/external stress [201] should also be considered carefully during practical cycling.

2.1.1.2 HER

The HER is a severe safety hazard in the industrialization of water-based batteries, which will potentially increase the internal pressure of cell packs, leading to battery swelling and even raising the risk of explosions [177,202]. The performance of Zn-ion batteries degrades due to the HER in several ways, including the decomposition of electrolytes and aggravation of dendrite formation, ultimately resulting in poor reversibility and capacity decay, significantly shortening the lifespan of Zn-ion batteries [145]. Consequently, this poses a big threat to the practical commercialisation of Zn-ion batteries. It should be noted that the HER is inevitable during both the rest and the cycling period of batteries. The reaction mechanism and impact on the battery performance of the HER during battery rest will be further discussed in the subsequent section.

Theoretically, the equilibrium potential of Zn^{2+}/Zn is lower than that of the H_2/H_2O across the entire pH range (*Figure 1.6*), indicating the thermodynamically spontaneous occurrence of HER on the Zn metal anode in aqueous electrolytes. The reduction potential of the Zn^{2+}/Zn redox couple in mildly acidic electrolytes is less negative, suggesting alleviated HER compared to that in alkaline solutions. Moreover, Zn metal intrinsically possesses a relatively high kinetic

overpotential for HER, thereby slowing down the HER rate to some extent [203]. However, given the susceptibility of the HER overpotential to multiple factors, such as the electrode morphology, byproducts, and electrolyte environments, the HER remains a threat to the long-term stability of Zn-ion batteries [175,204].

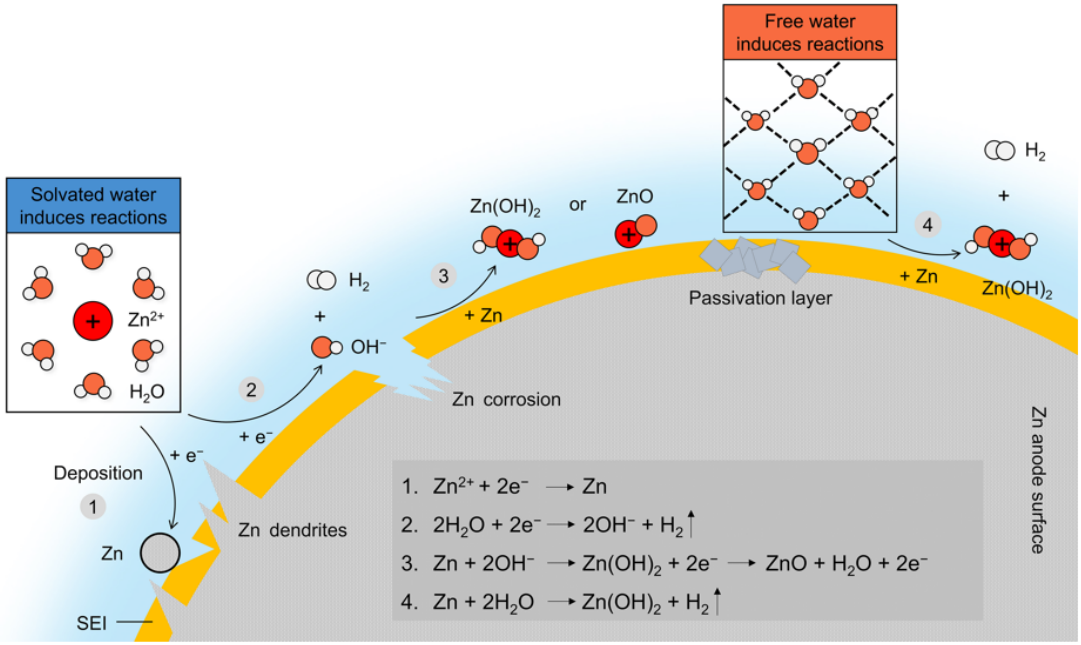


Figure 2.3 Overview of the HER mechanisms and the association with corrosion, passivation, and dendrite growth [205]**. Reproduced with permission, copyright 2023 The Authors.**

As shown in *Figure 2.3*, the decomposition of water molecules is a competitive reaction with the reduction of Zn. On one hand, in dilute aqueous mild acidic electrolytes, Zn ions, coordinated with six water molecules, will take off the water-containing solvation sheath before receiving electrons from the electrode to reduce to Zn adatoms. Such de-solvation process releases free water molecules with weakened H-O bonding, which are more active and easily reduced to form H_2 [206]. On the other hand, massive free water molecules in electrolytes can move and adsorb onto the electrode surface, further triggering water-involved side reactions [172]. Therefore, strategies to suppress the HER can be devoted to stabilizing water molecules through either

modification of the solvation structure modification or constraint of free water in the electrolyte, which will be further discussed in the following section.

2.1.1.3 Corrosion

Taking the most commonly used $ZnSO_4$ aqueous electrolyte as an example, the main corrosion byproducts, ZHS, typically exhibit porous and loose structures (*Figure 2.4 a*), which resemble Zn flakes [187]. As shown in the scanning electron microscopy (SEM) images in *Figure 2.4 b and c*, these corrosion-induced species lack the ability to shield the electrode surface from the electrolyte, leading to continuing consumption of active Zn, water and Zn salts [174,207].

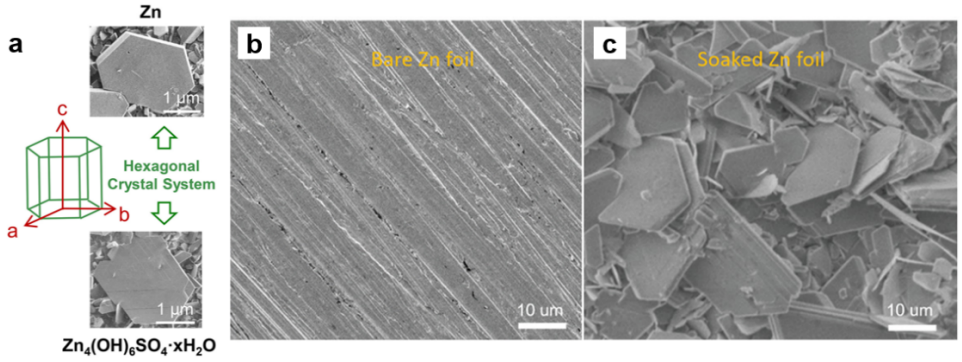


Figure 2.4 (a) Similarities between Zn and ZHS in the structure and morphology [187]**. Reproduced with permission. Copyright 2023 Elsevier. SEM images of the Zn foil (b) before and (c) soaking in the 1 M $ZnSO_4$ electrolyte** [207]**. Reproduced with permission, copyright 2020 Wiley-VCH.**

The corrosion process of the Zn metal anode in Zn-ion batteries is closely related to the HER occurring during both rest and cycling. Although the reduction potential of redox couples is increased in mildly acidic electrolytes compared to that in alkaline electrolytes, the Zn metal electrode actually experiences more severe HER during battery rest, due to a lower pH value of electrolytes [165,208]. After prolonged rest of sealed Zn-ion pouch cell batteries, apart from the safety hazard from volume swelling (*Figure 2.5 a*), hydrogen gas stemming from corrosion also

poses a risk of deactivating the zinc anode due to the screening effect of bubbles, which isolate Zn from contact with electrolyte (*Figure 2.5 b*) [209,210]. Both the decomposition of water molecules during cycling and consumption of H^+ ions during rest contribute to the extra OH^- ions, leading to a local pH increase and thus generating the precipitation of basic insoluble corrosion byproducts [165]. These challenges arising from corrosion significantly reduce not only the cycling life but also the shelf life after battery assembly even before use, thereby considerably constraining the practical application of Zn-ion batteries [177].

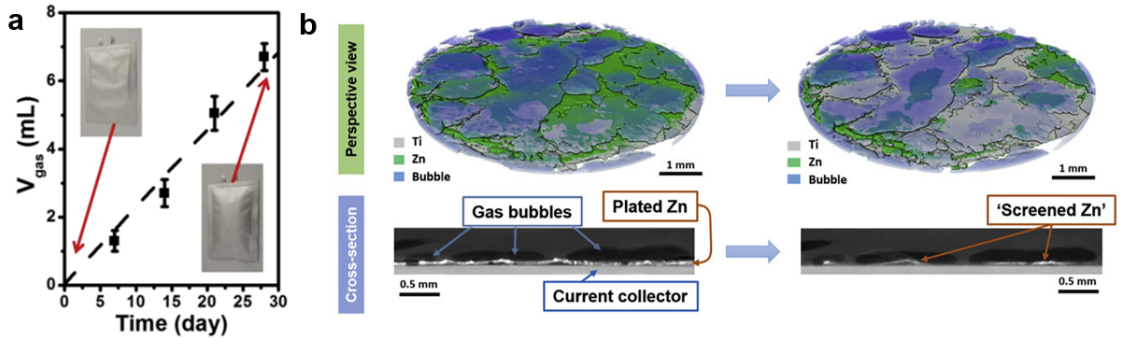


Figure 2.5 (a) The volume change of the Zn||Zn pouch cell using 3 M $ZnSO_4$ electrolyte [209]**. Reproduced with permission, copyright 2020 Elsevier. (b) Images of Ti anode surfaces after plating and 48 h rest, and after stripping, obtained by in situ X-ray computed tomography** [210]**. Reproduced with permission, copyright 2023 Elsevier.**

It is worth noting that the problems of dendrite formation and side reactions are correlated with each other. On one hand, the loose structure of Zn dendrites enlarges the volume and active area of the electrode, which exacerbates the corrosion process. On the other hand, the byproduct layer and morphological changes generated by parasitic reactions will induce uneven distribution of the electric filed and heterogeneous nucleation, further triggering the formation of dendrites. This vicious circle between dendrite growth and side reactions eventually results in the failure of Zn-ion batteries.

2.1.2 Electrolyte additives for stabilizing Zn metal anodes

A variety of strategies have been proposed from multiple perspectives to mitigate issues associated the Zn metal anode in Zn-ion batteries. For instance, controlling the composition and crystal structure of the Zn metal anode can effectively curb the growth of Zn dendrites [190,193,209]. Isolating the Zn metal from the electrode by applying artificial surface coatings not only suppresses side reactions but also promotes homogeneous deposition [211,212]. Furthermore, the electrolyte plays a crucial role in determining the overall performance of Zn-ion batteries. Consequently, numerous methods to enhance the properties of electrolytes have attracted significant research interest recently. These methods include optimising the types of salts and solvents [213,214], adjusting concentrations [215], incorporating additives [199,216], and developing innovative electrolyte formulations such as ionic liquids [217], deep eutectic electrolytes [218], gel electrolytes [219], and all-solid-state electrolytes [220].

Among these strategies, the addition of additives to electrolytes stands out as a most straightforward and efficient way to enhance the overall performance of Zn-ion batteries. In this section, various mechanisms through which additives contribute to the enhanced functionality and efficiency of the Zn metal anode are compared and summarised. These mechanisms include electrostatic shielding, adjustments to the solvation structure and water activity, in situ SEI formation, adsorption on the electrode surface, and texture regulation.

2.1.2.1 Electrostatic shielding additives

The concept of electrostatic shielding was first proposed as an effective mechanism for suppression of Li dendrites [221]. As demonstrated in *Figure 2.6 a*, caesium (Cs^+) and rubidium (Rb^+) cations, which have lower reduction potentials than Li^+ ions, are introduced into the electrolyte. These cations are preferentially adsorbed onto Li protrusions to form a positively charged shielding layer, thus repelling subsequent accumulation of Li on the tips, until a uniform

and smooth deposition layer is achieved. This electrostatic shielding effect has been widely adapted to alleviate Zn dendrites recently [222]. Many additives have been reported to function via the electrostatic shielding mechanism to ease the Zn dendrite formation.

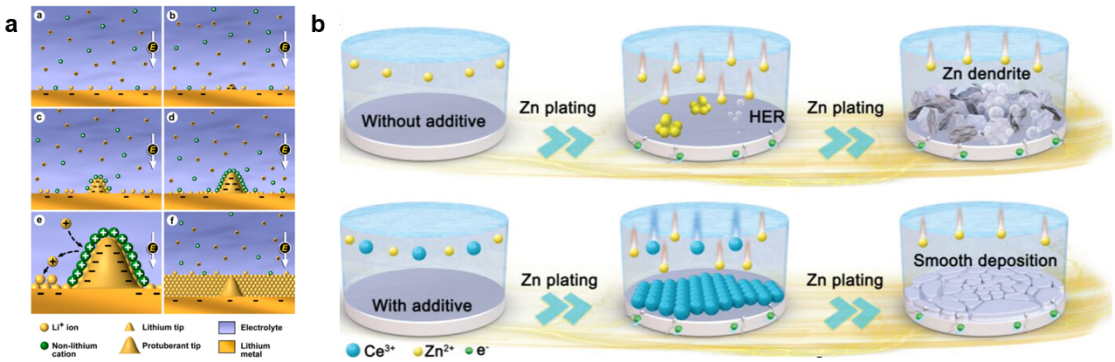


Figure 2.6 (a) Schematic illustration of Li deposition process based on the self-healing electrostatic shield mechanism [221]**. Reproduced with permission, copyright 2013 American Chemical Society. (b) Schematic illustration of the effect of $CeCl_3$ additive on the Zn deposition process** [223]**. Reproduced with permission, copyright 2022 Wiley-VCH.**

A series of metal ions with lower reduction potentials, including monovalent Li^+ [224], Na^+ [225], Rb^+ [226], divalent Mg^{2+} [227], Mn^{2+} [228], Ni^{2+} [229], and trivalent lanthanum (La^{3+}) [230], cerium (Ce^{3+}) [223], scandium (Sc^{3+}) [231] and yttrium (Y^{3+}) [232] ions, have been identified as effective electrostatic shielding additives. For example, as shown in *Figure 2.6 b*, the introduction of Ce^{3+} into the $ZnSO_4$ electrolyte has been reported to facilitate uniform Zn deposition and enhanced cycling stability, as evidenced by a variety of in situ characterisations and simulations. Furthermore, it has been demonstrated that by incorporating certain cations that are components of cathode materials of Zn-ion batteries, such as Na^+ and Mn^{2+}, into the electrolytes, not only is the Zn dendrite growth eliminated, but also dissolution from the cathode side is greatly reduced (*Figure 2.7 a*) [225]. Besides, several key descriptors, such as the differential capacitance [233] and the exchange rate constant (k_{ex}) [234], have been proposed to screen and evaluate the shielding ability of additive cations.

Except for the metal cations above, some non-metallic cations as well as organic molecules have also been identified as electrostatic shielding additives. For instance, the addition of ammonium salts [235] or ammonium hydroxide [236] into electrolytes has been reported to facilitate dendrite-free deposition due to the preferential adsorption of NH_4^+ cations onto Zn protrusions. Additionally, as illustrated in *Figure 2.7 b*, a cationic surfactant-type additive, tetrabutylammonium sulphate (TBA_2SO_4), has been shown to induce uniform Zn deposition through the electrostatic adsorption of TBA^+ cations on protuberances, which can drive Zn ions to deposit onto the adjacent flat regions [237]. Moreover, some highly polarized organic molecules, such as diethyl ether [238], theanine [239], etc., also exhibit the capability to prevent accumulation of subsequent Zn ions on the tips by providing similar shielding effects.

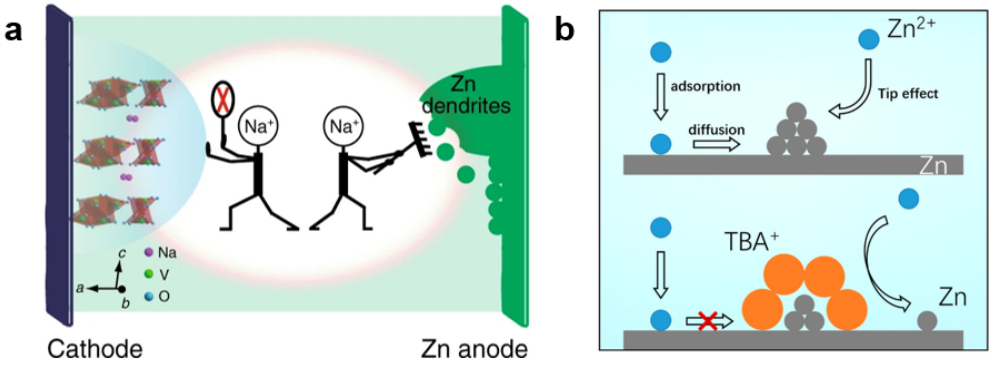


Figure 2.7 (a) Schematic diagram showing the Na_2SO_4 additive suppresses the dissolution of Na from the cathode and the formation of Zn dendrites on the anode side [225]**. Reproduced with permission, copyright 2018 The Authors. (b) Schematics of the Zn ion diffusion and reduction processes without and with TBA_2SO_4** [237]**. Reproduced with permission, copyright 2020 American Chemical Society.**

2.1.2.2 Solvation structure and water activity adjustment additives

As mentioned above, water decomposition is a competitive reaction with Zn deposition, thus inevitably leading to the HER during operation of Zn-ion batteries. Recent studies have shown

that the solvated water within the solvation sheath of Zn ions is endowed with a higher activity in HER [240]. Consequently, altering the solvation structure of Zn ions by substituting the active water molecules with other compounds is considered an effective strategy to supress HER and other side reactions [241,242].

A number of organic additive compounds containing polar hydroxyl and carbonyl groups, have been identified as preferentially involved in the solvation sheath of Zn ions, such as sulfone- [243,244], alcohol- [245,246], ether- [247–249], amide- [250], ester- [251], and ketone- [252] based chemicals. Common organic solvents that regulate Zn solvation structures include dimethyl sulfoxide (DMSO) [243], N-methyl-2-pyrrolidone (NMP) [253], tetrahydrofuran [249], ethylene glycol [245], glucose [254], and pyridine [255], etc.

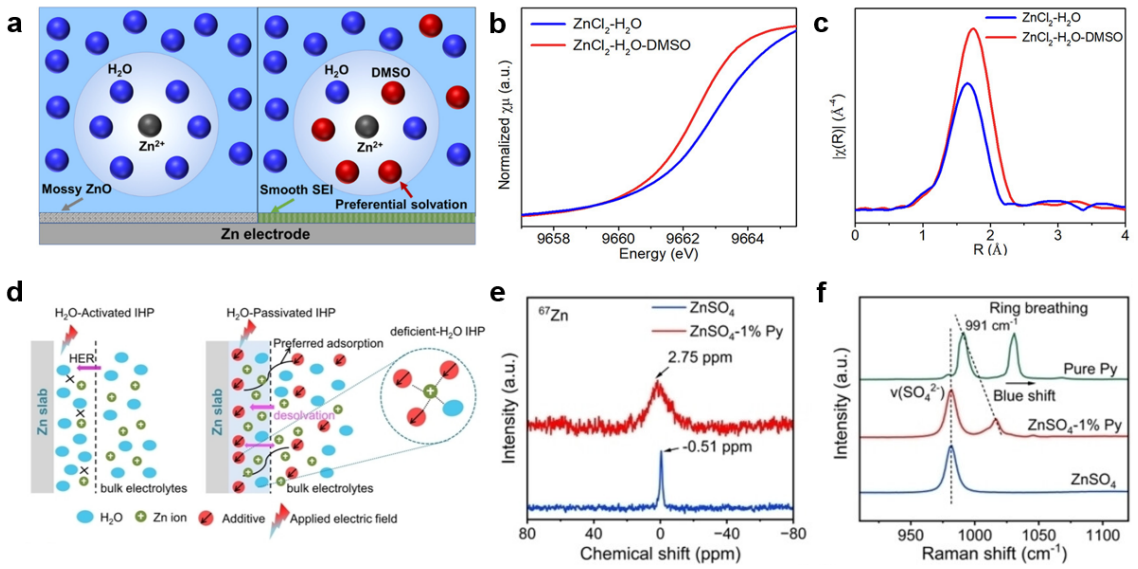


Figure 2.8 (a) Scheme of Zn solvation structures, as well as (b) XANES and (c) ft-EXAFS spectra of electrolytes without and with DMSO [243]. Reproduced with permission, copyright 2020 American Chemical Society. (d) Schematic illustration of pyridine-manipulated inner Helmholtz plane, (e) ^{67}Zn NMR and (f) Raman spectra of electrolyte without and with pyridine [255]. Reproduced with permission, copyright 2023 Wiley-VCH.

The successful integration of these organic additives into the solvation sheath can be verified through a series of spectroscopic characterisations, such as the Raman spectroscopy, Fourier transformed infrared (FTIR) spectroscopy, nuclear magnetic resonance spectroscopy (NMR), X-ray absorption near-edge structure (XANES) spectroscopy and Fourier transformed extended X-ray absorption fine structure (ft-EXAFS) spectroscopy. For example, as given in *Figure 2.8 a-c*, from the XANES and EXAFS spectra, the addition of DMSO led to a shift of the edge position to a lower energy and an increased Zn-O bond length, both indicative of the weakening interactions between Zn ions and water molecules within the solvation sheath, which is beneficial for inhibiting parasitic side reactions [243]. Pyridine ligand has been reported to effectively regulate the solvation sheath of Zn ions by replacing partial solvated water molecules, as evidenced by Raman and NMR measurements (*Figure 2.8 d-f*) [255].

Besides replacing water molecules in the solvation structure, some organic additives are also able to constrain free water molecules in the bulk electrolyte by hydrogen bonding (H-bond). Chao and co-workers [256] have systematically categorized the regulation strategies of hydrogen bond in the water network into three types: reconstructing, strengthening and breaking, as illustrated in *Figure 2.9 a*. The rapid proton transport can be blocked by adding additives consisting of H-bond acceptors with a high donor number, thus rebuilding the initial water-water H-bond network and forming new additive-water network. Additives working via such mechanism include DMSO [199], NMP [257], 1,3-dimethyl-2-imidazolidinone [258], and N, N-dimethylacetamide (DMA) [259]. For instance, as shown in *Figure 2.9 b*, the addition of 10% DMA in the $ZnSO_4$ electrolyte, which has a high donor number of 27.8, was found to effectively establish new bonding with free water molecules, thus enhancing the stability and reversibility of the Zn metal anode [259]. The activity of free water was successfully restricted by introduction of ectoine into the electrolyte as well [260]. The enhanced hydrogen bonding between water and

ectoine increased the energy barrier for the proton transfer between water molecules, thus suppressing the HER (*Figure 2.9 c*).

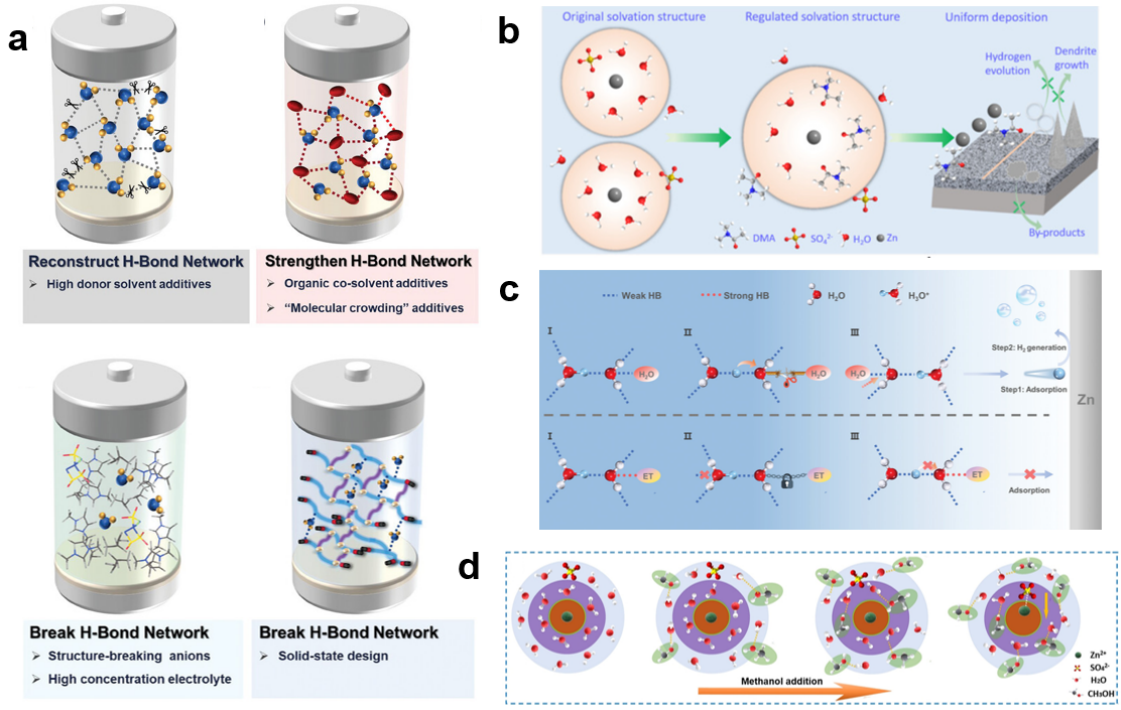


Figure 2.9 (a) Four strategies to regulate H-bond network in the bulk electrolyte [256]**. Reproduced with permission, copyright 2024 Wiley-VCH. (b) Schematic illustration of Zn solvation structure with and without DMA** [259]**. Reproduced with permission, copyright 2022 Elsevier. (c) Schematic illustration of the proton transfer through hydrogen bonds in the electrolyte without and b) with ectoine** [260]**. Reproduced with permission, copyright 2023 Wiley-VCH. (d) Schematic showing changes in the Zn solvent sheath with methanol addition** [261]**. Reproduced with permission, copyright 2021 Wiley-VCH.**

Furthermore, some additives functioning as co-solvents or molecular crowding agents are believed to strengthen the H-bond network due to their stronger dipole interactions, significantly impeding the motion of free water. These additives include co-solvents such as sulfolane [262], acetone [263], and other molecule crowding agents including cyclodextrin [264], xylitol [265], and maltose [266]. Additionally, some antisolvent additives have also been reported to restrict side reactions of Zn metal anodes, which can interact with both free and coordinated

water in the solvation sheath [261,267]. For example, Qiao et al. [261] demonstrated that in the low-cost methanol-based antisolvent electrolyte, the HER and dendrite formation were effectively suppressed, which is attributed to the reduced water activity and weakened solvation of Zn ions in the electrolyte (*Figure 2.9 d*).

2.1.2.3 In situ SEI formation additives

The strategy of regulating the in situ SEI has been widely adopted in Li-ion systems to facilitate durable electrode/electrolyte interfaces, which can inhibit dendrite growth and improve anode stability [105,268]. The in situ formed protective layer simultaneously develops upon contact between the electrode and the electrolyte or during battery cycling [269].

An ideal SEI layer should be electronically insulating and ionically conductive, and endowed with robust and uniform structures to prevent the electrode surface from coming into direct contact with the electrolyte [104]. However, the pristine by-products generated on the Zn electrode in Zn-ion batteries usually exhibit non-uniform structures and will lead to continuous active Zn consumption and gas production, thereby degrading rather than retaining battery performance [145,165,174]. To enable such by-products to work as functional SEI layers with dense structures, several studies have explored the possibility to form homogeneous byproduct-based protective interfaces, for instance, by adding $Zn(OH)_2$ to encourage the uniform formation of ZHS (*Figure 2.10 a*) [270], or by adding surfactants to generate the ZnO layer with a uniform honey-comb structure (*Figure 2.10 b*) [271].

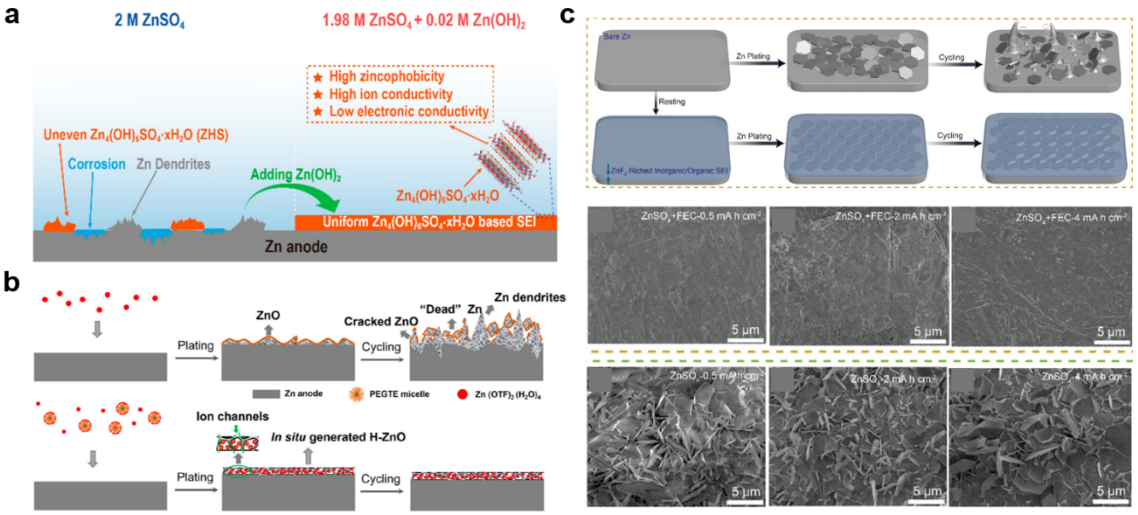


Figure 2.10 (a) Schematic of the Zn surface evolution in the $ZnSO_4$ electrolyte with $Zn(OH)_2$, generating the uniform ZHS-based SEI [270]**. Reproduced with permission, copyright 2021 American Chemical Society. (b) The formation mechanism of the honeycomb-like ZnO passivation protective layer by addition of the surfactant** [271]**. Reproduced with permission, copyright 2022 American Chemical Society. (c) Schematic illustrations for Zn deposition behaviours in $ZnSO_4$ and $ZnSO_4$/FEC electrolytes, and corresponding SEM images with various deposition capacities** [272]**. Reproduced with permission, copyright 2022 Wiley-VCH.**

Some recent research has turned to the compositional modification of the in situ SEI layer, which can be achieved by the decomposition of the additives [269,273]. For example, a fluorine-contained additive, fluoroethylene carbonate (FEC), was introduced to produce a Zn ZnF_2-riched inorganic/organic hybrid SEI layer on the Zn metal anode surface, as shown in *Figure 2.10 c* [272]. Due to its instability in the aqueous solution, FEC tends to hydrolyse to form HF and other new compounds, thus eliminating the passivation from the ZHS byproducts and facilitating the formation of the ZnF_2-rich SEI layer. Such a ZnF_2-rich SEI was able to suppress corrosion and induce uniform deposition.

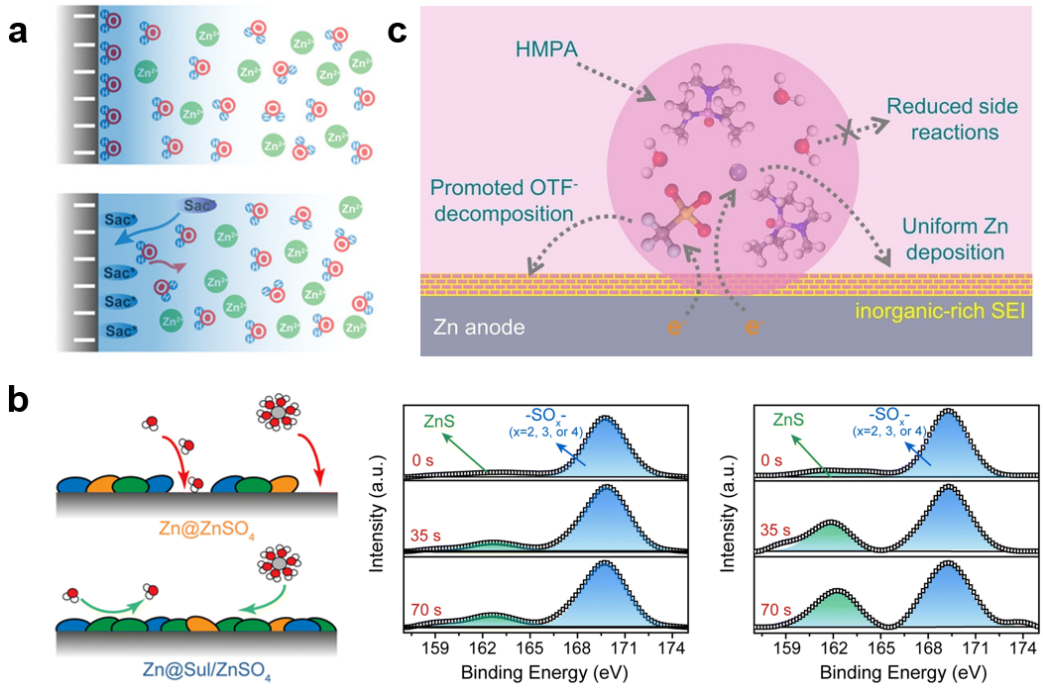


Figure 2.11 (a) Schematic descriptions of changes in EDL structures before and after introducing saccharin [274]**. Reproduced with permission, copyright 2021 Wiley-VCH. (b) Illustration of the improved protective effect by the SEI formed with Sulfolane, and corresponding XPS depth profiles** [275]**. Reproduced with permission, copyright 2023 Royal Society of Chemistry. (c) Schematic illustrating the underlying mechanism for HMPA to enhance the electrochemical performance** [276]**. Reproduced with permission, copyright 2023 Wiley-VCH.**

It has been widely accepted that the electric double layer (EDL) plays a significant role in building the SEI layer [277]. Many additives that function as EDL regulators are introduced to construct stable electrode/electrolyte interfaces [278]. As is shown in *Figure 2.11 a*, the additive of saccharin demonstrates a stronger affinity to the Zn surface, leading to a water-poor EDL structure and the saccharin derived SEI layer [274]. Hence, side reactions and dendrite formation were inhibited due to the isolation of water from the electrode surface and the modulation of Zn diffusion. Recently, a series of EDL regulators were systematically evaluated and the difference in their SEI capability was identified as a predominant factor that distinguished their cycling performance [275]. Among them, the electrolyte with 0.5 vol% sulfolane was found to

effectively impede corrosion behaviour and manipulate nucleation processes. The X-ray photoelectron spectroscopy (XPS) depth profiles confirmed the in situ formation of a ZnS-rich SEI layer derived from the decomposition of sulfolane (*Figure 2.11 b*).

It is also worth noting that even though some additives are not directly involved in the formation of the SEI, their participation in altering the solvation structures of Zn ions can promote the reduction of salt anions, thereby forming favourable products and protective layers [279]. For example, hexamethylphosphoric triamide (HMPA) is reported to be able to reshape the solvation structure of Zn ions [276]. As shown in *Figure 2.11 c*, the addition of HMPA into the electrolyte can promote the decomposition of the salt anions, trifluoromethane sulfonate ions (OTF^-), forming a ZnF_2 and ZnS-rich inorganic SEI layer on the Zn metal anode, due to their proximity to Zn ion centres.

2.1.2.4 Electrode surface adsorption additives

Besides the in situ SEI layers, another type of protective layers can also be formed by additives adsorbed onto the Zn electrode surface [216]. Surfactants are representative additive ingredients considered to follow this mechanism. They are a class of electrochemically inert compounds that possess a polar hydrophilic head, which can adsorb on the Zn surface, and a non-polar hydrophobic tail, which can prevent water contact and regulate Zn ion distribution, thereby inhibiting dendrite growth and side reactions, promoting the stability of the Zn anode [280].

Typical surfactants include ionic sodium dodecyl sulfonate [281], sodium dodecylbenzene sulfonate [282], ethylenediaminetetraacetic acid tetrasodium [283], etc. Recently, Guan and co-workers compared a series of quaternary ammonium cationic surfactants, as is shown in *Figure 2.12 a* [284]. Among them, the benzyltrimethylammonium ($TMBA^+$) with a main benzyl group was found to assemble a hydrophobic interface, which efficiently inhibited side reactions and

regulated zinc uniform deposition. In addition, some non-ionic surfactants and polymers, such as polyethylene oxide (PEO) [285], polyethylene glycol [286], polyvinylpyrrolidone [287], and polyaspartic acid [288], have also be employed to form the adsorption protective layer. As shown in *Figure 2.12 b*, the long-chain PEO was employed as the additive to regulate the Zn flux near the electrode surface, thus inducing smooth deposition and supressing gas generation [285].

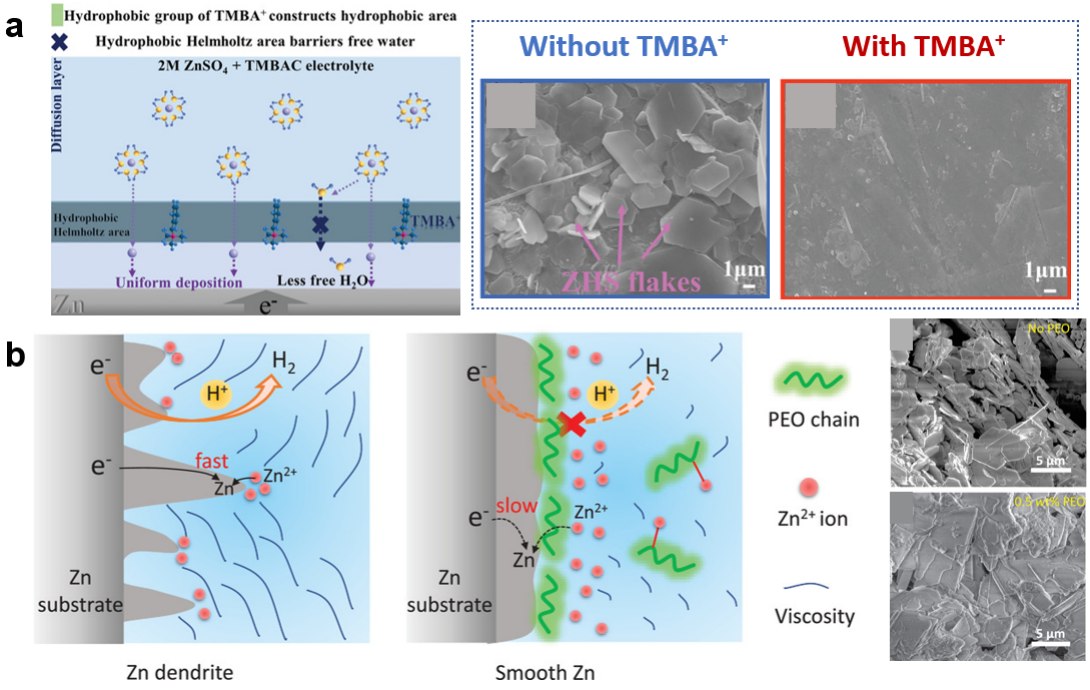


Figure 2.12 (a) Schematic diagram for comparisons of adding different quaternary ammonium cationic surfactants to form the hydrophobic interface and SEM images of Zn metal anodes after cycling [284]. Reproduced with permission, copyright 2022 Wiley-VCH. (b) Schematics of the Zn deposition without and with PEO and corresponding SEM images of Zn surfaces [285]. Reproduced with permission, copyright 2020 Wiley-VCH.

2.1.2.5 Texture regulation additives

Zn deposits typically exhibit a hexagonal flake morphology, primarily characterised by three major crystal planes: the (100), (101), and (002) facets [187]. It is generally believed that the (100) plane tends to accumulate Zn ions and promote dendrite formation. In contrast, the (002) plane

is known for its corrosion resistance and supports parallel growth according to both theoretical calculation and experiment results [289]. Certain texture regulation additives can manipulate the orientation of Zn deposits by selectively adhering to specific crystal planes, thereby controlling their growth to promote preferred textural development [216,290].

For example, phosphoric acid was used as a texturing agent to facilitate the (002) epitaxial growth of Zn deposits [291]. As is illustrated in the X-ray diffraction (XRD) pattern and SEM image (*Figure 2.13 a*), this effect was attributed to the less etched (002) planes by the acid treatment, creating a (002) textured substrate surface, thus leading to the epitaxial growth.

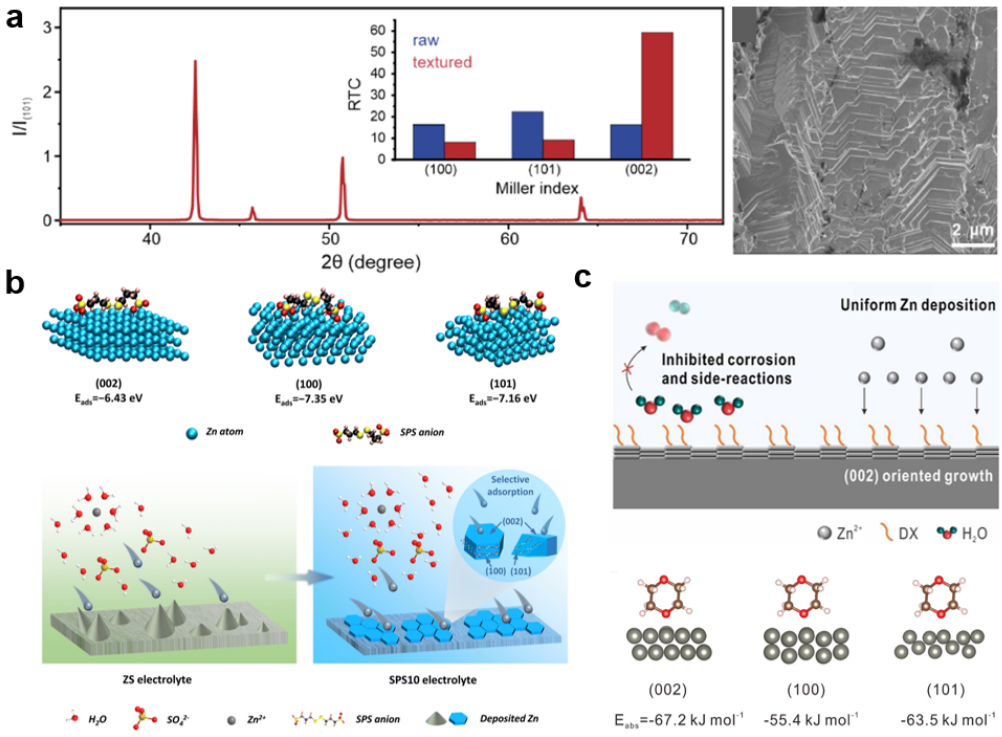


Figure 2.13 (a) XRD and SEM image of the textured Zn foil [291]. Reproduced with permission, copyright 2022 Elsevier. (b) The adsorption energy between SPS anion and Zn metal anode surface at the facets of (002), (100) and (101), and the schematic of the Zn deposition process without or with SPS [292]. Reproduced with permission, copyright 2023 Royal Society of Chemistry. (c) Schematic of Zn deposition process and the adsorption energy of 1,4-dioxane molecules on the Zn (002), (100), and (101) surfaces [293]. Reproduced with permission, copyright 2023 American Chemical Society.

More additives are believed to regulate the orientation of Zn deposits through their preferred adsorption onto specific facets, thus guiding the directional growth of Zn deposits. For instance, as shown in *Figure 2.13 b*, an anionic surfactant, sodium 3,3′-dithiodipropane sulfonate (SPS), was reported to preferentially adsorb onto other facets other than (002) planes, inducing the preferred growth in the (002) direction to form a compact deposition layer [292]. Additionally, 1,4-dioxane was also introduced to regulate the nucleation and diffusion of Zn to promote exposure of Zn (002) facets [293]. In contrast, the 1,4-dioxane additive exhibited a stronger adsorption onto the (002) facets compared to (100) and (101) planes, according to the calculations of adsorption energies, thus preventing deposition in the (002) direction and favouring its exposure (*Figure 2.13 c*).

2.1.3 Summary and outlook

Improving the performance of the Zn metal anode by electrolyte additive engineering has proven to be a straightforward and effective strategy by numerous studies. The functioning mechanisms of these additives involve regulating nucleation behaviours, altering the solvation structures, and contributing to the SEI formation. It should be noted that most additives function via several of the aforementioned mechanisms.

Although the benefits of additive engineering have been outlined, there are still challenges that remain to be addressed. For instance, despite improvements in the electrochemical performances, the underlying mechanisms for many additives remain complex and partially unclear. Advanced characterisation is necessary to validate proposed mechanisms and understand the effects of additives. In addition, there is a pressing need to exploit more scalable, low-cost and environmental-friendly methods, thereby paving the way for practical utilisation

of high-performance Zn-ion batteries. Moreover, exploring viable solutions under extreme conditions, such as ultra-low and ultra-high temperatures, holds immense potential for expanding the utility and applicability of Zn-based batteries across a broader spectrum of uses [294]. Furthermore, more attention should be given to the improvement of the overall performance of Zn-ion batteries. The effectiveness of many existing studies, which focus on enhancing the performance and increasing the stability of the anode side, should be evaluated from broader aspects. On one hand, it is essential to explore the adaptability of Zn electrode modification strategies across various Zn cathode materials. On the other hand, the feasibility of these strategies to be combined with other potential modification methods needs to be taken into account as well. This broader evaluation will facilitate a more holistic enhancement of overall battery performance.

2.2 The application of in situ liquid cell TEM in advanced battery research

Diverse characterisation techniques have been developed to understand the complicated reaction mechanisms in different battery systems [295,296], from aspects of anodes, cathodes or their interfaces. Based on the different battery conditions during characterisation, these techniques can be broadly divided into two categories; ex situ methods that are performed 'post-mortem' after cycling, and in situ methods that are conducted during cycling of a representative electrochemical cell. Typically, the ex situ methods are significantly easier in terms of sample preparation and requirements for equipment, but they can only give information about the initial and final states of batteries. However, the strength of in situ techniques is in providing dynamic information of the intermediate states, which brings more insight to understanding the evolution of the electrodes and interfaces within working batteries. Furthermore, the dismantling of a cycled battery cell for ex situ examination can cause

misleading changes to the sample, such as due to air exposure or physical damage, which are avoided if the characterisation is done in situ.

A range of characterisation techniques have been adapted to testing environments in electrochemical cells, such as in situ XRD [297], in situ XPS [298], in situ atomic force microscopy (AFM) [299], in situ X-ray computed tomography [300], in situ NMR [301], in situ FTIR [302], in situ Raman spectroscopy [303], differential electrochemical mass spectrometry [304], in situ optical microscopy [305], in situ SEM [306], and in situ transmission electron microscopy (TEM) [307]. These advanced in situ characterisation techniques have been independently or jointly applied to realize the analysis of SEI layers' chemical components and the visualisation of electrode microstructures, as well as the exploration of chemical or electrochemical side reactions in electrolytes.

Among the above in situ characterisation methods, in situ TEM is a type of powerful technique that can capture the nanoscale morphological evolution and structural properties of electrode materials and the interfaces between electrodes and electrolytes. Compared with other in situ characterisation methods, the advantage of in situ TEM is that it can give structural and morphological information on the micro- to nano- level, with both better spatial and temporal resolution than these other techniques. This for instance allows the identification of the initial nucleation stages of deposition processes, which usually is challenging to be observed by other techniques. A further advantage is that the mechanism for image contrast in TEM being sensitive to density/atomic number can give compositional information to help with the analysis. In addition, it is also possible to conduct other in situ spectroscopic characterisations by using the electron beam.

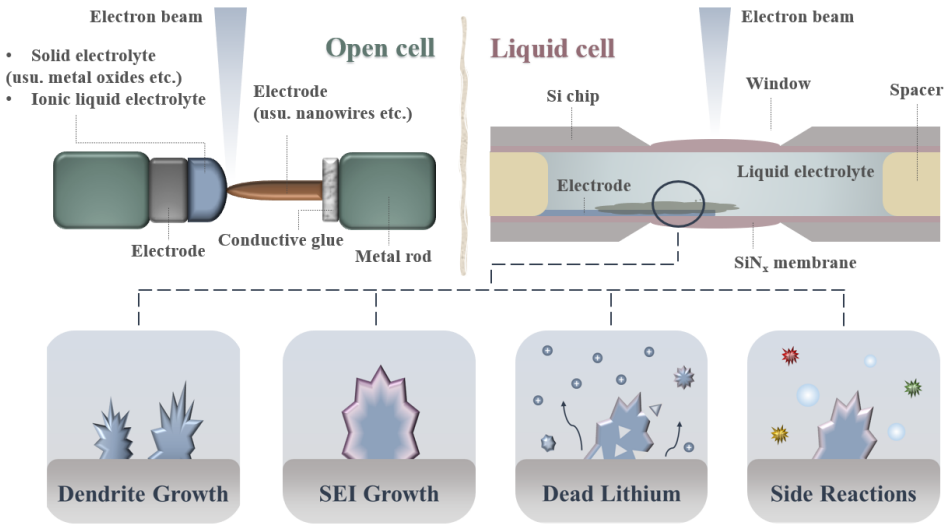


Figure 2.14 Comparisons of configurations in (a) the open cell and (b) the liquid cell approach for in situ electrochemical TEM experiments.

There are two main categories of in situ TEM, the open cell configuration and the closed cell configuration, as is shown in *Figure 2.14*. The in situ open cell TEM technique was initially used to observe Li dendrite formation. However, this open cell investigation only allows the use of non-volatile electrolytes, either an ionic liquid or a solid electrolyte [308,309], as it is exposed to the TEM vacuum. The in situ closed cell TEM, also known as in situ liquid cell TEM, has made it possible to monitor electrochemical dynamics and observe the growth of SEI and dendrites with more practical electrolytes [304,310]. As it is a sealed setup with liquids, gas evolution at the electrode/electrolyte interface can be detected by in situ liquid cell TEM experiments as well, which is of vital importance for investigating the properties of the SEI layer.

Additionally, there is also another closed cell design named the graphene liquid cell (GLC), which uses graphene as the covering layer on the window [311]. The image resolution of GLC is usually much higher due to the reduced thickness of the whole setup. However, it is not possible to apply biasing in the GLC for battery research so far, nor is it possible to replenish the limited cell volume by liquid flow.

Herein, recent research progress in research on rechargeable batteries facilitated by the application of in situ liquid cell TEM is outlined. Observations on the growth of dendrites and SEI, as well as other issues during cycling in Li, Zn and other novel electrolyte systems under in situ liquid cell TEM have been summarised. Furthermore, I also shed light on potential avenues for enhancing our understanding of battery mechanisms through utilisation of this technique in future research.

2.2.1 Application of in situ liquid cell TEM in Li batteries

The high activity of Li leads to severe instability of the anode/electrolyte interface, thus consequently causing the problems of dendrite growth, SEI overgrowth, and dead Li accumulation. Therefore, investigating the interfacial evolution is of great significance to find out possible solutions to improve the stability and cycling performances of Li batteries. Though various operando characterisation methods have been developed, it is still not feasible for most of them to provide direct observation of the electrode/electrolyte interfaces in a real battery working environment. This illustrates the necessity of using the in situ liquid cell to capture the operando morphological evolution processes of Li dendrites and SEI in various electrolytes.

In 2014, the in situ evolution process of the electrode/electrolyte interface was directly captured by Zeng and co-workers [312], using a homemade liquid cell chip with two electrodes and conducting cyclic voltammetry test (*Figure 2.15 a*). They observed inhomogeneous lithiation, lithium metal dendritic growth, electrolyte decomposition, and SEI formation on Au anodes from a commercial electrolyte of $LiPF_6$ in EC/DEC. The Li dendrites were found to nucleate and grow rapidly from the substrate. During the dissolution process, the stripping of dendrites started from the kink points and tip, leaving a branch-like structure on the substrate. Interestingly,

bubbles formed due to the decomposition of the electrolyte solvent were also observed during the Li plating process. They also observed that the SEI layer was of equivalent thickness as previously reported, but they could not resolve the normally accepted two-layer structure, of which the inner layer is more compact with inorganic components while the outer layer is more porous.

A study was reported by Sacci and co-workers [313], using similar cyclic voltammetry cycling measurements, where they used a commercially available chip with glassy carbon working electrode. In the standard electrolyte of $LiPF_6$ in EC/DMC, they found that the formation of SEI dendrites began before Li deposition, and that Li deposition occurred both beneath the SEI and also within the SEI, forming small crystalline particles (*Figure 2.15 b*). However, unlike normal dendritic morphologies, the Li electrodeposits in their images presented a more globular shape, and the secondary electrodeposits were a mixture of globular, faceted and needle-like nucleation morphologies. This could possibly result from the involvement of carbon substrates or higher current densities.

Mehdi et al. [314] also reported the identification of Li dendrites and SEI on Pt electrodes in the electrolyte of $LiPF_6$ in propylene carbonate (PC). They presented a detailed discussion as to the expected contrast of Li metal when observed in TEM or scanning transmission electron microscopy (STEM); Li has dark contrast when imaged in dark-field mode, e.g., in high angle annular dark field (HAADF)-STEM, and bright contrast in bright-field mode, e.g., in conventional TEM. This is due to the density of Li metal being lower than the surrounding electrolyte, and the contrast of TEM being sensitive to the density.

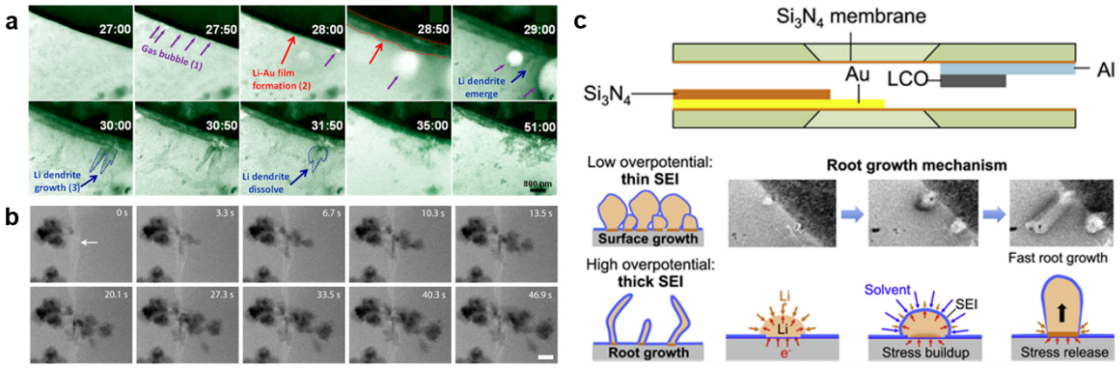


Figure 2.15 (a) The evolving electrode-electrolyte interface of an Au electrode cycled in $LiPF_6$ EC/DEC electrolyte [312]**. Reproduced with permission, copyright 2014 American Chemical Society. (b) Li dendrite growth from $LiPF_6$ EC/DMC electrolyte** [313]**. Scale bars are 1 µm. Reproduced with permission, copyright 2015 American Chemical Society. (c) Li deposition in a liquid cell with an application-relevant cathode material deposited on the counter electrode** [315]**. Reproduced with permission, copyright 2017 Elsevier.**

Apart from different dendrite and SEI morphologies, further research on exploring the nucleation mode and interaction of dendrites with SEI layers was conducted by Li and Bazant [315]. They reported a comprehensive observation of lithium metal deposition and dissolution in the electrolyte of LiTFSI in DMSO. A customized chip with $LiCoO_2$ film deposited on the counter electrode was studied (*Figure 2.15 c*). Li was observed to preferentially grow from existing root sites, and then grow away from the root to form kinks in the dendrites, due to the continually thickening SEI layer impeding ion transfer to the root. These types of complex, dynamically evolving growth dynamics can only be identified by direct nanoscale observation, and are thus ideally suited to in situ liquid cell TEM.

Electrolyte additives have proven to be a powerful and feasible tool to modify the Li SEI components. It is widely accepted that the LiF-rich SEI layers are helpful to suppress Li dendritic growth and dead Li formation [316]. A lot of evidence has confirmed the role of LiF in establishing flat and dense SEI structures and monitoring Li deposit morphologies. The effects of LiF-rich SEI layers were unveiled by Lee et al. [317], via a well-designed in situ imaging setup. They applied a

poly(diallyldimethylammonium chloride) (PDDA) cationic polymer film on the liquid cell TEM electrode surface with the help of Sn@SnO_2 nanostructures (Sn nanowires/nanoparticles with a thin layer of surface oxide). As shown in *Figure 2.16 a*, they observed Li nanogranule formation in the electrolyte of $LiPF_6$ in PC with the PDDA cationic polymer film, which normally arises from the LiF-rich SEI according to previous claims.

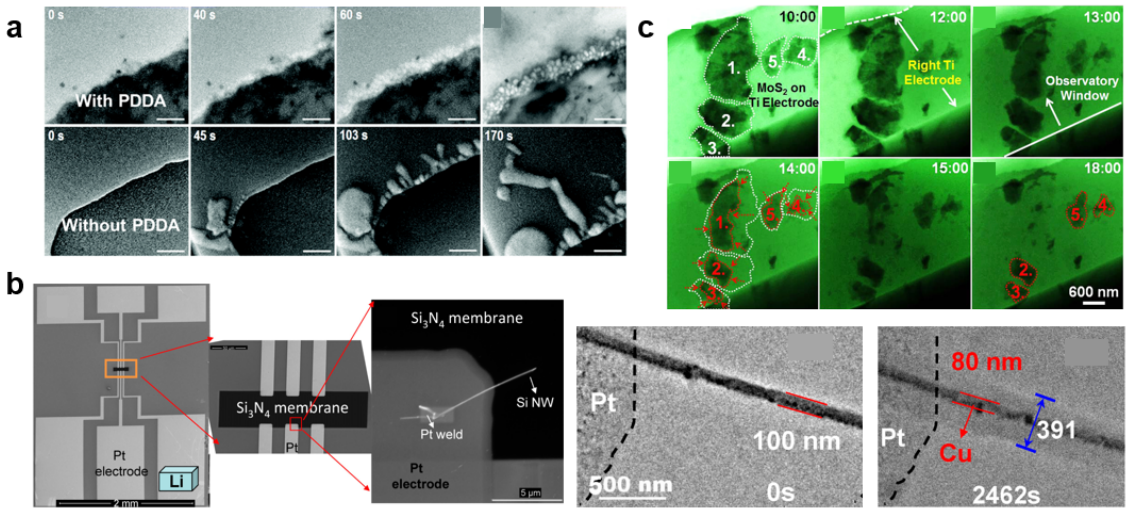


Figure 2.16 (a) Li plating with and without a fluoride-facilitating PDDA electrode coating [317]**. Scale bars are 1 µm. Reproduced with permission, copyright 2020 Royal Society of Chemistry. (b) Lithiation of a Si nanowire from $LiPF_6$ EC/DMC electrolyte** [318]**. Reproduced with permission, copyright 2013 American Chemical Society. (c) Lithiation and delithiation of MoS_2 nanosheets on a Ti current collector from $LiPF_6$ EC/DEC electrolyte** [319]**. Reproduced with permission, copyright 2015 American Chemical Society.**

In addition to the exploration of Li dendrites and the SEI layers, in situ liquid cell TEM has also been applied to investigate morphological and structural changes of other electrode materials. Si is considered one of the most promising anode candidates owing to its ultrahigh theoretical capacity (4200 mA h g^{-1}), low working potential, and its high abundance in the Earth's crust [320]. However, Si anodes suffer from severe volume changes during the lithiation and delithiation process, leading to the pulverization of active materials, the collapse of SEI layers and loss of electrical contact within the battery [38]. It has been proven that Si materials with nanostructures,

such as nanowires and nanotubes, show the capability of easing the negative consequences of volume expansion [37]. The lithiation behaviour of copper (Cu) coated Si nanowires in the electrolyte of $LiClO_4$ in EC/DMC was first captured by Gu and co-workers [318]. Compared with previous in situ open cell research on Si anodes, one big advantage of the in situ liquid cell setup is to allow the immersion of the whole Si nanowire into the electrolyte, instead of just a point contact. This helps to measure the volume expansion more accurately. As illustrated in *Figure 2.16 b*, a single Si nanowire was mounted on the Pt electrodes by focused ion beam (FIB) manipulation and Pt deposition welding. The diameter of the Cu coated Si nanowire was found to increase from 100 nm to 391 nm after lithiation, involving the anisotropic Si expansion and the SEI formation. In addition, Zeng et al. [319] also reported the observation of the lithiation/delithiation process of the layered MoS_2 nanosheets in an electrolyte of $LiPF_6$ in EC/DEC. The MoS_2 nanosheets were successfully loaded on the Ti electrode via the simple drop-casting method. The MoS_2 nanosheets were found to undergo irreversible decomposition and fragmentation into nanoparticles in the voltage range of 1.8-1.2 V, as shown in *Figure 2.16 c*.

Apart from anode materials, researchers have attempted to apply in situ liquid cell TEM to study cathode materials [321]. However, this is more difficult than on interfaces and anode materials. Most of structural changes of cathode materials happen at the unit cell level which requires very high resolution to resolve. This cannot be easily captured with the presence of liquid electrolytes, which reduce the imaging resolution.

2.2.2 Application of in situ liquid cell TEM in aqueous Zn batteries

Compared to Li and Na batteries, the use of aqueous electrolytes in Zn-based batteries offers advantages for the application of in situ liquid cell TEM, owing to the superior stability of water relative to many organic solvents under the electron beam.

The first observation of Zn deposition via in situ liquid cell TEM was reported by Park et al. [322] in a ZnAu alloy system with Bi additives. Later, the in situ nanoscale observations of pure Zn dendrites from $ZnSO_4$ aqueous electrolyte was reported by Sasaki et al. [323] and Li et al. [324] separately in 2021. Li et al. [324] demonstrated basic Zn deposition behaviour in the 0.3 M $ZnSO_4$ aqueous solution with the flow of electrolyte, and compared differences in the dendrite formation at the nucleation stage and the growth stage under various applied currents and flow rates.

In the meantime, Sasaki and co-workers studied the Zn electrodeposition behaviour from diluted 0.1 M $ZnSO_4$ electrolyte in a static state. The concentration of Zn^{2+} is equivalent to that of the 2.5 M KOH aqueous solution saturated with ZnO, which is widely used in rechargeable alkaline Zn batteries. This in situ electrochemical experiment was conducted in a static electrolyte condition, under a high current of 4 and 5 μA, equivalent to around 160 mA/cm^2 and 200 mA/cm^2 calculated from the active electrode surface area. Moreover, to avoid gas generation at the counter electrode, they also coated a layer of Zn on the Pt counter electrode via vacuum deposition beforehand. Similar work was reported by this group later, using the same experimental setup at lower current densities of 20 mA/cm^2 and 40 mA/cm^2, but with a modified potentiostat system that completely isolated the electrodes from the potential of the TEM column, achieving more reliable electrochemical data [325].

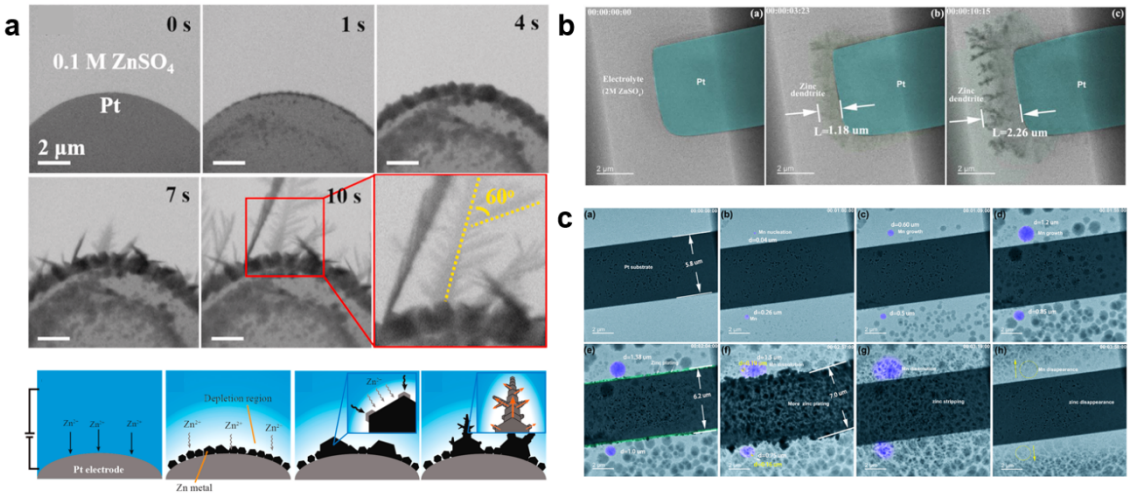


Figure 2.17 (a) Zn electrodeposition to a Pt working electrode from aqueous $ZnSO_4$ electrolyte and a schematic illustrating the changing morphology as Zn deposition advanced [323]. Reproduced with permission, copyright 2021 Elsevier. (b) Electrostripping of deposited Zn dendrites, leaving behind isolated dead Zn in the 2 M $ZnSO_4$ electrolyte [326]. (c) The plating and stripping behaviours of Zn in the electrolyte of 20 mM $ZnSO_4$ + 5 mM $MnSO_4$ [326]. Reproduced with permission, copyright 2022 Elsevier.

The evolution of Zn dendrites is shown in *Figure 2.17 a*. Clear hexagonal Zn facets formed on the tip of the Pt electrode right after the electrochemical deposition started. With prolonged plating, needle-like Zn deposits were found to precipitate at the edge of the former facets, forming branch-like or seaweed-like structures at the end. A mechanism of such Zn dendrite formation was proposed by the authors (*Figure 2.17 a*). As Zn nuclei form and grow into larger hexagonal planar crystals, Zn ions are consumed and their concentration decreases from the centre of nucleation, resulting in a concentration gradient of Zn ions surrounding the Zn deposits. This gradient favours nucleation and growth from the tips, which produces the branched Zn dendrites.

Recently, Huang et al. [326] further investigated the Zn plating/stripping and dendrite growth mechanisms in modified electrolyte systems. They first presented a typical formation process of Zn dendrite and dead Zn in a wildly used 2 M $ZnSO_4$ mild aqueous electrolyte. The dendrite issue

was verified, and a significant amount of dead Zn was observed left on the Pt electrode (*Figure 2.17 b*).

$MnSO_4$ additive and the $Zn(OTf)_2$ electrolyte have both been previously reported to be effective in optimising Zn-ion batteries, of which the effects are generally considered to act on the cathode side[138–141]. To explore their effects on the Zn metal anode, dynamic Zn plating/stripping behaviours in the above two electrolytes were also studied. With Mn ions in the electrolyte, nearly no dendrite-like Zn deposits were visible. Interestingly, some spherical particles were found to form and disintegrate around the Pt electrode during cycling (*Figure 2.17 c*). These particles were identified as insoluble Mn-based compounds, triggered by the change in the pH value due to H_2 evolution. It was claimed by the authors that these spherical particles mechanically regulated the flow of ions and thus inhibited dendrite growth. As to the observation in the $Zn(OTf)_2$ electrolyte, the Zn deposition was much more uniform and homogenous, and no obvious hydrogen evolution happened, consistent with its superior performance in the coin cell test.

2.2.3 Application of in situ liquid cell TEM in other advanced battery systems

Recently, the application of the in situ liquid cell TEM has also been extended to other novel systems, such as Na [327,328], Mg [329], Ca [310], metal-air batteries [330], and metal-sulphur batteries [331].

Na has been considered a competitive alternative energy storage material, due to its similar properties to Li but much lower cost [127]. However, these similar chemical properties also induce the analogous uncontrollable dendrite problem. Recent studies have revealed some fundamental differences between Li and Na dendrites [332], which has drawn great attention to

studying the in-depth mechanisms of Na dendrite growth. Zeng et al. [327] reported their recent findings on the effects of electrode roughness on Na electrodeposition behaviour. They patterned Ti electrodes with different curvatures on their homemade in situ liquid cell TEM chips, one with a flat surface and the other with a sharp tip. On the flat Ti electrode, relatively large Na grains were observed at the edge of the electrode, along with gas bubbles emerging. In contrast, Na nodules were much smaller on the sharp Ti electrode (*Figure 2.18 a*), and newly deposited Na was inclined to accumulate at the base of existing grains, indicating a "base growth" tendency, thus leading to an "explosive" growth behaviour.

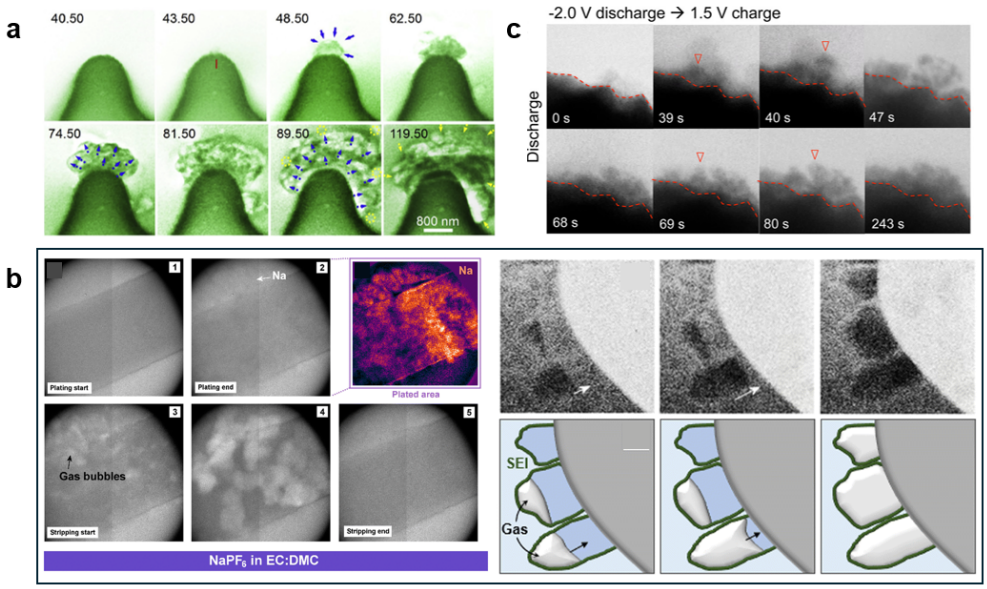


Figure 2.18 (a) Liquid cell TEM imaging of Na plating on a sharp tip of the Ti current collector electrode [327]**. Reproduced with permission, copyright 2020 Elsevier. (b) Liquid cell TEM and HAADF-STEM imaging of the Na stripping process and corresponding cartoon illustrations** [328]**. Reproduced with permission, copyright 2023 Royal Society of Chemistry. (c) Li_2O_2 deposits forming during cycling** [330]**. Reproduced with permission, copyright 2015 American Chemical Society.**

Recently, Gong et al. [328] investigated the mechanisms of how ether-based electrolytes facilitate better cycling performances of Na battery anodes. Under the in situ liquid cell TEM and HAADF-STEM imaging (*Figure 2.18 b*), severe gas evolution was observed in the carbonate electrolyte,

while similar phenomenon was not observed in the ether electrolyte. Further characterisations revealed that the enhanced elasticity of the ether-derived SEI played an important role in suppressing gas evolution and promoting uniform Na plating. This research also indicated the irreplaceable value of in situ liquid cell TEM in diagnosing battery reaction mechanisms.

Compared to aforementioned metal-ion batteries, the metal-air batteries possess exceptionally high theoretical energy density, as they rely on cathode oxygen reduction with air harvested from the atmosphere [333]. Li-O_2 batteries have been intensively studied over the past decades, which offer a theoretical energy density of 3458 Wh/kg, based on the weight of the discharge product Li_2O_2 [334]. However, the Li-O_2 batteries have suffered from a number of technical problems, such as limited practical energy efficiency, poor cycle life, low rate capability, as well as the noteworthy asymmetry between charging and discharging processes [335,336]. Kushima et al. [330] first reported the observation of the asymmetry in the morphological evolution of Li_2O_2 between charging and discharging in the electrolyte of LiTFSI in DMSO with the help of the in situ liquid cell TEM. As is shown in *Figure 2.18 c*, the Li_2O_2 dendrites grew at the Li_2O_2/electrolyte interface in discharging, while they decomposed from the root at the Li_2O_2/current collector interface. This tendency weakened the adhesion of Li_2O_2 to the current collector and reduced the contact area, contributing to the large observed overpotential. The detached insoluble Li_2O_2 fragments were also seen to be swept into the electrolyte upon minute flow agitations during cycling, which would be impossible to capture via traditional ex situ characterisation methods.

2.2.4 Summary and outlook

In situ liquid cell TEM occupies a unique role in allowing researchers to directly visualise nanoscale dynamic battery mechanisms that occur when cycling electrodes in liquid electrolytes, allowing for high spatial resolution, real-time imaging, high sensitivity contrast toward sample

density, and the ability to study a wide range of candidate electrolytes. This combination of advantages is not currently achievable with any other technique. It has allowed for new perspectives into battery degradation behaviours, particularly in terms of our understanding of dendrite growth, SEI layer formation, and other electrochemical properties. Its ability to capture morphological and structural evolution endows researchers with a direct and straightforward tool to gain knowledge of the battery behaviours during cycling.

A practical challenge with liquid cell TEM experiments for studying battery materials is the difficulty in preparing suitable samples. The introduction of desired electrode materials on the chip is hindered by the fragile membranes and the technical difficulty in using compatible pre-deposition techniques. In addition, there are also intrinsic limitations of liquid cell experiments. The correlation between the observed processes in the in situ TEM and the bulk battery performance is often difficult, as the electrochemical behaviours and mass transport are not equivalent due to very limited space within the liquid cell setup and thin-cell geometry. As a result, the open circuit potential can be less stable than in conventional electrochemical cells, and the ionic concentration gradients may not be comparable either. The influence of the electron beam can also cause issues in collecting accurate electrochemistry, with the beam electrons undergoing elastic and inelastic interactions with the sample, with the latter scattering events generating low energy secondary electrons that can go on to cause radiolysis, heating, and charging of the specimen. Therefore, electrochemical conditions within the liquid cell setup can be difficult to keep stable and reproducible for each reaction cycle, which makes obtained results less comparable to ‘lab bench’ experiments. The high-energy electron beam can markedly alter the electrochemical behaviour and reaction kinetics of samples. The issue of the confined sample volume and the influence of the beam make it challenging for the in situ liquid cell TEM technique to fully imitate the working conditions of real batteries.

Looking to the future, improving the imaging resolution of liquid-cell TEM is still of primary importance. One practical way is to reduce the thickness of the liquid cell and thereby reduce scattering of the beam, either by decreasing liquid layer thickness, window thickness, or alleviating window bulging. The use of low dose imaging and/or controlled dose and other advanced electron microscopy techniques, such as aberration correction TEM, pixelated detectors ("4D STEM"), or sub-sampling, can help to reduce the radiation damage and improve the image resolution and contrast. Beyond improving the spatial resolution, the future direction of in situ liquid cell TEM should aim to be more comprehensive, multifunctional, and cross-correlative. Advances in computational modelling and data analysis techniques will also enable more efficient and effective analysis of the vast amounts of data generated by in situ TEM experiments.

Chapter 3 Methodology

3.1 Electrochemical tests

Electrochemical tests are essential for evaluating the performance of batteries. By analysing a battery's response to controlled electrochemical stimuli, these tests provide insights into a battery's capacity, efficiency, reliability, lifespan, and overall stability under various operational conditions.

3.1.1 Galvanostatic cycling

Galvanostatic cycling is a fundamental electrochemical testing technique widely utilised in characterising the performance of batteries. In galvanostatic cycling, a specified constant current is applied to charge and discharge the cell, either until a certain amount of charge has been passed or until reaching a cutoff voltage. During this process, the voltage response over time is recorded. Several key parameters can be determined by the galvanostatic cycling measurement.

The capacity (C) of a cell, indicates the total charge that the cell can store, which is usually expressed in ampere-hours (Ah) or milliampere-hours (mAh). Specific capacity, on the other hand, quantifies the charge capacity relative to the mass of the active material in the electrode, or the area of the active electrode surface. Capacity can be measured by integrating the current over the time:

$$C = I \times t \qquad \text{(Equation 3.1)}$$

where *I* is the charge/discharge current in amperes (A), and *t* is the time in hours (h) over which the charge/discharge process occurs.

Coulombic efficiency is defined as the ratio of the discharging capacity to the charging capacity of the same cycle, describing the charge efficiency by which electrons are transferred:

$$Coulombic\ efficiency = {}^{C_{Discharging}}\Big/_{C_{Charging}} \times 100\% \qquad \text{(Equation 3.2)}$$

Rate capability is assessed by cycling the battery at various current densities and observing how the capacity and voltage profiles change. An optimal rate performance allows the battery to be charged rapidly and deliver high power within a short period of time.

In this thesis, galvanostatic cycling was mainly used to evaluate the coulombic efficiency and the specific capacity retention of Zn||Zn, Zn||Ti and Zn||V_2O_5 coin cells, to compare the performance of different electrolytes.

3.1.2 Linear sweep voltammetry (LSV) and cyclic voltammetry (CV)

Voltametric sweep methods are common potentiodynamic measurements to assess the redox behaviour in electrochemical systems. In linear sweep voltammetry (LSV), the voltage is linearly swept between two limits at a controlled rate, typically expressed in millivolts per second (mV/s). As the potential is varied, it induces electrochemical reactions at the electrode surface, leading to the flow of current. The current response, which is recorded as a function of the applied potential, is primarily influenced by the nature and speed of the electrochemical reactions. This technique can be used to determine the onset potential of electrochemical reactions and to study the electrochemical behaviour of a system under quasi-static conditions [337]. Cyclic voltammetry (CV) is similar to the LSV, but the potential is reversed between a set range, thus forming a cyclic potential sweep.

In this thesis, LSV and CV were performed to compare the onset potential of hydrogen evolution reaction and the differential capacitance, using Zn||Zn and Zn||Ti coin cells with different electrolytes, respectively.

3.1.3 Linear polarization (LP)

Linear polarization (LP) measurement, sharing similarities with LSV in terms of the experimental protocol, is distinct due to the much narrower potential range applied, typically ±10 mV around the open circuit potential. LP is primarily used to determine the corrosion property of the material. The corrosion current and corrosion potential can be obtained through the Tafel fit of the measured current-potential curve according to the Butler-Volmer relation [338]:

$$I = I_{\mathrm{Corrosion}}\left(e^{\frac{2.303\left(E-E_{\mathrm{Corrosion}}\right)}{\beta_a}} - e^{\frac{-2.303\left(E-E_{\mathrm{Corrosion}}\right)}{\beta_c}}\right) \qquad \text{(Equation 3.3)}$$

where E is the potential at the given current density I, $E_{\mathrm{Corrosion}}$ is the corrosion potential, $I_{\mathrm{Corrosion}}$ is the corrosion current density, β_a and β_c are the anodic and cathodic Tafel constants respectively. By fitting the $\log|I|$ versus E plot, it is possible to determine the values of the above parameters. Such fittings were employed in this thesis to compare the corrosion properties of Zn electrodes in various electrolytes.

3.1.4 Chronoamperometry

Chronoamperometry is a fundamental electrochemical technique wildly used to study the reaction kinetics, diffusion processes, adsorption properties, and nucleation mechanisms, in which the current resulted from an electric potential step of the working electrode is recorded as a function of time. In the measurement of the chronoamperometry curve, the working electrode is initially held at a potential where no redox reaction occurs, to ensure the surface is

stable at equilibrium. When a potential step is applied to the working electrode, the electrochemically active species will diffuse to the working electrode surface to balance the change in potential, and such ion flux will result in a capacitive current.

If the potential step applied to the working electrode is sufficient enough to ensure the complete reduction of active species, the reaction is under the diffusion control and the current decays following the Cottrell equation [339]:

$$i(t) = \frac{n\mathrm{F}AD_o^{1/2}C_o}{\pi^{1/2}t^{1/2}} \qquad \text{(Equation 3.4)}$$

where $i(t)$ is the current, n is the number of electrons transferred in the redox reaction, F is the Faraday constant, A is the electrode area, D_o is the diffusion coefficient of the redox species, C_o is the concentration of the active species, and t is the time. The curve can be further analysed by comparing it to the curves calculated from theoretical physical models, such as the Scharifker-Hills model, to determine whether the electrodeposition process is governed by instantaneous or progressive nucleation mechanisms [340].

In this thesis, the currents measured from chronoamperometry tests were utilised to estimate the active area of Zn electrodes, which provided insights into the uniformity and compactness of the deposits formed from different electrolytes.

3.1.5 Electrochemical impedance spectroscopy (EIS)

Electrochemical impedance spectroscopy (EIS) is a versatile but complicated technique. Different from measuring the conventional electrical resistance by applying a direct voltage or current, the impedance is measured using a small alternating sinusoidal signal [341]. For the poteniostatic EIS, the potential applied can be presented as below [342]:

$$E_t = E_0 \cdot \sin \omega t = E_0 \cdot \sin 2\pi f \qquad \text{(Equation 3.5)}$$

where E_0 is the amplitude, t is the time, ω is the angular frequency and f is the frequency of the sine wave.

The response of a linear time-invariant system to a sine wave is also a sine wave of the same frequency with a phase shift (φ), thus the current can be presented as below:

$$I_t = I_0 \cdot \sin \omega t + \varphi \qquad \text{(Equation 3.6)}$$

Therefore, the impedance Z can be expressed following a variant Ohm's law:

$$Z = \frac{E_t}{I_t} = \frac{E_0 \cdot \sin \omega t}{I_0 \cdot \sin \omega t + \varphi} = Z_0 \cdot \frac{\sin \omega t}{\sin \omega t + \varphi} \qquad \text{(Equation 3.7)}$$

where Z is thereby expressed by a magnitude Z_0 and a phase shift φ.

The magnitude Z and the phase φ can be defined as the polar coordinates, which can further be converted to into orthogonal coordinates (Cartesian coordinates):

$$\begin{cases} x = Re\ Z = |Z| \cdot \cos \varphi \\ y = Im\ Z = |Z| \cdot \sin \varphi \end{cases}$$

This can be written in the complex notation:

$$Z = Re\ Z + jImZ = |Z| \cdot (\cos \varphi + j \sin \varphi) \qquad \text{(Equation 3.8)}$$

The expression for *Z* is composed of a real part and an imaginary part. If the real part (*Re Z*) is plotted on the X-axis and the imaginary part is plotted on the Y-axis (usually inverted, -*Im Z*), the Nyquist plot is obtained, usually in a semicircle shape, which is one of the main representation ways to visualise EIS results [343]. Each point on the Nyquist plot is an impedance value at a frequency point. The diameter of the semicircle gives the charge transfer resistance. The EIS result can also be represented in the Bode plot, which display the magnitude of the impedance and the phase angle as functions of frequency.

Properties of the electrochemical cell, including electrolyte resistance, concentration gradients, and interactions such as charge and mass transfer, can all be evidenced by EIS. They can be represented by an electrical circuit, thus generating an equivalent circuit that can be fitted to the EIS results. In this thesis, EIS was employed to probe the charge transfer resistance and double layer capacitance in electrolytes containing various organic additives.

3.2 In situ electrochemical liquid cell transmission electron microscopy (TEM)

3.2.1 Basic working principles of TEM

Transmission electron microscopy (TEM) is an advanced analytical tool that enables detailed visualisation of the internal structure of materials at the atomic level. When an electron beam is transmitted through the sample, interactions such as scattering and absorption, convey comprehensive information about the specimen's structure, composition, and other properties, which can be used to form images or diffraction patterns.

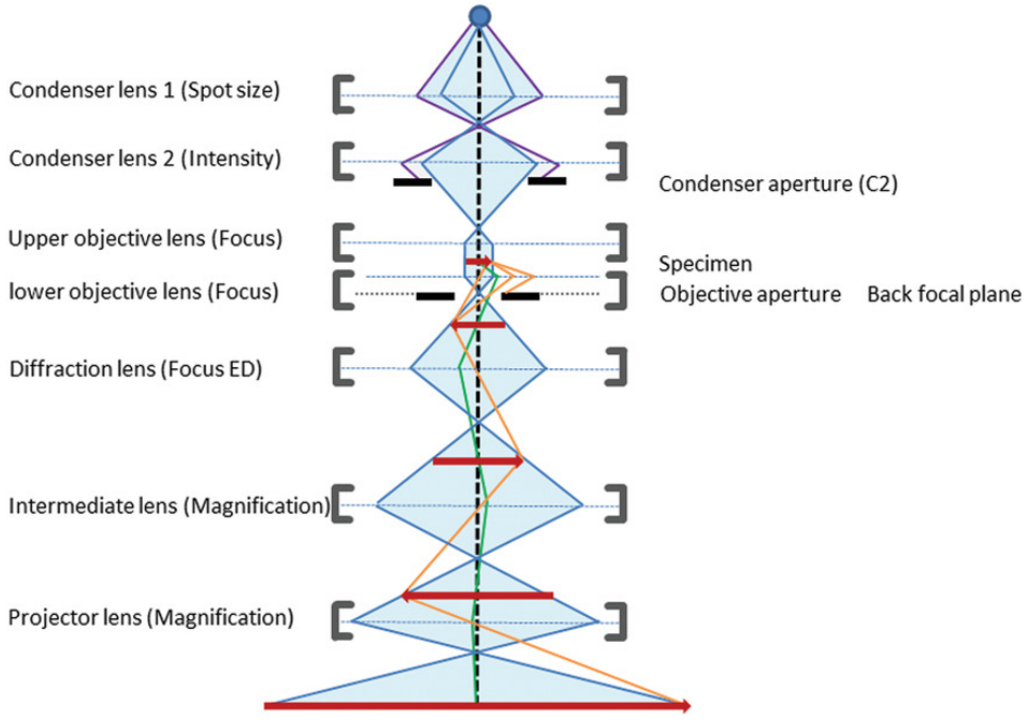


Figure 3.1 Schematic of an electron microscope column. The beam is shown in blue; the red arrow is the specimen and its (intermediate) images; the paths of scattered electrons are drawn in orange and green [344]. Reproduced with permission, copyright 2020 The Authors.

A schematic of a transmission electron microscope is illustrated in *Figure 3.1*. Electrons are generated by an electron gun, and focused by a series of electromagnetic condenser lenses into a coherent beam striking the specimen. The spot size and intensity are adjusted by the condenser lens, and high angle electrons are excluded by the condenser aperture. The transmitted electrons are further focused by the objective lens to construct images on the electron detector. Objective apertures can be optionally used to block diffracted electrons, thereby enhancing the image contrast.

TEM necessitates very thin specimens, often less than 100 nm thick, to enable electron transmission, and specimen preparation varies according to the sample's form. Small and thin materials, such as nanoparticles, can be simply dispersed onto TEM grids using appropriate solvents and dried prior to TEM imaging. In contrast, bulk materials often require additional

thinning and polishing treatments. Larger solid materials can be also prepared by extracting micro-scale sections using FIB, which are then mounted onto TEM grids.

When the incident beam strikes the sample, some electrons are transmitted, while others are scattered. Images of varying contrast are formed depending on which part of the electrons are utilised. If the transmitted electrons are used, the resulting image is known a bright field image, where areas allowing more electrons to pass through appear brighter. If the transmitted electrons are excluded by the aperture, the scattered electrons can form a dark field image, where areas scattering more electrons will be brighter.

The formation of imaging relies on contrast to distinguish between different areas of a sample. This contrast is derived primarily through three main mechanisms in TEM: mass-thickness contrast, diffraction contrast and phase contrast. Mass-thickness contrast arises from variations in density due to atomic numbers and thickness within the sample, affecting the ability to scatter electrons, thus resulting in different numbers of transmitted electrons. Diffraction contrast is commonly used to image defects and structural orientations that deflect electrons in crystalline materials. Hence, contrast can arise at defects, grain boundaries or dislocations between different regions. Phase contrast is mostly used for high-resolution images, to visualise atomic columns and lattice defects. The interference between the incident beam and the scattered beam causes changes in imaging intensity, thus generating contrast.

3.2.2 Configuration of the in situ electrochemical liquid cell TEM holder

The in situ liquid cell is prepared as a closed unit, in which silicon nitride (SiN_x) membranes screen the liquid sample to prevent leakage of liquid electrolyte into the vacuum of the TEM, while still allowing the electron beam to transmit through the cell and thus allow imaging of the sample.

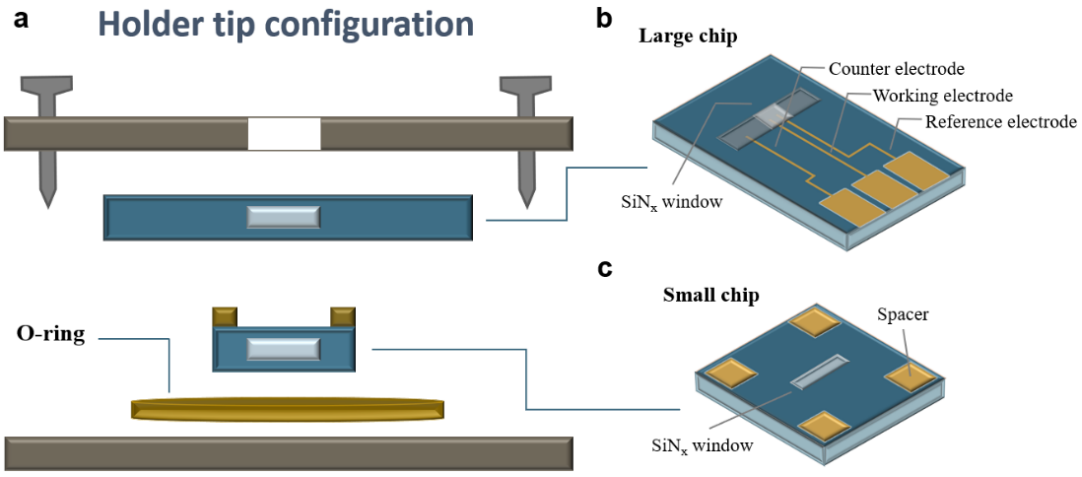


Figure 3.7 (a) The cross-section view of the liquid cell tip. Schematics of (b) the large chip with electrodes and (c) the small sealing chips used to form the liquid cell.

In the configuration of a typical commercial in situ liquid cell TEM holder, as is shown in *Figure 3.7*, inside the tip of the TEM holder there is an electrical biasing silicon (Si) chip and a sealing Si chip, as well as an O-ring, which helps these two chips to be aligned and sealed properly. The small Si chip is equipped with spacers of different heights at the edges or four corners, allowing the flow of liquids through the cell and accommodating electrochemical reactions on the electrode. The optical microscope image and corresponding schematic of the holder tip are given in Appendix *Figure A1*, showing the configuration and the flow pathway of liquids within the holder tip. Both Si chips have a window embedded in the centre, covered with an ultrathin, electron transparent layer, normally made of SiN_x for most commercialised chips. Normally three electrodes are pre-patterned on the surface of a large chip, acting as a reference, working, and counter electrode. The tip of the working electrode, where reactions of interest happen, is patterned on the SiN_x window so it is visible by TEM. The optical microscope image of the large chip is given in Appendix *Figure A2*, illustrating the layout of the working electrode, counter electrode and reference electrode.

3.2.3 Experimental setup for in situ liquid cell TEM

The setup of in situ liquid cell TEM is very fragile, as the thickness of SiN_x membranes is normally around 50 nm. Improper handling during the experiment could result in blocking of the microfluidics or cell rupture and leakage, thus possibly causing detrimental or even fatal effects on the TEM column. This requires a thorough consideration of various factors when determining testing parameters, in order to perform experiments safely without compromising too much on the imaging quality and desired information.

Comprehensive studies of factors that determine the resolution of liquid cell TEM and STEM have been reported previously [345]. The resolution of the electron microscope is inversely proportional to the thickness of samples and directly proportional to the beam dose rate. This means a thinner liquid cell setup and higher dose rate can bring better resolution. However, a delicate balance between these factors and the resolution should be carefully monitored during imaging.

The total thickness of the in situ liquid cell setup comes from the sum of the thickness of SiN_x membranes and the thickness of the liquid. Normally, a thinner liquid layer is desired, though thicker liquid allows better diffusion of ions, and more space within the cell chamber enables observation of larger particles. The liquid thickness is constrained by the height of the spacers on the small chip, but it is not even. There will always be membrane bulging due to the pressure difference between the interior of the cell and the TEM column. As a result, the liquid is much thicker in the centre of the SiN_x window than at the edges. Thicker SiN_x membranes and smaller window sizes can help to eliminate the bulging, while this will compromise the resolution and field of view, respectively.

The beam dose rate is another factor that should be carefully controlled during imaging. Beam dose refers to the number of electrons that have irradiated a given area, usually with a unit of $e^- Å^{-2}$, while dose rate is defined as the dose in a unit of time, with a unit of $e^- Å^{-2} s^{-1}$. The accelerated electrons coming from the beam can inelastically interact with liquids, resulting in different types of beam damage, such as knock-on effect, thermal effect, radiolysis, etc. [345,346]. Systematic investigations into the impacts of beam damage on commonly used Li electrolytes have been reported before [346]. Among them, radiolysis is the main concern that should be taken into consideration for liquid characterisation, especially for organic solvents, which can be less stable. It has been reported that radiolysis can cause the decomposition of liquids, resulting in changes in the local chemical environment and gas evolution [347]. This might give rise to misleading results of chemical properties and hinder the accurate acquisition of structural information. Therefore, it is necessary to conduct beam dose tests before performing in situ imaging and establish specific dose limits towards different samples experimentally. Related to beam dose control is the selection of an appropriate electron beam energy for the experiment. Typical electron beam energies used across TEM/STEM experiments are within the range of 60 kV to 300 kV, with 200 kV the most frequently used. More recently, lower beam energies such as 60 and 80 kV have been used to study beam sensitive 2D materials like graphene, as these are mainly susceptible to elastic (sputtering) damage from the electron beam, which is reduced for lower beam energies. However, for in situ liquid cell TEM, people need to ensure that (i) the beam transmits through the relatively thick liquid cell, and (ii) that any beam damage is minimised. As discussed above, the primary beam damage mechanism is via inelastic scattering for electrolyte studies, leading to radiolysis and charging, rather than elastic scattering, and so liquid cell studies are ideally performed with a high electron beam energy to ensure good beam transmission and to minimise inelastic scattering.

The in situ liquid cell setup allows observation in either a static or a flowing state of solutions. The flow of liquids can be achieved by a syringe pump, of which the flowing rate is normally controlled at several µl/min. As the cell and the syringe pump are usually connected by very fine channels, it is necessary to check the viscosity of the electrolyte to avoid any clogging. In terms of studies on batteries, a flowing liquid cell has several advantages. First, flowing fresh electrolytes into the small liquid cell can replenish the ions consumed during cycling, thus maintaining a consistent concentration of the electrolyte. Also, as discussed, most electrolytes are not so stable under the electron beam. In this case, a flowing electrolyte can help to refresh any potentially decomposed electrolytes induced by the beam, which may otherwise confuse the results.

Another point that should be taken into consideration is the choice of electrode materials on the chip. Though the chip system is designed to mimic the target system as far as possible, electrode materials of chips are still limited; normally gold, platinum, glassy carbon or titanium. An inappropriate base electrode material may interact with the electrolyte, potentially acting as an unwanted electrocatalyst for side reactions, or undergo alloying with electroplated material. Furthermore, the narrow gap and the extremely fragile membrane bring about more challenges to attaching desired materials to the chip. Several strategies for customizing electrodes have been developed to accommodate various requirements for battery systems, including drop-casting [319], vacuum deposition [323], sample attachment via FIB [71], etc.

For all the in situ liquid cell TEM experiments in this thesis, the TEM imaging was conducted with a beam energy of 200 kV. The beam dose rate was controlled at a low value to minimise beam damage by performing beam dose tests before experiments. Regarding the experimental configuration, small chips featuring a 550 µm × 50 µm window were paired with large chips with a 100 µm × 50 µm window, to balance the viewing area with the imaging resolution. Pt was

chosen as the electrode material due to its inert property within the aqueous Zn electrolyte system. Additionally, to ensure consistent and effective replenishment of the Zn source, the electrolyte was continuously circulated throughout the experiments during the plating and stripping processes.

3.3 Scanning electron microscopy (SEM) and energy dispersive X-ray (EDX) analysis

Scanning electron microscopy (SEM) is a versatile and powerful analytical tool widely used across various scientific fields, offering three-dimensional and high-resolution visualisations of the sample surface from micro to nanoscale. In the operation of SEM, a focused beam of electrons scans across the sample surface in a controlled manner. As the electron beam interacts with the sample, it induces the emission of secondary electrons, backscattered electrons, and characteristic X-rays from the surface. Secondary electrons, emitted when the primary electrons dislodge electrons near the surface, are particularly useful for imaging due to their sensitivity to topographical variations. Backscattered electrons, which are primary electrons deflected by the nuclei of atoms in the sample, can provide compositional contrast based on the atomic number of the elements present.

Additionally, when electron beam hits the sample and knocks off an electron from the shell of an atom, another electron is attracted from an outer shell to fill the vacancy, and the characteristic X-ray is released, which is unique to the specific element and transition. When equipped with an Energy Dispersive X-ray (EDX) detector to capture the characteristic X-rays from the excitation of the atoms in the sample, SEM can perform elemental analysis, enabling qualitative and quantitative compositional identification within the sample. It should be noted that EDX has limitations in detecting light elements. Hydrogen and helium, for example, do not

emit characteristic X-rays, and the X-rays from lithium (Li K) are too low in energy to be detected effectively. While EDX can detect X-rays from elements ranging from beryllium to neon, the electrons involved in generating these characteristic X-rays are also the valence electrons involved in chemical bonding, which can alter the shapes and positions of the peaks in different compounds. Additionally, light elements often produce peaks that overlap with those of other elements or background noise, complicating accurate quantification.

In this thesis, SEM images were acquired using a secondary electron detector at an accelerating voltage of 10 kV. SEM-EDX is used to explore the surface morphology of electrodes, as well as to detect the distribution of byproducts over the electrode surface.

3.4 X-ray diffraction (XRD)

X-ray diffraction (XRD) is widely used to determine the crystallographic structure, the particle size, and infer the chemical composition of materials. As is shown in *Figure 3.2*, when the X-ray interacts with a crystalline sample, it is scattered by the atomic planes at specific angles, which follows the Bragg's Law:

$$n\lambda = 2d \sin \vartheta \qquad \text{(Equation 3.9)}$$

where n is the order of reflection, λ is the wavelength of the incident X-rays, d is the spacing between the planes in the atomic lattice, and ϑ is the angle of incidence. The scattered beams can add together in specific directions and reinforce each other by constructive interference to yield diffraction patterns.

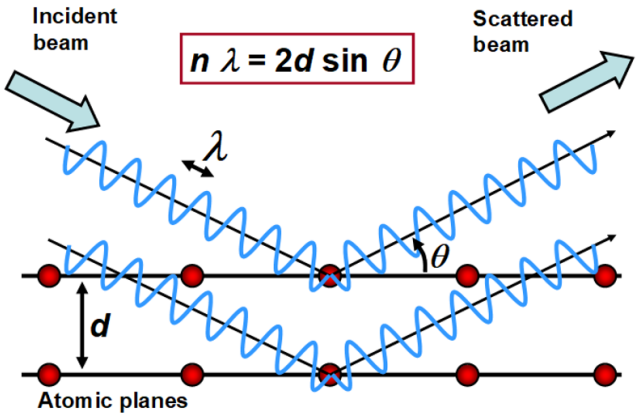


Figure 3.2 Schematic illustration of Bragg's Law [348]. Reproduced with permission, copyright 2019 The Authors.

XRD patterns provide detailed information about lattice parameters and symmetry, enabling the identification of the phase, texture (which refers to the preferred orientation of polycrystalline materials), as well as crystallinity and particle size of samples. These properties are reflected in the peak position, intensity, and width. Information about the unit cell metrics of a crystalline material determines the angular positions of the diffraction peaks. The intensity of these peaks provides insights into the relative abundance of different crystalline phases within the sample, while the width of the peaks is inversely proportional to the crystal size. The identity of an unknown compound can be verified by comparing its XRD pattern against those in the literature or a database, by matching the peak positions, widths, and relative intensities.

Herein, XRD characterisations were performed to the identify the byproduct formation and compare the texture change of the electrode surfaces after cycling in different electrolytes.

3.5 X-ray photoelectron spectroscopy (XPS)

X-ray photoelectron spectroscopy (XPS) is a surface-sensitive quantitative spectroscopic technique that measures the elemental composition, chemical state, and electronic state of the

elements within a material. The principle underlying XPS is based on the photoelectric effect. As is illustrated in *Figure 3.3*, when X-rays are directed onto a sample, some electrons are emitted from the top 1 to 10 nanometres of the surface, namely photoelectrons, which are characteristic of the specific atomic orbital. By measuring the binding energy and the number of electrons, which are reflected by the peak positions and intensities, the elements on the sample surface can be identified and quantified.

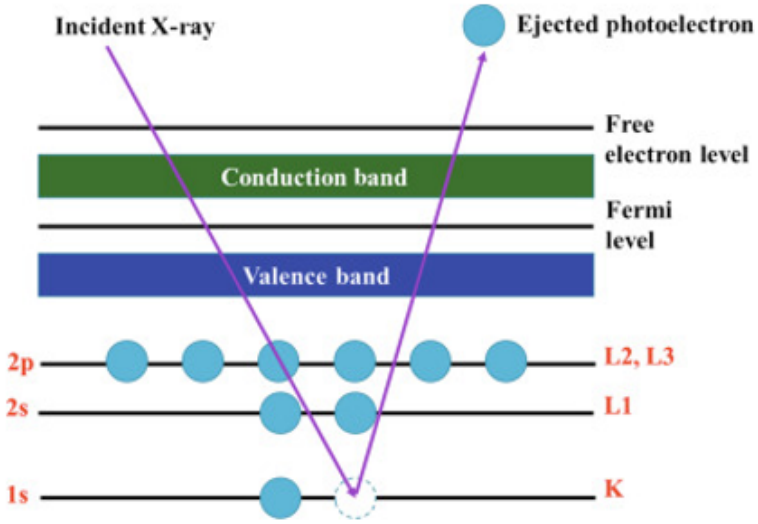


Figure 3.3 Schematic illustrating the ejection of photoelectron [349]. Reproduced with permission, copyright 2018 Elsevier.

Moreover, the energies of photoelectrons are dependent on their chemical environments, which can shift the binding energy values, thereby providing insights on the change in the oxidation states and presence of other chemical bonds. Furthermore, XPS can be combined with depth profiling to extend the analysis from the surface into the bulk material. This is achieved by sputtering the surface with ions, such as argon ions, and sequentially analysing the exposed layers, thus providing a detailed compositional depth profile of the sample.

The detection limit of XPS is often quoted as 0.1–1.0 % atomic percent. The interpretation of XPS spectra can be complex due to the need to accurately assign peaks to specific electron bonds and chemical states. Furthermore, overlaps and shifts in peak positions, which result from various factors, such as changes in chemical environments, surface charging accumulation, etc., can introduce uncertainties in interpretation and complicate peak fitting.

XPS combined with the depth profiling was employed to conduct qualitative and quantitative analysis of the elemental compositions of the deposits on Zn electrodes in the thesis.

3.6 Atomic force microscopy (AFM)

Atomic force microscopy (AFM) is a technique from the family of scanning probe microscopy techniques, which provides nanoscale imaging of sample surfaces. A typical setup of AFM is illustrated in *Figure 3.4*. In the operation of AFM, a cantilever equipped with a sharp tip is brought to the sample and scans across the surface. This tip is sensitive to various forces, such as van der Waals forces, electrostatic forces, chemical bonding forces, magnetic forces, and more. The force between the tip and the sample surface will bend the cantilever, which can be detected by a reflected laser. Therefore, a high-resolution topographical image of the sample surface can be provided, alongside a wide range of information, including roughness, adhesion, elasticity, as well as chemical, mechanical, electrical, or magnetic properties.

There are two main working modes of AFM: static mode and dynamic mode. The static mode is also known as the contact mode, where the AFM tip physically touches the sample surface and continuously drags across it. This mode is widely sued to provide topographical and mechanical information about hard samples. The dynamic mode can be further divided into the tapping mode and the non-contact mode. In tapping mode, the cantilever slightly oscillates to tap the

surface as it scans, which reduces the damage to soft samples. In non-contact mode, the oscillating tip moves across the surface without making direct contact, which is especially useful for extremely delicate or soft surfaces.

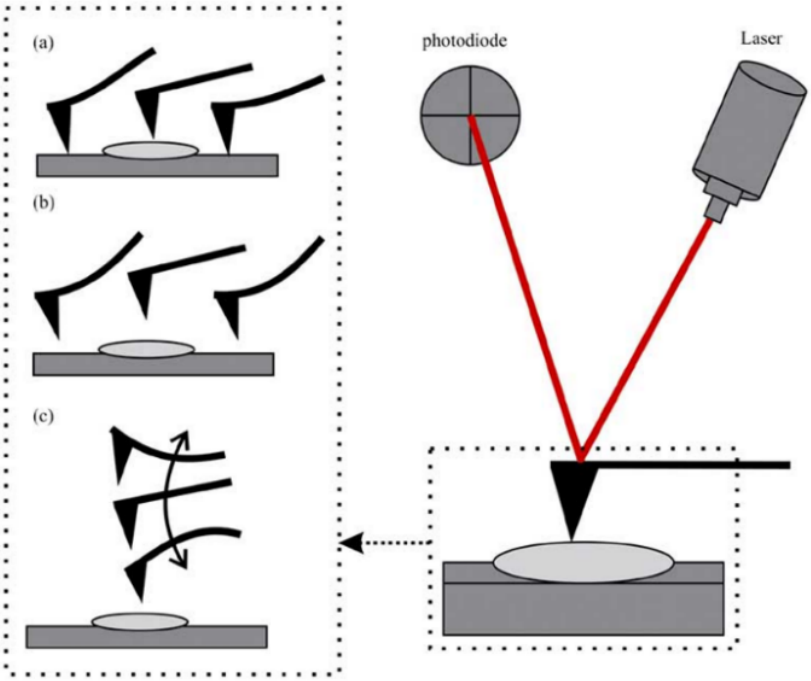


Figure 3.4 Schematic of the setup and working modes of AFM [350]. Reproduced with permission, copyright 2009 Bentham Science Publishers.

In this thesis, AFM was used in contact mode to capture the topography images of Zn electrodes, and measure their roughness and surface areas after cycling under different conditions.

3.7 Inductively coupled plasma-optical emission spectrometry (ICP-OES)

Inductively coupled plasma-optical emission spectrometry (ICP-OES) is a highly sensitive analytical technique to detect and quantify trace elements in various sample matrices. This technique is composed of two main procedures: the sample introduced into an argon plasma is first atomized and excited, leading to the emission of light at wavelengths characteristic to

specific elements; the wavelength and intensity of these emissions are then measured by an optical spectrometer to determine the presence and concentrations of elements within the sample.

Samples are treated with acids (e.g., nitric acid, hydrochloric acid) to dissolve solid materials and convert analytes into solutions. If sample solutions contain high analyte concentrations, they should be further diluted with suitable solvents to bring them within the calibration range of the instrument. The detection limits of ICP-OES can theoretically be as low as single digit parts-per-billion (ppb). In this thesis, ICP-OES was used to determine the composition of electrolytes with additives.

3.8 X-ray absorption fine structure spectroscopy (XAFS)

X-ray absorption fine Structure (XAFS) spectroscopy is a powerful technique to study the local structural and electronic properties of materials. XAFS spectroscopy is based on the measurement of the absorption coefficient of a material as a function of the energy of incident X-rays. The XAFS spectrum consists of two main regions, X-ray Absorption Near Edge Structure (XANES) and Extended X-ray Absorption Fine Structure (EXAFS), as illustrated in *Figure 3.5*.

The XANES region extends from slightly below to just above the absorption edge of an element, reflecting the electronic structure and oxidation state of the atom. The position of the absorption edge can be used to identify the oxidation state of the element, as higher oxidation states require more X-ray energy to eject a core electron. Additionally, the pre-edge feature, appearing as a shoulder before the absorption edge, is indicative of the coordination environment of the atom. The EXAFS is located beyond the XANES region, which provides detailed information about the bonding distances, coordination numbers, and disorder around

the atom. These properties of local structures can be determined by fitting the oscillations in the absorption waves to theoretical models.

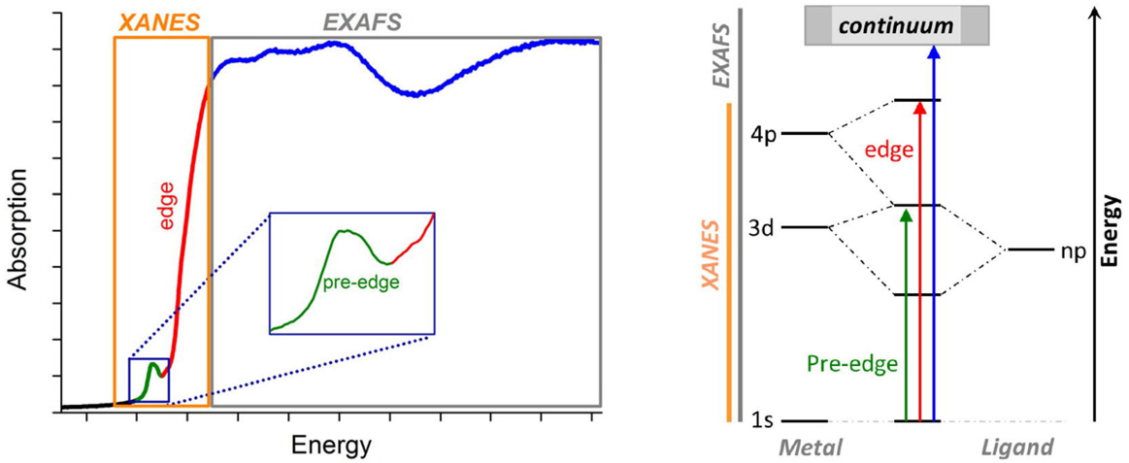


Figure 3.5 Illustration of the XANES and EXAFS regions in the XAFS spectrum, and the origin of the electronic transitions corresponding to the features [351]**. Reproduced with permission, copyright 2016 Wiley-VCH.**

In this thesis, XAFS measurements were performed by a lab-based X-ray spectrometer on liquid electrolytes, to analyse changes in the oxidation state of Zn ions with addition of different organic additives, thereby elucidating their roles in altering the solvation structures.

3.9 Raman spectroscopy

Raman spectroscopy is a non-destructive analytical technique widely employed to understand the molecular composition and chemical structure within materials. It is based on the analysis of inelastic scattering, or Raman scattering, of monochromatic light, usually from a laser source.

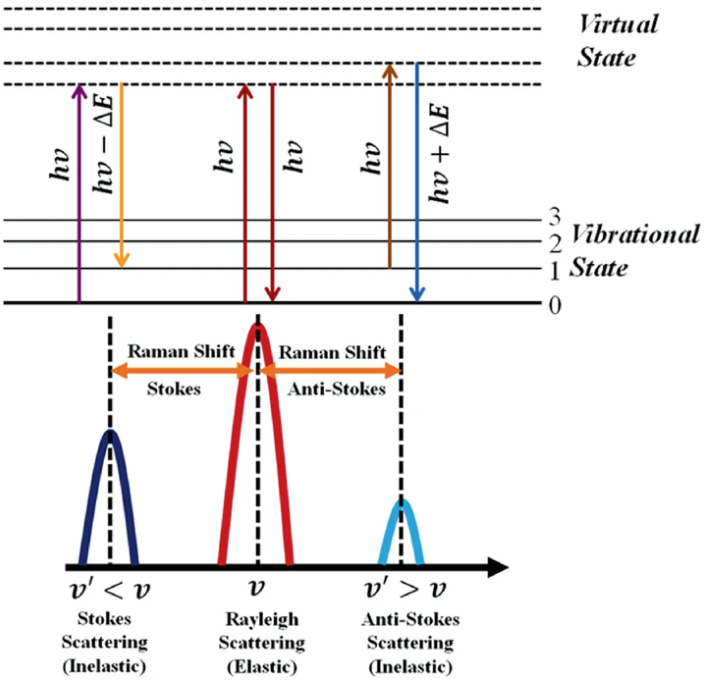


Figure 3.6 Schematic illustration of the Rayleigh and Raman scattering modes [352]. Reproduced with permission, copyright 2021 The Authors.

As shown in *Figure 3.6*, when the sample is irradiated by the laser light (ranging from the ultraviolet into the near-infrared and beyond), most photons are elastically scattered, which is known as the Rayleigh scattering. However, a very small fraction of the photons will undergo inelastic scattering, which results in either a decrease (Stokes scattering) or an increase (Anti-Stokes scattering) in the energy. This shift is known as the Raman shift, which provides information about the molecular vibration modes characteristic to each chemical bond, thus revealing the chemical structures of the sample.

In this thesis, Raman spectroscopy was employed to analyse the electrolytes with addition of various organic additives, aiming to understand their involvement into the water network and solvation sheath of Zn ions.

Chapter 4 Unveiling the anode corrosion process in Zn-ion batteries

4.1 Introduction

The degradation of the Zn metal anode due to corrosion presents significant challenges for the practical application of Zn-ion batteries. Theoretically, corrosion refers to a chemical or electrochemical process that denotes the deterioration of materials, commonly metals, instigated by exposure of materials to an external environment. Due to the high chemical activity and low electrochemical potential of Zn metal, corrosion of the Zn metal electrode is an inevitable and spontaneous process in an aqueous environment [145,170]. The parasitic reactions between the Zn metal electrode and the electrolyte can lead to the decomposition of electrolytes and loss of active Zn, which will severely degrade the performance of the whole battery with cycling proceeding or even during rest process [170,175]. Besides, the byproduct layer generated by parasitic reactions will induce heterogeneous Zn nucleation, triggering the formation of dendrites and uneven interfaces [165,174,208]. Such surface irregularities further enhance the active surface area of the electrode accessible to the electrolyte, and in turn, aggravate corrosion of the electrode and other side reactions. This vicious circle between corrosion and dendrite growth eventually results in the failure of Zn-ion batteries. Moreover, to enhance the energy density of Zn batteries, Zn electrodes with high specific surface area (e.g., porous and powder Zn electrodes) are normally adopted, in which case the corrosion rate of Zn electrode will also increase significantly [165,353].

Although the utilisation of mild or acidic electrolytes avoids the generation of ZnO or $Zn(OH)_2$ byproducts that cause a series of issues in alkaline systems, other byproducts, such as ZHS, $Zn_5Cl_2(OH)_8 \cdot H_2O$ [354], $Zn_x(CF_3SO_3)_y(OH)_{2x-y} \cdot xH_2O$ [355], still contribute to the degradation of the whole battery performance due to continuous hydrogen evolution and consumption of active

Zn, water and Zn salts [174]. These corrosion-induced species typically exhibit porous and loose structures, as opposed to a continuous layer that would shield the electrode surface from the electrolyte. As a result, the corrosion reactions are not naturally self-limiting and will continue to proceed throughout the lifetime of the cell. These challenges arising from corrosion significantly reduce the shelf life after battery assembly even before use, thereby considerably constraining the practical application of Zn-ion batteries [177].

This chapter delves into the intricate processes of the Zn metal anode corrosion when the battery rests at open circuit without cycling. The self-corrosion process of Zn under various conditions was explored. By utilising in situ liquid cell TEM, the dissolution behaviour of Zn was observed during the rest period. It was discovered that this self-dissolution issue is closely associated with the initial pH of the electrolyte. By adjusting the pH of the 1 M $ZnSO_4$ electrolyte, the self-dissolution was effectively eliminated, as evidenced by in situ liquid cell TEM observations. Such dissolution of Zn was identified as being the initial stage of the self-corrosion process, which eventually leads to the generation of ZHS products. These observations by liquid cell TEM reveal the corrosion mechanism of the Zn metal anode in the $ZnSO_4$ electrolyte, which suggests a significant role of the electrolyte pH in affecting the battery shelf life.

4.2 Experimental

4.2.1 Chemicals and materials

All chemicals were used directly without any further treatment. 2 M $ZnSO_4$ electrolytes were purchased from Merck Life Science UK Limited, and 1 M $ZnSO_4$ electrolytes were prepared by diluting the 2 M electrolytes. Zinc acetate dihydrate [$Zn(CH_3CO_2)_2{\cdot}2H_2O$, $Zn(OAc)_2$], V_2O_5, Zn foil, Ti foil, Cu foil and glass fibre were purchased from Sigma Aldrich. Celgard 3501 was purchased from Celgard, LLC. LIR 2032-coin cell components were purchased from MTI Corporation.

4.2.2 Setup for in situ TEM characterisation

The in situ liquid cell TEM holder (Poseidon 510) and chips (EPB-55DNF and ECT-15WR) used in this work are from Protochips Ltd. The liquid cell holder tip is composed of two silicon chips with electron transparent SiN_x windows, one of which is patterned with platinum (Pt) electrodes. The electrolyte was injected into the holder tip by a syringe pump at a flow rate of 300 µl/h during system purging and at a flow rate of 120 µl/h during TEM imaging.

A Gamry reference 600 was used for galvanotactic measurements. The applied currents in the in situ TEM experiments were 7.5 nA, 12 nA, 15 nA and 30 nA respectively, and the current densities were calculated from the electrode areas of the electrodes patterned on the chips (around 150 μm^2 for in situ experiments and around 300 μm^2 for ex situ experiments). TEM imaging was carried out with a JEOL JEM-2100 operated at 200 kV with a tungsten filament, with a 70 µm condenser aperture inserted and a spot size of 3 set up to minimise the beam damage. The beam current was calibrated by a Faraday cup before experiment, and 2 nA was measured under this condition, corresponding to a low dose rate of 4 electrons $Å^{-2}\ s^{-1}$. The dose test results under these conditions are shown in Appendix *Figure A3*. The movies were recorded using DigitalMicrograph software, and specific images of interest were extracted.

4.2.3 Electrochemical tests

All coin cells were assembled with a volume of 140 µl electrolyte added and pressed to 1000 psi. The self-supporting V_2O_5 cathode films were prepared by mixing commercial V_2O_5 powder with carbon black and polytetrafluoroethylene in the 6:3:1 mass ratio. Zn||Ti and Zn||Zn coin cells were assembled with two layers of glass fibre. The long-term cycling of coin cells was carried out using a Maccor Series 4000, and all other electrochemical measurements were conducted on a

Biologic VMP3 system at a temperature of 30 °C.

4.2.4 Characterisations

Surface morphologies and elemental analysis of Zn electrodes were achieved by a Carl Zeiss Merlin field emission analytical SEM coupled with an Oxford instruments Xmax 150 energy dispersive spectrometer. It features a 150 mm^2 silicon drift detector. The qualitative EDX mapping was obtained at an accelerating voltage of 10 kV. XRD patterns of Zn electrodes were obtained using a Cu source Rigaku Smartlab 3kW diffractometer (wavelength λ = 1.5418 Å). The pH values of electrolytes were determined by a Mettler Toledo Seven Excellence pH/mV conductivity meter.

4.3 Results and discussion

4.3.1 ZHS formation on the Zn metal anode during rest under different conditions

The role of ZHS and its analogues initially did not attract much interest in research, as they were considered detrimental byproducts and not directly involved in electrochemical reactions. However, recent studies have confirmed the reversible formation and dissolution of ZHS on the cathode surface during discharge and charge, which is generally believed to be related to the insertion/extraction of protons to/from the cathode or the oxygen reduction reaction near the cathode surface [[174]].

In contrast, ZHS formation on the anode surface is still considered irreversible and accumulates as the rest duration and cycling period are prolonged. Unlike the dense $ZnO/Zn(OH)_2$ layer formed in alkaline systems, the ZHS layer generated in the $ZnSO_4$ electrolyte usually has a loose structure, hence it is not able to protect the anode surface from continuous corrosion. However,

very recently, researchers have been working on transforming such adverse side products into 'wealth'. Several strategies have been developed to modify the structure of ZHS to form a uniform layer covering the electrode surface. This byproduct-based protective layer would help prevent continuous corrosion by minimizing direct contact between the Zn metal anode and the electrolyte [270,356]. Additionally, it has also been demonstrated by recent work that a thin protective ZHS layer will form on the Zn electrode under specific resting conditions, which can largely enhance the stability and durability of the Zn metal anode [357]. Therefore, understanding the nucleation and formation mechanism of ZHS on the Zn electrode surface is of great importance.

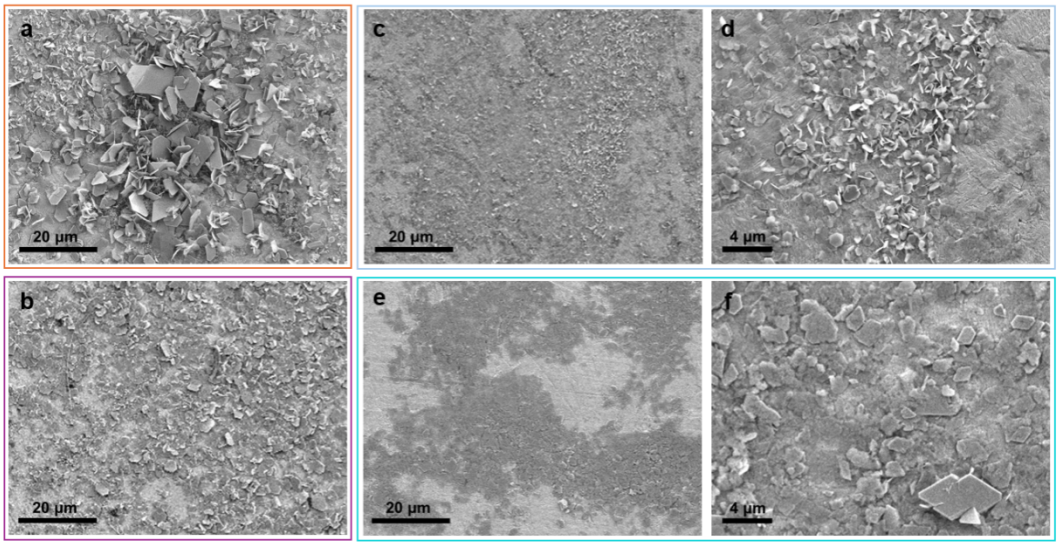


Figure 4.1 ZHS forming on Zn foils under different conditions. (a) Zn foil soaked in the vial. (b) Zn foil in the pouch cell. (c, d) Zn foil in the coin cell with glass fibre. (e, f) Zn foil in the coin cell with Celgard.

The formation of ZHS was first compared across different setups; resting the Zn electrode in a vial, pouch cell and coin cell, to investigate the influence of the electrolyte volume, external pressure and separator type. *Figure 4.1* shows the morphologies of ZHS forming under different cell assembly conditions. Zn foil was soaked in a vial with 2 ml 2 M $ZnSO_4$ electrolyte for 18 hours (*Figure 4.1 a*). The same Zn foils were also used to assemble the pouch cell, using glass fibre as

the separator with a volume of 140 µl electrolyte added (*Figure 4.2 b*). *Figure 4.1 c-f* shows the Zn electrodes after resting in coin cells, to study the effect of pressure on the ZHS formation. Coin cells were prepared with 140 µl of electrolyte and pressed to 1000 psi, using glass fibre and Celgard as the separators, respectively.

It was found that the size and amount of ZHS flakes formed in the vial with an excess of electrolyte are much larger than those in the pouch cell and coin cell with a limited quantity of electrolytes. Moreover, external pressure applied to the cell favours a uniform ZHS layer with a denser structure. However, ZHS flakes forming in the coin cell using Celgard separator were less evenly distributed on the electrode surface compared to those using glass fibre, despite the ZHS flakes showing a stronger tendency of parallel flat growth along the electrode surface. This discrepancy could be attributed to the smoother surface structure of the Celgard film, and its worse wettability that limits ion diffusion.

From the comparisons of Zn electrodes above, it is worth noting that the amount of electrolyte is a crucial factor to affect the formation of ZHS. An excess of electrolyte can promote more extensive formation of ZHS during the rest period.

4.3.2 Self-corrosion property of the Zn metal anode in Zn-ion batteries

It is argued that the formation of ZHS on the electrode/electrolyte interface is a spontaneous process as long as the chemical equilibrium condition is satisfied with an adequate supply of Zn^{2+}, OH^-, SO_4^{2-} and H_2O in the electrolyte environment, regardless of the electrode substrate material used [187]. Despite the mildly acidic condition of $ZnSO_4$ electrolytes, OH^- ions may also be generated due to a series of side reactions, such as water decomposition reaction during cycling, which can lead to a local alkaline environment to conducive to ZHS formation [165]. However,

during battery rest, the presence of Zn metal is essential to promote the formation of ZHS; it is not sufficient for the Cu and Ti substrate materials to merely be present in just the electrolyte.

To confirm this, Zn foil, Cu foil and Ti foil were soaked in 2 M $ZnSO_4$ electrolyte respectively in vials for 18 hours. As is shown in *Figure 4.2*, flaky byproducts formed on the Zn foil, while the surfaces of the Cu and Ti foil remained clean. Even though it was reported that there was ZHS and $Zn(OH)_2$ formation on the surface of Cu foil after soaking in 1 M $ZnSO_4$ [187], the hexagonal flakes in the SEM image were more likely to be corrosion byproducts of Cu in acidic solutions with the presence of oxygen, such as CuO and Cu_2O particles, and this interpretation is supported by their XRD patterns.

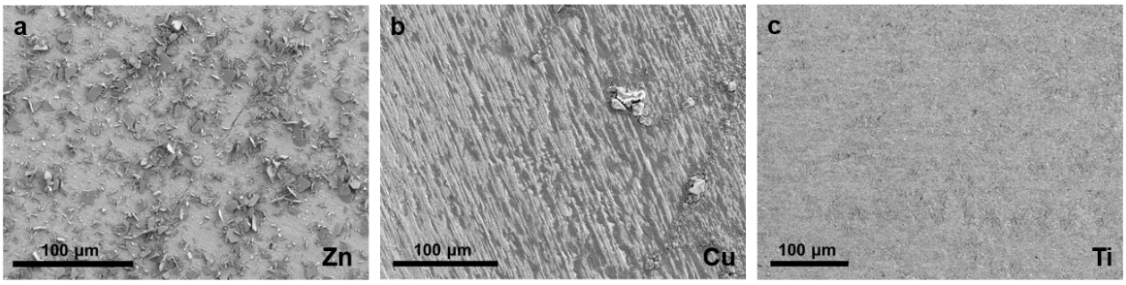


Figure 4.2 (a) Zn foil, (b) Cu foil and (c) Ti foil soaked in vials 18 hours.

Interestingly, after soaking the Cu and Ti foil together with the Zn foil in the same vial, it was found that their surfaces were covered by Zn byproducts instead (*Figure 4.3*). The presence of ZHS on the Cu and Ti foils was confirmed by their XRD patterns (*Figure 4.3 c*). This phenomenon can be attributed to the additional Zn^{2+} ions provided by the Zn foil, thus promoting the achievement of the chemical equilibrium necessary for ZHS precipitation on these surfaces.

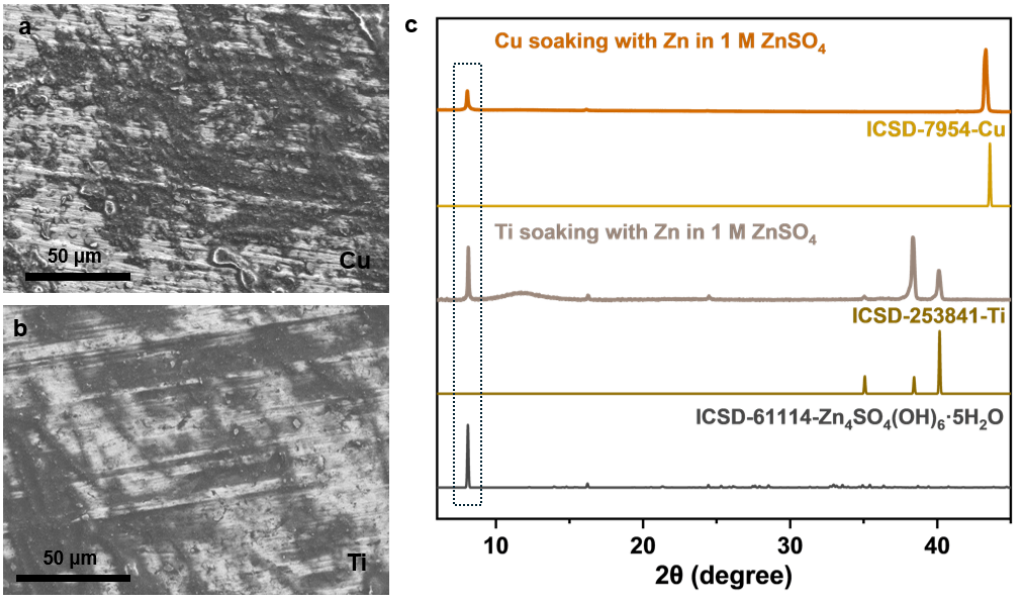


Figure 4.3 SEM images of (a) Cu and (b)Ti foil soaked together with the Zn foil in the same vial, and (c) their corresponding XRD patterns. The main XRD peak of ZHS is highlighted with the dotted rectangle.

These findings highlight the self-corrosion property of Zn metal anode in Zn-ion batteries, which is the primary cause for severe ZHS byproduct formation and hydrogen evolution during battery rest periods. The self-corrosion of metals is described as a process where the metal material undergoes degradation due to reactions with its environment without the influence of external galvanic action from a more noble metal. This type of corrosion is purely chemical (in dry environments) or electrochemical (in wet environments) and depends on the metal's inherent properties and the nature of its environment [358].

4.3.3 Investigation of the ZHS formation via ex situ liquid cell experiments

As demonstrated above, the Zn metal electrode plays an active role in the formation process of ZHS. Therefore, to further understand the nucleation behaviour of ZHS on the Zn surface, a specific amount of Zn was deposited onto the inert Ti foil, to provide a confined area for the formation of ZHS flakes. Zn was deposited on the Ti foil in a beaker cell at a current density of

100 mA/cm^2 with a capacity of 5 mAh/cm^2, and then soaked in the 1 M electrolyte in a vial for 40 hours.

SEM images of the Ti foil surface before and after soaking are presented in *Figure 4.4 a-d*. Initially, the Zn deposit layer exhibited a relatively smooth surface. After soaking in the electrolyte for 40 hours, numerous larger hexagonal flakes were observed growing from the deposition layer. The presence of ZHS was confirmed by the XRD results of the Ti foil, with a pronounced peak emerging after soaking (*Figure 4.4 e*). The ZHS byproducts share a similar crystal structure and morphology with the Zn metal deposits, thus making it challenging to identify ZHS flakes from SEM imaging of the Zn electrode. Consequently, SEM-EDX analysis was conducted to determine the distribution of ZHS and Zn flakes. The pixel size was 150 nm × 150 nm and the total acquisition time was 6 minutes. From the EDX elemental mapping in *Figure 4.4 f*, the larger ZHS flakes showed a stronger oxygen signal compared to the adjacent smaller Zn deposits. The raw EDX spectrum is also attached in Appendix *Figure A4*, showing strong signal peak of oxygen.

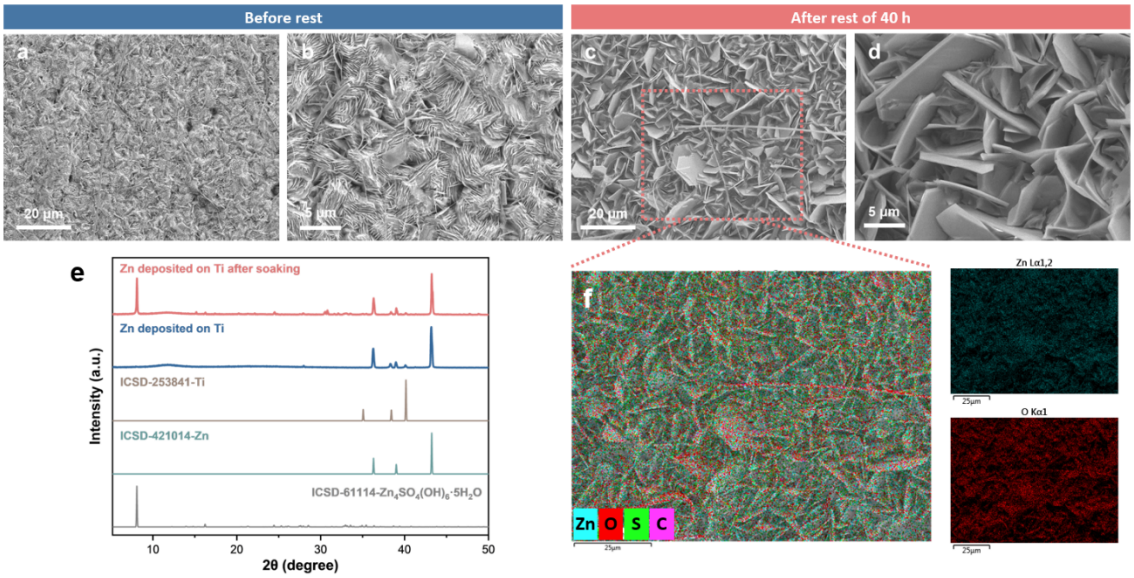


Figure 4.4 SEM images of Ti foil with Zn deposits (a, b) before and (c, d) after rest. (e) XRD patterns of the Ti foil with Zn deposits before and after rest. (f) The EDX mapping of the Ti foil surface after rest.

We attempted to deposit a smaller amount of Zn onto the Ti foil to gain detailed insight into the nucleation behaviour of ZHS. However, due to the poor affinity of Zn for Ti, the Zn deposits were easily removed, thus making it difficult to trace changes in composition and morphology. Therefore, additional ex situ liquid cell experiments were conducted to investigate the formation mechanism of ZHS during battery rest, which allows for more detailed observation.

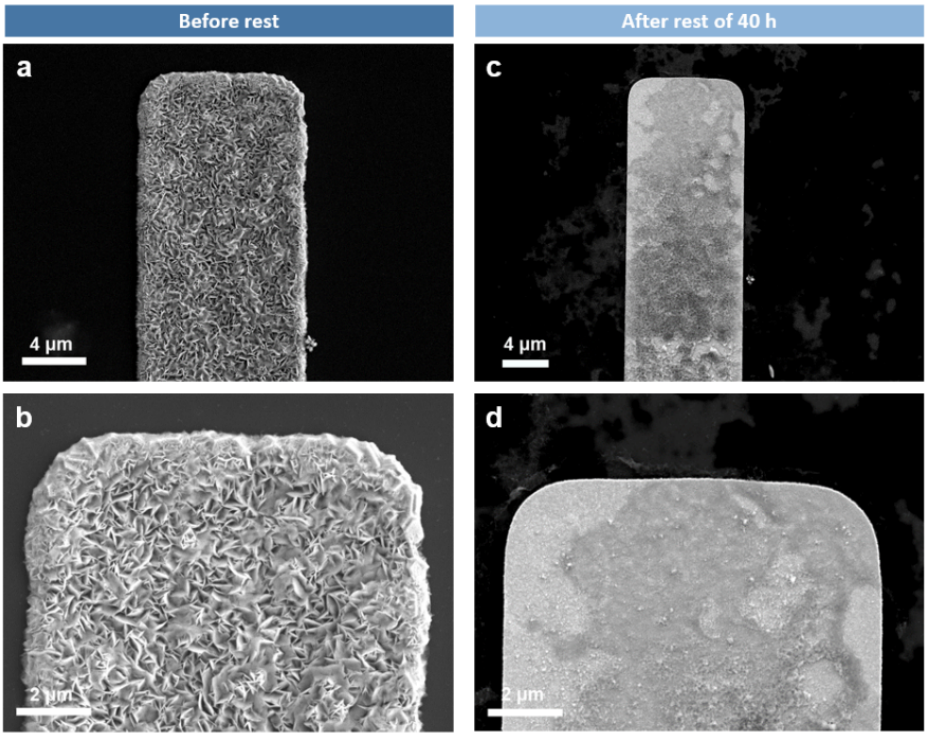


Figure 4.5 SEM images of the chip after electrodeposition (a, b) before and (c, d) after rest.

The liquid cell setup was assembled using the chip with a Pt working electrode with a surface area of 300 μm^2, and 1 M $ZnSO_4$ electrolyte was injected into the holder tip at a flow rate of 120 µl/h. Zn was deposited onto the Pt substrate at a current density of 50 mA/cm^2 with a smaller areal capacity of 1 mAh/cm^2, compared to the prior deposition on the Ti foil of 5 mAh/cm^2. Afterward, the liquid cell setup was dismantled carefully and the chip with Pt electrode was then immersed in the 1 M electrolyte in a vial for 40 hours. The morphologies of Zn deposits on the Pt electrode were characterised by SEM before and after the rest procedure, as shown in *Figure*

4.5. Zn flakes with a loose structure covered the Pt electrode surface after the electrodeposition. However, after resting for 40 hours, instead of forming ZHS byproducts on the Zn surface, most deposits had disappeared and only few residues were left on the Pt electrode. In other words, the rate of loss of the Zn deposits significantly exceeded the rate at which byproducts formed on the electrode.

As mentioned above, ZHS formation on the anode surface is usually considered irreversible [[174]]. ZHS can form during both self-corrosion process and electrochemical cycling, and the formation of ZHS during cycling is primarily due to the water decomposition reaction that accompanies the de-solvation process of Zn plating. To confirm the reliability of the ex situ liquid cell setup and exclude the influence from the flowing electrolyte, three plating/stripping cycles were performed at a current density of 20 mA/cm^2. The liquid cell setup was then dismantled after cycling and was characterised by SEM-EDX. The pixel size was 35 nm × 35 nm and the total acquisition time was 3 minutes. ZHS formation was clearly observed on the Pt electrode, as shown in *Figure 4.6*.

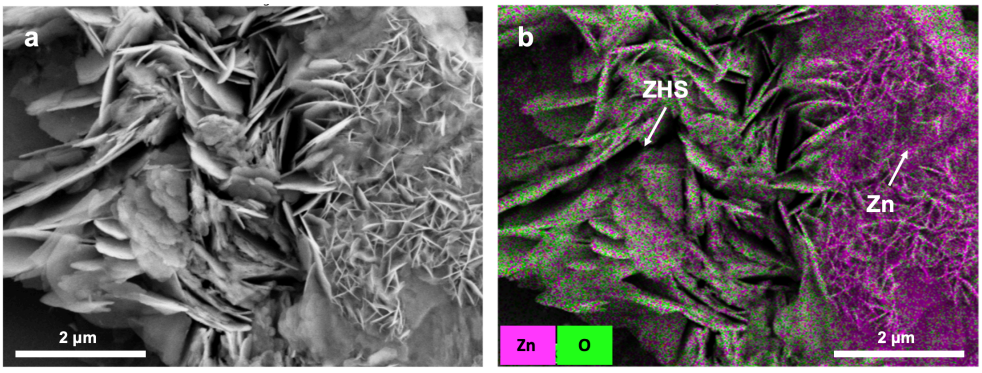


Figure 4.6 (a) The SEM image and (b) the EDX mapping of the chip after cycling, illustrating the mixture of Zn deposits and ZHS.

These results indicate that the dissolution process of Zn precedes the formation of ZHS byproducts during the rest period. The self-dissolution of the Zn metal electrode is a crucial

process in alkaline Zn batteries, where Zn continuously forms soluble zincate ions according to the Pourbaix diagram [154,165]. However, the nature and impact of this dissolution in mild acidic systems can be quite different from that in alkaline batteries. The mild acidity of $ZnSO_4$ electrolytes has less aggressive interactions with the Zn metal anode, which is supposed to help to maintain a more stable zinc ion environment and reduce the rate of Zn dissolution. Therefore, to better understand the relationship between the Zn loss and the ZHS formation, in situ experiments are necessary.

4.3.4 Decrease in the coulombic efficiency during rest via in situ liquid cell experiments

The liquid cell setup for in situ experiments was assembled using the chip with a narrower Pt working electrode with a surface area of 150 μm^2, to provide a suitable field of view. The 1 M $ZnSO_4$ electrolyte was injected into the holder tip at a flow rate of 120 µl/h.

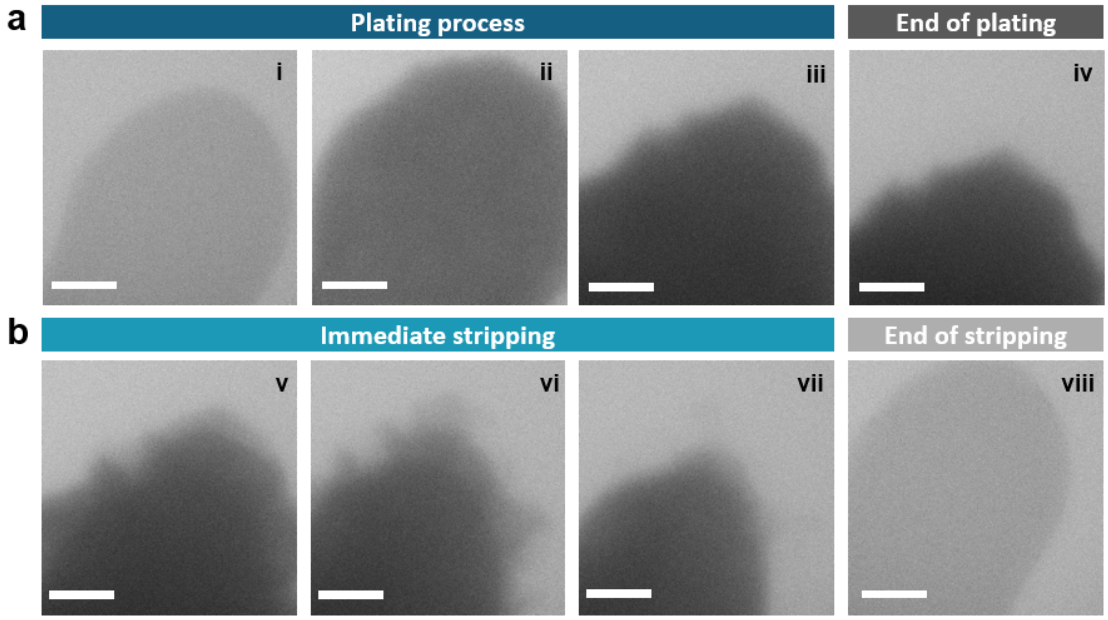


Figure 4.7 In situ liquid cell TEM imaging of (a) the plating and (b) the immediate stripping of Zn. Scale bars are 1.5 µm.

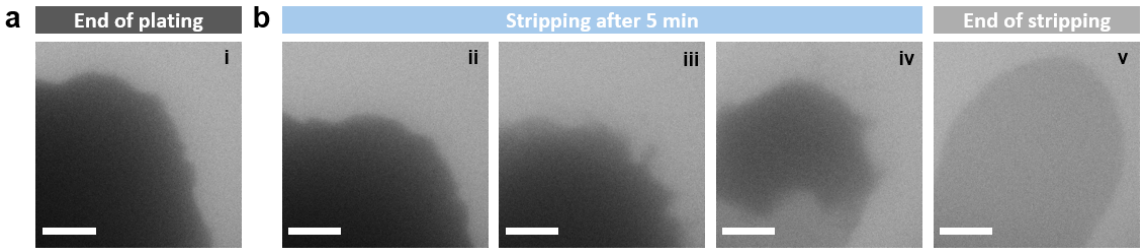


Figure 4.8 In situ liquid cell TEM imaging of (a) end of plating and (b) stripping after 5 minutes rest after plating. Scale bars are 1.5 µm.

We performed two experiments. In both, Zn was deposited onto the Pt working electrode at a current density of 20 mA/cm^2 to a capacity of 0.4 mAh/cm^2, then the deposited Zn was either stripped immediately (*Figure 4.7*) or after a resting period of 5 minutes (*Figure 4.8*). For the sample with a rest period, the viewing field was moved outside of the chip window to avoid the electron beam damage during the five-minute rest period. A schematic illustration of the field of view around the Pt working electrode before and after plating is provided in Appendix *Figure A5*, to aid in understanding the liquid cell TEM results. The galvanostatic voltage profiles recorded while plating and stripping for the two cycles are shown in *Figure 4.9*, with points in time corresponding to sequential TEM images highlighted.

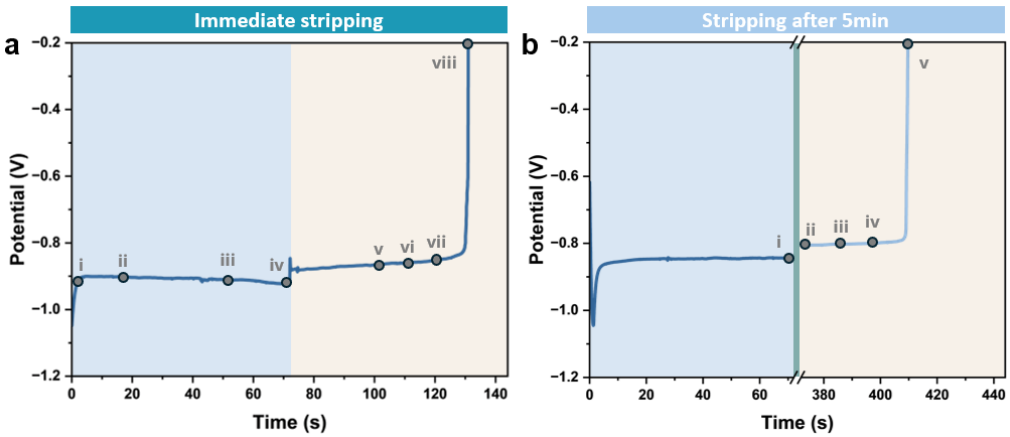


Figure 4.9 Galvanostatic voltage profiles of in situ liquid cell TEM experiments. (a) Plating and immediate stripping. (a) Plating and stripping after 5 minutes. The blue, beige and green regions represent the plating, stripping and rest process respectively.

The coulombic efficiency can be calculated based on the plating and stripping duration according to the following equation:

$$Coulombic\ efficiency = {}^{t_{\text{stripping}}}\!/_{t_{\text{plating}}} \times 100\% \qquad \text{(Equation 4.1)}$$

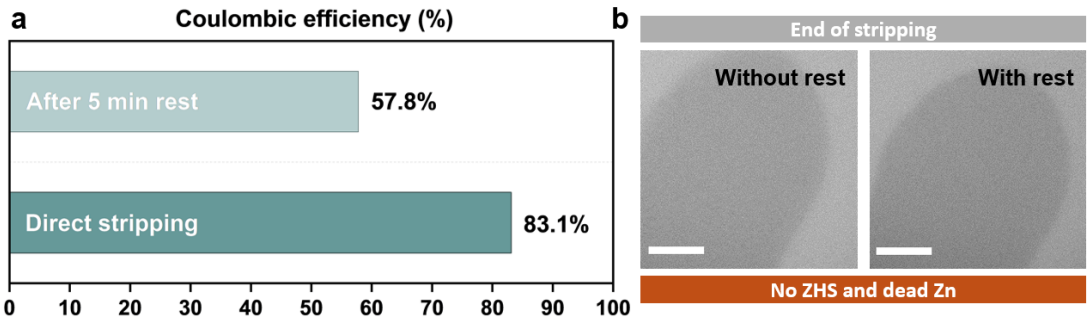


Figure 4.10 Comparison of (a) the coulombic efficiency and (b) TEM images at end of plating without and with rest of 5 minutes. Scale bars are 1.5 µm.

As is shown in *Figure 4.10 a*, the coulombic efficiency of the cycle after resting for 5 minutes was reduced from 83.1% to 57.8% compared with that of stripping immediately after plating. Since the images of the Pt electrode after stripping for both the without and with rest runs are both completely bare of ZHS or Zn deposit, as shown in *Figure 4.10 b*, the difference in coulombic efficiency must be due to some Zn being lost during the rest period, and so leaving less capacity to be removed by the stripping process.

The coulombic efficiency can be influenced by various cycling parameters in the study of Zn metal anodes, such as the current density and depth of discharge [197,263]. To compare the coulombic efficiency under other conditions, Zn was also deposited at different current densities with the same capacity (0.1 mAh/cm^2).

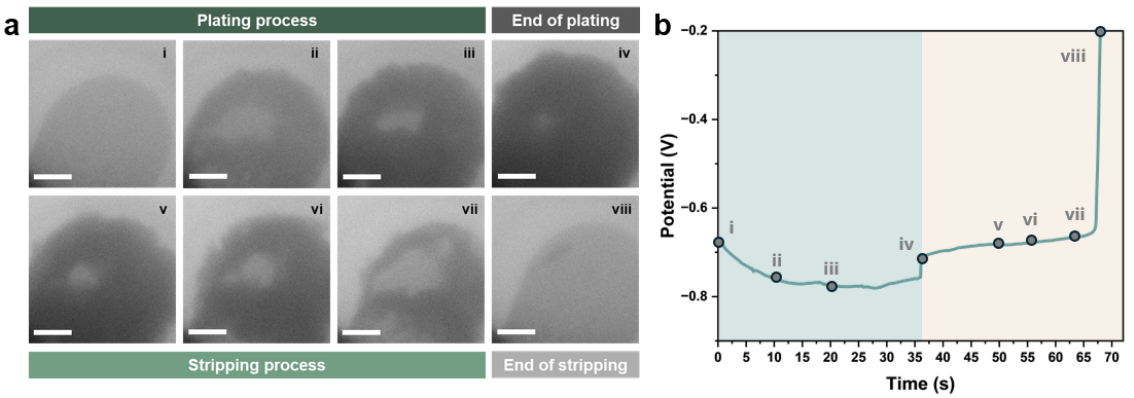


Figure 4.11 (a) In situ liquid cell TEM imaging of plating and stripping at 10 mA/cm^2 and (b) the corresponding voltage profile. Scale bars are 1.5 µm. The green and beige regions represent the plating and stripping process respectively.

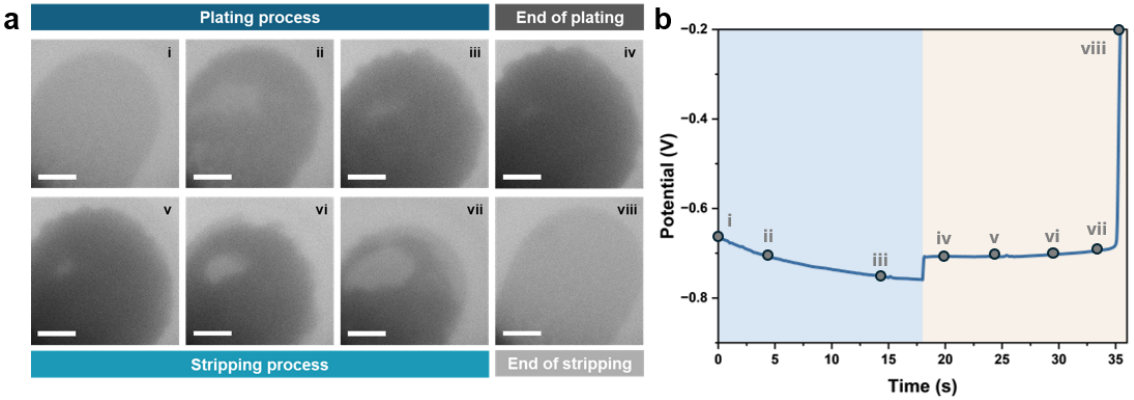


Figure 4.12 (a) In situ liquid cell TEM imaging of plating and stripping at 20 mA/cm^2 and (b) the corresponding voltage profile. Scale bars are 1.5 µm. The blue and beige regions represent the plating and stripping process respectively.

Sequential liquid cell TEM images of Zn plating and stripping at current densities of 10 mA/cm^2 and 20 mA/cm^2 are shown in *Figure 4.11* and *Figure 4.12*, respectively. Zn deposits under these two current densities exhibited similar morphologies, with no obvious residues left at the end of stripping. A higher coulombic efficiency was achieved using a higher current density of 20 mA/cm^2 (*Figure 4.13*), which is consistent with previous studies in coin cells [359]. In fact, ultra-high current densities are frequently used in research studies of Zn-ion batteries to demonstrate

good cycling performance based on cycle numbers, as longer cycling durations will significantly deteriorate the performance of Zn cells due to severe side reactions [197].

Comparing the results of using 20 mA/cm^2 for different deposition capacities, the coulombic efficiency increased from 83.1% from 96.1% by decreasing the capacity to a quarter (*Figure 4.10 a* and *Figure 4.13*). Considering the much longer time required for higher capacities, it is anticipated that the side reactions occurring simultaneously during plating/stripping periods should also be taken into account as an important factor affecting the coulombic efficiency.

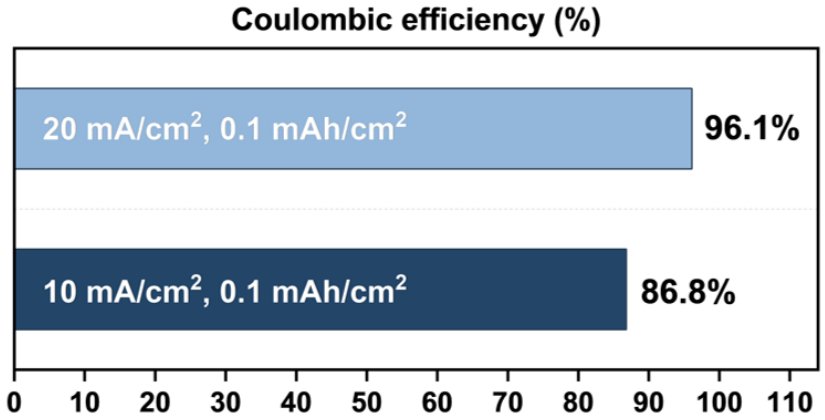


Figure 4.13 Comparison of the coulombic efficiency at different current densities.

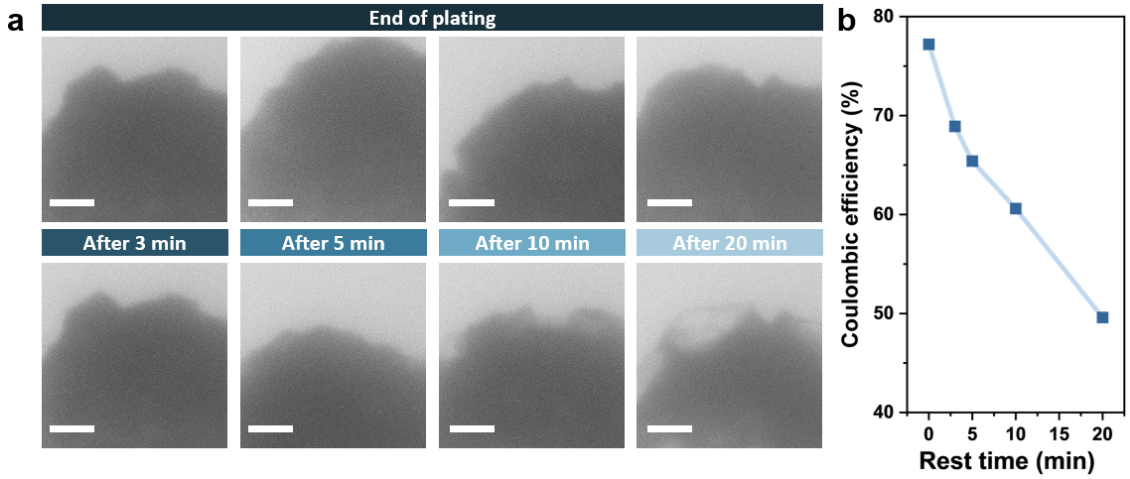


Figure 4.14 (a) In situ liquid cell TEM imaging before and after rest for different periods of time and (b) the corresponding coulombic efficiency. Scale bars are 1 µm.

To further investigate the capacity loss and examine the influence of side reactions during rest, Zn was deposited at a smaller current density of 8 mA/cm^2 for 72 seconds for a capacity of 0.16 mAh/cm^2, and was left for varying time before stripping. The images of Zn deposits before and after rest were compared in *Figure 4.14 a*. There was no significant change in the shape and darkness of Zn deposits after resting for a short period of 3 minutes. However, it was found that the contrast of the edge of deposits started to fade after 10 minutes, and a partial disappearance of the deposition was clearly observed after 20 minutes. Moreover, the coulombic efficiency was also found to decrease from 77.2% from 49.6% after resting for 20 minutes (*Figure 4.14 b*). This observation aligns with those from ex situ liquid cell experiments discussed above. Therefore, it is anticipated that such self-dissolution behaviour of Zn deposits accounts for the capacity loss during rest, rather than the formation of byproducts.

4.3.5 Dissolution behaviour of Zn during rest in the $ZnSO_4$ electrolyte

The current density and deposition capacity were further reduced to 5 mA/cm^2 and 0.05 mAh/cm^2 to highlight the dissolution process. Sequential images of plating and the corresponding voltage profile are shown in *Figure 4.15*.

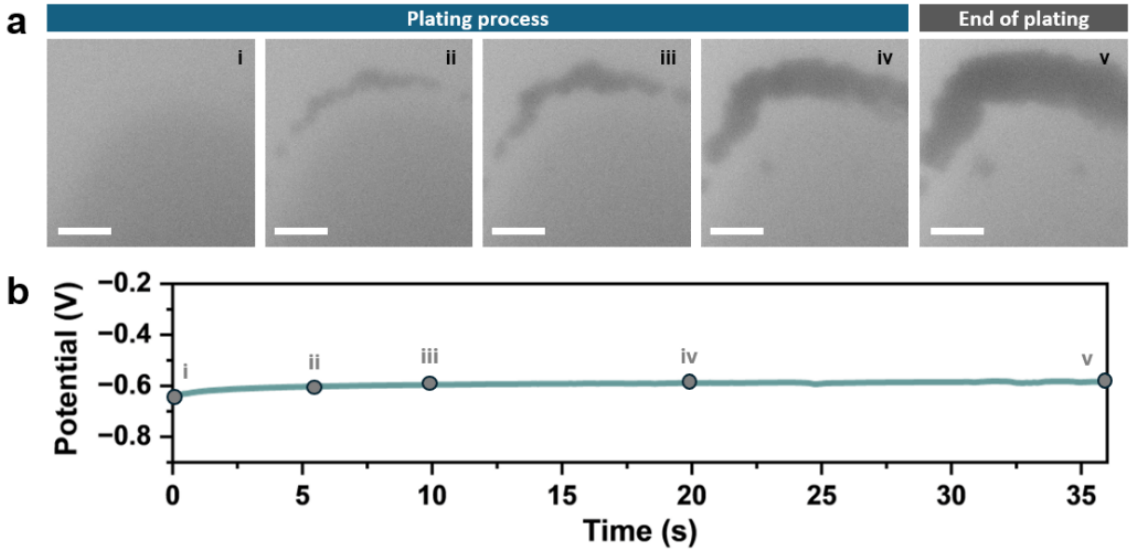


Figure 4.15 (a) In situ liquid cell imaging of plating at a current density of 5 mA/cm^2 and (b) the corresponding voltage profile. Scale bars are 1 µm.

To reveal the self-dissolution behaviour of Zn during rest, changes of Zn deposits on the Pt electrode were continuously recorded after deposition. The viewing field was initially moved to the other side of the Pt electrode, which had a relatively smaller amount of deposits. As shown in *Figure 4.16*, it was observed that the contrast of deposits began to fade within 20 seconds of the rest period. The deposits continued dissolving as the rest period extended, and distinct gaps were observed from stage iii. Zn deposits on this side of Pt electrode almost completely disappeared after resting for approximately 200 seconds.

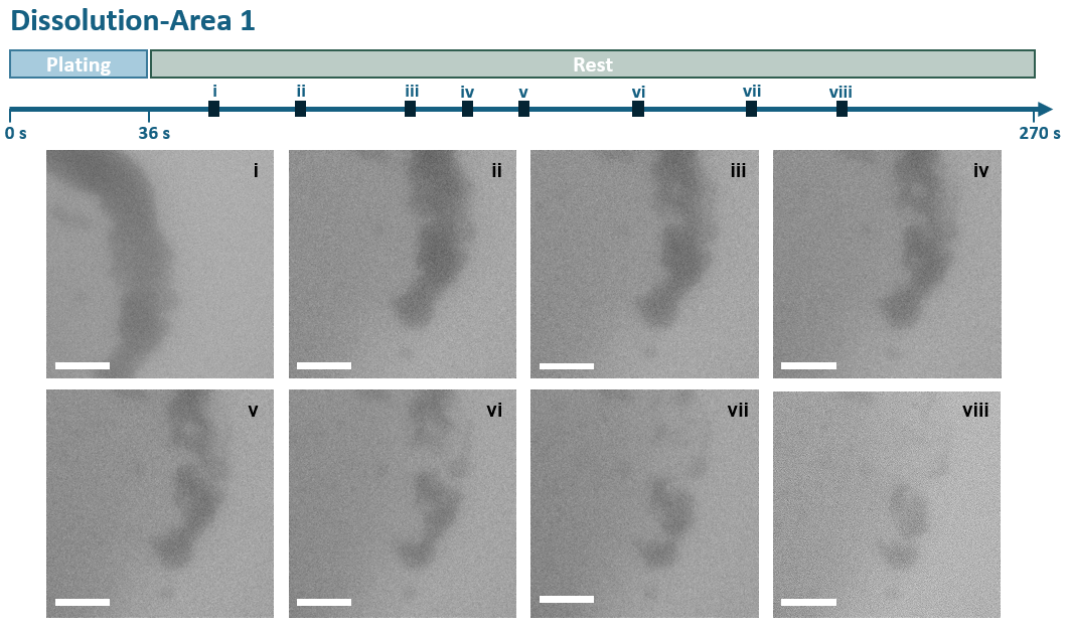


Figure 4.16 In situ liquid cell TEM imaging of the dissolution of Zn deposits (Area 1). Scale bars are 1 µm.

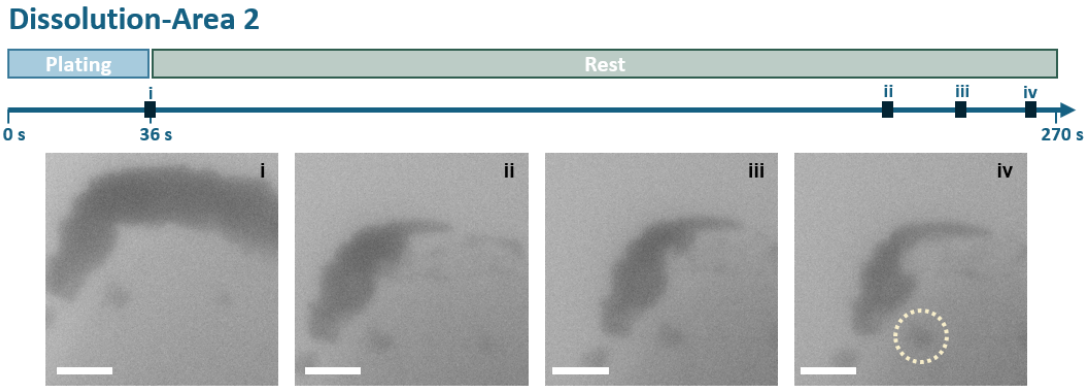


Figure 4.17 In situ liquid cell TEM imaging of the dissolution of Zn deposits (Area 2). Scale bars are 1 µm. A thin Zn flake deposited on top of the Pt electrode is enclosed within the dotted circle.

The viewing field was then moved back to the initial side of the Pt electrode. As is shown in *Figure 4.17*, compared with the end of plating, the majority of Zn deposits had been dissolved. Besides, the shape of the residues remained the same, indicating no obvious new byproducts had formed on the electrode. The starting point of the dissolution appears to be random when comparing images recorded from the two dissolution areas on the Pt electrode. However, the self-dissolution of Zn is believed to be a self-accelerating process, which tends to continue at

where the reaction initially starts. It is worth noting that a thin Zn flake deposited near the centre of the Pt electrode could still be seen after an extended rest period, as denoted by the dashed circle in *Figure 4.17 iv*. This flake is not the byproduct formed during rest as it was also observed at the end of plating (*Figure 4.15 a*). One possible explanation for this is that the electrolyte was very limited near the upper surface of the Pt electrode. As can be seen in the image of the Pt electrode with a clean surface before plating in *Figure 4.15 a*, the contrast is darker in the centre, indicating a higher thickness of the Pt electrode deposited on the window of the chip. Given that the space in within the chamber at the tip of the liquid cell holder that allows the electrolyte to flow is very limited, the amount of electrolyte should be reduced where the Pt electrode is thicker, thus restricting the interaction between Zn deposits and the electrolyte.

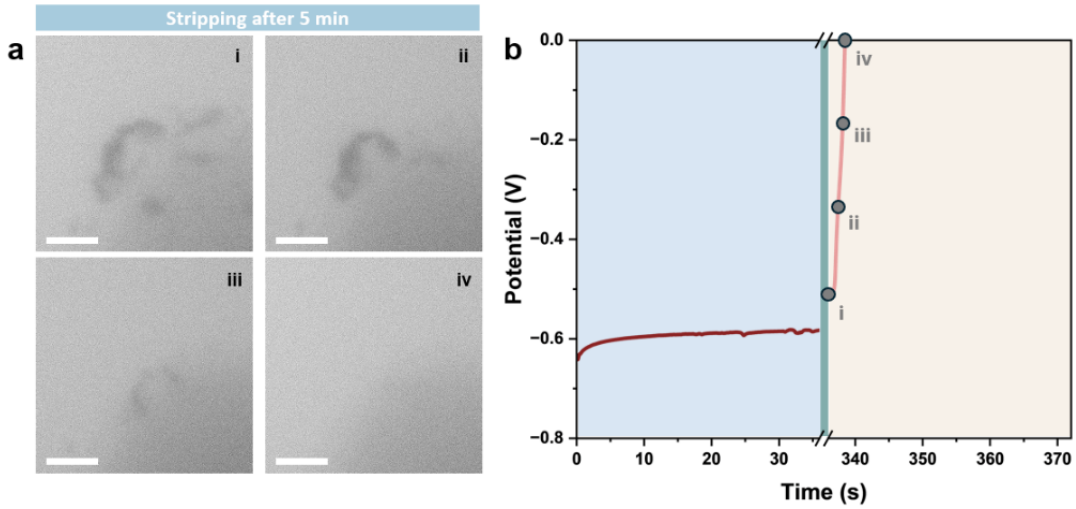


Figure 4.18 (a) In situ liquid cell TEM imaging of stripping after 5 minutes at a current density of 5 mA/cm^2 and (b) the corresponding voltage profile. Scale bars are 1 µm. The blue and beige regions represent the plating and stripping process respectively.

The stripping process was conducted after resting for a total time of 5 minutes, and sequential TEM images, as well as the voltage profile, are shown in *Figure 4.18*. It was found that nearly all Zn deposits were dissolved and the coulombic efficiency, calculated based on the stripping time, was less than 10%. The Pt electrode surface after stripping remained clean, and the thin Zn flake

was also removed at the beginning of stripping, further demonstrating the non-existence of byproducts.

4.3.6 Mitigation of Zn dissolution behaviour by initial pH adjustment of the electrolyte

As presented above, upon contact between the Zn metal anode and electrolyte, self-dissolution of Zn automatically initiates. However, the formation of ZHS does not always occur simultaneously with such self-corrosion process.

The generation of ZHS is widely believed to be closely associated with the pH of the local electrolyte environment [165]. Zn metal generally suffers more severe corrosion in more acidic environments due to its intrinsic instability [145]. Nevertheless, while an increase in the pH of electrolytes is thought to suppress the hydrogen evolution, it may also pose a threat to aggravated precipitation of ZHS byproducts [174,187]. Therefore, extensive studies have been focused on modifying the electrolyte by using pH buffer additives to maintain the interfacial pH near the Zn electrode within an appropriate range, in order to alleviate generation of OH^- ions without exacerbating corrosion [360–362].

Thus, the relatively low initial pH of the electrolyte is possibly one of the main factors contributing to the Zn dissolution issue discussed above. It has been reported that the pH values of $ZnSO_4$ electrolytes were mildly adjusted by adding small amounts of weak-basic and weak-acidic salts, which resulted in varying levels of corrosion on the Zn foils after soaking [240,360]. Consequently, 0.025 M $Zn(OAc)_2$ was introduced into the 1 M $ZnSO_4$ electrolyte as a regulator of the pH value. To uncover the underlying mechanism of Zn dissolution and ZHS formation during the self-corrosion process of Zn, operando observations of the plating/stripping behaviour and the dissolution process of Zn deposits were performed in the electrolyte with

$Zn(OAc)_2$ to compare with that in pure $ZnSO_4$, which has a relatively lower pH value.

Zn was deposited at a low current density of 5 mA/cm^2, but with a capacity that was doubled to 0.1 mAh/cm^2 compared to the results in *Figure 4.15*. The deposits were stripped after resting for 5 minutes, and the dissolution process was recorded during rest. Sequential in situ liquid cell TEM images acquired during the plating process and the stripping process after the rest period are shown in *Figure 4.19 a*. The morphology of Zn deposits with $Zn(OAc)_2$ was found to be slightly less compact compared to those in the pure $ZnSO_4$ electrolytes, with more nucleation sites evident on the Pt electrode surface. The coulombic efficiency is calculated to be as high as 77.7%, based on the voltage profile given in *Figure 4.19 b*. Similarly, the Pt electrode surface remained clean, with no residues left.

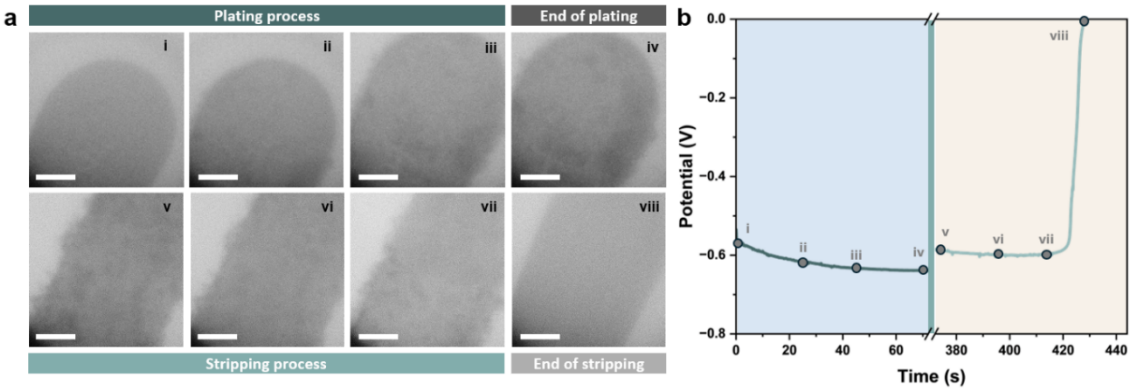


Figure 4.19 (a) In situ liquid cell TEM imaging of plating and stripping after 5 minutes at a current density of 5 mA/cm^2 in the electrolyte with $Zn(OAc)_2$ and (b) the corresponding voltage profile. Scale bars are 1.5 µm. The blue, beige and green regions represent the plating, stripping and rest process respectively.

The dissolution of Zn deposits was recorded at areas around both the tip and the bottom of the Pt electrode. As shown in *Figure 4.20*, the shape of Zn deposits remained unchanged after 180 seconds of rest. This indicates that neither the Zn dissolution nor the formation of byproducts occurred during the rest period.

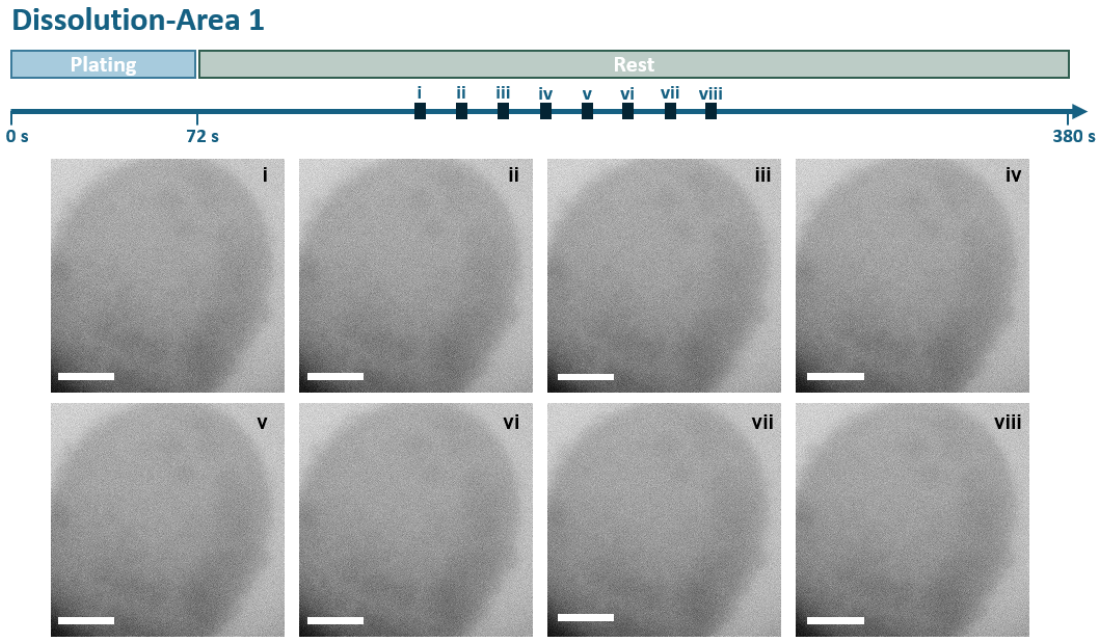


Figure 4.20 In situ liquid cell TEM imaging of Zn deposits in the electrolyte with $Zn(OAc)_2$ (Area 1). Scale bars are 1.5 µm.

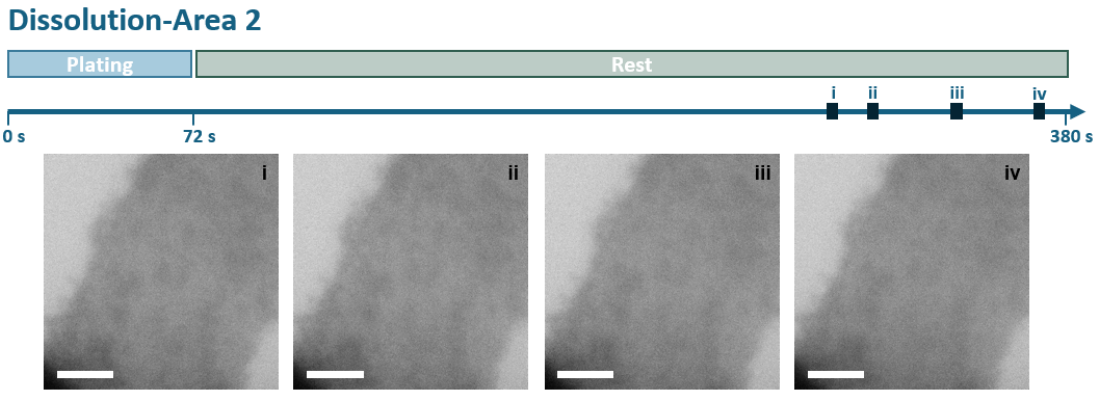


Figure 4.21 In situ liquid cell TEM imaging of Zn deposits in the electrolyte with $Zn(OAc)_2$ (Area 2). Scale bars are 1.5 µm.

The viewing field was then shifted to the bottom of the Pt electrode, where Zn deposits with a looser structure were found. As previously demonstrated in *Figure 4.16* and *Figure 4.17*, the dissolution of Zn tends to be more visible at the edge of the electrode and in areas where a smaller amount of Zn was deposited, due to both a more sufficient supply of electrolytes and a

more distinct change in the contrast of the images. It was observed that the small Zn deposits at the edge of the electrode were preserved well even after resting for 5 minutes (*Figure 4.21*).

The observations from the series of in situ liquid cell TEM experiments revealed the self-dissolution of Zn as an initial part of the self-corrosion process. The self-dissolution of Zn is closely related to the pH value of electrolytes. Furthermore, it is hypothesised that the formation of ZHS is a consequence of the accumulation of such self-dissolution behaviour.

4.3.7 In situ monitoring of pH change near the Zn metal anode surface during rest

To further explore the relationship between the pH of electrolytes and the self-corrosion property of Zn metal, the in situ pH change near the Zn surface was monitored using a home-made setup (*Figure 4.22*). The Zn foil was placed at the bottom of a vial with 2 ml electrolyte added, and the pH probe was inserted, and the pH probe was fixed to ensure the close contact of the tip with the Zn foil surface.

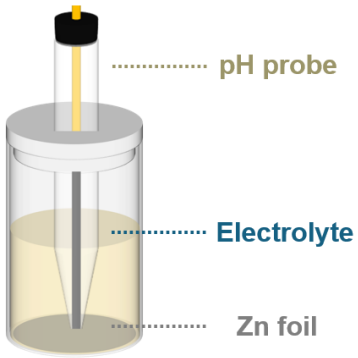


Figure 4.22 Illustration of the home-made setup for in situ pH monitoring.

The results of in situ pH monitoring in the 1 M $ZnSO_4$ electrolyte and the 1 M $ZnSO_4$ electrolyte with $Zn(OAc)_2$ were compared in *Figure 4.23*. The initial pH values of two electrolytes were

determined to be 4.46 and 5.43 respectively. After immersion of the Zn foil into the 1 M $ZnSO_4$ electrolyte, a quick increase in pH was observed from 4.46 to 4.73 within two minutes. The pH value continued to grow with the resting time prolonging to 20 hours. In contrast, with $Zn(OAc)_2$ added to the electrolyte, the pH value first increased slightly to 5.5 after 10 minutes and then remained steady within the whole rest period. It is worth noting that after resting for 20 hours, the pH value of near the Zn surface in the 1 M $ZnSO_4$ electrolyte was even higher than that in the 1 M $ZnSO_4$ electrolyte with $Zn(OAc)_2$.

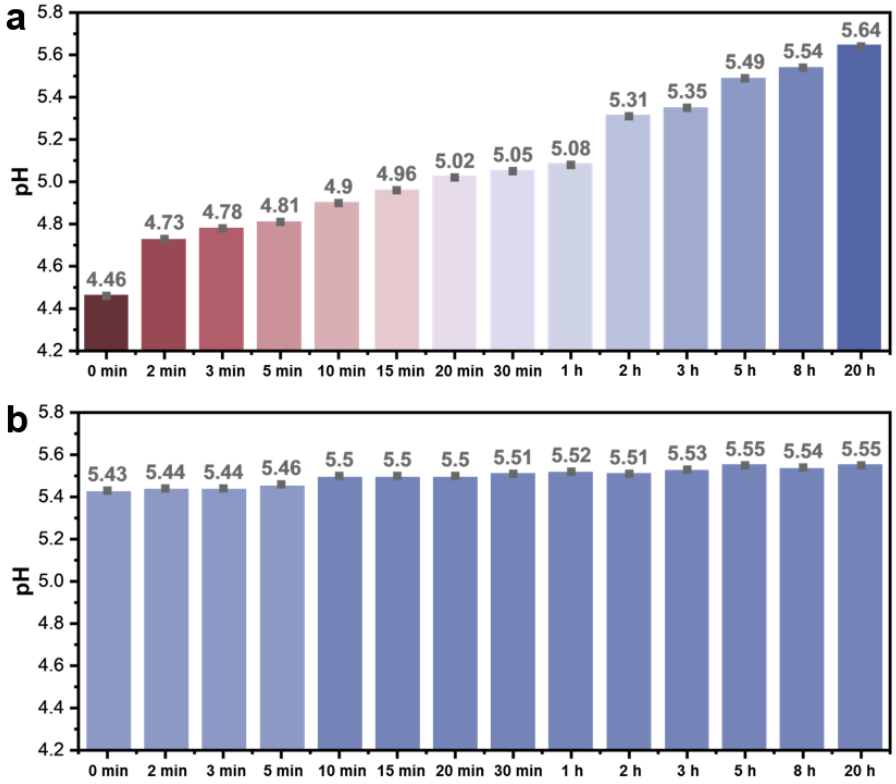


Figure 4.23 In situ pH record (a) in the 1 M $ZnSO_4$ electrolyte and (b) 1 M $ZnSO_4$ electrolyte with $Zn(OAc)_2$.

According to previous research, the pH threshold for ZHS precipitation is around 5.47 [363]. However, as indicated by the pH record in *Figure 4.23 b*, the duration of pH levels above 5.47 in the 1 M $ZnSO_4$ electrolyte with $Zn(OAc)_2$ was significantly longer than in the electrolyte without $Zn(OAc)_2$. The comparison of ZHS formation under various conditions and the impact of these pH changes will be discussed in detail in the next section.

Additionally, the pH of the 1 M $ZnSO_4$ electrolyte exhibited a continuous rising tendency, whereas with $Zn(OAc)_2$ added, slight fluctuations of increasing and decreasing pH were observed after resting for 1 hour till the end of recording. This could be due to the role of acetate ions as a buffering agent, which helps to stabilize pH changes by neutralizing extra OH^- ions generated during the self-corrosion process of Zn [360].

4.3.8 Influence of the pH adjustment on the corrosion process

The self-corrosion property of Zn was further investigated by ex situ SEM and XRD analysis of Zn foils after resting under different conditions. Zn foils were sealed in pouch cells (PC) containing 140 µl of 1 M $ZnSO_4$ electrolyte without and with $Zn(OAc)_2$ added, respectively. The pouch cells were then left to rest for 18 hours. Also, Zn foils were immersed in these two electrolytes in vials for an extended rest period of 40 hours. SEM images of Zn foils after rest and corresponding XRD patterns are displayed in *Figure 4.24*.

The formation of ZHS byproducts was observed on all the Zn foils after resting under different conditions. However, as demonstrated in SEM images in *Figure 4.24 a-d*, the diameter of large ZHS flakes reached over 100 µm in the $ZnSO_4$ electrolyte, while in the presence of $Zn(OAc)_2$, it remained around 15 µm. Both the size and the thickness of the ZHS flakes were reduced with the addition of $Zn(OAc)_2$, indicating the constrained growth of byproducts. Also, the byproduct layer on the Zn foils generated in the $ZnSO_4$ electrolyte with $Zn(OAc)_2$ was found to be more compact. The XRD peaks of ZHS also exhibited lower intensity with the addition of $Zn(OAc)_2$, indicating a smaller quantity and the suppression of ZHS growth. The intensity of the strongest ZHS peak in the $ZnSO_4$ electrolyte was 7.5 times that in the presence of $Zn(OAc)_2$ after resting in the vial, and 3.5 times after resting in the PC.

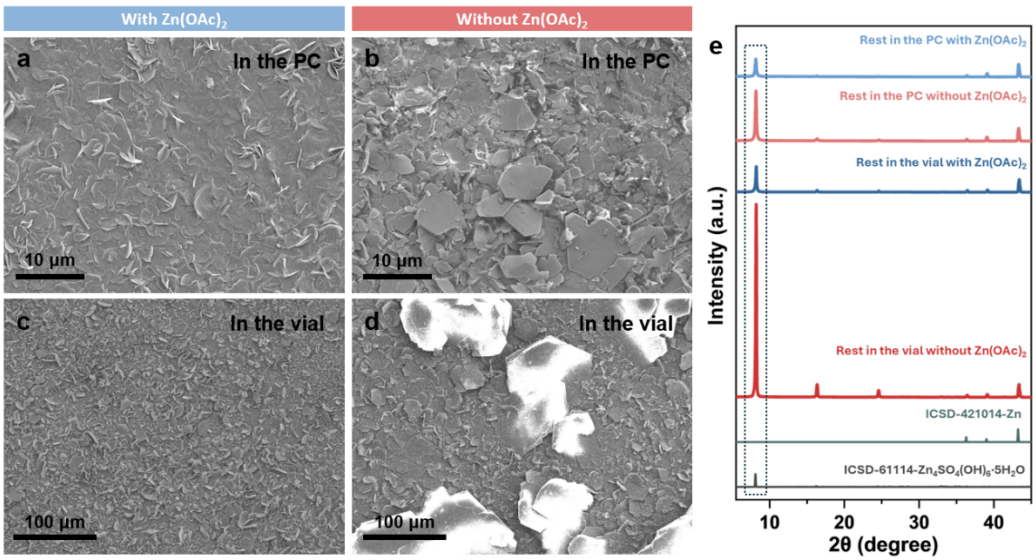


Figure 4.24 SEM images of Zn foils soaked in the electrolyte (a, b) with and (c, d) without $Zn(OAc)_2$ under different conditions, in the vial and in the PC, and (e) the corresponding XRD patterns. The main XRD peak of ZHS is highlighted with the dotted rectangle.

As mentioned above, the duration of pH levels above the threshold for ZHS precipitation in the 1 M $ZnSO_4$ electrolyte with $Zn(OAc)_2$ was longer than in the electrolyte without $Zn(OAc)_2$, over a recording period of 20 hours. However, the amount of ZHS products decreased, as evidenced by the SEM and XRD analysis of Zn foils after resting for 18 hours in pouch cells and for 40 hours in vials. It is believed that the formation of ZHS is more closely associated with the interfacial pH increase, which results from the self-dissolution behaviour of Zn. The dissolution of Zn into the electrolyte creates a higher concentration of OH^- ions near the electrode surface, which may be difficult to detect using a traditional pH probe. Moreover, considering the continuous rise in pH of the $ZnSO_4$ electrolyte and the higher pH value recorded at the end of 20 hours, it can be inferred that the self-corrosion of Zn would be further aggregated if the rest period were extended.

What needs to be emphasised is that the formation of ZHS byproducts occurs only when sufficient Zn is dissolved to the electrolyte during the self-corrosion process. By comparing the XRD patterns in *Figure 4.4 f* and *Figure 4.24 e*, it is evident that the peak intensity ratio of ZHS to Zn was significantly higher when soaking the entire Zn foil compared to soaking the Ti foil with a small amount of Zn deposits in the electrolyte for the same rest duration. This indicates that the excess of Zn facilitates the byproduct growth. This phenomenon can also be supported by the ex situ liquid cell experiments in *Figure 4.5*. Only Zn dissolution, instead of byproducts, was observed during the self-corrosion process in both in situ and ex situ liquid cell experiments. This is because only a very tiny amount of Zn was deposited on the Pt electrode in these liquid cell experiments, as the electrode area is small, and so the interfacial pH did not reach the precipitation threshold even after the complete dissolution of Zn deposits. Therefore, no byproducts were observed even after extended periods of rest (40 hours) in the liquid cell setup.

It is also necessary to take the salt concentration of the $ZnSO_4$ electrolyte into account in the study of the self-corrosion process of the Zn metal anode. *Figure 4.25* shows the SEM images and XRD patterns of Zn foils after resting in vials in $ZnSO_4$ electrolytes of varying concentrations for 18 hours. The Zn foil immersed in the 1 M electrolytes experienced a more severe corrosion issue, as evidenced by a greater presence of ZHS flakes and stronger XRD peaks for ZHS. The 1 M and 2 M $ZnSO_4$ electrolytes share close pH values, which are around 4.46 and 4.21 respectively, according to my measurement. Although the pH of the 2 M $ZnSO_4$ electrolyte is even slightly lower, much fewer ZHS byproducts were observed. It is generally believed that higher concentrations of electrolytes will reduce the interactions between the active metal anode and the active agents, such as the solvent [215]. Hence, the self-corrosion of Zn could also be alleviated by using electrolytes of high concentrations.

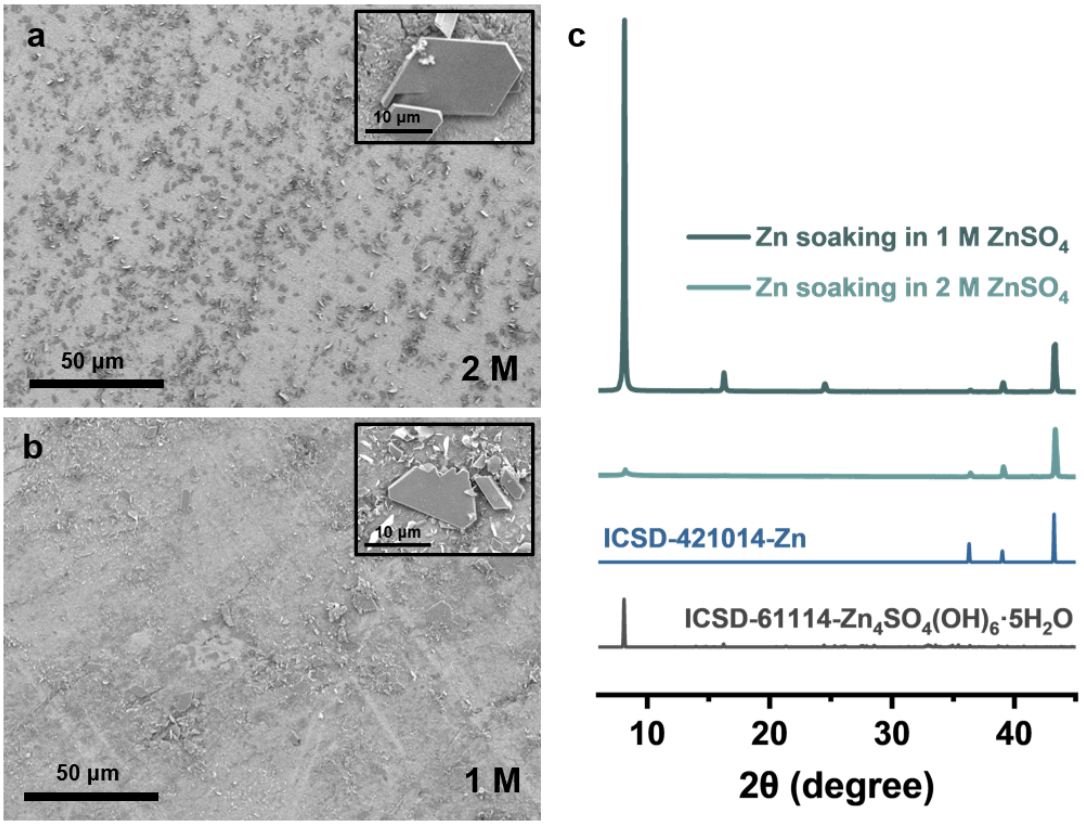


Figure 4.25 SEM images of Zn foils soaked in (a) the 2 M $ZnSO_4$ electrolyte and (b) the 1 M $ZnSO_4$ electrolyte, and (c) the corresponding XRD patterns. Insets are the enlarged SEM images showing ZHS flakes.

Interestingly, several recent studies have also proposed that the corrosion and hydrogen evolution during cycling can be mitigated by using ultra-low-concentration $ZnSO_4$ electrolytes [364]. This counterintuitive strategy is thought to work because the hydrated species and the sum of Zn^{2+}-solvated water are considered to be responsible for the hydrogen evolution, which can be effectively reduced by lowering the concentration of Zn salt in electrolytes. However, the underlying mechanisms for reduced corrosion during rest in these electrolytes of ultra-low concentrations are still unclear. From the perspective of pH, $ZnSO_4$ electrolytes of ultra-low concentrations have slightly higher pH values according to previous research [240]. This may have a positive influence on easing Zn self-dissolution, but other factors should also be considered. It should be noted that not only the OH^- concentration, but also the concentrations of other

species, including Zn^{2+} and SO_4^{2-} ions, play a crucial role in the precipitation of ZHS. Consequently, it is also reasonable to see the reduced formation of ZHS during battery rest in electrolytes of lower salt concentrations.

It has also been reported in a recent study that the ZHS formation during both battery rest and cycling can be eliminated by using a strong Brønsted acid additive to keep the pH of the electrolyte as low as 1.57 [365]. However, the in situ pH monitoring of the electrolyte with the acid additive revealed a continuous increase from 1.57 to around 3.5 after only 10 hours of rest, indicating that the self-dissolution of Zn and hydrogen evolution during battery rest should also be taken into account under such circumstances. As a matter of fact, the utilisation of additives that will influence the pH of electrolytes should be carefully examined in future research.

4.3.9 Comparison of electrochemical performances

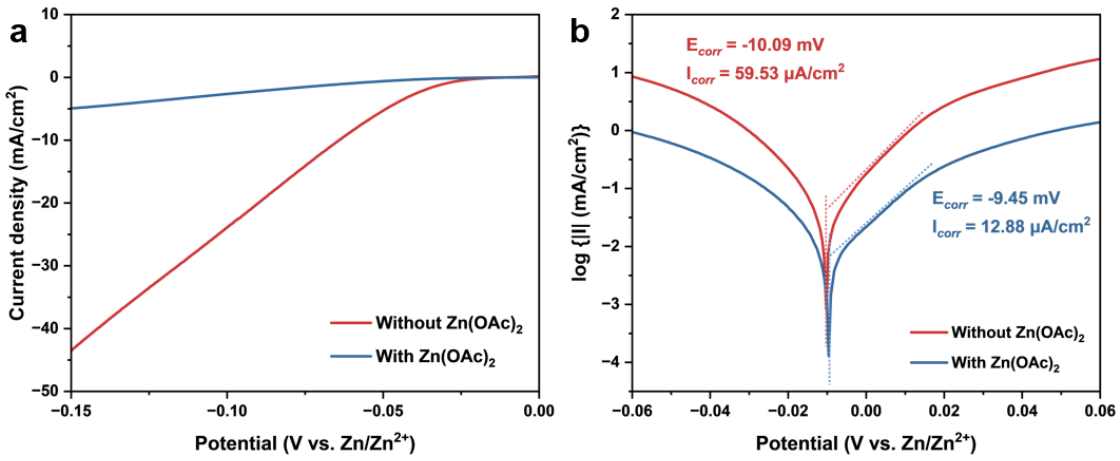


Figure 4.26 (a) The LSV curves tested at a scan rate of 10 mV/s and (b) Tafel plots of the electrolyte of $ZnSO_4$ with and without $Zn(OAc)_2$ addition.

To further investigate the corrosion process in the 1 M $ZnSO_4$ electrolyte without and with $Zn(OAc)_2$, LSV measurements were performed. As shown in *Figure 4.26 a*, the current response at -0.15 V in the electrolyte containing $Zn(OAc)_2$was lower, indicating a suppression of the

hydrogen evolution reaction. Tafel plots were also constructed to determine the corrosion rates in different electrolytes (*Figure 4.26 b*). The exchange current density of the electrolyte with $Zn(OAc)_2$ was found to be lower than that of the pure 1 M $ZnSO_4$ electrolyte.

Chronoamperometry tests were conducted with Zn||Zn coin cells using two electrolytes at a fixed potential of -150 mV (*Figure 4.27*). A slightly higher current density in the electrolyte with $Zn(OAc)_2$ was observed, suggesting a larger active surface area, which is consistent with the more nucleation sites observed in the liquid cell TEM images.

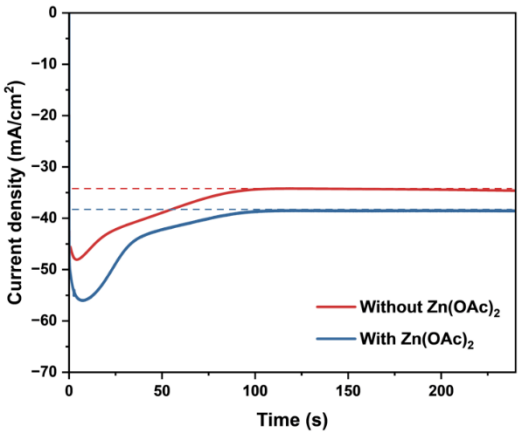


Figure 4.27 The chronoamperometry curves tested at a fixed potential of -150 mV in the electrolyte of $ZnSO_4$ with and without $Zn(OAc)_2$ addition.

As previously discussed, the addition of $Zn(OAc)_2$ can alleviate the self-corrosion of the Zn metal electrode, which is supposed to be beneficial for improving the shelf life of Zn-ion batteries. To gain a deeper insight into the influence of pH adjustment on the electrochemical properties of the Zn metal anode after long-term rest, symmetric Zn||Zn coin cells were prepared and left to rest for different durations before cycling. As is shown in *Figure 4.28*, after resting for 5 days, Zn||Zn coin cells using both electrolytes exhibited steady curves with similar voltage polarization, despite slight fluctuations using the pure 1 M $ZnSO_4$ electrolyte (denoted by red arrows). After an extended rest period of 35 days, the Zn||Zn coin cell using the 1 M $ZnSO_4$

electrolyte with $Zn(OAc)_2$ continued to exhibit stable cycling performance, while the cell without the addition of $Zn(OAc)_2$ displayed significant voltage fluctuations from the beginning of cycling, indicating poor performance after long-term rest.

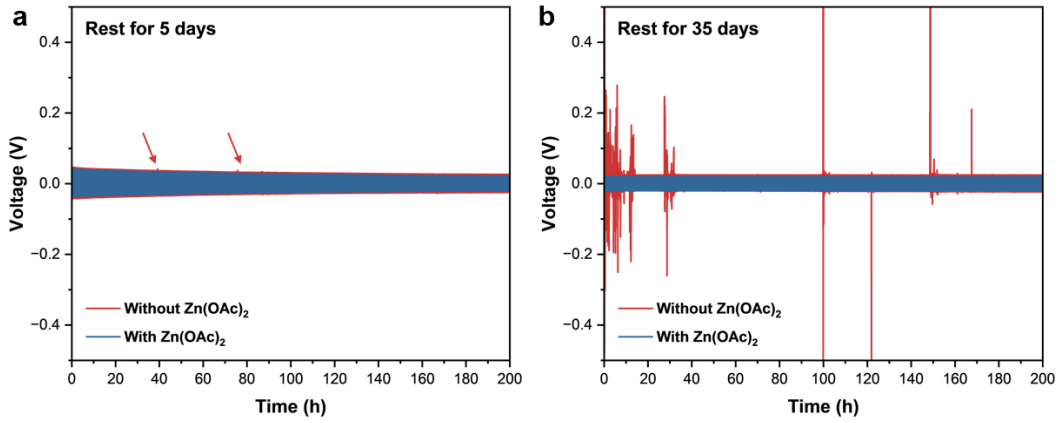


Figure 4.28 The voltage profiles of Zn||Zn symmetric cells after rest for (a) 5 days and (b) 35 days using the electrolyte of $ZnSO_4$with and without $Zn(OAc)_2$ addition.

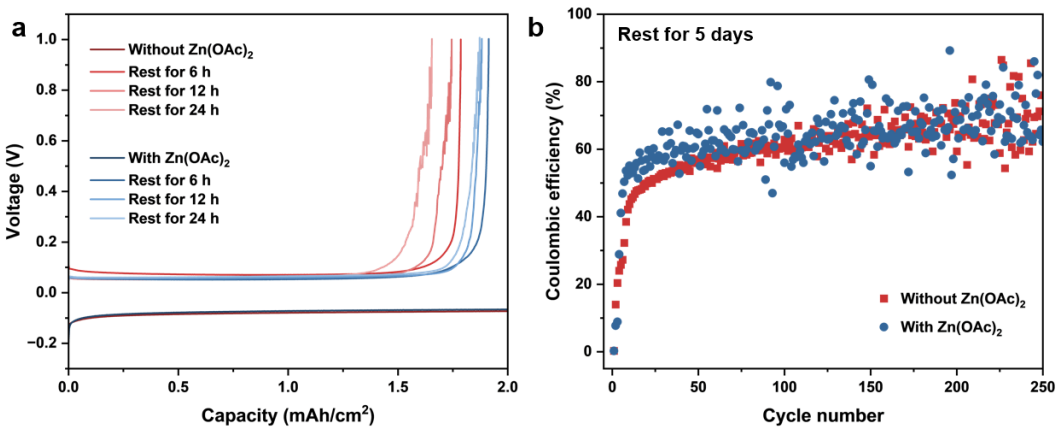


Figure4.29 (a) Voltage profiles of Zn||Ti coin cells after rest for different time before stripping and (b) the coulombic efficiency of Zn||Ti coin cells after rest for 7 days using the electrolyte of $ZnSO_4$ with and without $Zn(OAc)_2$ addition.

The self-dissolution of Zn in different electrolytes was further quantified in Zn||Ti coin cells. Zn was deposited on the Ti electrode at a current density of 10 mA/cm^2 with a capacity of 2 mAh/cm^2. The Zn deposits were then stripped after resting for 6, 12 and 24 hours, respectively.

According to the voltage profiles shown in *Figure 4.29 a*, the capacity loss in the cell with the addition of $Zn(OAc)_2$ was significantly reduced. The Zn||Ti coin cells were also cycled at a current density of 10 mA/cm^2 after resting for 7 days, and a higher coulombic efficiency was also achieved in the cell with $Zn(OAc)_2$ added (*Figure 4.29 b*).

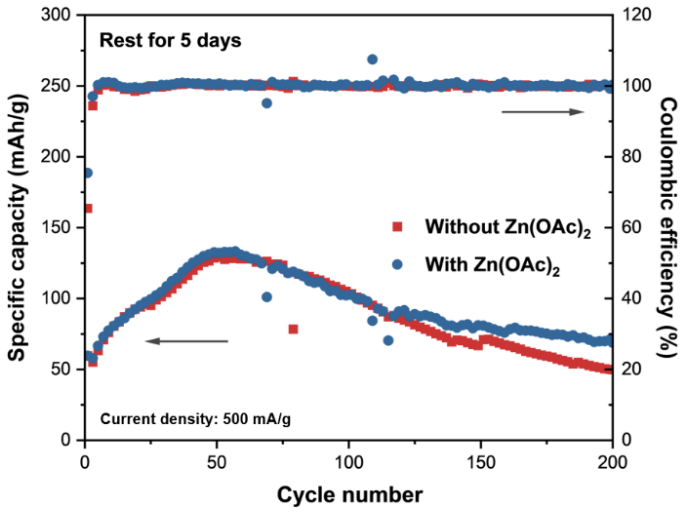


Figure 4.30 The long-term cycling performance for Zn||V_2O_5 coin cells using the electrolyte of $ZnSO_4$ with and without $Zn(OAc)_2$ addition.

The cycling performances of full cells with V_2O_5 as the cathode using the electrolyte with and without $Zn(OAc)_2$ after resting for 5 days were also compared. As is shown in *Figure 4.30*, the induction of with $Zn(OAc)_2$ to the electrolyte barely had impact on the capacity and coulombic efficiency of the V_2O_5||Zn cell during initial cycling. However, a slight increase in capacity was found after 100 cycles. It should be noted that the pH of electrolytes not only affects the Zn metal anode, but also plays a vital role in directing the performance of the cathode side, such as various Mn and V based materials [179,181]. This again underscores the importance of considering the potential influence of various electrolyte engineering strategies on the pH of electrolytes.

4.4 Conclusion

In this chapter, the self-corrosion process of Zn during the battery rest period was explored via in situ liquid cell TEM. The self-dissolution of Zn was observed, and this dissolution was believed to contribute to the majority of capacity loss during the initial phase of the corrosion process. The relationship between the self-dissolution and the formation of ZHS products was also investigated, which has highlighted the crucial role of the electrolyte pH in affecting corrosion during rest. The addition of $Zn(OAc)_2$ as a pH regulator in the 1 M $ZnSO_4$ electrolyte was found to mitigate the self-dissolution behaviour significantly. In situ pH monitoring near the Zn surface in different electrolytes confirmed the distinct pH changes attributable to Zn dissolution during self-corrosion. SEM and XRD analysis of Zn foils soaked in electrolyte with $Zn(OAc)_2$ demonstrated the additive alleviated the formation of ZHS byproducts. To corroborate the results with complementary techniques, the amount of ZHS on the surface can be further analysed using XPS and Raman spectroscopy; the thickness of ZHS particles can be measured with AFM; and the thickness of the byproduct layer can be compared through cross-sectional analysis using SEM.

Moreover, the cycling performance of Zn||Zn and Zn||Ti coin cells after extended rest was significantly improved with the electrolyte of a slightly higher pH value. These experimental results have elucidated the underlying mechanisms for the self-corrosion of Zn in the mild acidic environment, emphasising the importance of considering the electrolyte pH in future electrolyte modification research. As the formation of ZHS products and hydrogen evolution during the battery rest are believed to result from the accumulation of the Zn dissolution, the feasibility of using excess Zn metal in Zn-ion batteries should also be carefully evaluated.

A schematic of the proposed corrosion process of the Zn metal anode in Zn-ion batteries during rest is shown in *Figure 4.31*. In an acidic electrolyte environment, Zn metal undergoes the self-

dissolution process first, which consumes H^+ ions and leaves excess OH^- ions, leading to hydrogen evolution and a local pH increase. The accumulation of the OH^- ions fosters the formation of a ZHS corrosion byproduct layer and morphological changes to the anode surface, which will induce uneven distribution of the electric field and heterogeneous nucleation, further triggering the formation of dendrites during operation. These parasitic corrosion reactions persist throughout the entire storage period and are exacerbated by the use of excess Zn within the battery system.

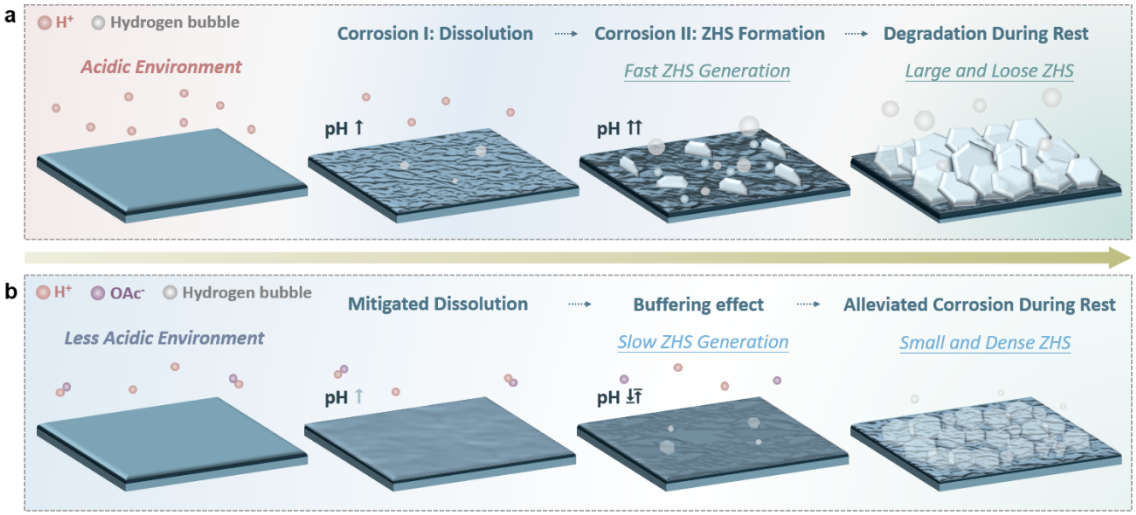


Figure 4.31 (a) Schematic illustrations of (a) the underlying mechanism of the Zn metal anode corrosion process during rest in mildly acidic electrolytes, and (b) the mechanism for mitigating corrosion through pH adjustment with addition of the buffer additive.

To mitigate corrosion during battery rest and extend the shelf life of Zn-ion batteries, it is essential to control the Zn dissolution process to enhance the stability of the Zn metal anode. One viable strategy to eliminate the Zn dissolution is to control the acidity of the electrolyte. As shown in *Figure 4.31 b*, by adding $Zn(OAc)_2$ to the $ZnSO_4$ electrolyte, the interfacial pH value is adjusted and stabilized, lowing the number of protons and thereby decreasing the activity of the Zn metal anode during the self-corrosion process. The $Zn(OAc)_2$ functions as a pH buffer, helping to balance fluctuations in the chemical microenvironment, and suppressing the accumulation of

OH^- ions and the development of corrosion byproducts. Consequently, a more stable pH value can be maintained, leading to improved overall battery performance, especially after extended periods of rest.

Some previous studies have also reported the elimination of ZHS corrosion byproducts by addition of strong acidic additives [[365]], but this can result in more severe Zn self-dissolution under such circumstances, and may also trigger issues to the cathode materials. Furthermore, most of the Zn-ion batteries have been evaluated with excess electrolytes and Zn metal to ensure a sufficient supply of active species, thereby prolonging the cycling life of the entire battery. Previous studies have reported that a large electrolyte dosage can help mitigate changes in the microenvironment, whereas with limited electrolytes, the local pH value is likely to become perturbed due to side reactions such as HER and corrosion. However, it should be noted that excessive electrolyte does not prevent the dissolution of the Zn metal anode, which will consequently lead to the formation of corrosion byproducts after long-term storage. Moreover, although Zn depletion can be compensated by these additions, the excessive use of both electrolyte and Zn metal may exacerbate the corrosion issues, resulting in an increased formation of byproducts that pierce the separator, which will ultimately contribute to battery failure. A high utilization rate of Zn in Zn-ion batteries is crucial not only for achieving higher energy density but also for reducing corrosion.

Chapter 5 Diagnosing the electrostatic shielding mechanism for Zn dendrite suppression

5.1 Introduction

As mentioned before, the practical application of Zn metal anode in aqueous Zn-ion batteries is still impeded due to a number of significant degradation and failure issues, and the severe growth of Zn dendrites is one of them [188,192], which can puncture the cell separators and cause short circuit of the battery. These Zn dendrites can also easily become detached during cycling, resulting in the formation of electrically isolated 'dead Zn' and thus contributing to capacity loss [187], and the increased surface area of the exposed dendrites leads to faster corrosion and more parasitic reactions [145].

Dendrite growth is a common issue for metal electrodes, which is a direct consequence of the quality of the electroplating and stripping process [287]. Uniform and homogenous Zn deposition during cycling is critical for maintaining a high coulombic efficiency, yet uneven Zn deposition is practically inevitable due to the intrinsic inhomogeneity of the microenvironments (e.g., the ion concentration and the electric field distribution) across the anode surface [366]. At the start of electrodeposition, the adsorption and nucleation of Zn ions on the rough electrode surface will initially be uneven, and as the deposition progresses further Zn ions absorbed will tend to undergo 2D diffusion and move to these initial nuclei. Continuous Zn aggregation on to these initial 'hot sites' will culminate with Zn protrusions, which exacerbates the inhomogeneous distribution of the electric field due to the 'tip effect', where the protrusions act as focal points for concentrating the electric field. This 'tip effect' will further encourage uneven growth of Zn and the formation of dendrites, as there is preferential accumulation of Zn ions on the tips, leading to vertical growth of protrusions [192,207]. This process is described in *Figure 5.1*.

Subsequently, such self-amplified Zn dendrite growth perpendicular to the substrate with a large amount of sharp edges exposed will give rise to degradation and capacity fade of the whole battery [189].

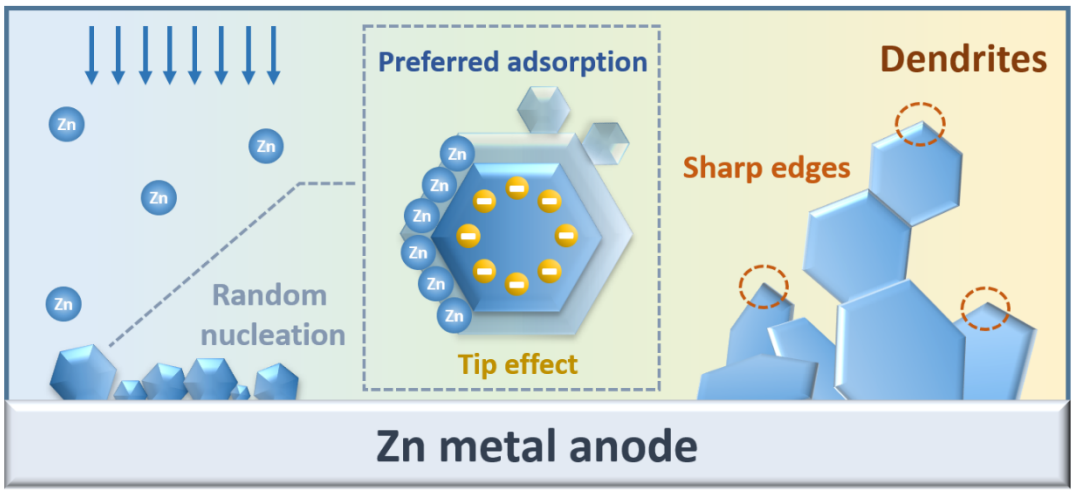


Figure 5.1 Schematic illustration of the Zn dendrite growth process. Zn ions preferentially adsorb to the tips and edges of existing Zn deposits due to the tip effect.

A number of strategies have been reported to suppress the growth of Zn dendrites induced by the 'tip effect' and mitigate its intrinsic self-accumulating property. Broadly summarised in *Figure 5.2*, there are two approaches to ease the growth of dendritic Zn structures. The first is to control the crystallographic orientation of the initial deposits and generate epitaxial growth of specific facets, usually favouring the low surface energy Zn (002) plane. This can be achieved by ensuring lattice matching and improving the affinity of the target Zn plane with a modified electrode substrate [190,367,368]. An alternative approach is to manipulate the nucleation behaviour, introducing more nucleation sites on the substrate or limiting further growth of already existing protrusions, thus leading to an even deposition layer of many smaller deposits. For example, substrates with modified structures [369] or functional composites [194,370] possess a more zincophilic interface, which can trigger more nucleation sites. High-performance

separators or coating layers on the surface of substrates can be applied to physically inhibit growth of Zn dendrites or regulate Zn^{2+} flux and electric field [371,372].

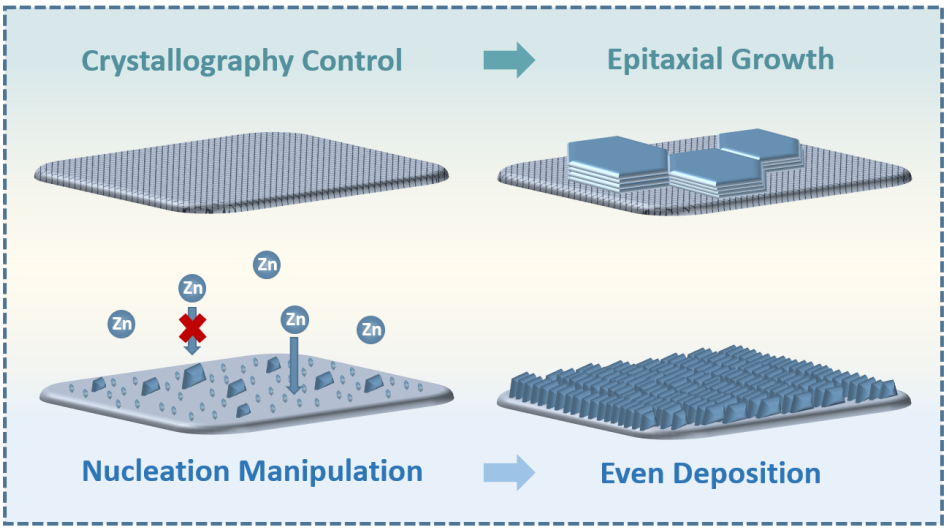


Figure 5.2 Schematic illustration of two approaches for limiting Zn dendrite formation; favouring (002) Zn deposition via substrate epitaxy, or encouraging the formation of many small nucleation sites.

Besides strategies relying on modifying the electrode and interlayers mentioned above, engineering the electrolyte also offers a potentially simpler and cheaper approach to overcome dendrite issues [213,357], and adding additives into electrolytes has been found to be one of most facile methods [216,235,290].

As discussed in Chapter 2.1.2.1, several additives have been reported to effectively alleviate the 'tip effect' and inhibit the self-accelerating growth at Zn protrusions, and are understood to work via an 'electrostatic shielding mechanism' [222,226,232]. This theory was first put forward and utilised in Li metal battery systems [221]. Specifically, cations with lower reduction potentials are introduced to the electrolyte as an additive, which will preferentially accumulate around the tips of already existing protrusions. Under this condition, a positively charged layer will form and prevent further deposition on the protrusions by the electrostatic force. Several cations have

been applied to ease the growth of Zn dendrites according to this logic, such as Li^+ [224], Na^+ [225], Ce^{3+} [223], as well as some organic additives [238,360]. Though these additives are believed to suppress dendrite growth by manipulating nucleation behaviour, as has been found from the well-studied field of additives in Li electrolytes, the role of the additive in battery chemistry can be complex, as it can also influence side reactions, the composition of the interfacial interphase layer, and the solvation structure of the active cation [222,226].

This complexity makes reliably diagnosing the role(s) additives play in achieving higher performances particularly challenging, yet this understanding is desirable so that researchers can design better electrolytes from an informed vantage. Operando and in situ characterisation processes are required for these insights. Currently, such studies into Zn electrolyte additives have often been restricted to the dynamic monitoring of Zn plating and stripping processes at the micro-scale, including X-ray computed tomography [210], optical microscopy [223,360], and TEM [323,324]. Among the in situ imaging techniques above, only in situ TEM can be utilised to analyse the initial nucleation behaviours of Zn deposition and dissolution, and reveal the details of microenvironments during cycling.

In this chapter, I aim to expose the underlying mechanism by which the electrostatic shielding effect is realized in the mildly acidic aqueous Zn system via a suitable additive, aided by in situ electrochemical liquid cell TEM to reveal the nucleation and growth process of Zn deposits. LiCl is chosen as a typical representative from a series of additives which have been reported to function according to the electrostatic shielding mechanism [224]. I first image Zn deposition and dissolution at the nanoscale from the standard aqueous 2 M $ZnSO_4$ electrolyte to reveal the nucleation dynamics that lead to dendritic growth, which showed preferential nucleation of Zn on the edges of initially deposited Zn flakes. Formation of Zn dendrites, obtained under a current density of 100 mA/cm^2, showed a ‘daisy-chain’ like structure of consecutive nucleated Zn grains.

Introducing LiCl additive into $ZnSO_4$ electrolyte was found to alleviate the growth of Zn dendrites by inhibiting the formation of the secondary Zn nuclei that cause this daisy-chaining phenomenon. Unlike how additives causing an electrostatic shielding effect work in Li batteries, which favour the creation of new nucleation sites on lower regions of the electrode surface, instead inclusion of LiCl triggered preferential secondary nucleation on Zn (002) planes of previously deposited Zn flakes, thus forming Zn blocks composed of stacked Zn flakes. This observation by liquid cell TEM reveals that the electrostatic shielding effect has a fundamentally different mechanistic influence on electroplating of the Zn metal anode compared with that of the Li metal anode.

5.2 Experimental

5.2.1 Chemicals and materials

All chemicals were used directly without any further treatment. 2 M $ZnSO_4$ electrolytes were purchased from Merck Life Science UK Limited. LiCl, V_2O_5, Zn foil, Ti foil and glass fibre were purchased from Sigma Aldrich. The hydrated LiCl ($LiCl{\cdot}xH_2O$) was used for the prepared electrolyte, with their concentration measured afterwards by ICP-OES (Perkin Elmer Optima 8000), to assess the LiCl concentration. Subsequent LiCl concentration studies were performed with electrolyte prepared with anhydrous LiCl, subjected to an additional drying stage to ensure no hydration. Celgard 3501 was purchased from Celgard, LLC. LIR 2032-coin cell components were purchased from MTI Corporation.

5.2.2 Setup for in situ TEM characterisation

The in situ liquid cell TEM holder (Poseidon 510) and chips (EPB-55DNF and ECT-15WR) used in this work are from Protochips Ltd. The liquid cell holder tip is composed of two silicon chips with

electron transparent SiN_x windows, one of which is patterned with platinum (Pt) electrodes. The electrolyte was injected into the holder tip by a syringe pump at a flow rate of 300 µl/h during system purging and at a flow rate of 120 µl/h during TEM imaging.

A Gamry reference 600 was used for galvanotactic measurements. The applied currents in the in situ TEM experiments were 50 nA, 100 nA and 150 nA respectively, and the current densities were calculated from the electrode areas of the electrodes patterned on the chips (around 150 μm^2). TEM imaging was carried out with a JEOL 3000F operated at 200 kV, which is equipped with a 2k × 2k charge coupled device (CCD) camera, with a 50 µm condenser aperture inserted and a spot size of 2 set up to minimise the beam damage. The beam current was calibrated by a Faraday cup before experiment, and 20 pA was measured under this condition, corresponding to a low dose rate of 0.04 electrons $Å^{-2}$ s^{-1}. The dose test results under these conditions are shown in Appendix *Figure A6*. The movies were recorded using screen recording software, and specific images of interest were extracted.

5.2.3 Electrochemical tests

All coin cells were assembled with a volume of 140 µl electrolyte added and pressed to 1000 psi. The self-supporting V_2O_5 cathode films were prepared by mixing commercial V_2O_5 powder with carbon black and polytetrafluoroethylene in the 7:2:1 mass ratio. Zn||Ti and Zn||Zn coin cells for SEM imaging after cycling were assembled with one layer of glass fibre and one layer of Celgard 3501 as the separator, while Zn||Ti, Zn||Zn and Zn||V_2O_5 coin cells for long-term cycling and other electrochemical tests were with two layers of glass fibre. The long-term cycling of coin cells was carried out using a Maccor Series 4000, and all other electrochemical measurements were conducted on a Biologic VMP3 system at a temperature of 30 °C.

5.2.4 Characterisations

Surface morphologies of Zn electrodes were imaged by a Carl Zeiss Zeiss Merlin field emission analytical SEM. XRD patterns of Zn electrodes were obtained using a Cu source Rigaku MiniFlex diffractometer (wavelength λ = 1.5418 Å) with a Hypix 2D detector. 3D morphologies of electrodes after cycling were obtained by the Bruker Dimension Icon AFM and reconstructed by NanoScope Analysis 2.0 software, by mapping a 40 μm × 40 μm scan area for each sample. Raman spectra of electrolytes were measured with a Renishaw inVia Qontor spectrometer using a laser of 532 nm.

5.2.5 Density functional theory (DFT) calculation

The DFT calculations in this chapter are credited to my colleague, Dr Miguel A. Pérez-Osorio.

All calculations were carried out using the Quantum Espresso package. As exchange-correlation functional, we employed the generalised gradient approximation (GGA) via the Perdew, Burke and Ernzerhof (PBE) functional [373]. The interaction between core and valence electrons was described via using optimised norm-conserving Vanderbilt pseudopotentials (ONCVSP) [374]. The wavefunctions and charge density were represented via plane-wave basis sets with energy cut-offs of 120 and 480 Ry, respectively. The energy threshold was set to 1×10^{-7} eV. 12 × 12 × 1 and 1 × 12 × 12 Monkhorst–Pack k-point grids were employed for the Zn (002) and (100) surfaces, respectively. All the structural models were optimised until forces on the atoms were less than 0.02 eV/Angstrom. 4 × 4 and 5 × 3 surface slabs were constructed to model the Zn (100) and (002) surfaces, respectively. In all the cases, a vacuum region of 20 Å vacuum was applied. The surface energy of the pristine Zn (100) and (002) planes was investigated as a function of the number of Zn layers in the slab, considering 12, 18 and 24 layers of Zn. The surface energy γ was computed as:

$$\gamma = \frac{1}{2A}(E_{slab} - nE_{bulk}) \qquad \text{(Equation 5.1)}$$

where E_{slab} is the total energy of the surface slab, E_{bulk} is the energy per atom of bulk Zn, n is the number of Zn atoms contained in the slab, and A is the surface area of the slab. The factor two is because the slabs here used are symmetric. E_{bulk} was computed using the conventional unit cell of Zn (which contains two Zn atoms per cell), employing a 20 × 20 × 20 Monkhorst–Pack k-point grid.

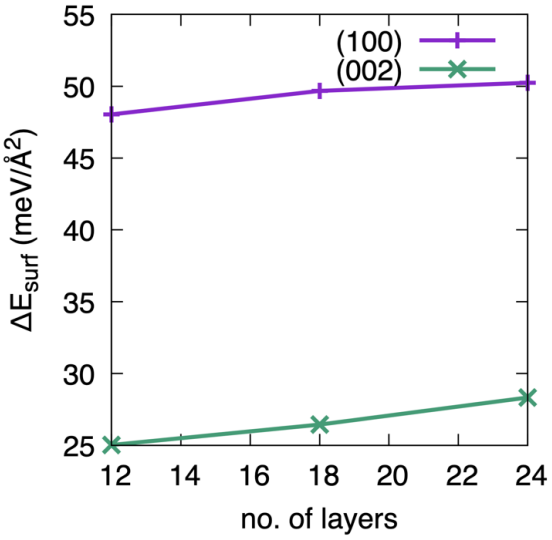


Figure 5.3 DFT surface energies of Zn (100) and Zn (002) planes as a function of the number of Zn layers in the surface slab.

The surface energy was converged with slabs containing 12 layers of Zn, see *Figure 5.3*. We used this slab size to simulate the adsorption of single Li and Zn atoms on the Zn (100) and (002) planes. The adsorption binding energy E_{ads} was calculated as

$$E_{ads} = E_{slab+atom} - E_{slab} - E_{atom} \qquad \text{(Equation 5.2)}$$

where $E_{slab+atom}$ is the total energy of the surface slab with the adsorbed i atom (i = Zn, Li), E_{slab} is the total energy of the pristine surface slab, and E_{atom} is the total energy of an isolated i atom.

To compute E_{atom}, a cubic supercell of 30 Å per side was used, with the *i* atom located in the centre of the supercell.

5.3 Results and discussion

5.3.1 Electrodeposition behaviour in the $ZnSO_4$ electrolyte

To explore the underlying electrodeposition behaviours under various cycling conditions and to screen for appropriate observing parameters, I first conducted in situ TEM characterisation of Zn plating and stripping with different current densities and capacities with standard 2 M $ZnSO_4$ aqueous electrolyte. The working electrode used in the in situ liquid cell TEM experiments was made of Pt. Electrodeposited morphologies onto the Zn substrate and Pt substrate were compared in previous ex situ studies, where similar flaky shape with dendrite structures were found under both conditions [368]. The liquid cell contents were continually replenished to maintain the electrolyte concentration during cycling, and to remove any beam-induced by-products. The in situ liquid cell TEM observation of Zn electrodeposition from $ZnSO_4$ solution has been reported in previous studies [323,324,326], however they have used small currents or low concentrations of electrolyte. For example, hexagonal facets were observed during Zn deposition from low concentration 0.1 M $ZnSO_4$ at 4 and 5 µA plating currents, equivalent to areal rates of 160 mA/cm^2 and 200 mA/cm^2 [323]. Needle-like precipitates were found following the formation of Zn hexagonal platelets. Considering the high plating current density and low electrolyte concentration, it was argued that the mossy Zn was generated due to a concentration gradient forming as Zn ions became depleted at the surface region of the electrode. A low concentration 0.3 M $ZnSO_4$ electrolyte was also studied [324], where the growing process of mossy Zn dendritic structures was again observed due to diffusion limited growth. In order to gain a better understanding of Zn plating/stripping behaviours under the cycling conditions of a

typical coin cell, I studied a range of current densities with the standard 2 M $ZnSO_4$ aqueous electrolyte.

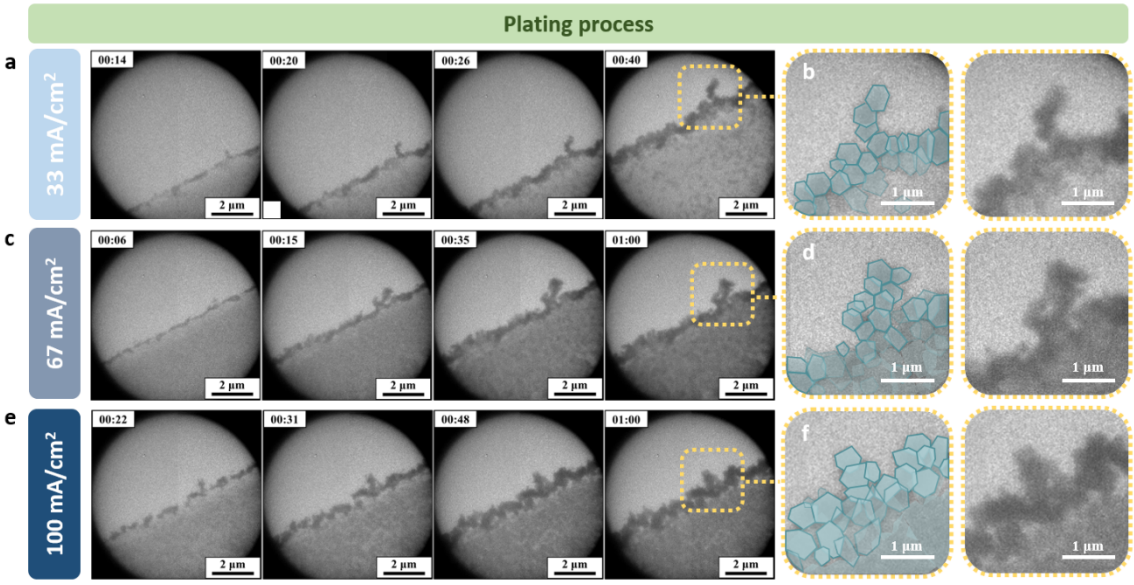


Figure 5.4 In situ liquid cell TEM imaging of Zn nucleation and growth at different current densities from $ZnSO_4$ aqueous electrolyte. (a, c, e) TEM image time series of Zn electroplating and dendrite growth at 33, 66, and 100 mA/cm². (b, d, f) Magnified views with and without annotations of the indicated areas in a, c, and e.

Sequential liquid cell TEM images of Zn plating (*Figure 5.4*) and stripping (*Figure 5.5*) processes at 33 mA/cm², 67 mA/cm² and 100 mA/cm² were acquired with the standard 2 M $ZnSO_4$ aqueous electrolyte. For the Zn cycling process at 33 mA/cm² (*Figure 5.4 a*), small sub-micron (< 100 nm) Zn particles with darker contrast started to nucleate along the edge of the Pt electrode within the first 6 seconds. As the plating proceeded, the Zn nuclei grew into small Zn flakes, while more nucleation sites were generated over the surface of the electrode. It was found that some of the newly deposited Zn flakes grew from the edges of the previously deposited ones, shown in the yellow dashed frame of *Figure 5.4 a*, which is magnified and annotated in *Figure 5.4 b*.

Doubling the current density to 67 mA/cm^2 led to the formation of larger Zn flakes with darker contrast, suggesting more Zn was deposited (*Figure 5.4 c*). More nucleation events were observed, including thin Zn flakes forming on the top working electrode surface in addition to along the electrode edge, which gradually covered the surface of the electrode. The tendency for edge-depositing on existing Zn deposits was also observed, leading to extended protrusions and dendrites, such as in *Figure 5.4 d*.

The current density was further increased to 100 mA/cm^2, with the corresponding image series shown in *Figure 5.4 e*. Both the size and the thickness of the deposited Zn flakes protruding along the edge of the electrode continually increased, as well as a concomitant increase in the number of Zn islands lying on the electrode surface. A similar tendency was seen for further Zn deposition along the existing Zn deposit edges, as in the previous results. There was also a clear dendrite-like structure of the deposited Zn, similar to what has been widely reported in previous ex situ coin cell tests [188,189].

Previous observations of Zn dendrites with liquid cell TEM have showed needle-like or mossy morphologies with irregular branches [323,326], and irregular dissolution of the deposited Zn [323], which started from the root of Zn dendrites instead of the tip. Considering diluted electrolytes or non-replenishing static conditions were used, these phenomena could be due to the fast consumption of Zn cations in the electrolytes around the surface of the electrode, thus leading to a large concentration gradient in the thin electrolyte layer of the confined liquid cell. Flowing the electrolyte and providing continued replenishment can be important for maintaining a more realistic ionic concentration gradient. Using a representative electrolyte concentration (2 M $ZnSO_4$) that was continually replenished by microfluidic tubing should minimise the resulting concentration gradient around the electrode during cycling, and thus the Zn deposits in my observations did not exhibit mossy or needle-like morphology. As shown in *Figure 5.5*, the

dissolution process started from the tips of the deposited Zn, which also suggests a lower concentration gradient is present in the liquid cell.

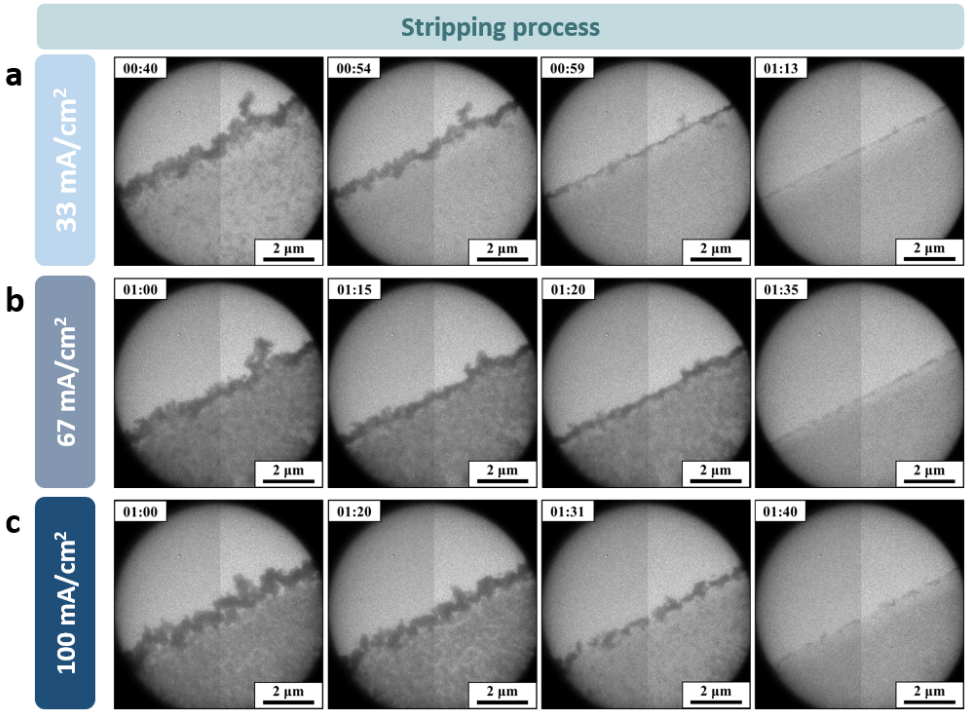


Figure 5.5 In situ liquid cell TEM imaging of Zn stripping from $ZnSO_4$ electrolyte at (a) 33 mA/cm², (b) 66 mA/cm² and (c) 100 mA/cm².

To better understand the formation process and micro-structure of the formed Zn dendrites, the viewing field was moved to other parts of the working electrode after the 100 mA/cm² plating process ended. Further examples of Zn dendrites showing secondary nucleation along the edges of the primary Zn flakes were found (*Figure 5.6 a*), exhibiting evidence of hexagonal Zn facets with a mutual orientation angle of 120° between them (*Figure 5.6 b*), corresponding to the exposed (002) planes of the hexagonal closed-packed (hcp) Zn. This secondary nucleation behaviour, where further Zn nucleation events occur on existing Zn deposits rather than existing Zn flakes growing further, tended to happen at the sharp edges of the previously deposited Zn flakes. This is usually ascribed to the inhomogeneous distribution of the electric field due to the 'tip effect' [375]. This tendency for Zn to preferentially deposit at the flake edges, rather than the

flat surface, is illustrated with annotations in *Figure 5.6 c*. Additionally, it has been shown via DFT modelling that the adsorption energy of Zn cations on the Zn (100) surface is lower than that of the Zn (200) surface [223,289], which would also favour the adsorption of Zn cations and new nucleation sites on flake edges, as the flake edges exhibit the (100) face. This secondary nucleation phenomenon ultimately promotes the growth of protruding Zn dendrites, constituting a 'daisy chain' of edge-linked Zn flakes (*Figure 5.6 d and e*).

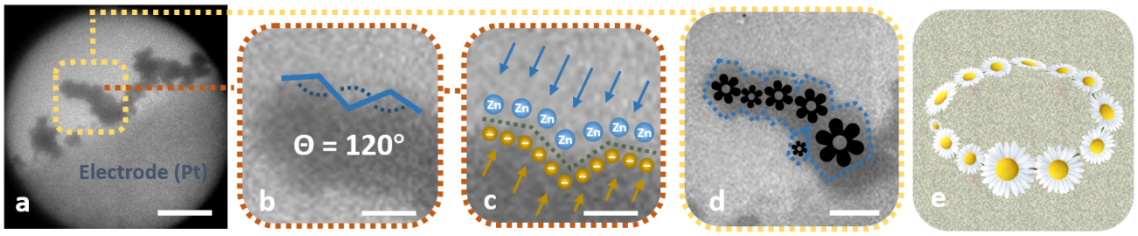


Figure 5.6 (a) TEM image of Zn dendrites at 100 mA/cm^2 in another electrode region. Scale bar is 2 µm. (b) Magnified view of the indicated area in (a), with the inter-island mergence angle indicated. Scale bar is 250 nm. (c) Schematic of the tendency of Zn to accumulate along edges due to 'tip effect' and preferred adsorption on the Zn (100) plane. Scale bar is 250 nm. (d) Magnified and annotated view of the 'daisy-chain' edge-joint Zn dendrite structure in (a). Scale bar is 500 nm. (e) Cartoon diagram of the daisy-chain.

5.3.2 Electrodeposition behaviour in the $ZnSO_4$ electrolyte with LiCl

To investigate the role of LiCl additive in inhibiting the growth of Zn dendrites, 1.1 M LiCl was added into the 2 M $ZnSO_4$. A current density of 100 mA/cm^2 was used for comparison with my 2 M $ZnSO_4$ electrolyte cycling experiments. The sequential liquid cell TEM images of Zn plating and stripping processes are shown in *Figure 5.7 a*. Small hexagonal Zn deposits were found to form during the initial stage of plating within 4 s. These Zn hexagons expanded and thickened with plating time. Unlike the thin Zn flakes and 'daisy-chain' structured Zn dendrites observed in the pure $ZnSO_4$ electrolyte, Zn nuclei in the electrolyte with LiCl additive developed into block-

shaped structures, and these thicker blocks were found to be well-merged. Fewer nucleation events were observed over the course of the plating process compared with that seen from the pure $ZnSO_4$ electrolyte, and these relatively few nucleations were found to occur only along the edge of the working electrode. Zn plating was found to instead favour the growth of existing deposits, rather than new secondary nucleations forming along the deposit edges. During the stripping process, first the contrast of the Zn blocks faded, suggesting the dissolution of Zn proceeding first with a decrease in the deposit thickness, rather than a contraction of the flakes in the lateral plane. An enlarged annotated TEM image of the Zn blocks is shown in *Figure 5.7 b* to highlight the hexagonal morphology of the deposits, with connection angles of 120° between merged Zn deposits (*Figure 5.7 c*). This indicates the planar orientation of the deposited Zn blocks, which were built up by Zn flakes stacked along the [001] direction, with the exposed (002) plane pointing upwards (*Figure 5.7 d*).

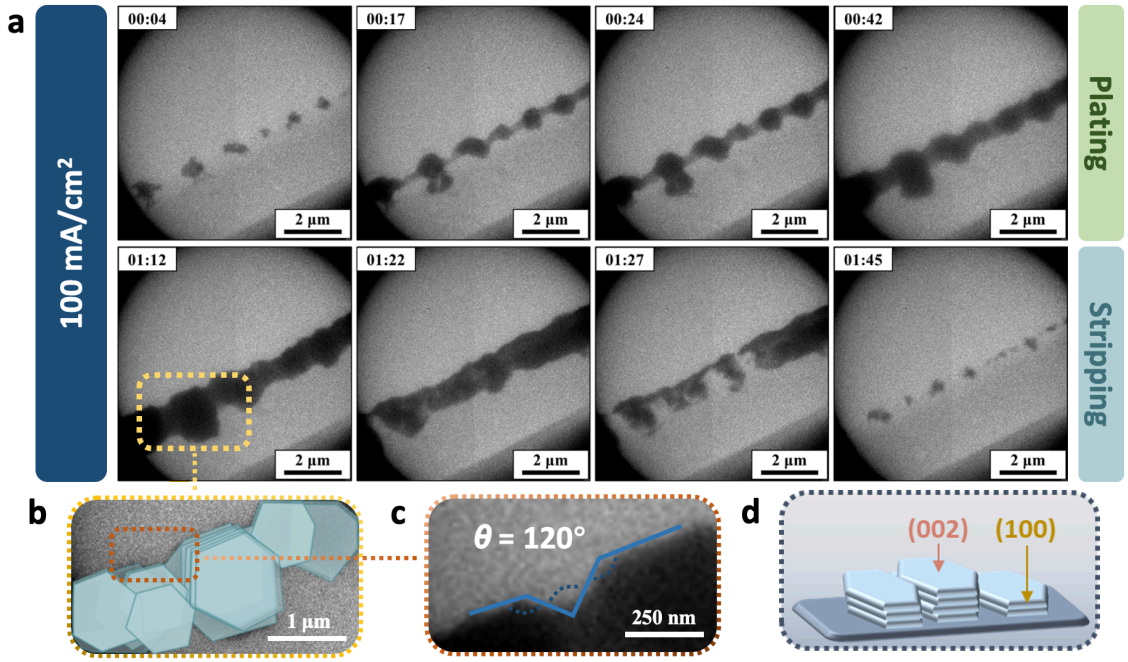


Figure 5.7 In situ liquid cell TEM imaging of Zn electroplating and stripping from $ZnSO_4$ electrolyte with LiCl additive. (a) LC-TEM image time series of electroplating and stripping of Zn at 100 mA/cm^2. (b) Magnified and annotated view of the indicated area in (a). (c) Magnified view of the indicated area in

(b), with the inter-island mergence angle indicated. (d) 3D schematic of Zn deposits on the electrode, with different planes annotated.

After the stripping process ended there were still small amounts of residual Zn observable on the electrode surface; however, according to the galvanostatic voltage profiles recorded while imaging (*Figure 5.8*), the coulombic efficiency of the in situ liquid cell with LiCl additive was higher than that of the cell without LiCl, suggesting less residual Zn was left behind when additive was included.

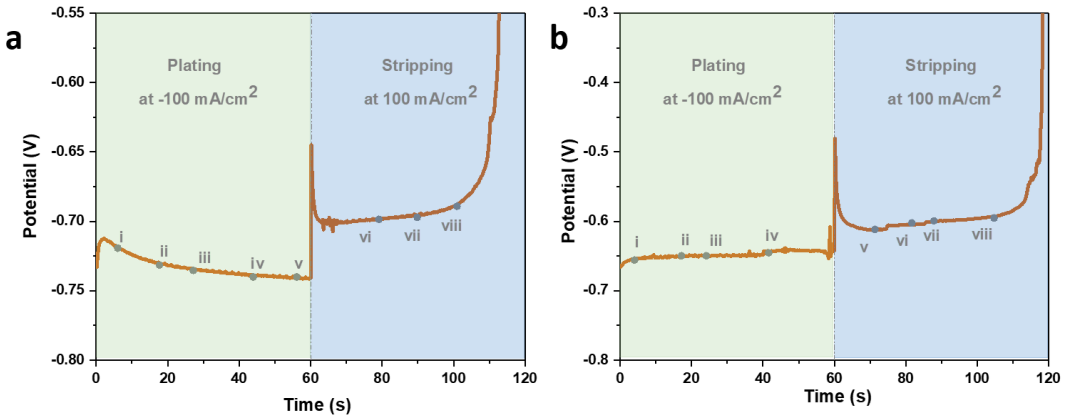


Figure 5.8 Galvanostatic voltage profiles of in situ liquid cell TEM experiments at 100 mA/cm^2 in the electrolyte of (a) $ZnSO_4$ and (b) $ZnSO_4$ with LiCl.

5.3.3 Illustration of different nucleation and growth processes

The whole Zn plating process from the electrolyte with LiCl additive is illustrated schematically in *Figure 5.9 a*: First, random initial nucleation occurs on the edge of the working electrode, as seen in the pure $ZnSO_4$ electrolyte. These initial Zn deposits then continue to grow and expand into planar shapes due to the intrinsic crystallographic energetic preference of Zn metal [376]. Afterwards, instead of the formation of new nucleation sites on the sharp deposit edges or on the electrode surface, the secondary nucleation events preferentially occur on the flat (002)

surfaces of previously deposited Zn crystal flakes, followed by their epitaxial growth on top of the existing deposit. Thus, the deposited Zn is stacked layer-by-layer, and emerges into Zn blocks with a hexagonal prism structure. Similar stacked structures of Zn flakes have been observed in other recent studies with electrostatic shielding additives [230,377].

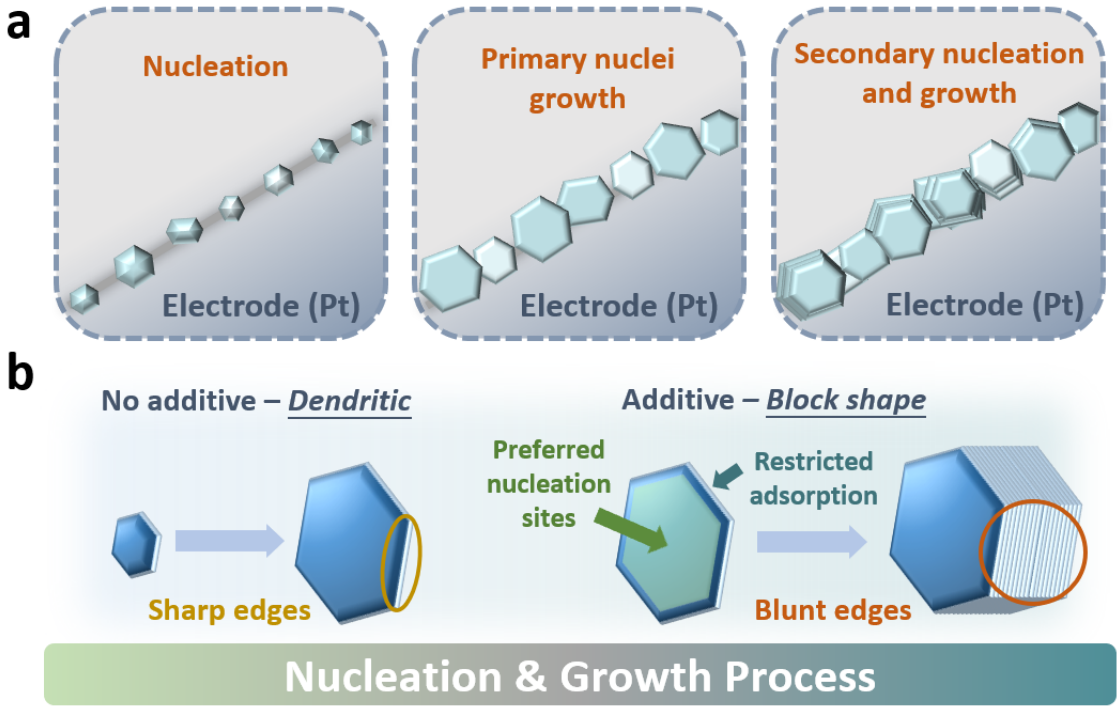


Figure 5.9 (a) Schematic of nucleation and growth process of Zn. (b) Schematic illustration of the possible mechanism leading to formation of Zn blocks.

The nucleation and growth process of an individual Zn block, as well as the proposed formation mechanism, are illustrated in *Figure 5.9 b*. Compared with normal Zn flakes obtained from pure $ZnSO_4$, such Zn blocks are believed to be advantageous for cell cycling performances due to their favourable shape. Zn flakes are endowed with sharp edges, which can pierce cell separators easily and thus cause short circuits and capacity loss during cycling [189]. However, as Zn blocks are composed of layered Zn flakes, the sharp edges are eliminated and only the flat Zn (002) planes and blunt aggregated Zn (100) planes are exposed, as is shown in *Figure 5.9 b*.

The usually accepted explanation for the beneficial role of 'electrostatic shielding' is additive cations preferentially adsorb at sharp edges or protrusions due to the stronger local electric field, thus forming a 'shielding' layer and leading to electrodepositing to instead occur at lower and smoother regions of the electrode [221]. However, from above in situ liquid cell TEM results with LiCl additive, the subsequently deposited Zn did not nucleate on the adjacent electrode surfaces, as suggested by the standard 'electrostatic shielding' explanation, but accumulated on the (002) planes of existing Zn flakes instead. An alternative underlying mechanism is proposed that can explain this secondary nucleation and growth behaviour observations; it is suggested that the sharp edges of the initial Zn flakes attract more additive cations than the flat (002) surfaces of the flakes. The edges are thus 'shielded' to a greater extent than the faces, thus restricting the adsorption of Zn along the flake edges. As a result, the exposed Zn (002) planes become the preferred adsorption and nucleation sites (*Figure 5.9 b*).

5.3.4 Computational modelling results of binding energies

To confirm this hypothesis, further theoretical and experimental analyses were conducted to explore the proposed Zn dendrite suppression process. The morphologies of metal electrodeposits formed at electrode surfaces will be determined by their crystal atomic structures at the micro scale, although continued growth can lead to various macroscopic shapes depending on the cycling conditions [378]. As a hcp metal, Zn has an anisotropic lattice structure, and its electrodeposited morphology follows this intrinsic crystal symmetry [379]. According to the Wulff construction method, which indicates the equilibrium crystalline shapes that exhibit minimum surface energies, the preferred crystal planes for Zn are (002) and (100) [376], while in practice (002), (100) and (101) planes are normally dominant and coexist in neutral electrolytes [380]. Thus, Zn deposits usually show an intrinsic hexagonal flake shape, of which their sizes and spatial distribution, as well as their orientation, can influence the electrochemistry performance.

For example, short-circuiting is believed to be closely related to the large exposure of sharp tips of Zn hexagons standing vertically on the electrode surface [189]; and homogenously distributed Zn deposits with smaller sizes can contribute to ultrahigh rate of Zn plating and stripping [190].

Based on the speculation that the preferable adsorption of Li ions on the sharp Zn (100) plane restricts further growth of Zn along this direction, DFT calculations were conducted to compare the adsorption energies of Li and Zn on surfaces of Zn (100) and Zn (002). Comparison of binding energies of Zn on different Zn planes from DFT calculation in this work with those in other previously published work is given in *Table 5.1*.

Table 5.1 Comparison of binding energies of Zn on different Zn planes from DFT calculation in this work with those in other previously published work.

Team	Binding energy (eV)		DFT setup
	Zn on (002)	Zn on (100)	
This work	-0.34	-0.51	GGA exchange-correlation functional; energy cutoff: 1560 eV; k-point grid: 12 × 12 × 1 and 1 × 12 × 12 for (002) and (100) surfaces, respectively; energy threshold: 2 × 10^{-7} eV; force threshold: 0.02 eV/Å; surface slab with 12 Zn layers; 20 Å vacuum region.
Hu et al. [223]	-0.97	----	GGA exchange-correlation functional; energy cutoff: 800 eV; k-point grid: gamma point only; energy threshold: 1 × 10^{-5} eV; force threshold: 0.02 eV/ Å; 15 Å vacuum region.
Zhang et al. [369]	-0.37	-0.50	GGA exchange-correlation functional; energy threshold: 2 × 10^{-5} eV; force threshold: 0.02 eV/ Å; 20 Å vacuum region.
Yuan et al. [380]	-2.2	-2.8	GGA exchange-correlation functional; energy cutoff: 450 eV; energy threshold: 1 × 10^{-5} eV; force threshold: 0.02 eV/ Å; vdW: DFT-D2.

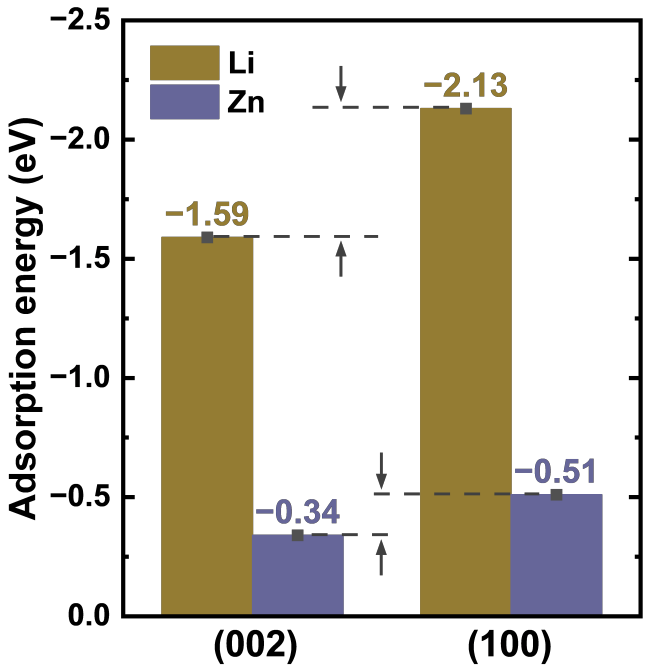


Figure 5.10 DFT results of binding energies of Li and Zn on Zn (002) and (100) planes.

Zn ions have the strongest tendency to initiate individual nucleation sites on the Zn (100) plane [289]. However, as is shown in *Figure 5.10*, the adsorption energies of Li on Zn (100) and Zn (002) are -2.13 eV and -1.59 eV respectively, lower than those of Zn on both facets. Furthermore, the difference between the adsorption energies for Li adsorbing on to the Zn (002) and Zn (100) planes is greater than that of Zn on these two planes, indicating that Li also has a stronger relative preference to adsorb on to the Zn (100) plane. This indicates the role of Li as an efficient inhibitor to limit Zn adsorption on the Zn (100) plane. Thus, the remaining exposed Zn (002) planes of the Zn flakes become more relatively advantageous as Zn adsorption sites. And, contrary to the Zn (100) plane, it has been reported that Zn adsorbed on the Zn (002) plane prefer to maintain a horizontal growth parallel to the basal plane, instead of forming new nucleation sites on the top of it [30]. These results provide supporting evidence for my observation of the formation of Zn blocks composed of stacked Zn flakes.

5.3.5 Ex situ structural and morphological characterisations of electrodes after cycling

In order to better understand the changes in the morphological and structural properties, I prepared electrodeposited Zn electrodes from $ZnSO_4$ electrolyte with and without LiCl additive. The electrodes were prepared using a two-electrode Swagelok cell, as this avoids the confounding damage to the electrode surfaces that occurs from dismantling a coin cell. XRD patterns, SEM images, and AFM images of the Zn electrodes after 30 cycles in the different electrolytes are compared, at a current density of 100 mA/cm^2 with a capacity of 2 mAh/cm^2. Commercial Zn foils with (101) texture were used as both working and counter electrodes.

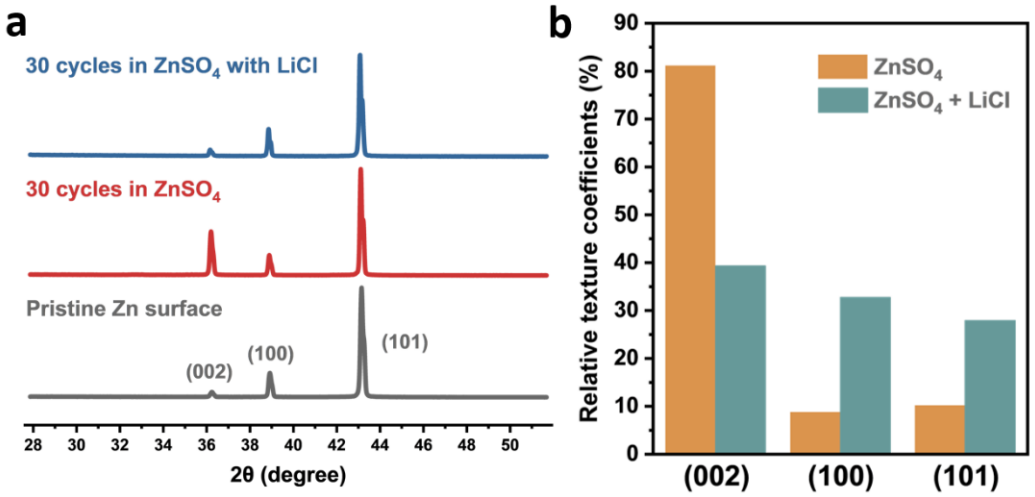


Figure 5.11 (a) XRD patterns of Zn electrodes before and after cycling in different electrolytes. (b) RTCs of Zn (002), (100) and (101) planes from Zn electrode after cycling.

As is shown in *Figure 5.11 a*, the Zn electrode cycled in the pure $ZnSO_4$ electrolyte showed an increasing XRD signal for (002) facets, while the XRD pattern of Zn electrode cycled in the electrolyte of $ZnSO_4$ with LiCl did not show obvious changes [377]. To further compare their structure properties, the relative texture coefficients (RTCs) are given in *Figure 5.11 b* and *Table 5.2*, which were calculated according to the following formula [381]:

$$\mathrm{RTC}_{(hkl)} = \frac{I_{(hkl)}/I_{0(hkl)}}{\sum I_{(hkl)}/I_{0(hkl)}} \times 100\% \qquad \text{(Equation 5.3)}$$

where $I_{(hkl)}$ is the measured intensity of a plane (*hkl*), and $I_{0(hkl)}$ is the intensity of the plane (*hkl*) from the original sample. The high $RTC_{(002)}$ of Zn from the pure $ZnSO_4$ corresponds to larger exposure of (002) planes due to a loose deposition structure of Zn flakes on the electrode surface. The $RTC_{(100)}$ of the electrode cycled with LiCl exhibits a much higher value than that of without LiCl, indicating a strong tendency of alignment along the (100) plane.

Table 5.2 Calculations of RTCs of Zn (002), Zn (100) and Zn (101) planes from Zn electrodes cycled in pure $ZnSO_4$ and in $ZnSO_4$ with LiCl.

RTCs	(002)	(100)	(101)
Zn cycled in pure $ZnSO_4$	81.15%	8.72%	10.13%
Zn cycled in $ZnSO_4$ with LiCl	39.33%	32.75%	27.92%

Figure 5.12 and *Table 5.3* also shows the results of calculations of the texture coefficients (TCs), which demonstrates how much the texture orientation deviates from the original (TC = 1). The calculation of TCs follows the formula [382]:

$$\mathrm{TC}_{(hkl)} = \frac{I_{(hkl)}/I_{0(hkl)}}{N^{-1}\sum_n I_{(hkl)}/I_{0(hkl)}} \qquad \text{(Equation 5.4)}$$

where *N* is the number reflection peaks analysed. The $TC_{(002)}$ of the electrode cycled in $ZnSO_4$ with LiCl is slightly above 1, which can be attributed to minimal exposure of (002) planes; this is due to the stocky shape of the Zn blocks, with exposed (002) faces only at the top and the bottom of each block.

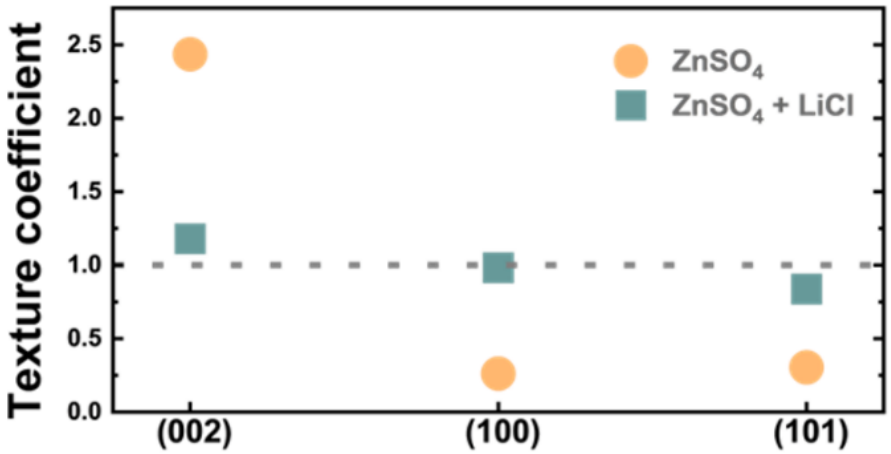


Figure 5.12 TCs of Zn (002), Zn (100) and Zn (101) planes from Zn electrodes after cycling.

Table 5.3 Calculations of TCs of Zn (002), Zn (100) and Zn (101) planes from Zn electrodes cycled in pure $ZnSO_4$ and in $ZnSO_4$ with LiCl.

TCs	(002)	(100)	(101)
Zn cycled in pure $ZnSO_4$	2.4345	0.2616	0.3039
Zn cycled in $ZnSO_4$ with LiCl	1.1799	0.9825	0.8376

SEM images of Zn electrodes after direct electrodepositing (2 mAh/cm^2) in different electrolytes are shown in *Figure 5.13*, which exhibited similar nucleation behaviour as observed by the in situ liquid cell TEM experiments, where Zn deposits from the electrolyte with LiCl tended to grow layer by layer and form blocks.

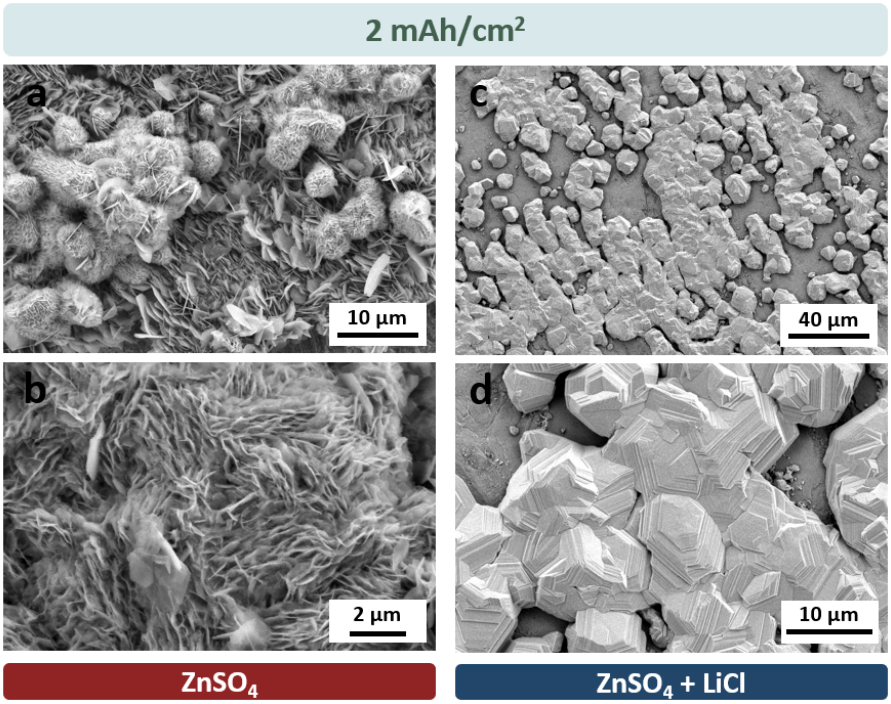


Figure 5.13 SEM images of Zn electrodes after electrodepositing using a two-electrode Swagelok cell in the electrolytes of $ZnSO_4$ without and with LiCl.

The Zn electrodes after cycling in different electrolytes are compared in *Figure 5.14*. For just $ZnSO_4$ electrolyte, the electrode revealed randomly distributed Zn flakes with sharp edges (*Figure 5.14 a*), while with LiCl additive (*Figure 5.14 b*) a dense and uniform surface was found on the electrode. AFM topographic images (*Figure 5.14 c-f*) showed a much smoother surface for the Zn electrode cycled with LiCl additive, while there was significant variation in the height distribution for that cycled in pure $ZnSO_4$, where the arithmetic roughness (Ra) of which was 2.5 times of that with LiCl (*Table 5.4*). The surface area of the scanned 40 × 40 μm^2 field increased by 63% after cycling in the pure $ZnSO_4$, whereas it only increased by 10% with LiCl added.

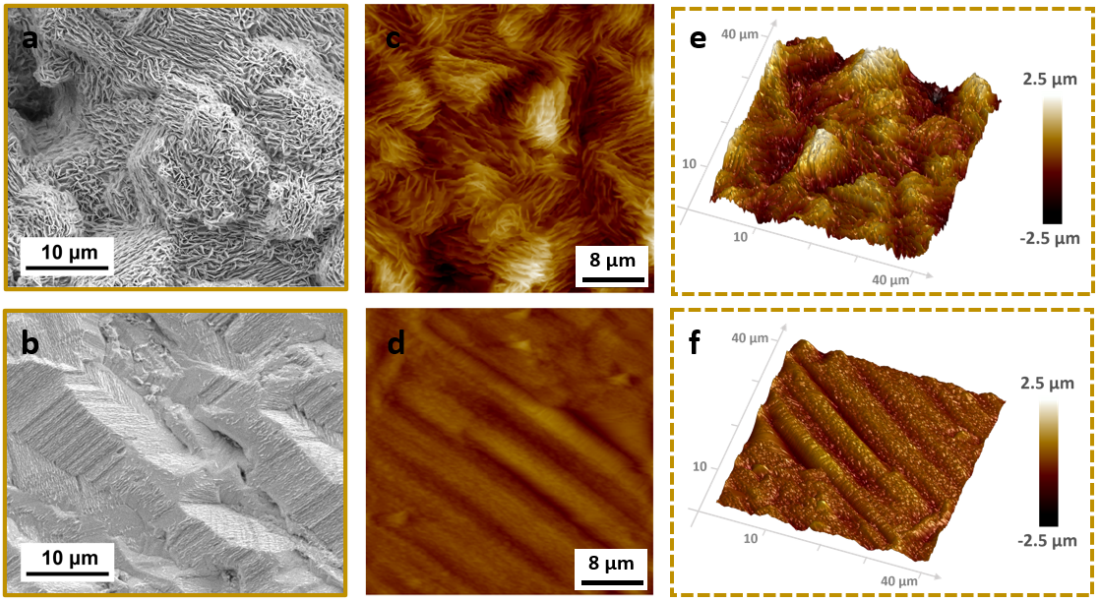


Figure 5.14 SEM and AFM images of Zn electrodes cycled using a two-electrode Swagelok cell in the $ZnSO_4$ electrolytes without (a, c, e) and with the LiCl additive (b, d, f).

Table 5.4 Calculations of roughness (Ra) and surface area increase (S) of Zn electrodes cycled in different electrolytes as extracted from the AFM images.

	Zn cycled in $ZnSO_4$ with LiCl	Zn cycled in $ZnSO_4$
Ra (nm)	229.5 ± 31.46	580.3 ± 81.62
S (%)	10 ± 0.73	62.6 ± 2.59

The rougher surface seen for the electrode cycled from pure $ZnSO_4$ would initially seem to contradict my previous XRD results, which showed an increased prevalence of (002) planes on the Zn electrode cycled in pure $ZnSO_4$, as electrode surfaces with more (002) planes exposed are normally considered to be beneficial to alleviating dendrite formation and improving cycling performance [289,368]. However, this neglects to consider the microstructure of the electrode over which these various crystal faces are expressed, as the SEM images (*Figure 5.13* and *Figure 5.14 a-b*) and AFM scans (*Figure 5.14 c-f*) show a significant increase in the overall surface roughness and surface area exposed for the no additive case. This looser deposit structure allows for more corrosion and side reactions, thus causing a decrease in the CE.

5.3.6 Influences of the additive concentration

The influence from changing the concentration of LiCl additive in directing the deposition morphology was also studied. The LiCl concentration was varied from 0.1 M to 2 M, and the electroplated Zn morphology was examined by SEM, as shown in *Figure 5.15*.

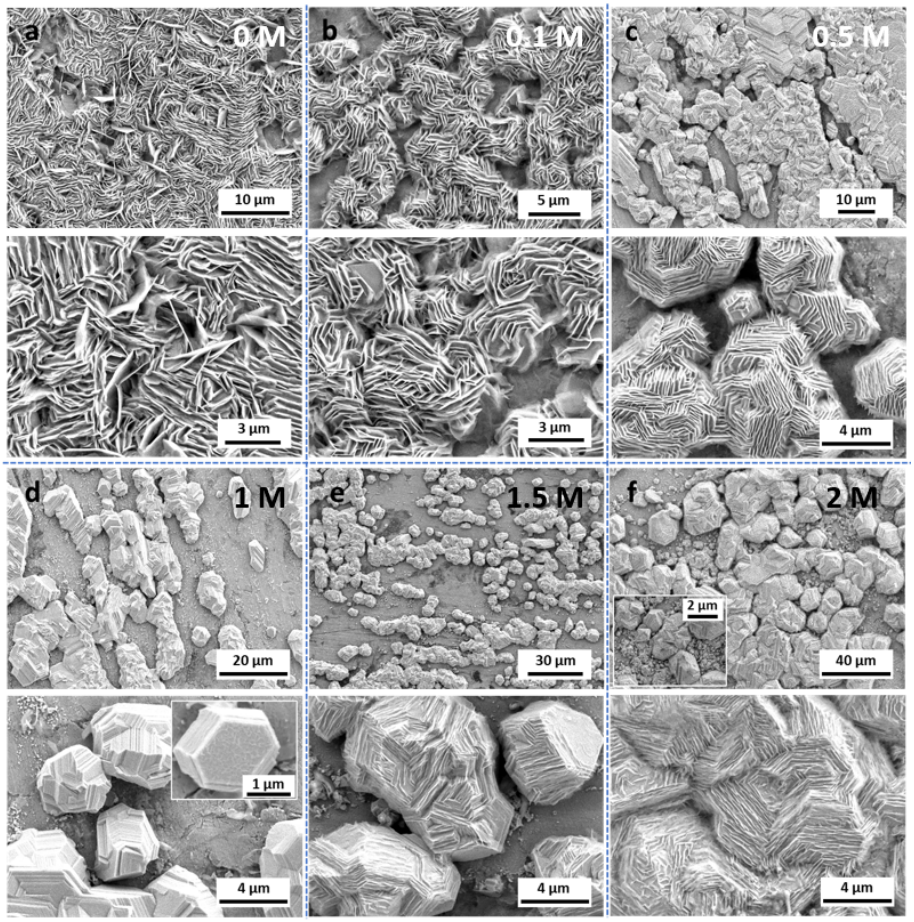


Figure 5.15 SEM images of Zn electrodes after electrodepositing from electrolytes of (a) $ZnSO_4$, and $ZnSO_4$ with (b) 0.1 M LiCl, (c) 0.5 M LiCl, (d) 1 M LiCl, (e) 1.5 M LiCl, (f) 2 M LiCl.

The SEM images show that the deposited Zn only started to emerge into more clearly defined block shapes when the concentration of LiCl reached 0.5 M, with a smoothly faceted morphology appearing for 1 M, however the surface of Zn blocks became slightly crinkled when the

concentration exceeded 1.5 M. When the concentration was further increased to 2 M, more nucleation sites were found on the electrode surface. Electrolytes with 0.5 M, 1 M and 2M LiCl were chosen as representatives to further study the influence of the additive concentration on the electrochemistry.

Chronoamperometry tests were conducted with Zn||Zn coin cells at a fixed potential of -150 mV (*Figure 5.16 a*). The lower current densities observed with the 0.5 M and 1 M LiCl additive electrolytes suggests a smaller active surface area and denser deposition layer, while in the electrolyte with 2 M LiCl additive the value was even increased compared to that found with pure $ZnSO_4$. Similarly, according to the voltage profiles of Zn||Zn coin cells using different electrolytes in *Figure 5.16 b*, the overpotential of the electrolyte with 2 M LiCl was not improved compared to those with lower LiCl concentration, which could be due to the increased viscosity or the reduced ion conductivity [224]. These results are consistent with the deposition morphologies shown in *Figure 5.15 f*, with roughened faceted surfaces on the Zn blocks and additional small nucleation sites.

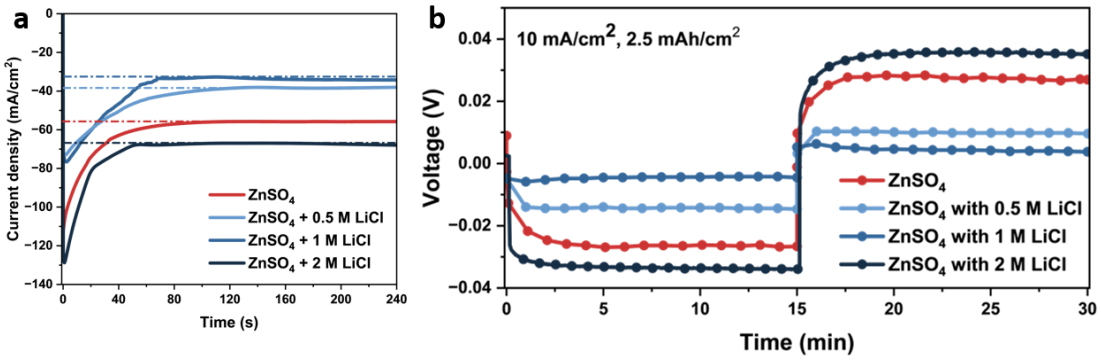


Figure 5.16 (a) The chronoamperometry curves tested at a fixed potential of -150 mV and (b) voltage profiles of Zn||Zn coin cells in the electrolyte of $ZnSO_4$ and $ZnSO_4$ with 0.5 M LiCl, 1 M LiCl and 2 M LiCl.

5.3.7 Comparison of cycling performances

To gain a deeper insight into the influence of LiCl on the electrochemical properties of Zn batteries, Zn||Ti coin cells and symmetric Zn||Zn coin cells were prepared and cycled under different conditions. To better analyse surface morphologies after cycling, one layer of glass fibre on the Ti side and one layer of surfactant coated Celgard membrane (Celgard 3501) on the Zn side were used as separators to maintain good cycling performance as well as minimising surface damage from peeling off the separators during cell disassembly. The schematic of the Zn||Ti cell is given in *Figure 5.17*.

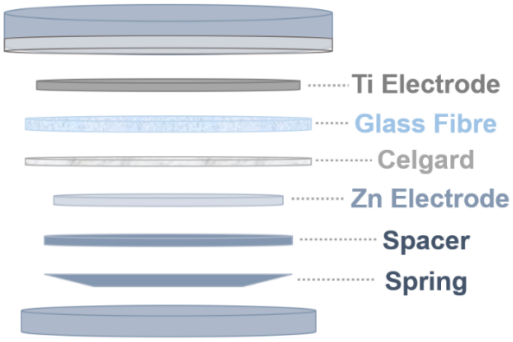


Figure 5.17 Schematic of the Zn||Ti coin cell set-up used for electrochemical tests and for SEM imaging of electrode surface after cycling.

The voltage profiles of Zn||Ti cells at selected cycles at 10 mA/cm^2 with a capacity of 1 mAh/cm^2 with $ZnSO_4$ electrolyte without and with LiCl added are presented in *Figure 5.18*. The coulombic efficiency of the Zn||Ti cell in $ZnSO_4$ with LiCl was higher than that in pure $ZnSO_4$, and kept at 99.9% after 30 cycles.

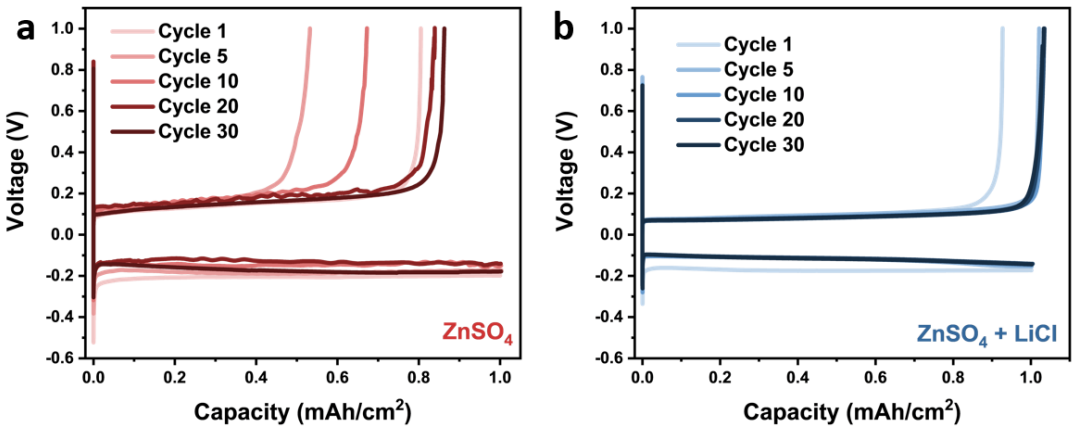


Figure 5.18 Voltage profiles at different cycling numbers of Zn||Ti coin cells using the electrolyte of (a) $ZnSO_4$ and (b) $ZnSO_4$ with LiCl.

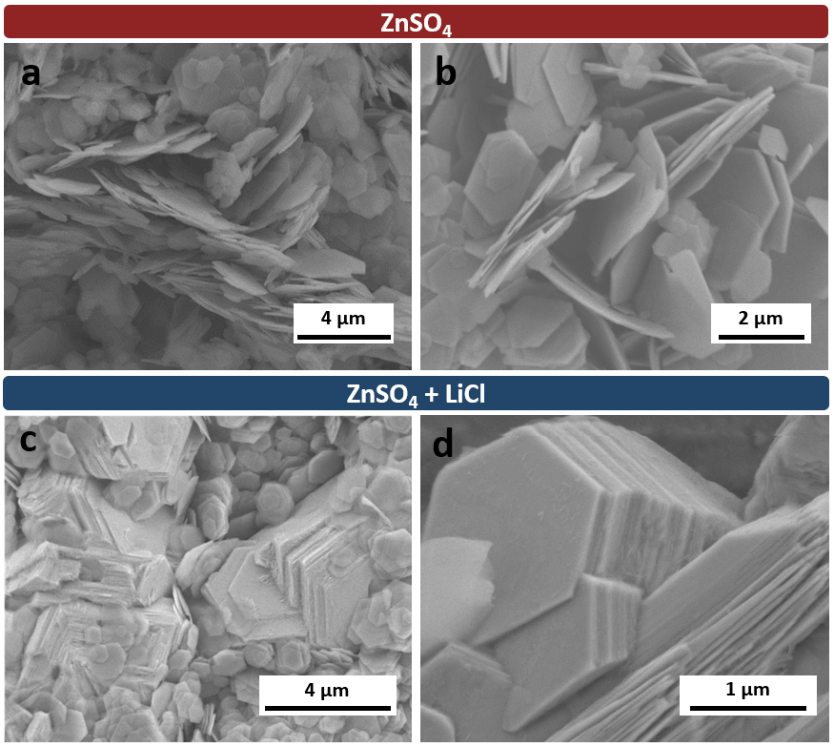


Figure 5.19 SEM images of Zn electrodes after cycling in the electrolyte of (a, b) $ZnSO_4$ and (c, d) $ZnSO_4$ with LiCl.

The Zn||Ti cells were dismantled after cycling without and with LiCl and Zn electrodes were characterised by SEM imaging (*Figure 5.19*). The Zn electrode showed a similar morphology of

stacked Zn flakes as observed in the liquid cell TEM and the Swagelok cell with the presence of LiCl in the electrolyte.

The schematics in *Figure 5.20 a and b* illustrate how Zn blocks with fewer exposed sharp edges are less susceptible to puncturing the separators, forming a denser deposition layer and a blunt surface on the Zn electrode. Photographs of both separators from the Zn||Ti cells after cycling (*Figure 5.20 c and d*) show plenty of residue was found in the glass fibre used in the cell without LiCl additive, indicating the existence of Zn dendrites that pierced the separators, as well as dead Zn. Separators from Zn||Ti cells with LiCl additive were found to be cleaner.

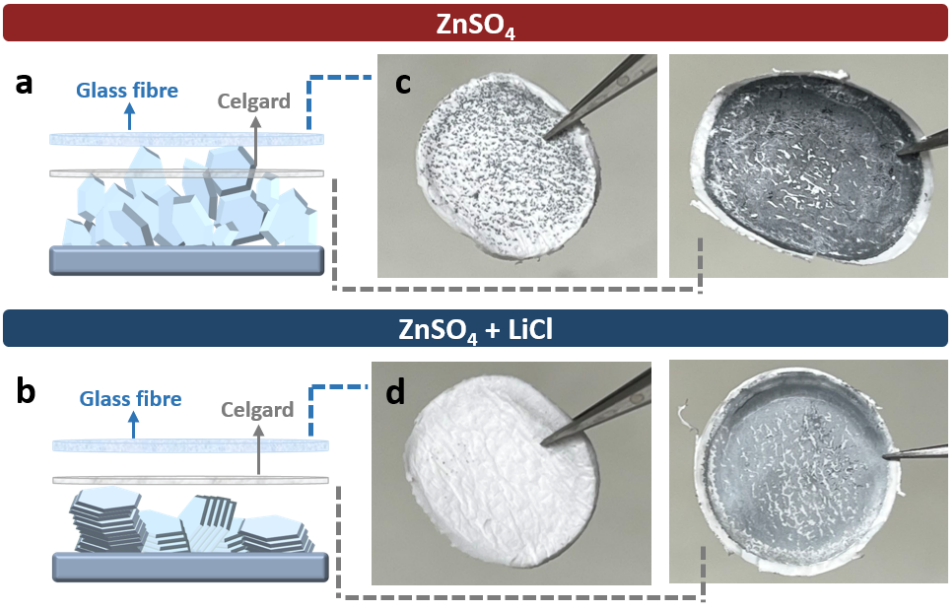


Figure 5.20 Schematic and photographic images of separators after cycling in the electrolyte of (a, c) $ZnSO_4$ and (b, d) $ZnSO_4$ with LiCl.

Cycling tests with symmetric Zn||Zn cells were performed at 10 mA/cm^2 with a capacity of 2.5 mAh/cm^2. SEM images of the cycled electrode surfaces are shown in *Figure 5.21 a-f*. According to the voltage curves shown in *Figure 5.21 g*, the Zn||Zn cell cycled in $ZnSO_4$ with LiCl electrolyte exhibited a lower polarization of 40 mV with stable curves. By comparison, the

voltage-time profile of the Zn||Zn cell with pure $ZnSO_4$ electrolyte had large fluctuations and a much higher voltage hysteresis of nearly 300 mV at the beginning cycle and around 130 mV for the following cycles.

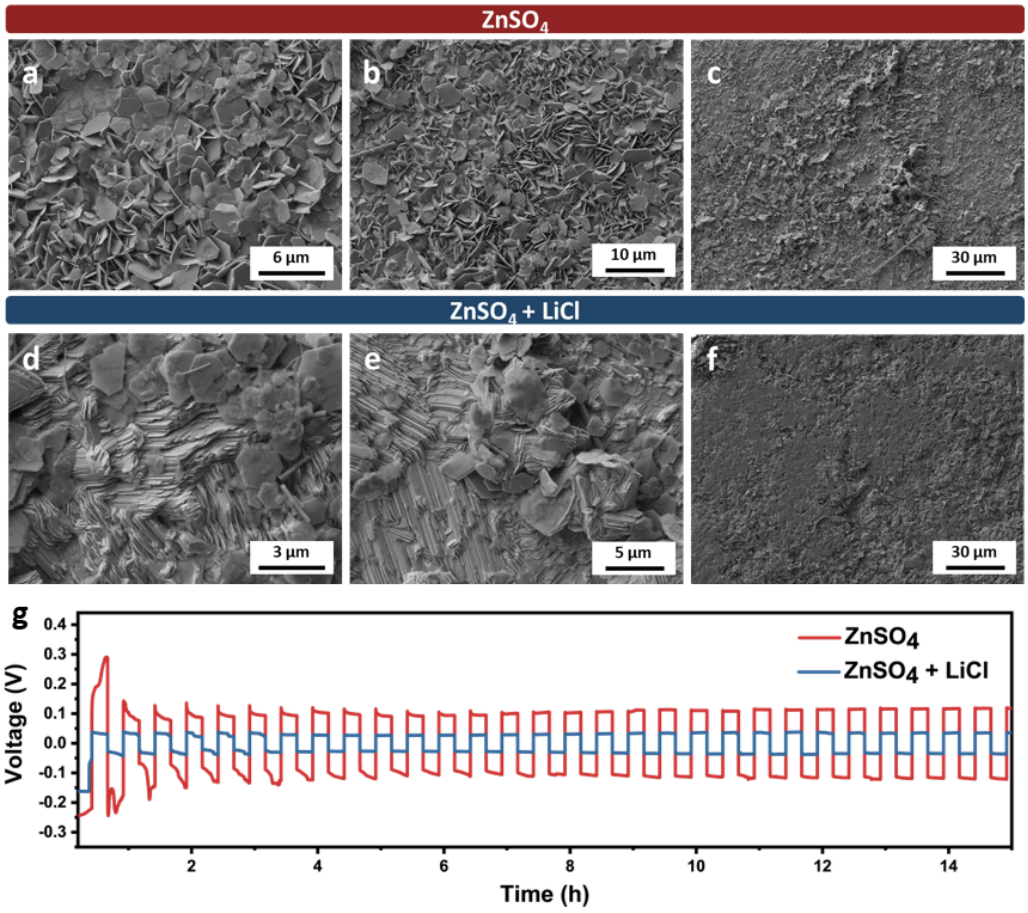


Figure 5.21 SEM images of Zn electrodes from symmetric Zn||Zn coin cells after cycling in (a-c) $ZnSO_4$ and (d-e) $ZnSO_4$ with LiCl. Voltage profiles of Zn||Zn symmetric cells using $ZnSO_4$ without and with LiCl.

Long-term cycling curves of Zn||Zn coin cells using just glass fibre as the separator were performed (*Figure 5.22*), with the cell cycled with LiCl additive exhibiting a lower voltage plateau of 15 mV after 100 cycles, while the cell without LiCl showed a fluctuating voltage curve at around 35 mV. A similar trend in the overpotentials was also observed in the Zn||Ti cell tests shown in *Figure 5.18*. A high nucleation overpotential of over 0.5 V during the initial stage and fluctuating plateau overpotentials between 0.11 V and 0.21 V were obtained from the Zn||Ti

cell cycled in pure $ZnSO_4$ electrolyte, while only a small overpotential of 0.3 V was needed for the initial stage and a stable plateau of 0.1 V for the following deposition for the $ZnSO_4$ electrolyte with LiCl.

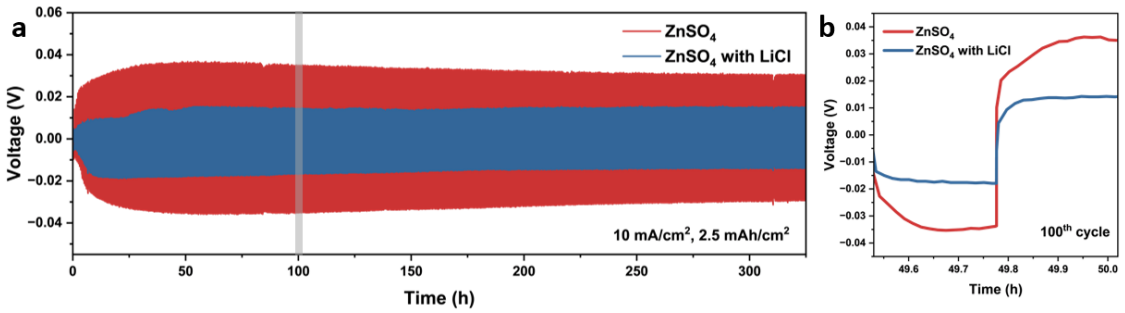


Figure 5.22 (a) The long-term and (b) the 100th cycle voltage profiles of Zn||Zn symmetric cells cycled in $ZnSO_4$ and $ZnSO_4$ with LiCl. Voltages are vs. Zn/Zn^{2+}.

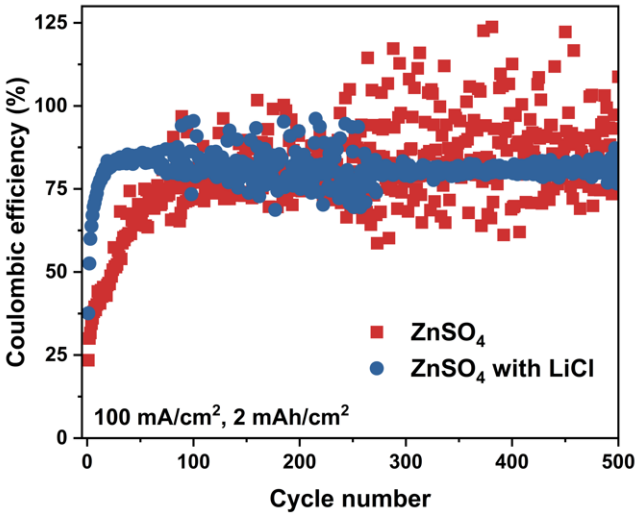


Figure 5.23 The coulombic efficiency of Zn||Ti cells cycled in the electrolyte of $ZnSO_4$ and $ZnSO_4$ with LiCl.

A Zn||Ti coin cell with $ZnSO_4$ and LiCl electrolyte also exhibited a steadier coulombic efficiency over long-term cycling at ultra-high current density (*Figure 5.23*). The >100% coulombic efficiency cycles visible in the unstable $ZnSO_4$ electrolyte are indicative of capacity recovery; i.e., dendrite reattachment or gas bubbles moving away from the electrode surface [210]. Therefore,

the more stable coulombic efficiency of the additive electrolyte suggests fewer dendrites and corrosion reactions. The latter is supported by XRD patterns of Zn electrodes after cycling for 30 cycles (*Figure 5.24 a*), with peaks from the typical by-product, ZHS, being weaker for the cell cycled with electrolyte containing LiCl. In addition, LSV results (*Figure 5.24 b*) also confirmed the inhibited hydrogen evolution after adding a moderate amount of LiCl.

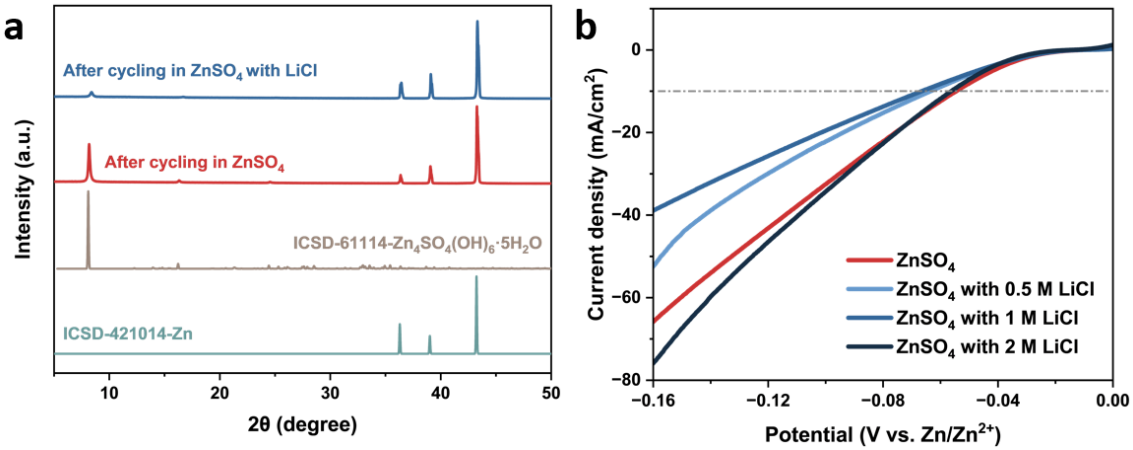


Figure 5.24 (a) XRD patterns of Zn electrodes after cycling in $ZnSO_4$ and $ZnSO_4$ with LiCl. (b) The LSV curves tested at a scan rate of 1 mV/s in the electrolyte of $ZnSO_4$ and $ZnSO_4$ with 0.5 M LiCl, 1 M LiCl and 2 M LiCl.

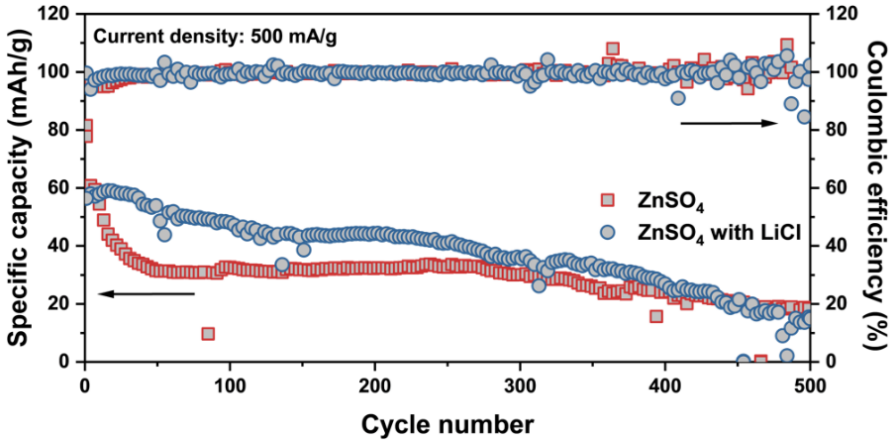


Figure 5.25 The long-term cycling performance at a current rate of 500 mA/g for Zn||V_2O_5 coin cells with the electrolyte of $ZnSO_4$ and $ZnSO_4$ with LiCl additive.

The cycling and rate performances of full cells with V_2O_5 as the cathode using the electrolyte with and without LiCl were also compared. As is shown in *Figure 5.25*, the introduction of LiCl was found to be beneficial for increasing the capacity, but the lifespan was not improved due to the chloride anions damaging the cathode side of the cell during cycling [383]. However, from the rate performances and the first-cycle charge-discharge curves at different current densities (*Figure 5.26*), there was relative improvement to the capacity with increasing current density.

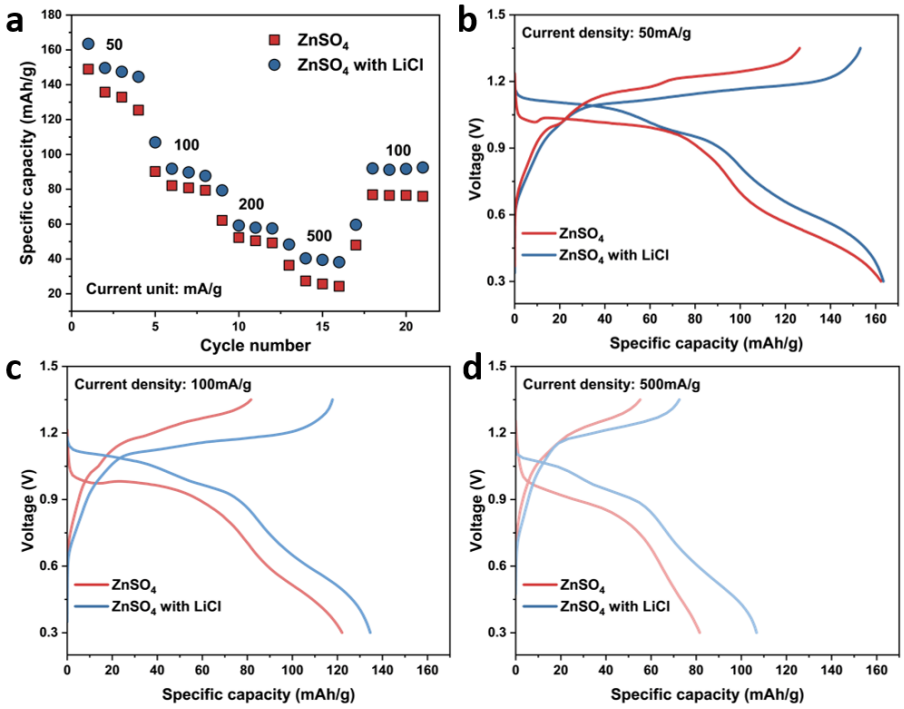


Figure 5.26 (a) The rate performance of the Zn||V_2O_5 coin cells using electrolytes of $ZnSO_4$ and $ZnSO_4$ with LiCl. (b-d) The first-cycle charge-discharge curves at different current densities for the Zn||V_2O_5 coin cells in the electrolyte of $ZnSO_4$ and $ZnSO_4$ with LiCl. Voltages are versus Zn/Zn^{2+}.

Together, these results about the improved electrochemical performances imply that the interfacial side reactions and dendrite formation issues were alleviated with the presence of additive in the electrolyte.

5.3.8 Other potential influencing factors

Beyond the role the additive has in introducing cations that facilitate electrostatic shielding, it is also worth considering the possible influence from the addition of the anion, for example, the contribution of additive LiCl to the solvation structure of Zn^{2+}.

In low concentration aqueous electrolyte, the Zn^{2+} presents a saturated hydration configuration, which can aggravate the parasitic water reduction reaction [384]. It has been reported that replacing H_2O with other anions in the Zn^{2+} solvation sheath can effectively decrease water activity in the electrolyte [385,386]. Previous studies have confirmed the role of high concentration Cl^- ions in aqueous $ZnCl_2$ electrolytes in altering the solvation structure Zn ions [385–387]. A recent work reported a novel dual-ion electrolyte system of $Li_2ZnCl_4{\cdot}RH_2O$, by adding LiCl as a supporting salt into the $ZnCl_2$ aqueous electrolyte [388]. It was found that the Li^+ ions exhibited a stronger ability to coordinate with water molecules, which can further help to exclude water from solvating Zn^{2+} even at low salt concentration. In addition to restraining side reactions, the change of solvation structure can also impact the de-solvation and deposition process [389,390], as the $[Zn(H_2O)_6]^{2+}$ presents a high energy barrier (289.3 kcal mol^{-1}) against de-solvation and deposition [391,392]. For example, replacing H_2O with Cl^- in the solvation structure of Zn^{2+} is reported to contribute to moderating the de-solvation energy from DFT studies [393,394], leading to a reduced overpotential [385,388].

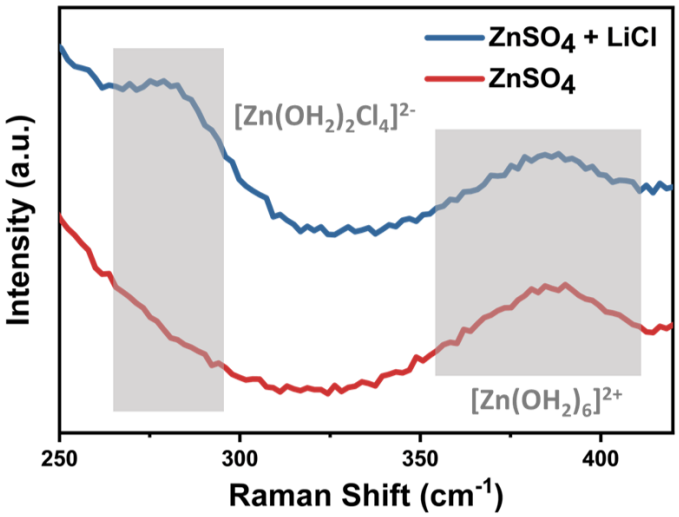


Figure 5.27 Raman spectra of the $ZnSO_4$ electrolyte and the $ZnSO_4$ with LiCl electrolyte (from 250 to 440 cm^{-1}).

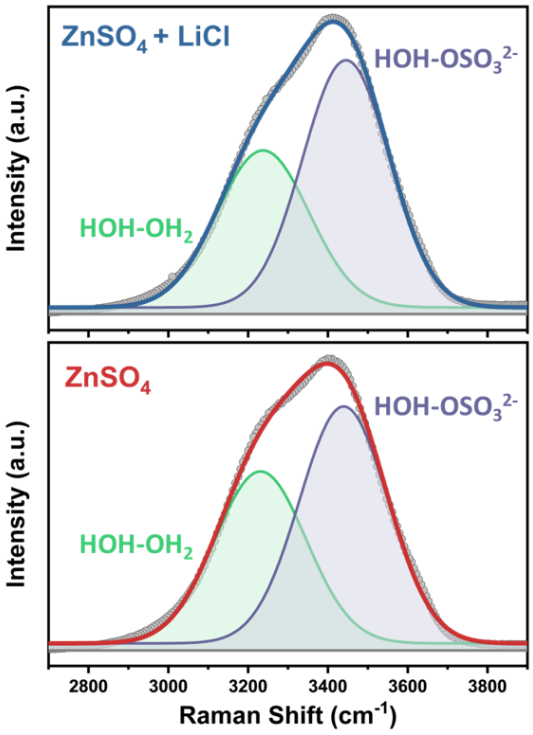


Figure 5.28 Raman spectra of the electrolyte of $ZnSO_4$ and the electrolyte of $ZnSO_4$ with LiCl (from 2700 to 3900 cm^{-1}).

In the aqueous electrolyte of 2 M $ZnSO_4$ with 1.1 M LiCl additive, I found a stretching vibration peak associated with $[Zn(H_2O)_2Cl_4]^{2-}$ appeared in the Raman spectrum (*Figure 5.27*) [224,385]. The

band assigned to the $[Zn(OH_2)_6]^{2+}$ vibration was found in both electrolytes but was weakened in the additive case [384,395]. After addition of LiCl, the relative intensity ratio between the peak corresponding to the HOH-OH_2 stretching mode and the peak corresponding to the HOH-OSO_3^{2-} stretching mode was reduced from 0.74 to 0.65 (*Figure 5.28*), suggesting less free water in the additive electrolyte [384,385,388,395].

This slight change of the solvation structure with the presence of LiCl could explain the lower overpotentials observed in the Zn||Ti and Zn||Zn cell tests, and the resulting promoted plating kinetics also supports the phenomenon in my in situ liquid cell TEM experiments that fewer new nucleation sites were observed. These results evidence the involvement of the Cl^- anion in the solvation structure of Zn^{2+}, which helps to inhibit hydrogen evolution and also contributes to maintaining a high cycling efficiency. Though several studies have tried to exclude influence from anions and confirmed the effectiveness of individual cations by comparative experiments when introducing additives [230,383], my findings show the importance of selecting additives based on an understanding of the influence of both the anion and the cation when wishing to introduce an electrostatic shielding effect.

5.3.9 Studies of other additive analogues

To further verify the role of Li cations, I also investigated other Li compounds and other types of cations as additives.

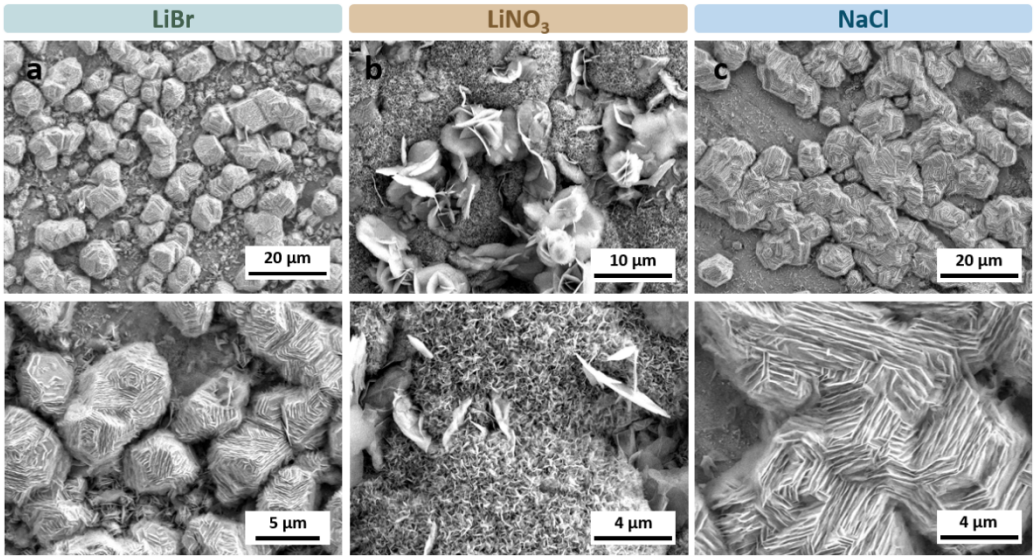


Figure 5.29 SEM images of Zn electrodes after electrodepositing in the electrolyte of $ZnSO_4$ with (a) 2 M LiBr, (b) 2 M $LiNO_3$ and (c) 2 M NaCl.

LiBr and $LiNO_3$ were first chosen as comparisons to study the influence of the anion. As is shown in *Figure 5.29 a and b*, it was found that the deposited Zn with LiBr additive also showed a similar block shape Zn deposition morphology as was observed in electrolyte with LiCl, while only deposits with a very loose structure were found after using $LiNO_3$ additive. To exclude the effect of the anion, NaCl was selected and found to introduce preferred nucleation on the (002) facets as well, but deposited Zn flakes were stacked less smoothly together (*Figure 5.29 c*). These results, taken together, suggest the importance of Li paired with a halide anion as an effective electrostatic shielding additive.

We also tested several other additives which were reported to effectively suppress dendrite growth and work via the electrostatic shielding mechanism (*Figure 5.30*) [[230,377]], which all showed a similar blocky morphology.

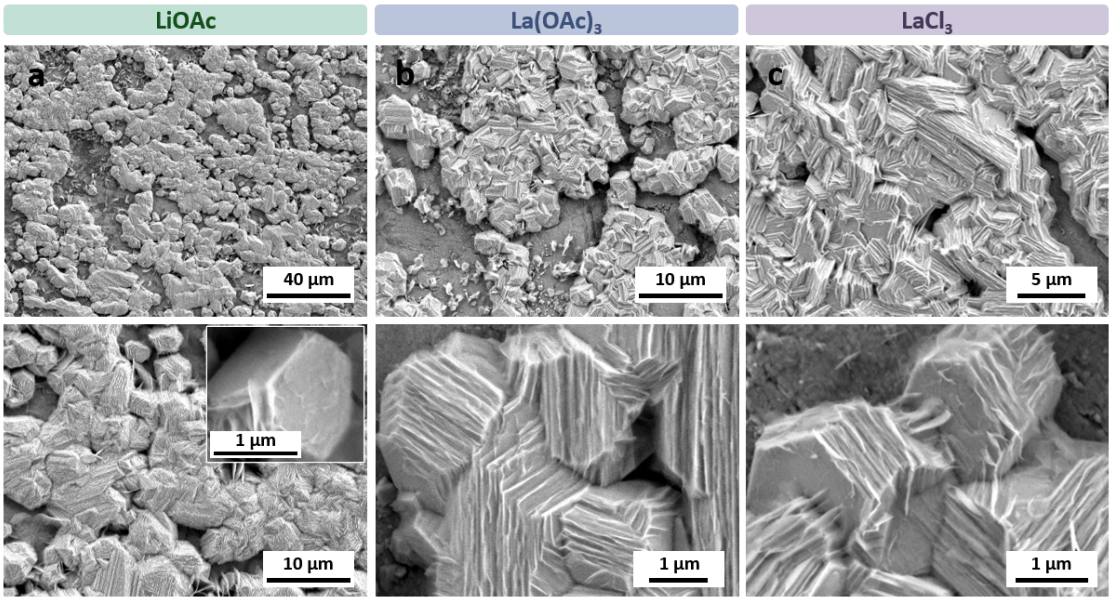


Figure 5.30 SEM images of Zn electrodes after electrodepositing in the electrolyte of $ZnSO_4$ with 'electrostatic shielding' additives reported in the literature, (a) 0.3 M lithium acetate (LiOAc), (b) 0.0085 M lanthanum acetate [$La(OAc)_3$] and (c) 0.0085 M lanthanum chloride ($LaCl_3$).

Chronoamperometry and LSV tests were also conducted for the electrolytes with LiOAc and lanthanum chloride ($LaCl_3$), which confirmed their ability to alleviated dendrite formation and side reactions (*Figure 5.31*). The cycling and rate performance of Zn||V_2O_5 coin cells cycled in an electrolyte with 0.3 M lithium acetate (LiOAc) additive [377] was also studied (*Figure 5.32*).

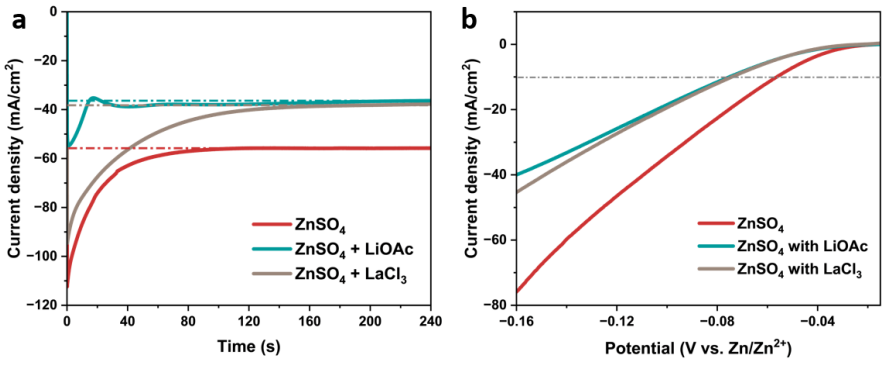


Figure 5.31 (a) Chronoamperometry curves tested at a fixed potential of -150 mV and (b) LSV curves tested at a scan rate of 1 mV/s, for electrolytes of $ZnSO_4$, and $ZnSO_4$ with LiOAc and $LaCl_3$.

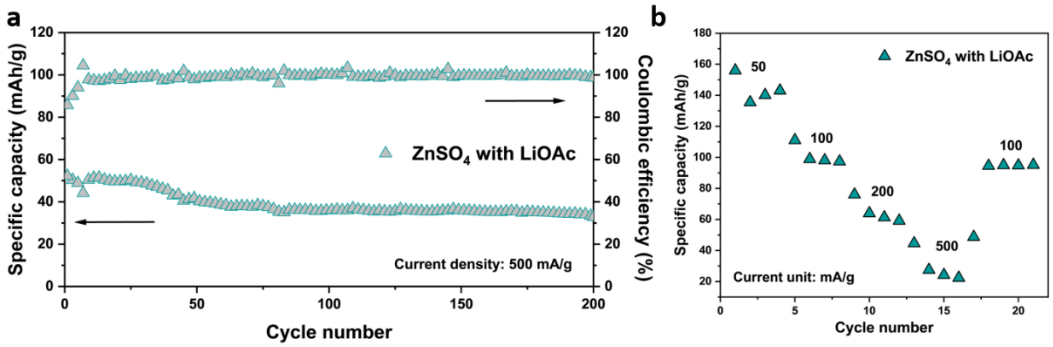


Figure 5.32 (a) The long-term cycling performance at a current of 500 mA/g and (b) the rate performance of the Zn||V_2O_5 coin cells in the electrolyte of $ZnSO_4$ with LiOAc.

5.3.10 Comparison of the 'Electrostatic shielding' mechanism in different battery systems

The schematic in *Figure 5.33* summarises the mechanism for how LiCl additive mitigates Zn dendrite growth via the 'electrostatic shielding effect'. In brief, the suppression of Zn dendrites occurs due to the altering of the secondary nucleation behaviour of electrodeposited Zn. First, primary Zn nuclei form on the rough electrode surface. This behaviour is similar with or without additive, with small Zn protrusions forming along the electrode surface as a result. These initial nuclei have a hexagonal flake morphology due to the crystal structure of Zn. Then, Li ions preferentially adsorb along the sharp (100) planes of these primary nuclei due to a combination of the 'tip effect' enhancing the local electric field, and a lower binding energy of the Li cations with the (100) facets (*Figure 5.33 b*). Meanwhile, instead of forming new primary nucleation sites on the adjacent electrode surface, Zn ions are inclined to nucleate and grow on the exposed (002) planes. This secondary nucleation behaviour facilitates the parallel stacking of Zn flakes, thus leading to the formation of Zn blocks. As the deposition capacity increases, the stacked Zn blocks constitute a dense layer with few sharp edges exposed, as illustrated in the top view (*Figure 5.33 c*). The deposition of stacked blocks occurs instead of the edge-to-edge 'daisy chain' linking of Zn flakes that occurs when no additive is present; such Zn daisy chain morphologies

form due to consecutive secondary Zn nucleations occurring at the edges of sequential flakes, ultimately yielding an undesirable dendritic morphology.

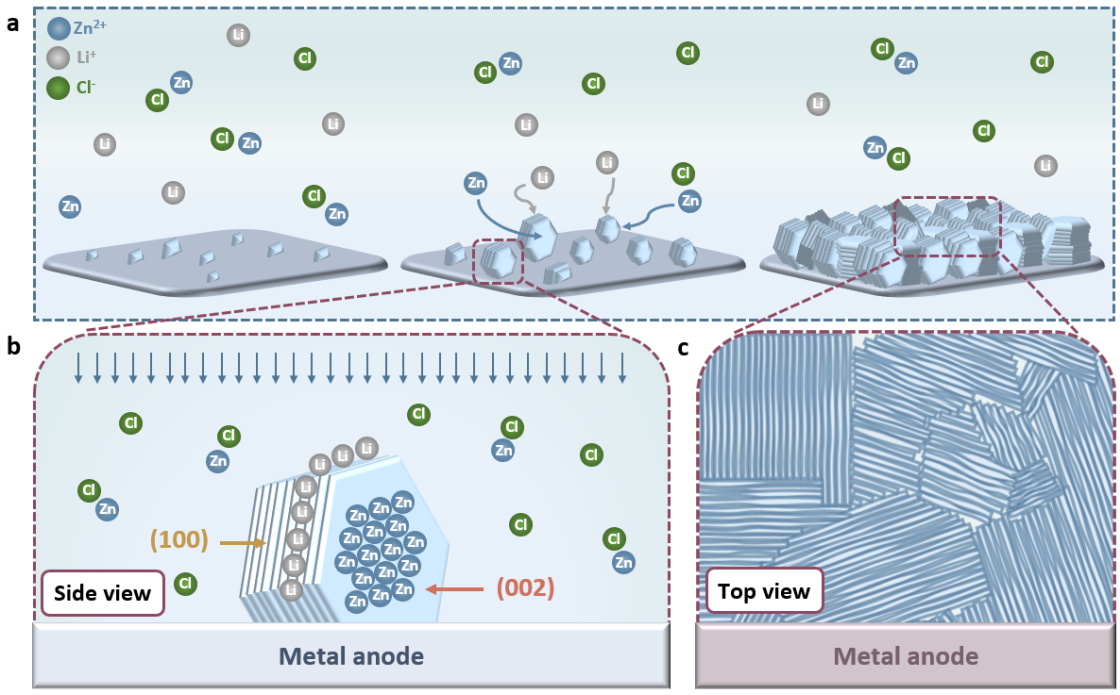


Figure 5.33 Schematic illustration of the underlying mechanism of the 'electrostatic shielding effect' in aqueous Zn-ion batteries. Species indicated in circles are ions. (a) Secondary nucleation behaviour and evolution of Zn blocks triggered by including LiCl electrolyte additive. (b) Enlarged Zn block structure, indicating preferential adsorption of Li cations on the Zn (100) plane and the favoured secondary nucleation of Zn ions on the Zn (002) plane. (c) Top view of flat and dense electrode surface composed of Zn blocks.

It is also relevant to note that for the primary nucleation events, that is Zn initially nucleated onto the current collector metal, there will also be an influence from the substrate material as well. Some metals have a greater affinity toward Zn, as has been recently shown by a detailed study [396]. This may in turn also influence the relative preference for primary versus secondary nucleation, and so may also have an additional contribution in influencing the overall deposition morphology.

The above description of Zn dendrite suppression directed by the 'electrostatic shielding effect' is notably different to that used for Li dendrites. As is shown in *Figure 5.34 a*, with the electrostatic shielding effect on a Li anode, the Li ions are directed away from the sharp tips and toward other areas of the electrode surface, and thus leads to a flatter electrode. This is distinct from above observations for electrostatic shielding at the Zn metal anode (*Figure 5.34 b*), where it was found that while Zn is still prevented from depositing at sharp edges, it instead deposits on the (002) surface of the Zn flakes; i.e., there is a crystallographic influence. In contrast with Zn, which has an anisotropic hcp lattice structure, Li has an isotropic body-centred cubic (bcc) structure, for which the surface energies of most facets are about the same [376,378]. Hence, additive cations in the Li electrolyte systems tend to shield all protrusions without distinction, as they are solely influenced by the electric field concentration at the protrusion tips.

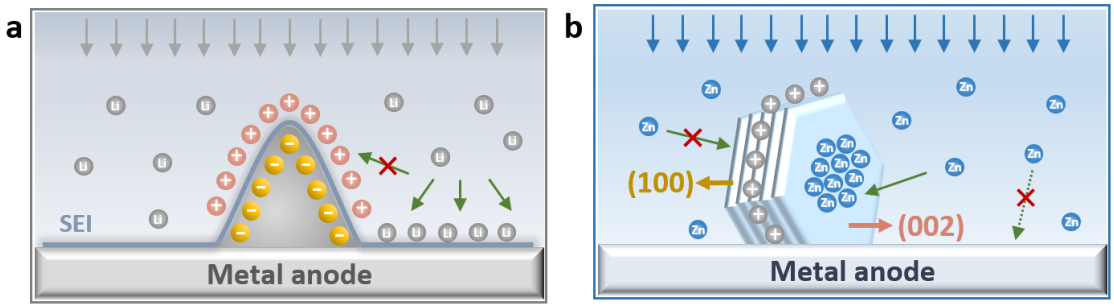


Figure 5.34 Schematic illustration of how the 'electrostatic shielding effect' directs (a) Li deposition process in Li batteries versus how it directs (b) Zn deposition in Zn batteries.

5.4 Conclusion

Manipulating the electrolyte composition in batteries is an effective way of improving cycling performance. Understanding the mechanistic action of such alterations is crucial for the informed optimisation of battery performance by tailoring of the electrolyte. In the work of this Chapter, it has shown that electrolyte additive cations, introduced to form an electrostatic

shielding layer in order to prevent dendrite growth, do not operate via the same mechanism proposed for Li anode batteries. The in situ electrochemical liquid cell TEM observations revealed the additive's suppression of dendrite growth occurs instead due to it preventing secondary Zn nucleation on Zn (100) faces, and encouraging deposition on Zn (002) faces, leading to stockier block morphologies that culminate in a denser, smoother anode surface following charging. This relative preference for Zn (002) deposition in the presence of additive cation was confirmed by DFT modelling, and shows that the role of the anisotropic Zn crystallography is an important parameter to consider when translating mechanistic explanations over from the related field of Li battery chemistry.

Chapter 6 Exploring roles of organic additives in alleviating Zn dendrites and side reactions: a comparative research

6.1 Introduction

Improving the stability of the Zn metal anode by regulating electrolyte formulations has been recognized as perhaps the most facile and efficient strategy. As summarised in Chapter 2, various additives have been introduced to the electrolytes to suppress dendrite growth and side reactions through different working mechanisms. Among these, certain organic compounds are believed to be able constrain the activity of the solvated and free water molecules, while others preferentially participate into the EDL by adsorbing onto the electrode surface [253,262,274,275]. In addition, some organic additives are reported to facilitate the formation of more SEI layers via electrochemical decomposition, thereby suppressing both dendrite formation and side reactions [216,272].

Extensive research has been conducted to identify critical descriptors that more accurately assess the efficiency of these organic additives. Various factors, including susceptibility to forming an SEI [275], hydrogen bond donor number [259], dielectric constant [397], adsorption energy [293], and de-solvation energy barrier [398], have been proposed as significant. However, the underlying mechanisms and guidelines for optimising additive design still as yet remain unclear. Consequently, it is crucial to elucidate the roles and mechanisms through which these organic additives influence the performance of the Zn metal anode across multiple dimensions.

In this chapter, I select several representative organic additives, which have been reported to influence the properties of the Zn metal anode from various aspects, including altering the solvation sheath of Zn ions, participating in EDL structures, constraining free water by hydrogen

bonding, and inducing preferred texture deposition by adsorption onto the electrode surface. Through parallel comparisons of their effects, I aim to identify efficient characterisation methods, as well as critical parameters and descriptors that can effectively evaluate the performance of organic additives.

6.2 Experimental

6.2.1 Chemicals and materials

All chemicals were used directly without any further treatment. 1 M $ZnSO_4$ electrolytes were prepared by diluting the 2 M electrolytes purchased from Merck Life Science UK Limited. Sulfolane, 1,4-dioxane, N-methyl pyrrolidone, V_2O_5, Zn foil, Ti foil, Cu foil and glass fibre were purchased from Sigma Aldrich. The electrolytes with organic solvents were prepared with a volume ratio of 5 vol%. Celgard 3501 was purchased from Celgard, LLC. LIR 2032-coin cell components were purchased from MTI Corporation.

6.2.2 Electrochemical tests

All coin cells were assembled with a volume of 140 µl electrolyte added and pressed to 1000 psi. The self-supporting V_2O_5 cathode films were prepared by mixing commercial V_2O_5 powder with carbon black and polytetrafluoroethylene in the 6:3:1 mass ratio. Zn||Zn coin cells for XRD testing after cycling were assembled with one layer of glass fibre and one layer of Celgard 3501 as the separator, while other coin cells for long-term cycling and other electrochemical tests were with two layers of glass fibre. The cycling of Zn||V_2O_5 cells was carried out using a Maccor Series 4000, and all other electrochemical measurements were conducted on a Biologic VMP3 system at a temperature of 30 °C.

6.2.3 Characterisations

Raman spectra of electrolytes were measured with Horiba LabRam HR Evolution Spectrometer using a laser of 488 nm. Zn k-edge X-ray absorption fine structure spectroscopy was measured by the easyXAFS300+. Surface morphologies and elemental analysis of Zn electrodes were achieved by a Carl Zeiss Zeiss Merlin field emission analytical SEM coupled with an Oxford instruments Xmax 150 energy dispersive spectrometer. It features a 150 mm^2 silicon drift detector. The qualitative EDX mapping was obtained at an accelerating voltage of 10 kV. The pixel size was 120 nm × 120 nm, and the total acquisition time was 5 minutes. XRD patterns of Zn electrodes were obtained using a Cu source Rigaku SmartLab 3kW diffractometer (wavelength λ = 1.5418 Å).

X-ray photoelectron spectroscopy measurements were performed using a Kratos Axis Ultra DLD spectrometer, with the sample being illuminated using a monochromated Al Kα x-ray source (hν = 1486.7 eV). The core level spectra were recorded using a pass energy of 20 eV, from an analysis area of 300 x 700 microns. Sputtering was performed using Ar^+ ions with an incident energy of 4 keV and a beam spot of 4 x 4 mm on the sample surface.

6.3 Results and discussion

Herein, I choose these three organic additives, Sulfolane (SFL), 1,4-Dioxane (DOE), and N-methyl pyrrolidone (NMP), as representatives for comparison, as shown in *Figure 6.1*. The electrolytes were prepared by incorporating these additives into the $ZnSO_4$ solution to obtain the 1 M $ZnSO_4$ electrolyte with a 5% additive volume ratio. Sulfolane is noted for its ability to facilitate the formation of a beneficial SEI layer on the electrode surface through its decomposition during cycling [275]. 1,4-Dioxane is believed to manipulate both the solvation structure and nucleation behaviour, by its preferred adsorption on the electrode surface, which promotes the exposure

of Zn (002) facets [293]. N-methyl pyrrolidone has been argued to not only assist in reshaping the solvation structure of Zn ions but also to stabilize the hydrogen bond network of water molecules [253].

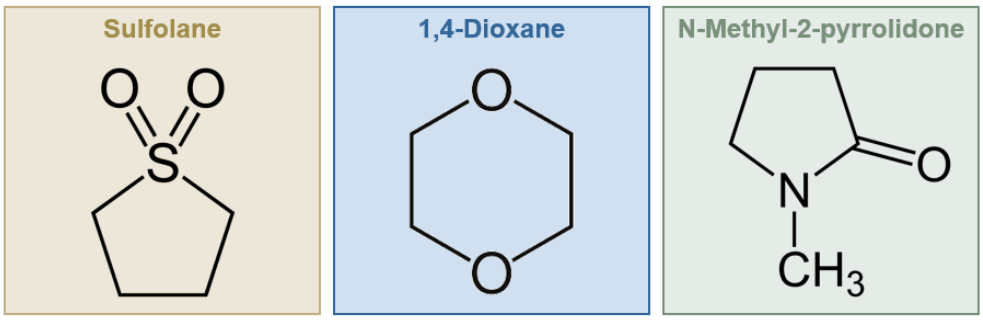


Figure 6.1 Chemical structures of SFL, DOE and NMP.

6.3.1 Effects on the bulk solvation structure of electrolytes

The chemical state of Zn ions and water molecules in the electrolyte plays a vital role in the overall performance of Zn-ion batteries, which is closely related to the Zn dendrite formation and water decomposition reaction, directly impacting the coulombic efficiency and cycling life of the batteries. To investigate changes in the bulk solvation structure, Raman spectroscopy and X-ray absorption fine structure spectroscopy (XAFS) were utilised for different electrolytes. Notable, these three additives demonstrated distinct roles in altering the bulk solvation structures.

The Raman spectra of water and 1 M $ZnSO_4$ electrolyte, both without and with additives in the region of O-H stretching, are shown in *Figure 6.2* respectively, which represents the hydrogen bond state. As given in *Figure 6.2 a*, the area corresponding to the HOH-OH_2 stretching continuously decreased with addition of the Zn salt and SFL, indicating the suppressed activity of water molecules [249,262,384]. In contrast, with addition of NMP and DOE, the intensity of the

HOH-OH_2 stretching area remained unchanged (*Figure 6.2 b*). These results illustrate the different effects of these additives on the reconstruction of water network, stemming from their varying ability to constrain free water molecules.

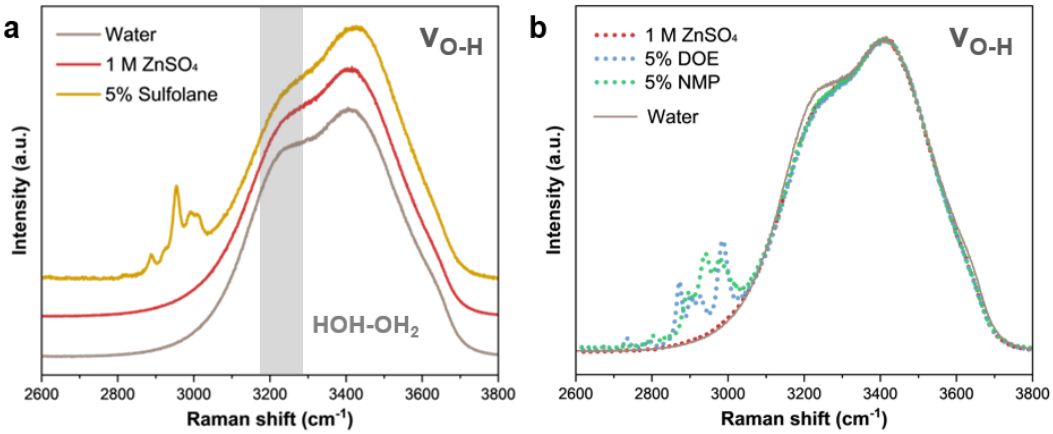


Figure 6.2 Comparisons of Raman spectra in the range of 2600 to 3800 cm^{-2} of (a) water, 1 M $ZnSO_4$ electrolyte without and with SFL, and (b) water, 1 M $ZnSO_4$ electrolyte without and with DOE and NMP.

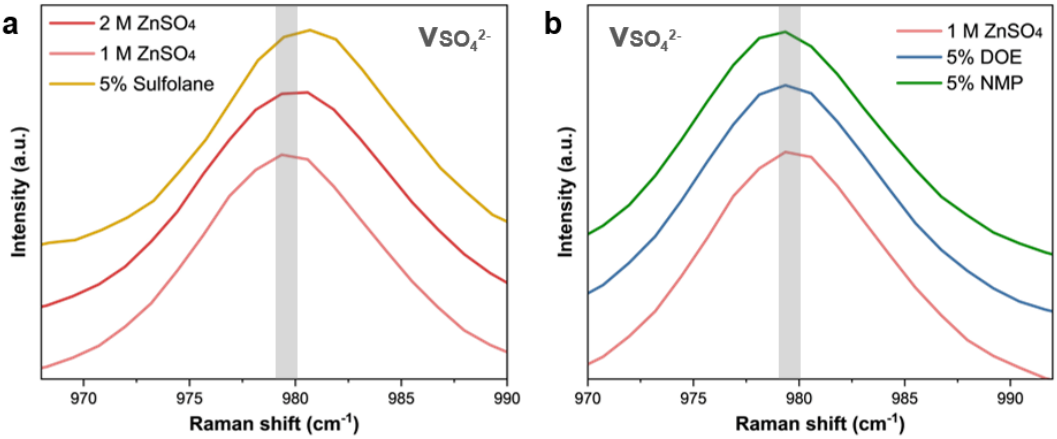


Figure 6.3 Comparisons of Raman spectra in the range of 970 to 990 cm^{-2} of (a) 2 M $ZnSO_4$ electrolyte, 1 M $ZnSO_4$ electrolyte without and with SFL, and (b) 1 M $ZnSO_4$ electrolyte without and with DOE and NMP.

The Raman spectra of electrolytes without and with additives, in the region of the SO_4^{2-} band vibration, are presented in *Figure 6.3*. In aqueous $ZnSO_4$ electrolytes, the interactions between

SO_4^{2-} ions and solvated Zn ions consist of solvent-separated ion pairs (SSIP) and contact ion pairs (CIP) [389,395]. Previous studies have demonstrated that the presence or the increasing percentage of CIP in the solvation structure results in a shift of SO_4^{2-} vibration peak to a higher frequency [395]. As revealed in *Figure 6.3 a*, such a shift was observed in both the 2 M $ZnSO_4$ electrolyte and the 1 M $ZnSO_4$ electrolyte with SFL, indicating a stronger interaction between Zn ions and SO_4^{2-} ions in these electrolytes. Conversely, with the addition of DOE and NMP, the SO_4^{2-} vibration shifted slightly to a lower frequency instead. This could be possibly attributed to the replacement of solvated water molecules by DOE and NMP, which have stronger interaction force with Zn ions, thereby hindering the entry of the SO_4^{2-} ions into the solvation sheath [293].

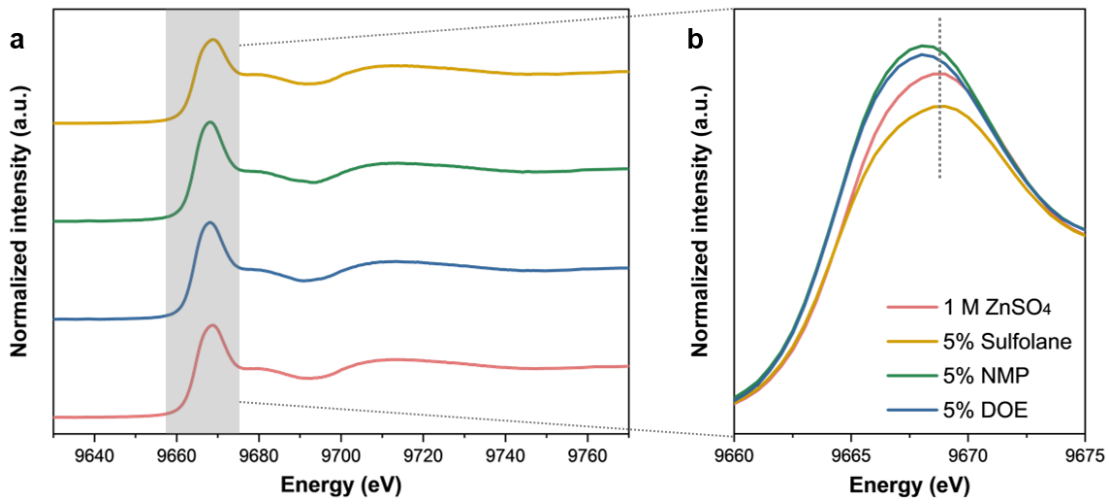


Figure 6.4 (a) The Zn k-edge XANES spectra of electrolytes without and with additives, and (b) the enlarged pre-edge areas.

Additionally, the shift in the Zn k-edge was measured in different electrolytes as well, which provides valuable insights into the oxidation state of Zn ions, thus reflecting their coordination with water molecules and other organic compounds. This evidence can also illustrate the interactions between Zn ions and surrounding atoms, revealing the involvement of organic molecules into the first solvation sheath of Zn ions [399]. The Zn K-edge X-ray absorption near-edge structure (XANES) spectrum of electrolytes without and with additives are shown in *Figure*

6.4. With presence of SFL in the electrolyte, the oxidation state of Zn ions barely changed. Interestingly, however, after adding NMP and DOE, the Zn k-edge both shifted to a lower energy compared to its position in the 1 M $ZnSO_4$ electrolyte. This downward shift of Zn k-edge suggests a higher electron density around Zn ions, which could be due to the electron donation from NMP and DOE, or the constrained electron transfer from Zn to oxygen in the solvated water [400,401].

Both the Raman and XANES results indicate different roles of SFL and NMP/DOE additives in the bulk solvation structure of electrolytes. Specifically, SFL has stronger interactions with free water molecules, while NMP and DOE are more actively integrated into the solvation sheath.

6.3.2 Effects on the EDL adsorption at electrode/electrolyte interfaces

The property of EDL is a vital factor that influence the electrochemical process. To investigate the effects of these organic additives on the EDL structure, the differential capacitance measurements were employed to compare the adsorption of organic molecules at the electrode/electrolyte interface. Differential capacitance is defined as the derivative of the charge stored at the electrode interface with respect to the applied potential, reflecting how the ability of the interface to store electrical charge changes when the electrode potential is varied [233,255,275]. Herein, the differential capacitance was derived from the cyclic voltammetry curves of Zn||Ti coin cells according to previous research [275,402].

As is shown in *Figure 6.5 a*, the capacitance decreased with addition of organic additives, with the electrolyte containing SFL exhibiting the lowest value. This implies the participation of these organic molecules in the EDL structure, where their adsorption at the interfaces inhibits the accumulation of Zn ions onto the electrode surface [255,274,275].

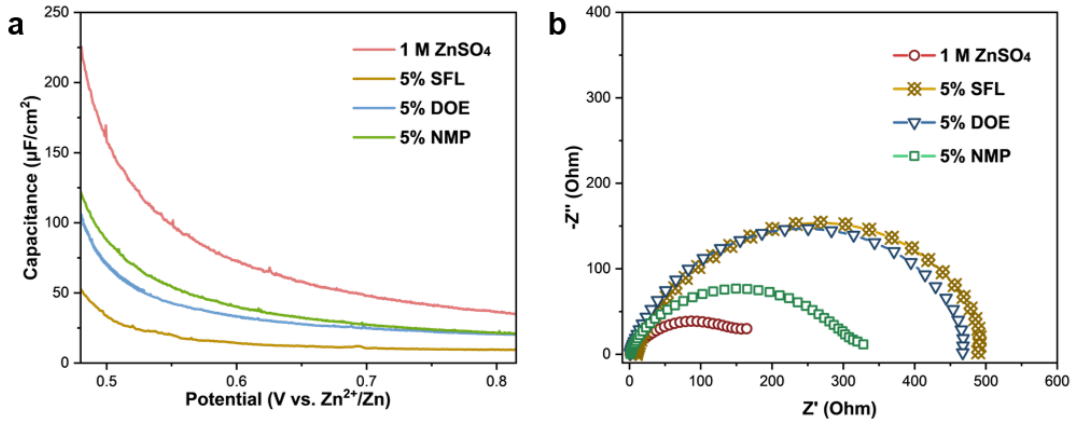


Figure 6.5 (a) The differential capacitance curves of Zn||Ti cells, and (b) the EIS spectra of Zn||Zn cells, collected in electrolytes without and with additives.

Furthermore, the electrochemical impedance spectroscopy (EIS) analysis was performed. The Nyquist plots of Zn||Zn symmetric cells using 1 M $ZnSO_4$ electrolytes without and with a series of organic additives are shown in *Figure 6.5 b*. Introduction of organic compounds resulted in all cells displaying increased charge transfer resistances compared to the electrolyte without additives. This not only confirms their robust adsorption onto the electrode surface but also suggests more sluggish de-solvation processes [251,275,398].

6.3.3 Implications on the nucleation and growth behaviours

The influence of organic additives on the nucleation and growth behaviours was further examined. The voltage profiles of Zn||Zn symmetric cells at a current of 10 mA/cm^2 with a capacity of 2.5 mAh/cm^2 using different electrolytes are shown in *Figure 6.6*. Similarly, all cells with organic additives exhibited higher polarization overpotentials than that using the pure 1 M electrolyte. This observation aligns with the EIS results above, which related to the sluggish interfacial kinetics of the electrode/electrolyte interfaces, indicating the hindered nucleation process [398].

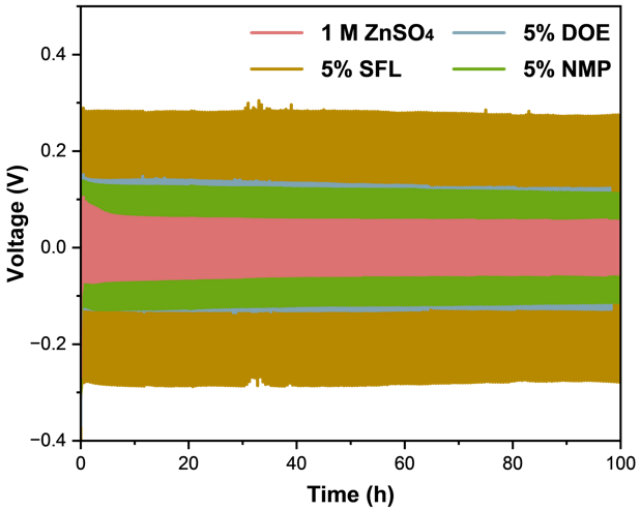


Figure 6.6 The voltage profiles of Zn||Zn cells cycling in the electrolytes without and with additives.

To further investigate the nucleation behaviours in different electrolytes, chronoamperometry tests were also conducted with Zn||Zn coin cells at a fixed potential of -150 mV. As shown in Figure 6.7, in the blank electrolyte, a higher current density was found, indicating random nucleation behaviour and a larger active nucleation area, which can lead to the less compact deposition and dendrite formation. In contrast, with addition of SFL, a more steady and much lower current was recorded, suggesting limited 2D diffusion of Zn ions and more uniform nucleation [191,275,339].

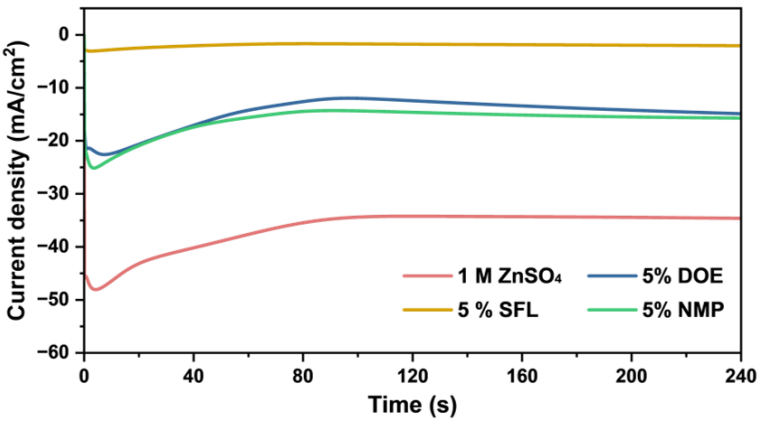


Figure 6.7 The chronoamperometry curves tested at a fixed potential of -150 mV in the electrolyte of $ZnSO_4$ without and with additives.

To better compare the implications on the nucleation and growth, Zn was deposited onto the Zn metal anode in a beaker cell at a current of 10 mA/cm^2 with a capacity of 1 mAh/cm^2 using electrolytes without and with different organic additives. As shown in *Figure 6.8*, the overpotentials of the organic additives followed the same trend as observed in *Figure 6.6*. Nucleation and growth overpotentials were summarised and compared in *Figure 6.9*. The smaller gap between the nucleation and growth overpotentials in the electrolyte with DOE and SFL may suggest a more hindered growth process [187,200,398].

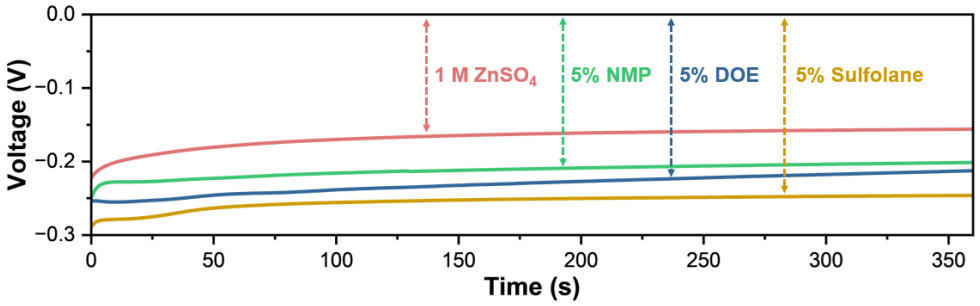


Figure 6.8 The overpotential curves of the deposition process in the electrolytes without and with additives.

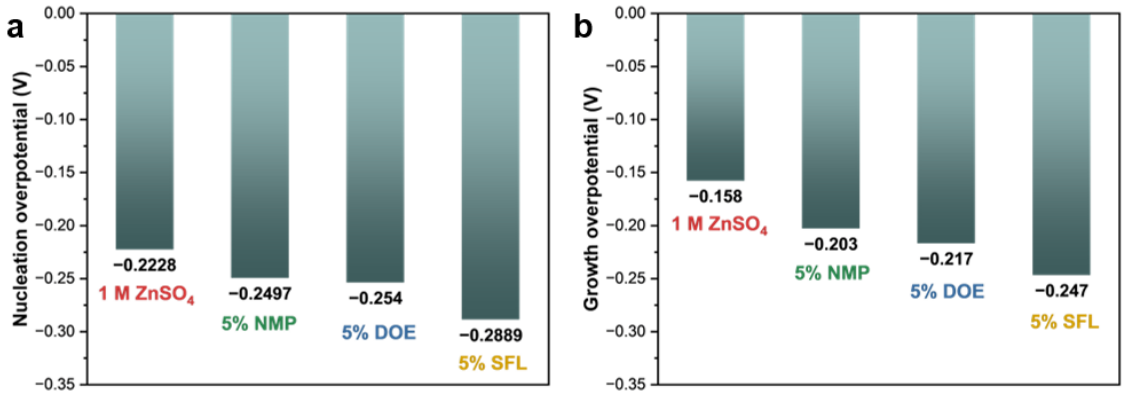


Figure 6.9 Comparison of (a) the nucleation overpotentials and (b) the growth overpotentials in the electrolytes without and with additives.

The morphologies of the Zn electrodes after deposition in various electrolytes were analysed by SEM imaging. As is shown in *Figure 6.10*, Zn flakes in the pure $ZnSO_4$ electrolyte were larger than those in electrolytes with additives, while Zn deposits in the electrolyte with SFL displayed the smallest size and most uniform morphology. Besides, with addition of DOE, a smoother surface with a stacked structure was observed, consistent with the previous report [293]. Moreover, on the surface of the Zn deposits in the electrolytes with NMP, small Zn cubes were mixed with larger and brighter flakes, which are likely byproducts or other less conductive residuals.

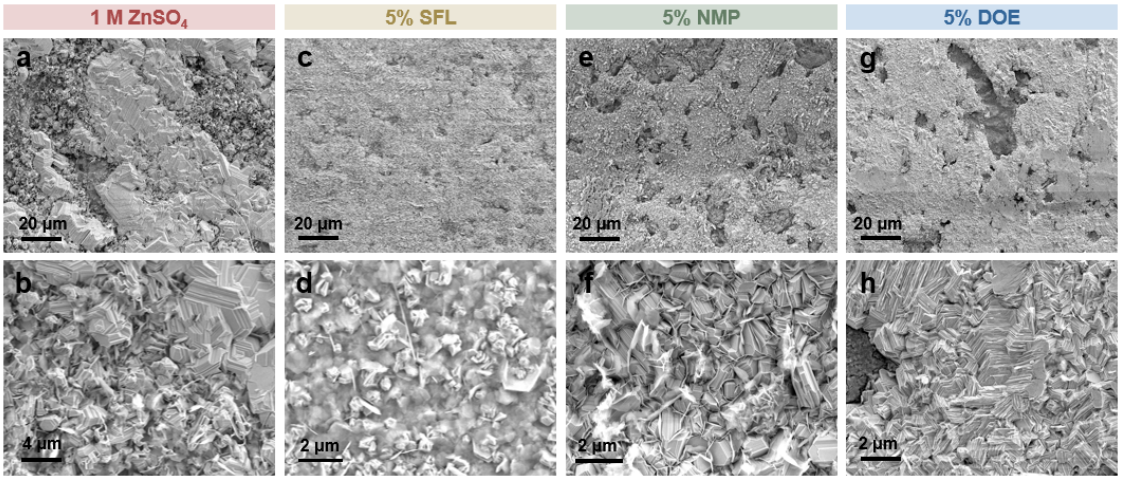


Figure 6.10 The SEM images of Zn deposits in the (a, b) pure 1 M $ZnSO_4$ electrolyte, and 1 M $ZnSO_4$ electrolyte with (c, d) 5% SFL, (e, f) 5% NMP, and (g, h) 5% DOE.

The improved uniformity of deposition was further confirmed by the EDX elemental analysis. The raw EDX spectra of the two electrodes with Zn deposition from the 1 M $ZnSO_4$ electrolyte without and with 5% SFL, are included in *Figure A7* and *Figure A8* in the appendix, where similar elemental ratios are observed. However, as shown in the EDX mapping in *Figure 6.11*, on the surface of the electrode in the pure $ZnSO_4$ electrolyte, obvious accumulation of sulphur and oxygen was noted around the Zn deposits, whereas with the addition of SFL, the elemental distribution on the electrode surface was more homogeneous, with no apparent aggregation of byproducts or other residuals.

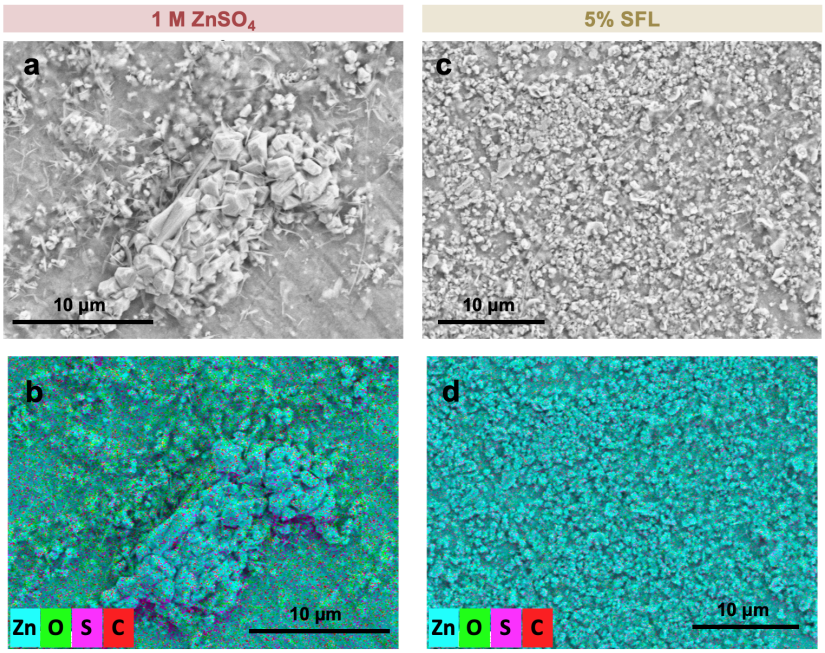


Figure 6.11 The SEM images and corresponding EDX mapping results of the electrode surface in the (a, b) 1 M $ZnSO_4$ electrolyte and (c, d) 1 M $ZnSO_4$ electrolyte with 5% SFL.

6.3.4 Comparison of compositional distribution over the Zn metal anode

To further evaluate the influence of organic additives in other aspects, such as the formation of byproducts and SEI layers, the XPS depth profiles of Zn metal anodes after deposition in various electrolytes at a current density of 10 mA/cm^2 with a capacity of 2 mAh/cm^2 were collected and compared. The starting surface composition of Zn metal anodes is summarised in *Figure 6.12*. Although the overall elemental composition of different electrodes before sputtering was similar, the ratio of Zn in the electrode from the electrolyte with SFL was slightly higher than in the others, indicating fewer side products or residuals left on the surface.

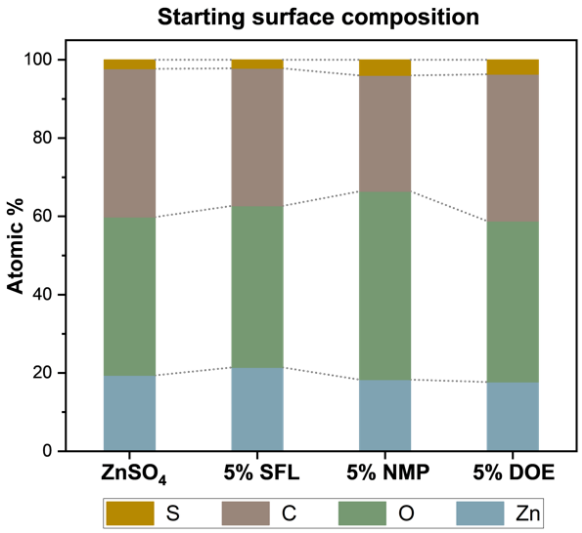


Figure 6.12 Comparison of the initial compositional ratios in the deposits from electrolytes without and with additives before sputtering.

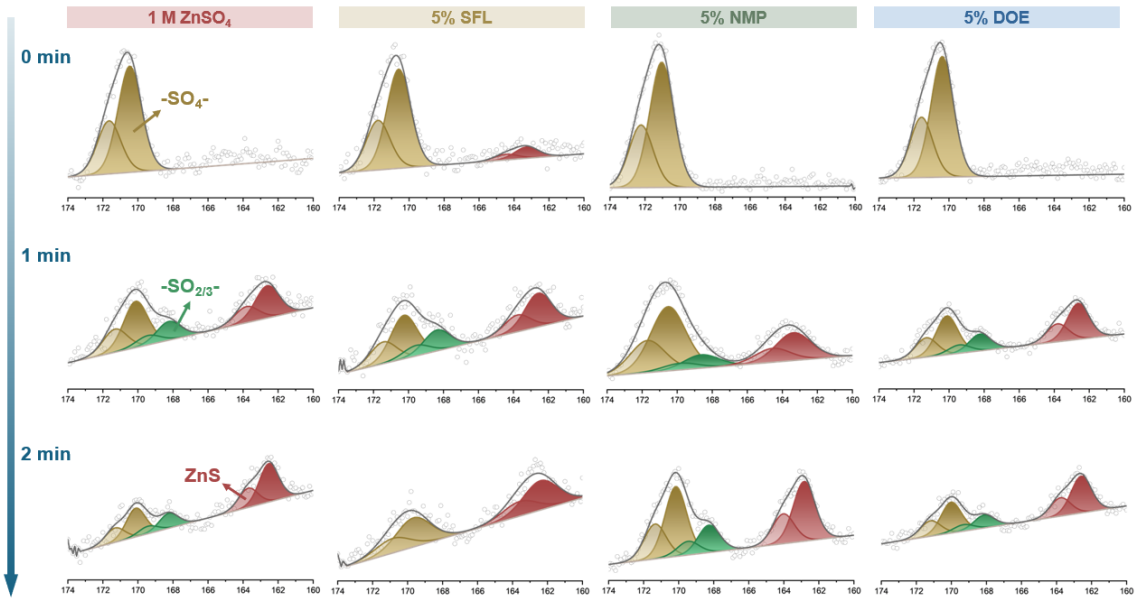


Figure 6.13 The XPS depth profiles of S 2p spectra of the deposits in the electrolytes without and with additives.

The depth profiles of S 2p spectrum are shown in *Figure 6.13*. All the samples demonstrated the existence of -SO_4- species both before and after sputtering, which could be resulted from the salt residues or ZHS byproducts. However, it should be noted that for the Zn metal anode in the electrolyte containing SFL, the presence of trace ZnS was observed on the surface of the

electrode before sputtering. After sputtering, the depth profiles revealed an increasing ratio of ZnS across all samples. Previous studies have confirmed that the formation of ZnS on the Zn surface after cycling could be ascribed to the reduction of SO_4^{2-} ions, accompanied by the hydrogen evolution [275,403]. The presence of other -$SO_{2/3}$- species is likely related to the derivation of the SO_4^{2-} ions as well [404].

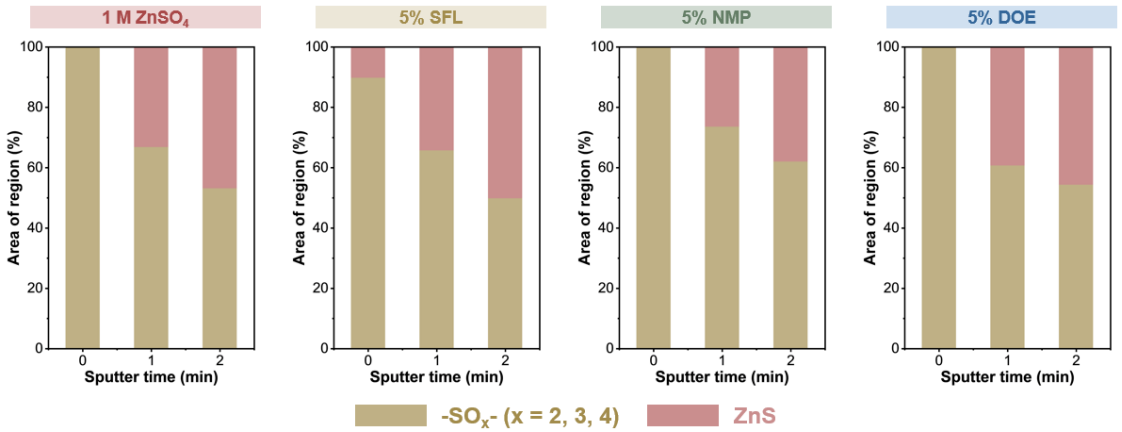


Figure 6.14 Comparison of the -SO_x- and ZnS ratios of the deposits in the electrolytes without and with additives, calculated from the S 2p spectra.

The ratios of the -SO_x- and ZnS species on the electrodes are compared in *Figure 6.14*. Generally, the electrodes from the pure electrolyte and those with SFL and DOE showed similar -SO_x-/ZnS ratios, while the electrode surface with addition of NMP showed an increased presence of -SO_x- species, possibly from the byproducts mixed with Zn deposits. It should also be noted that in the case of the pure $ZnSO_4$ electrolyte and with additional DOE, the Zn deposits and byproducts were not homogeneously distributed, as evidenced by SEM images in *Figure 6.10*. This could potentially lead to misleading interpretations of the composition quantifications given by the localized XPS results.

Previous research has argued that more ZnS is generated on the electrode surface in the electrolyte with SFL than in the pure $ZnSO_4$ electrolyte, due to the electrochemical reduction of

SFL during cycling, resulting in the formation of a ZnS-rich SEI [275,404]. However, from my results, it is ambiguous to assume that there is a ZnS-rich SEI is forming on the electrode surface with addition of SFL, but the presence of ZnS before sputtering could suggest the uniformity of the deposits and participation of SFL in the de-solvation process.

6.3.5 Contributions to the suppression of HER and corrosion

To further investigate the effects of organic additives on suppressing HER and corrosion, LSV measurements were performed in the 1 M $ZnSO_4$ electrolyte without and with additives. As shown in *Figure 6.15 a*, the introduction of organic additives resulted in a much lower hydrogen evolution current density compared to the pure $ZnSO_4$ electrolyte. In particular, the current response at -0.15 V in the electrolyte with SFL was as low as around 2 mA/cm^2, indicating the reducing activity of water.

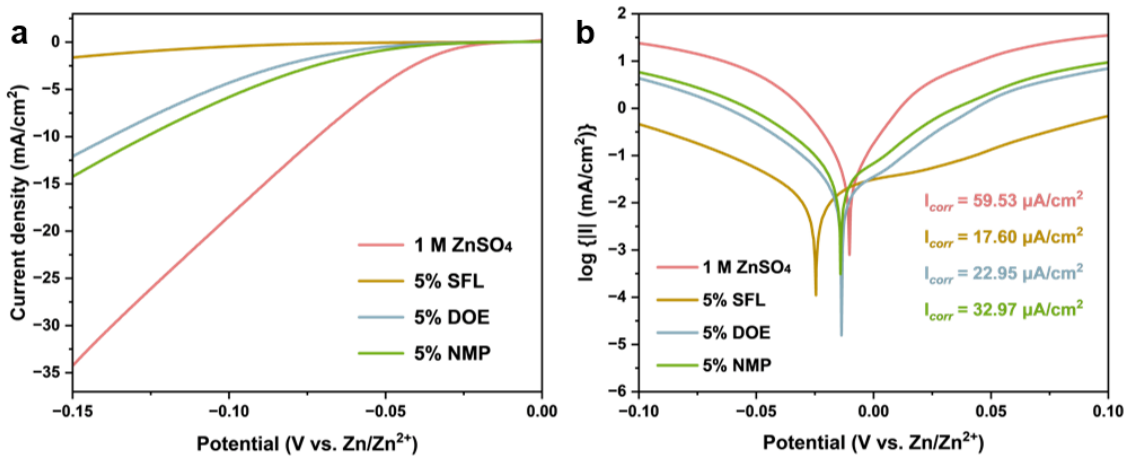


Figure 6.15 (a) The LSV curves tested at a scan rate of 10 mV/s and (b) the Tafel plots of the electrolytes without and with additives.

Tafel plots were also constructed to determine the corrosion rates in different electrolytes (*Figure 6.15 b*). The exchange current densities in the electrolytes with all three additives were lower than in the pure 1 M $ZnSO_4$ electrolyte, with the electrolyte containing SFL exhibiting the

lowest value. The enhanced ability to suppress HER and side reactions by SFL can be attributed to its preferred adsorption on the electrode surface and stronger interactions with free water molecules, while in electrolytes with NMP and DOE, reduced water decomposition can be explained by their participation in the solvation sheath, thus decreasing the possibility of water reduction during the de-solvation process [243,253,254,364,389].

6.3.6 Further concerns of organic additive in overall performance of Zn-ion batteries

While the replacement of solvated water in the solvation structure of Zn ions or enhanced interactions with free water molecules are believed to improve the stability of the Zn metal anode, the introduction of organic additives into electrolytes typically results in increased polarization potential. This increase may consequently trigger HER and side reactions. This dilemma warrants careful consideration. For instance, despite using electrolytes with organic additives, the formation of ZHS on the Zn metal anodes was still observed after cycling in coin cells at a current density of 10 mA/cm^2 with a capacity of 2 mAh/cm^2, as depicted in *Figure 6.16*.

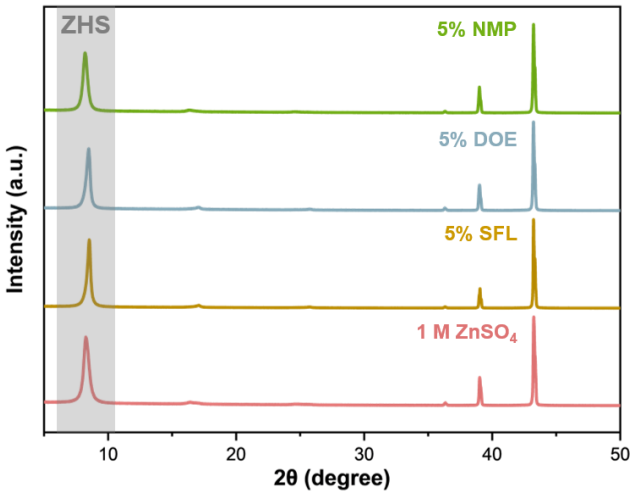


Figure 6.16 The XRD patterns of Zn metal anodes after 30 cycles using electrolytes without and with additives.

Moreover, as illustrated in *Figure 6.17*, the cycling stability and capacity retention of the Zn||V_2O_5 full cell employing the SFL electrolyte were significantly below expectations, even when compared to those using the pure $ZnSO_4$ electrolyte. This could be possibly attributed to the sluggish de-solvation process and stronger interactions between SFL and water molecules, which hinder the insertion of Zn ions and protons to the cathode structure [215,280,398].

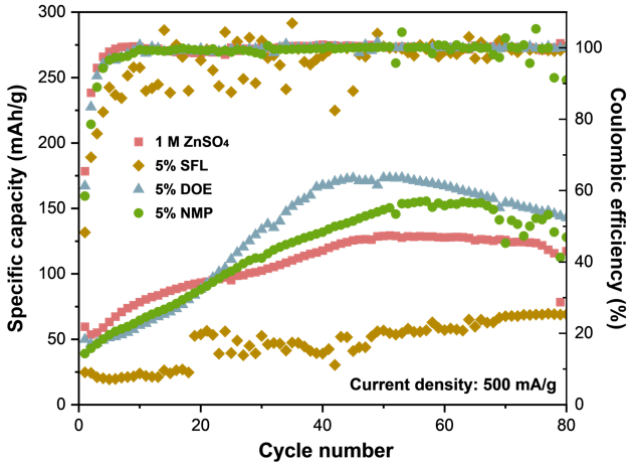


Figure 6.17 The cycling performances for Zn||V_2O_5 coin cells using the electrolytes without and with additives.

6.4 Conclusion

In this chapter, the implications of several organic additives, including SFL, DOE, and NMP, on the bulk solvation structures, EDL properties, nucleation and deposition behaviours and suppression of side reactions, were comparatively investigated. It was found that the roles of SFL in stabilizing the Zn metal anode are distinct compared to those of NMP and DOE. Both Raman and XANES results confirmed the SFL molecules exhibited stronger interactions with the bulk water network, whereas NMP and DOE were more involved in the solvation sheath of Zn ions. According to a series of electrochemical test, SFL also demonstrated strong adsorption onto the electrode

surface, facilitating uniform deposition and constraining byproduct formation. Despite their similar cyclic chemical structures, these additive molecules exhibit significant variations in their influence on electrolyte properties and electrochemical performances. The comparisons derived from above the experimental studies are summarised in *Table 6.1*.

Table 6.1 Comparison of additive effects on various aspects of electrolyte properties.

Free water constraint	**SFL > DOE ≈ NMP**
Solvation sheath involvement	**DOE ≈ NMP > SFL**
EDL involvement	**SFL >> DOE > NMP**
Overpotential	**SFL >> DOE > NMP**
Nucleation uniformity	**SFL >> DOE > NMP**
SEI forming capability	**SFL > DOE ≈ NMP**
Corrosion resistance	**SFL >> DOE > NMP**

It is worth noting that an increase in polarization potential was observed in all cases of organic additives, with SFL exhibiting the highest value. This suggests a higher energy barrier for the de-solvation process, due to their adsorption on the electrode surface and involvement in the solvation shell [398,405,406]. Despite the suppression of HER and corrosion current densities, such elevated polarization can, in turn, trigger side reactions during extended cycling periods [398]. Moreover, the potential effects of these organic additives on the cycling performance of full cells and their compatibility with cathode materials should be carefully evaluated in future studies.

In future work, I plan to further investigate the role of these organic additives in directing the deposition behaviour of Zn using in situ liquid cell TEM, which will enable detailed insights into

how alterations in the solvation structures and EDL properties, induced by various organic additives, affect nucleation and growth of Zn deposits. This approach promises to yield robust and direct evidence clarifying the specific roles of different additives, which have long been challenging to delineate.

Chapter 7 Conclusion and future work

Aqueous Zn-ion batteries are promising energy storage systems due to their advantages in cost and safety. However, their practical utilisation is still hindered by several challenges. Zn metal is considered the ideal anode material, yet it still faces issues such as dendrite formation, HER and corrosion that remain to be solved. Modifying electrolytes by adding additives is recognized as a straightforward and effective strategy to address these problems associated with the Zn metal anode. In this thesis, with the help of in situ electrochemical liquid cell TEM, I have investigated the degradation process of the Zn metal anode and explored the underlying mechanisms by which additives mitigate these issues.

In Chapter 4, I explored the self-corrosion process of Zn during the battery's rest period. I observed significant capacity loss due to the self-dissolution behaviour of Zn before the formation of ZHS byproducts, using liquid cell TEM. The initial pH value of the electrolyte was identified as a crucial factor influencing the corrosion process during rest. In an acidic electrolyte environment, Zn metal undergoes a more severe self-dissolution process first, which consumes H^+ ions and leaves excess OH^- ions, leading to hydrogen evolution and a local pH increase. The accumulation of the OH^- ions then fosters the formation of a ZHS corrosion byproduct layer and morphological changes to the anode surface. The addition of $Zn(OAc)_2$ as a pH regulator effectively mitigated this self-dissolution behaviour and slowing down the formation of ZHS byproducts, confirmed by both in situ liquid cell TEM experiments and electrochemical tests. These results elucidated the underlying mechanisms for the self-corrosion of Zn in the mild acidic environment, emphasising not only the importance of the initial electrolyte pH for future electrolyte modification research but also the necessity to consider the feasibility of using excess Zn metal in Zn-ion batteries.

In Chapter 5, the process of Zn dendrite formation and alleviation was studied by in situ liquid TEM. I demonstrated that electrolyte additive cations, introduced to form an electrostatic shielding layer to prevent dendrite growth, do not operate via the same mechanism as proposed for Li anode batteries. My observations revealed that the additive's suppression of dendrite growth instead occurs by preventing secondary Zn nucleation on Zn (100) faces and promoting deposition on Zn (002) faces. This process results in stockier block morphologies, culminating in a denser, smoother anode surface after charging. These findings underscore the significance of anisotropic Zn crystallography as a critical parameter when adapting mechanistic explanations from Li battery chemistry.

In Chapter 6, I systematically examined the effects of several organic additives on Zn-ion battery properties, including bulk solvation structures, EDL characteristics, and nucleation behaviours. SFL stood out for its strong interactions with the water network, unlike NMP and DOE, which mainly affected the solvation sheath. Despite their similar chemical structures, these additives significantly varied in their impact on electrolyte properties and electrochemical performance. Furthermore, all additives increased polarization potential, particularly SFL, suggesting a higher energy barrier for the de-solvation process. This increase might trigger side reactions during extended cycling. The study highlights the necessity for more effective descriptors to select organic additives, and emphasises the need for careful evaluation of these additives' effects on full cell cycling performance and cathode material compatibility.

In future work, to further explore degradation mechanisms of Zn-ion batteries via in situ liquid cell TEM, several aspects as follow can be considered:

(1) Building on the research in Chapter 6, the roles of organic additives in directing Zn nucleation behaviours could be further investigated using in situ liquid cell TEM. This will help to clarify the complexity of their effects on solvation and EDL structures.

(2) Despite significant efforts to understand and enhance the performance of aqueous Zn-ion batteries, interest in 'beyond aqueous' electrolytes has surged recently, driven by the need to avoid intrinsic issues such as HER caused by the presence of water. However, research on organic Zn-ion battery systems using in situ liquid cell TEM remains limited, which is crucial for identifying potential differences between aqueous and organic systems. Future work could include comparative research on the degradation of Zn anodes in organic electrolytes, while potential beam damage on organic compounds during TEM experiments should be carefully assessed beforehand.

(3) The influence of Zn metal anode modification strategies on the cathode side, such as electrolyte engineering, could be further explored. For example, pH adjustments and solvation regulations improve Zn anode performance. However, how they affect cathode materials has often been overlooked in many current studies, yet it is of significant importance to improve the overall performance of Zn-ion batteries. For example, the investigation on the degradation progress of cathode materials in Zn-ion batteries by in situ liquid cell TEM could be achieved via pre-deposition of manganese oxide on the Pt electrode of the liquid cell chip, which enable following in situ observation of the cathode material behaviours under TEM.

(4) The configuration of the liquid cell TEM setup could be optimised to enhance imaging quality and introduce advanced capabilities, such as the electron energy loss spectroscopy, for conducting elemental analysis. This would provide deeper insights into the electrochemical reactions.

Appendix

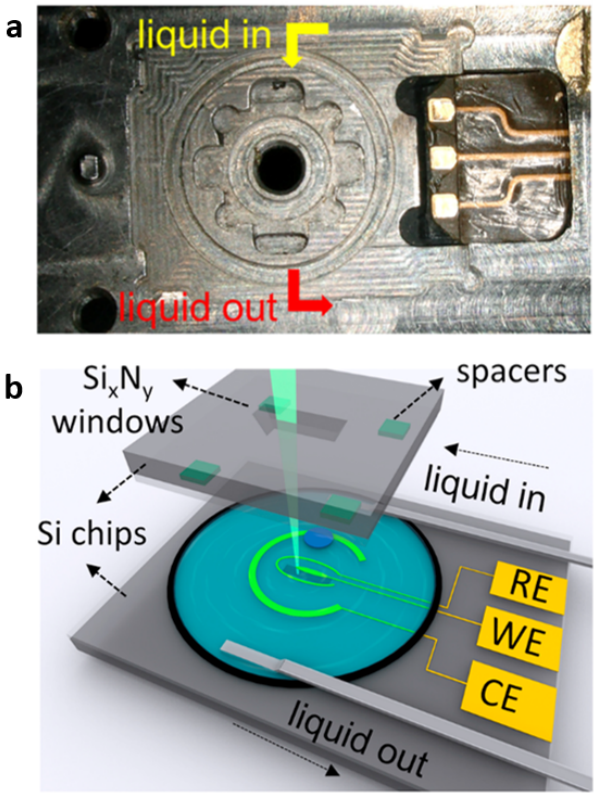


Figure A1. (a) Optical microscope image of the in situ liquid cell TEM holder tip, and (b) corresponding schematic illustration, showing the configuration of chips and the flow pathway of liquids [407]. Reproduced with permission. Copyright 2018 Elsevier.

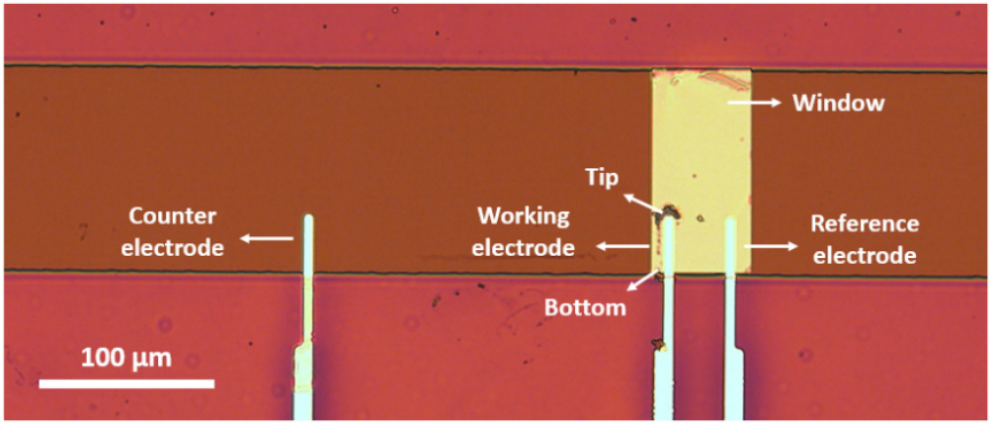


Figure A2. Optical microscope image of the large chip used for in situ liquid cell TEM experiments, illustrating the layout, including the patterned window and three electrodes.

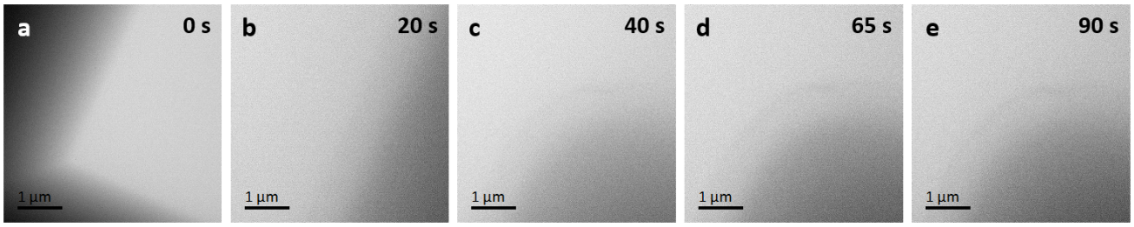


Figure A3. Dose test results for in situ liquid cell TEM experiments discussed in Chapter 4 (1 M $ZnSO_4$ electrolyte). The window of the chip was exposed to the electron beam, and the field of view was moved around to examine potential beam-induced changes. (a) The corner of the window. (b) The side of the Pt working electrode. (c-e) The tip of the Pt working electrode.

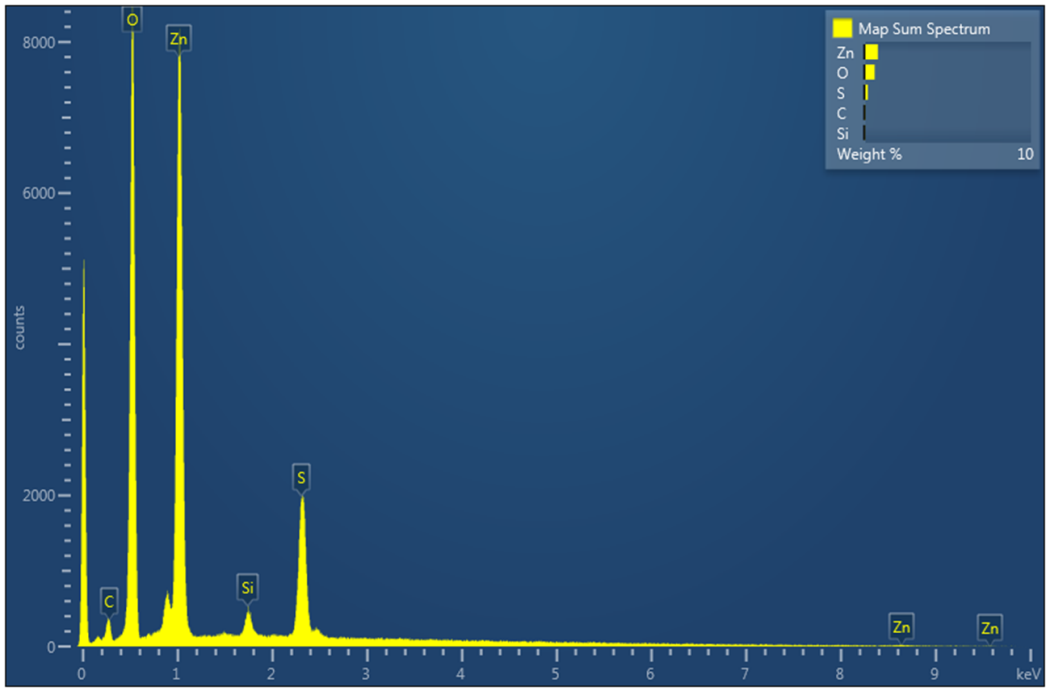


Figure A4. Raw EDX spectrum of the Ti foil with Zn deposits after resting in a vial with 1 M $ZnSO_4$ electrolyte for 40 hours.

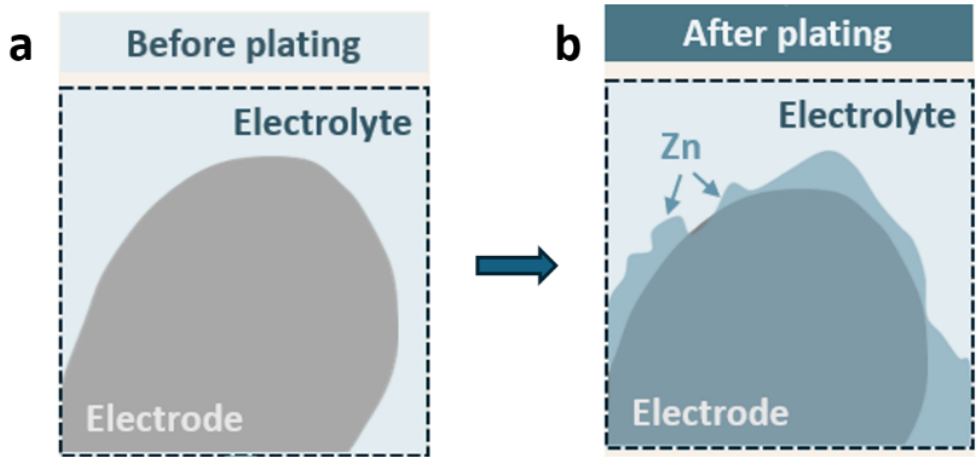


Figure A5. Schematic illustration of the field of view during the plating process in liquid cell TEM experiments. (a) The Pt working electrode immersed in the electrolyte before plating, showing a slightly darker contrast compared to the electrolyte. (b) The Pt working electrode is covered by Zn deposits after plating, which show darker contrast than both the Pt electrode and the electrolyte.

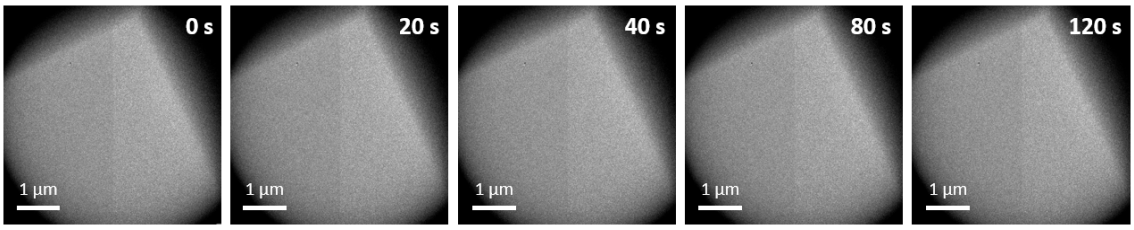


Figure A6. Dose test results for in situ liquid cell TEM experiments discussed in Chapter 5 (2 M $ZnSO_4$ electrolyte). The corner of the window was exposed to the electron beam, and the resulting potential beam damage to the electrolyte was examined.

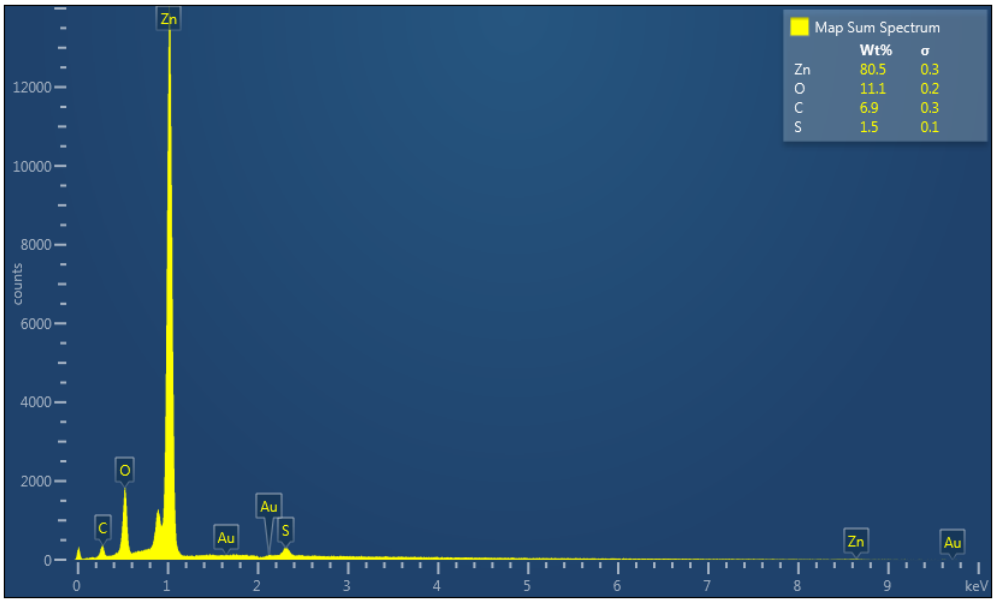


Figure A7. Raw EDX spectrum of the electrode surface with Zn deposits from the 1 M $ZnSO_4$ electrolyte.

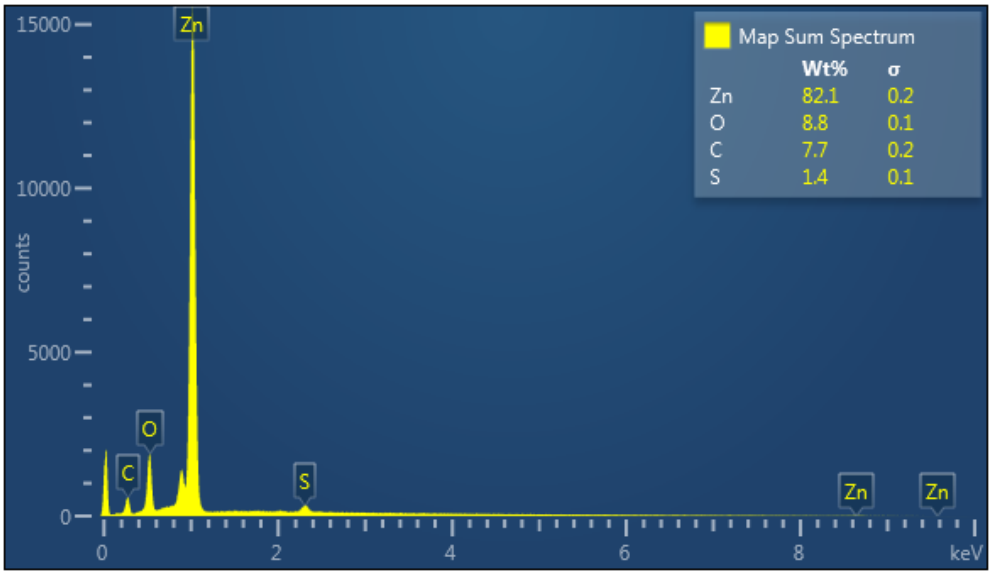


Figure A8. Raw EDX spectrum of the electrode surface with Zn deposits from the 1 M $ZnSO_4$ electrolyte with 5% SFL.

References

1. D. J. Davidson. Exnovating for a renewable energy transition. *Nat. Energy* **4**, 254–256 (2019).

2. M. S. Whittingham. History, Evolution, and Future Status of Energy Storage. *Proc. IEEE* **100**, 1518–1534 (2012).

3. J. B. Goodenough. Evolution of Strategies for Modern Rechargeable Batteries. *Acc. Chem. Res.* **46**, 1053–1061 (2013).

4. H. Kim, *et al.* Liquid Metal Batteries: Past, Present, and Future. *Chem. Rev.* **113**, 2075–2099 (2013).

5. M. R. Palacín. Recent advances in rechargeable battery materials: a chemist's perspective. *Chem. Soc. Rev.* **38**, 2565–2575 (2009).

6. Z. Zhu, *et al.* Rechargeable Batteries for Grid Scale Energy Storage. *Chem. Rev.* **122**, 16610–16751 (2022).

7. Y. Liang, *et al.* A review of rechargeable batteries for portable electronic devices. *InfoMat* **1**, 6–32 (2019).

8. P. P. Lopes & V. R. Stamenkovic. Past, present, and future of lead–acid batteries. *Science* **369**, 923–924 (2020).

9. V. Arun, *et al.* Review on Li-Ion Battery vs Nickel Metal Hydride Battery in EV. *Adv. Mater. Sci. Eng.* **2022**, 7910072 (2022).

10. S. K. Dhar, *et al.* Nickel/metal hydride technology for consumer and electric vehicle batteries—a review and up-date. *J. Power Sources* **65**, 1–7 (1997).

11. J. B. Goodenough & K.-S. Park. The Li-Ion Rechargeable Battery: A Perspective. *J. Am. Chem. Soc.* **135**, 1167–1176 (2013).

12. M. Li, J. Lu, Z. Chen & K. Amine. 30 Years of Lithium-Ion Batteries. *Adv. Mater.* **30**, 1800561 (2018).

13. V. Etacheri, R. Marom, R. Elazari, G. Salitra & D. Aurbach. Challenges in the development of advanced Li-ion batteries: a review. *Energy Environ. Sci.* **4**, 3243–3262 (2011).

14. X.-B. Cheng, C.-Z. Zhao, Y.-X. Yao, H. Liu & Q. Zhang. Recent Advances in Energy Chemistry between Solid-State Electrolyte and Safe Lithium-Metal Anodes. *Chem* **5**, 74–96 (2019).

15. K. B. Hatzell, *et al.* Challenges in Lithium Metal Anodes for Solid-State Batteries. *ACS Energy Lett.* **5**, 922–934 (2020).

16. Y. Tian, *et al.* Promises and Challenges of Next-Generation "Beyond Li-ion" Batteries for Electric Vehicles and Grid Decarbonization. *Chem. Rev.* **121**, 1623–1669 (2021).

17. K. Kubota, M. Dahbi, T. Hosaka, S. Kumakura & S. Komaba. Towards K-Ion and Na-Ion Batteries as "Beyond Li-Ion". *Chem. Rec.* **18**, 459–479 (2018).

18. Y. Gao, Z. Pan, J. Sun, Z. Liu & J. Wang. High-Energy Batteries: Beyond Lithium-Ion and Their Long Road to Commercialisation. *Nano-Micro Lett.* **14**, 94 (2022).

19. J. B. Goodenough. How we made the Li-ion rechargeable battery. *Nat. Electron.* **1**, 204–204 (2018).

20. J. B. Goodenough. Changing Outlook for Rechargeable Batteries. *ACS Catal.* **7**, 1132–1135 (2017).

21. M. S. Whittingham. Electrical Energy Storage and Intercalation Chemistry. *Science* **192**, 1126–1127 (1976).

22. K. Mizushima, P. C. Jones, P. J. Wiseman & J. B. Goodenough. Li_xCoO_2 (0<x<-1): A new cathode material for batteries of high energy density. *Mater. Res. Bull.* **15**, 783–789 (1980).

23. A. Yoshino. The Birth of the Lithium-Ion Battery. *Angew. Chem. Int. Ed.* **51**, 5798–5800 (2012).

24. G. Pistoia. *Lithium-Ion Batteries: Advances and Applications* (2013).

25. J. Xu, *et al.* High-Energy Lithium-Ion Batteries: Recent Progress and a Promising Future in Applications. *Energy Environ. Mater.* **6**, e12450 (2023).

26. A. Masias, J. Marcicki & W. A. Paxton. Opportunities and Challenges of Lithium Ion Batteries in Automotive Applications. *ACS Energy Lett.* **6**, 621–630 (2021).

27. J. Asenbauer, *et al.* The success story of graphite as a lithium-ion anode material – fundamentals, remaining challenges, and recent developments including silicon (oxide) composites. *Sustain. Energy Fuels* **4**, 5387–5416 (2020).

28. L. Zhao, *et al.* Revisiting the Roles of Natural Graphite in Ongoing Lithium-Ion Batteries. *Adv. Mater.* **34**, 2106704 (2022).

29. S. J. An, *et al.* The state of understanding of the lithium-ion-battery graphite solid electrolyte interphase (SEI) and its relationship to formation cycling. *Carbon* **105**, 52–76 (2016).

30. D. Aurbach, B. Markovsky, I. Weissman, E. Levi & Y. Ein-Eli. On the correlation between surface chemistry and performance of graphite negative electrodes for Li ion batteries. *Electrochimica Acta* **45**, 67–86 (1999).

31. J.-Y. Li, *et al.* Research progress regarding Si-based anode materials towards practical application in high energy density Li-ion batteries. *Mater. Chem. Front.* **1**, 1691–1708 (2017).

32. M. N. Obrovac & L. J. Krause. Reversible Cycling of Crystalline Silicon Powder. *J. Electrochem. Soc.* **154**, A103 (2006).

33. M. Ashuri, Q. He & L. L. Shaw. Silicon as a potential anode material for Li-ion batteries: where size, geometry and structure matter. *Nanoscale* **8**, 74–103 (2016).

34. W.-R. Liu, *et al.* Effect of electrode structure on performance of Si anode in Li-ion batteries: Si particle size and conductive additive. *J. Power Sources* **140**, 139–144 (2005).

35. H. Wu & Y. Cui. Designing nanostructured Si anodes for high energy lithium ion batteries. *Nano Today* **7**, 414–429 (2012).

36. P. Li, *et al.* Recent progress on silicon-based anode materials for practical lithium-ion battery applications. *Energy Storage Mater.* **15**, 422–446 (2018).

37. L. Wang, *et al.* Recent advances in interface engineering of silicon anodes for enhanced lithium-ion battery performance. *Energy Storage Mater.* **66**, 103243 (2024).

38. E. Feyzi, *et al.* A comprehensive review of silicon anodes for high-energy lithium-ion batteries: Challenges, latest developments, and perspectives. *Energy* **5**, 100176 (2024).

39. Y. Zhao, *et al.* Recent Developments and Understanding of Novel Mixed Transition-Metal Oxides as Anodes in Lithium Ion Batteries. *Adv. Energy Mater.* **6**, 1502175 (2016).

40. M. Zheng, *et al.* Hierarchically Nanostructured Transition Metal Oxides for Lithium-Ion Batteries. *Adv. Sci.* **5**, 1700592 (2018).

41. M. V. Reddy, G. V. Subba Rao & B. V. R. Chowdari. Metal Oxides and Oxysalts as Anode Materials for Li Ion Batteries. *Chem. Rev.* **113**, 5364–5457 (2013).

42. Z. Cheng, *et al.* Fundamental Understanding and Facing Challenges in Structural Design of Porous Si-Based Anodes for Lithium-Ion Batteries. *Adv. Funct. Mater.* **33**, 2301109 (2023).

43. N. Mahmood, T. Tang & Y. Hou. Nanostructured Anode Materials for Lithium Ion Batteries: Progress, Challenge and Perspective. *Adv. Energy Mater.* **6**, 1600374 (2016).

44. N. Kim, Y. Kim, J. Sung & J. Cho. Issues impeding the commercialization of laboratory innovations for energy-dense Si-containing lithium-ion batteries. *Nat. Energy* **8**, 921–933 (2023).

45. J. W. Fergus. Recent developments in cathode materials for lithium ion batteries. *J. Power Sources* **195**, 939–954 (2010).

46. A. Manthiram. A reflection on lithium-ion battery cathode chemistry. *Nat. Commun.* **11**, 1550 (2020).

47. F. Lin, *et al.* Surface reconstruction and chemical evolution of stoichiometric layered cathode materials for lithium-ion batteries. *Nat. Commun.* **5**, 3529 (2014).

48. S.-T. Myung, *et al.* Nickel-Rich Layered Cathode Materials for Automotive Lithium-Ion Batteries: Achievements and Perspectives. *ACS Energy Lett.* **2**, 196–223 (2017).

49. Y. Huang, *et al.* Lithium Manganese Spinel Cathodes for Lithium-Ion Batteries. *Adv. Energy Mater.* **11**, 2000997 (2021).

50. Z. Gong & Y. Yang. Recent advances in the research of polyanion-type cathode materials for Li-ion batteries. *Energy Environ. Sci.* **4**, 3223–3242 (2011).

51. Y. Lyu, *et al.* An Overview on the Advances of $LiCoO_2$ Cathodes for Lithium-Ion Batteries. *Adv. Energy Mater.* **11**, 2000982 (2021).

52. M. D. Radin, *et al.* Narrowing the Gap between Theoretical and Practical Capacities in Li-Ion Layered Oxide Cathode Materials. *Adv. Energy Mater.* **7**, 1602888 (2017).

53. J. Zheng, *et al.* Li- and Mn-Rich Cathode Materials: Challenges to Commercialization. *Adv. Energy Mater.* **7**, 1601284 (2017).

54. X. Wang, Y.-L. Ding, Y.-P. Deng & Z. Chen. Ni-Rich/Co-Poor Layered Cathode for Automotive Li-Ion Batteries: Promises and Challenges. *Adv. Energy Mater.* **10**, 1903864 (2020).

55. W.-J. Zhang. Structure and performance of $LiFePO_4$ cathode materials: A review. *J. Power Sources* **196**, 2962–2970 (2011).

56. A. S. Andersson, J. O. Thomas, B. Kalska & L. Häggström. Thermal Stability of $LiFePO_4$ - Based Cathodes. *Electrochem. Solid-State Lett.* **3**, 66 (1999).

57. L.-X. Yuan, *et al.* Development and challenges of $LiFePO_4$ cathode material for lithium-ion batteries. *Energy Environ. Sci.* **4**, 269–284 (2011).

58. J. Li & Z.-F. Ma. Past and Present of $LiFePO_4$: From Fundamental Research to Industrial Applications. *Chem* **5**, 3–6 (2019).

59. K. Xu. Electrolytes and Interphases in Li-Ion Batteries and Beyond. *Chem. Rev.* **114**, 11503–11618 (2014).

60. G. E. Blomgren. Liquid electrolytes for lithium and lithium-ion batteries. *J. Power Sources* **119–121**, 326–329 (2003).

61. L. O. Valøen & J. N. Reimers. Transport Properties of $LiPF_6$-Based Li-Ion Battery Electrolytes. *J. Electrochem. Soc.* **152**, A882 (2005).

62. H. Yang, G. V. Zhuang & P. N. Ross. Thermal stability of $LiPF_6$ salt and Li-ion battery electrolytes containing LiPF6. *J. Power Sources* **161**, 573–579 (2006).

63. K. Kim, *et al.* Understanding the thermal instability of fluoroethylene carbonate in $LiPF_6$-based electrolytes for lithium ion batteries. *Electrochimica Acta* **225**, 358–368 (2017).

64. L. Sheng, *et al.* Unraveling the Hydrolysis Mechanism of $LiPF_6$ in Electrolyte of Lithium Ion Batteries. *Nano Lett.* **24**, 533–540 (2024).

65. V. Sharova, *et al.* Comparative study of imide-based Li salts as electrolyte additives for Li-ion batteries. *J. Power Sources* **375**, 43–52 (2018).

66. B. S. Parimalam & B. L. Lucht. Reduction Reactions of Electrolyte Salts for Lithium Ion Batteries: $LiPF_6$, $LiBF_4$, LiDFOB, LiBOB, and LiTFSI. *J. Electrochem. Soc.* **165**, A251 (2018).

67. S. S. Zhang, K. Xu & T. R. Jow. Study of $LiBF_4$ as an Electrolyte Salt for a Li-Ion Battery. *J. Electrochem. Soc.* **149**, A586 (2002).

68. J. Kalhoff, G. G. Eshetu, D. Bresser & S. Passerini. Safer Electrolytes for Lithium-Ion Batteries: State of the Art and Perspectives. *ChemSusChem* **8**, 2154–2175 (2015).

69. Y. Yamada, J. Wang, S. Ko, E. Watanabe & A. Yamada. Advances and issues in developing salt-concentrated battery electrolytes. *Nat. Energy* **4**, 269–280 (2019).

70. A. Mauger, C. M. Julien, A. Paolella, M. Armand & K. Zaghib. A comprehensive review of lithium salts and beyond for rechargeable batteries: Progress and perspectives. *Mater. Sci. Eng. R Rep.* **134**, 1–21 (2018).

71. K. Xu. Nonaqueous Liquid Electrolytes for Lithium-Based Rechargeable Batteries. *Chem. Rev.* **104**, 4303–4418 (2004).

72. Y.-K. Liu, *et al.* Research Progresses of Liquid Electrolytes in Lithium-Ion Batteries. *Small* **19**, 2205315 (2023).

73. N. Yao, *et al.* An Atomic Insight into the Chemical Origin and Variation of the Dielectric Constant in Liquid Electrolytes. *Angew. Chem.* **133**, 21643–21648 (2021).

74. E. R. Logan, *et al.* A Study of the Physical Properties of Li-Ion Battery Electrolytes Containing Esters. *J. Electrochem. Soc.* **165**, A21 (2018).

75. N. Yao, *et al.* Probing the Origin of Viscosity of Liquid Electrolytes for Lithium Batteries. *Angew. Chem.* **135**, e202305331 (2023).

76. J. T. Dudley, *et al.* Conductivity of electrolytes for rechargeable lithium batteries. *J. Power Sources* **35**, 59–82 (1991).

77. H. Moon, *et al.* Solvent Activity in Electrolyte Solutions Controls Electrochemical Reactions in Li-Ion and Li-Sulfur Batteries. *J. Phys. Chem. C* **119**, 3957–3970 (2015).

78. S. Uchida & T. Kiyobayashi. How does the solvent composition influence the transport properties of electrolyte solutions? $LiPF_6$ and LiFSA in EC and DMC binary solvent. *Phys. Chem. Chem. Phys.* **23**, 10875–10887 (2021).

79. D. S. Hall, J. Self & J. R. Dahn. Dielectric Constants for Quantum Chemistry and Li-Ion Batteries: Solvent Blends of Ethylene Carbonate and Ethyl Methyl Carbonate. *J. Phys. Chem. C* **119**, 22322–22330 (2015).

80. S. Uchida & T. Kiyobayashi. What differentiates the transport properties of lithium electrolyte in ethylene carbonate mixed with diethylcarbonate from those mixed with dimethylcarbonate? *J. Power Sources* **511**, 230423 (2021).

81. G. G. Botte, R. E. White & Z. Zhang. Thermal stability of $LiPF_6$–EC:EMC electrolyte for lithium ion batteries. *J. Power Sources* **97–98**, 570–575 (2001).

82. S. S. Zhang, T. R. Jow, K. Amine & G. L. Henriksen. $LiPF_6$–EC–EMC electrolyte for Li-ion battery. *J. Power Sources* **107**, 18–23 (2002).

83. J.-G. Han, K. Kim, Y. Lee & N.-S. Choi. Scavenging Materials to Stabilize $LiPF_6$-Containing Carbonate-Based Electrolytes for Li-Ion Batteries. *Adv. Mater.* **31**, 1804822 (2019).

84. S. S. Zhang. A review on electrolyte additives for lithium-ion batteries. *J. Power Sources* **162**, 1379–1394 (2006).

85. D. Aurbach, *et al.* On the use of vinylene carbonate (VC) as an additive to electrolyte solutions for Li-ion batteries. *Electrochimica Acta* **47**, 1423–1439 (2002).

86. W. Zhao, *et al.* Recent advances in the research of functional electrolyte additives for lithium-ion batteries. *Curr. Opin. Electrochem.* **6**, 84–91 (2017).

87. A. M. Haregewoin, A. S. Wotango & B.-J. Hwang. Electrolyte additives for lithium ion battery electrodes: progress and perspectives. *Energy Environ. Sci.* **9**, 1955–1988 (2016).

88. X.-Q. Zhang, X.-B. Cheng, X. Chen, C. Yan & Q. Zhang. Fluoroethylene Carbonate Additives to Render Uniform Li Deposits in Lithium Metal Batteries. *Adv. Funct. Mater.* **27**, 1605989 (2017).

89. X.-B. Cheng, R. Zhang, C.-Z. Zhao & Q. Zhang. Toward Safe Lithium Metal Anode in Rechargeable Batteries: A Review. *Chem. Rev.* **117**, 10403–10473 (2017).

90. M. S. Whittingham. Ultimate Limits to Intercalation Reactions for Lithium Batteries. *Chem. Rev.* **114**, 11414–11443 (2014).

91. D. Lin, Y. Liu & Y. Cui. Reviving the lithium metal anode for high-energy batteries. *Nat. Nanotechnol.* **12**, 194–206 (2017).

92. M. Weiss, *et al.* Fast Charging of Lithium-Ion Batteries: A Review of Materials Aspects. *Adv. Energy Mater.* **11**, 2101126 (2021).

93. Y. Liu, H. Shi & Z.-S. Wu. Recent status, key strategies and challenging perspectives of fast-charging graphite anodes for lithium-ion batteries. *Energy Environ. Sci.* **16**, 4834–4871 (2023).

94. Y. Sun, N. Liu & Y. Cui. Promises and challenges of nanomaterials for lithium-based rechargeable batteries. *Nat. Energy* **1**, 1–12 (2016).

95. W. Xu, *et al.* Lithium metal anodes for rechargeable batteries. *Energy Environ. Sci.* **7**, 513–537 (2014).

96. P. Zhai, L. Liu, X. Gu, T. Wang & Y. Gong. Interface Engineering for Lithium Metal Anodes in Liquid Electrolyte. *Adv. Energy Mater.* **10**, 2001257 (2020).

97. P. G. Bruce, S. A. Freunberger, L. J. Hardwick & J.-M. Tarascon. Li–O_2 and Li–S batteries with high energy storage. *Nat. Mater.* **11**, 19–29 (2012).

98. Y. Zhao, *et al.* Anode Interface Engineering and Architecture Design for High-Performance Lithium–Sulfur Batteries. *Adv. Mater.* **31**, 1806532 (2019).

99. X. Yu & A. Manthiram. Electrode–Electrolyte Interfaces in Lithium–Sulfur Batteries with Liquid or Inorganic Solid Electrolytes. *Acc. Chem. Res.* **50**, 2653–2660 (2017).

100. X. Zhang, Y. Yang, & Z. Zhou.Towards practical lithium-metal anodes. *Chem. Soc. Rev.* **49**, 3040–3071 (2020).

101. S. S. Zhang. Problem, Status, and Possible Solutions for Lithium Metal Anode of Rechargeable Batteries. *ACS Appl. Energy Mater.* **1**, 910–920 (2018).

102. M. D. Tikekar, S. Choudhury, Z. Tu & L. A. Archer. Design principles for electrolytes and interfaces for stable lithium-metal batteries. *Nat. Energy* **1**, 1–7 (2016).

103. S. Li, *et al.* Developing High-Performance Lithium Metal Anode in Liquid Electrolytes: Challenges and Progress. *Adv. Mater.* **30**, 1706375 (2018).

104. X.-B. Cheng, *et al.* A Review of Solid Electrolyte Interphases on Lithium Metal Anode. *Adv. Sci.* **3**, 1500213 (2016).

105. N.-W. Li, Y.-X. Yin, C.-P. Yang & Y.-G. Guo. An Artificial Solid Electrolyte Interphase Layer for Stable Lithium Metal Anodes. *Adv. Mater.* **28**, 1853–1858 (2016).

106. S. Chen, C. Pan, Q. Wang, J.-L. Luo & X.-Z. Fu. Advancements in Current Collectors for Composite Lithium Metal Anodes. *Adv. Funct. Mater.* **34**, 2409812 (2024).

107. Q. Li, S. Zhu & Y. Lu. 3D Porous Cu Current Collector/Li-Metal Composite Anode for Stable Lithium-Metal Batteries. *Adv. Funct. Mater.* **27**, 1606422 (2017).

108. C.-P. Yang, Y.-X. Yin, S.-F. Zhang, N.-W. Li & Y.-G. Guo. Accommodating lithium into 3D current collectors with a submicron skeleton towards long-life lithium metal anodes. *Nat. Commun.* **6**, 8058 (2015).

109. J. Qian, *et al.* High rate and stable cycling of lithium metal anode. *Nat. Commun.* **6**, 6362 (2015).

110. H. Zhang, *et al.* Electrolyte Additives for Lithium Metal Anodes and Rechargeable Lithium Metal Batteries: Progress and Perspectives. *Angew. Chem. Int. Ed.* **57**, 15002–15027 (2018).

111. S. Li, *et al.* Recent progress on electrolyte additives for stable lithium metal anode. *Energy Storage Mater.* **32**, 306–319 (2020).

112. K. Liu, Z. Wang, L. Shi, S. Jungsuttiwong & S. Yuan. Ionic liquids for high performance lithium metal batteries. *J. Energy Chem.* **59**, 320–333 (2021).

113. T. Krauskopf, F. H. Richter, W. G. Zeier & J. Janek. Physicochemical Concepts of the Lithium Metal Anode in Solid-State Batteries. *Chem. Rev.* **120**, 7745–7794 (2020).

114. O. B. Chae & B. L. Lucht. Interfacial Issues and Modification of Solid Electrolyte Interphase for Li Metal Anode in Liquid and Solid Electrolytes. *Adv. Energy Mater.* **13**, 2203791 (2023).

115. Q. Wang, *et al.* Leap of Li Metal Anodes from Coin Cells to Pouch Cells: Challenges and Progress. *Electrochem. Energy Rev.* **6**, 22 (2023).

116. B. Acebedo, *et al.* Current Status and Future Perspective on Lithium Metal Anode Production Methods. *Adv. Energy Mater.* **13**, 2203744 (2023).

117. S. Rana, R. Kumar & R. S. Bharj. Current trends, challenges, and prospects in material advances for improving the overall safety of lithium-ion battery pack. *Chem. Eng. J.* **463**, 142336 (2023).

118. Y. Zheng, *et al.* Thermal state monitoring of lithium-ion batteries: Progress, challenges, and opportunities. *Prog. Energy Combust. Sci.* **100**, 101120 (2024).

119. S.-J. Yang, *et al.* Life cycle safety issues of lithium metal batteries: A perspective. *Electron* **1**, e8 (2023).

120. Y. Wang, *et al.* Challenges and Opportunities to Mitigate the Catastrophic Thermal Runaway of High-Energy Batteries. *Adv. Energy Mater.* **13**, 2203841 (2023).

121. A. Yang, *et al.* Benchmarking the Safety Performance of Organic Electrolytes for Rechargeable Lithium Batteries: A Thermochemical Perspective. *ACS Energy Lett.* **8**, 836–843 (2023).

122. L. Qi, *et al.* Manufacturing processes and recycling technology of automotive lithium-ion battery: A review. *J. Energy Storage* **67**, 107533 (2023).

123. N. Sharmili, R. Nagi & P. Wang. A review of research in the Li-ion battery production and reverse supply chains. *J. Energy Storage* **68**, 107622 (2023).

124. X. Wang, *et al.* Economic and environmental characterization of an evolving Li-ion battery waste stream. *J. Environ. Manage.* **135**, 126–134 (2014).

125. B. K. Sovacool, *et al.* Sustainable minerals and metals for a low-carbon future. *Science* **367**, 30–33 (2020).

126. M. Gutsch & J. Leker. Costs, carbon footprint, and environmental impacts of lithium-ion batteries – From cathode active material synthesis to cell manufacturing and recycling. *Appl. Energy* **353**, 122132 (2024).

127. T. Yu, *et al.* The research and industrialization progress and prospects of sodium ion battery. *J. Alloys Compd.* **958**, 170486 (2023).

128. T. Hosaka, K. Kubota, A. S. Hameed & S. Komaba. Research Development on K-Ion Batteries. *Chem. Rev.* **120**, 6358–6466 (2020).

129. K. Sada, J. Darga & A. Manthiram. Challenges and Prospects of Sodium-Ion and Potassium-Ion Batteries for Mass Production. *Adv. Energy Mater.* **13**, 2302321 (2023).

130. M. H. Han, E. Gonzalo, G. Singh & T. Rojo. A comprehensive review of sodium layered oxides: powerful cathodes for Na-ion batteries. *Energy Environ. Sci.* **8**, 81–102 (2015).

131. H. Park, *et al.* Review on Cathode Materials for Sodium- and Potassium-Ion Batteries: Structural Design with Electrochemical Properties. *Batter. Supercaps* **6**, e202200486 (2023).

132. J. Liao, *et al.* Recent Progress and Prospects of Layered Cathode Materials for Potassium-ion Batteries. *ENERGY Environ. Mater.* **4**, 178–200 (2021).

133. Z.-X. Huang, *et al.* Advanced layered oxide cathodes for sodium/potassium-ion batteries: Development, challenges and prospects. *Chem. Eng. J.* **452**, 139438 (2023).

134. Y. Liang, H. Dong, D. Aurbach & Y. Yao. Current status and future directions of multivalent metal-ion batteries. *Nat. Energy* **5**, 646–656 (2020).

135. R. J. Gummow, G. Vamvounis, M. B. Kannan & Y. He. Calcium-Ion Batteries: Current State-of-the-Art and Future Perspectives. *Adv. Mater.* **30**, 1801702 (2018).

136. Y. Zhang, S. Liu, Y. Ji, J. Ma & H. Yu. Emerging Nonaqueous Aluminum-Ion Batteries: Challenges, Status, and Perspectives. *Adv. Mater.* **30**, 1706310 (2018).

137. Y. Zhang, *et al.* Challenges and recent progress in the design of advanced electrode materials for rechargeable Mg batteries. *Energy Storage Mater.* **20**, 118–138 (2019).

138. P. Meng, *et al.* Electrolyte design for rechargeable aluminum-ion batteries: Recent advances and challenges. *Energy Storage Mater.* **63**, 102953 (2023).

139. M. E. Arroyo-de Dompablo, A. Ponrouch, P. Johansson & M. R. Palacín. Achievements, Challenges, and Prospects of Calcium Batteries. *Chem. Rev.* **120**, 6331–6357 (2020).

140. M. Song, H. Tan, D. Chao & H. J. Fan. Recent Advances in Zn-Ion Batteries. *Adv. Funct. Mater.* **28**, 1802564 (2018).

141. J. Shin, J. Lee, Y. Park & J. W. Choi. Aqueous zinc ion batteries: focus on zinc metal anodes. *Chem. Sci.* **11**, 2028–2044 (2020).

142. A. Ponrouch & M. R. Palacín. Post-Li batteries: promises and challenges. *Philos. Trans. R. Soc. Math. Phys. Eng. Sci.* **377**, 20180297 (2019).

143. H. Kim & J. C. Kim. Opportunities and challenges in cathode development for non-lithium-ion batteries. *eScience* **4**, 100232 (2024).

144. L. Tang, *et al.* Zn-based batteries for sustainable energy storage: strategies and mechanisms. *Chem. Soc. Rev.* **53**, 4877–4925 (2024).

145. Z. Cai, J. Wang & Y. Sun. Anode corrosion in aqueous Zn metal batteries. *eScience* **3**, 100093 (2023).

146. B. Scrosati History of lithium batteries. *J. Solid State Electrochem.* **15**, 1623–1630 (2011).

147. T. Placke, R. Kloepsch, S. Dühnen & M. Winter. Lithium ion, lithium metal, and alternative rechargeable battery technologies: the odyssey for high energy density. *J. Solid State Electrochem.* **21**, 1939–1964 (2017).

148. H. S. Lim, A. M. Lackner & R. C. Knechtli. Zinc-Bromine Secondary Battery. *J. Electrochem. Soc.* **124**, 1154 (1977).

149. T. A. Edison. Reversible galvanic battery. (1901).

150. P. A. Marsal, K. Karl & L. F. Urry. Dry cell. (1960).

151. A. P. Karpinski, B. Makovetski, S. J. Russell, J. R. Serenyi & D. C. Williams. Silver–zinc: status of technology and applications. *J. Power Sources* **80**, 53–60 (1999).

152. Y. Li & H. Dai. Recent advances in zinc–air batteries. *Chem. Soc. Rev.* **43**, 5257–5275 (2014).

153. J. Fu, *et al.* Recent Progress in Electrically Rechargeable Zinc–Air Batteries. *Adv. Mater.* **31**, 1805230 (2019).

154. W. Shang, *et al.* Rechargeable alkaline zinc batteries: Progress and challenges. *Energy Storage Mater.* **31**, 44–57 (2020).

155. T. Yamamoto & T. Shoji. Rechargeable Zn|$ZnSO_4$|MnO_2-type cells. *Inorganica Chim. Acta* **117**, L27–L28 (1986).

156. C. Xu, B. Li, H. Du & F. Kang. Energetic Zinc Ion Chemistry: The Rechargeable Zinc Ion Battery. *Angew. Chem. Int. Ed.* **51**, 933–935 (2012).

157. S. Lei, *et al.* Opportunities for biocompatible and safe zinc-based batteries. *Energy Environ. Sci.* **15**, 4911–4927 (2022).

158. J. Islam, *et al.* Rechargeable metal-metal alkaline batteries: Recent advances, current issues and future research strategies. *J. Power Sources* **563**, 232777 (2023).

159. X. Zeng, J. Hao, Z. Wang, J. Mao & Z. Guo. Recent progress and perspectives on aqueous Zn-based rechargeable batteries with mild aqueous electrolytes. *Energy Storage Mater.* **20**, 410–437 (2019).

160. D. Lin & Y. Li. Recent Advances of Aqueous Rechargeable Zinc-Iodine Batteries: Challenges, Solutions, and Prospects. *Adv. Mater.* **34**, 2108856 (2022).

161. A. Mahmood, Z. Zheng & Y. Chen. Zinc–Bromine Batteries: Challenges, Prospective Solutions, and Future. *Adv. Sci.* **11**, 2305561 (2024).

162. Z. Xie, *et al.* Rechargeable alkali metal–chlorine batteries: advances, challenges, and future perspectives. *Chem. Soc. Rev.* **53**, 8424–8456 (2024).

163. D. Chao, *et al.* An Electrolytic Zn–MnO_2 Battery for High-Voltage and Scalable Energy Storage. *Angew. Chem.* **131**, 7905–7910 (2019).

164. X. Guo, *et al.* Zn/MnO_2 battery chemistry with dissolution-deposition mechanism. *Mater. Today Energy* **16**, 100396 (2020).

165. J. Hao, *et al.* Deeply understanding the Zn anode behaviour and corresponding improvement strategies in different aqueous Zn-based batteries. *Energy Environ. Sci.* **13**, 3917–3949 (2020).

166. X. Jia, C. Liu, Z. G. Neale, J. Yang & G. Cao. Active Materials for Aqueous Zinc Ion Batteries: Synthesis, Crystal Structure, Morphology, and Electrochemistry. *Chem. Rev.* **120**, 7795–7866 (2020).

167. N. Wang, *et al.* A review of zinc-based battery from alkaline to acid. *Mater. Today Adv.* **11**, 100149 (2021).

168. D. Qiu, *et al.* A review on zinc electrodes in alkaline electrolyte: Current challenges and optimization strategies. *Energy Storage Mater.* **61**, 102903 (2023).

169. M. B. Lim, T. N. Lambert & E. I. Ruiz. Effect of ZnO-Saturated Electrolyte on Rechargeable Alkaline Zinc Batteries at Increased Depth-of-Discharge. *J. Electrochem. Soc.* **167**, 060508 (2020).

170. A. Bayaguud, Y. Fu & C. Zhu. Interfacial parasitic reactions of zinc anodes in zinc ion batteries: Underestimated corrosion and hydrogen evolution reactions and their suppression strategies. *J. Energy Chem.* **64**, 246–262 (2022).

171. G. Fang, J. Zhou, A. Pan & S. Liang. Recent Advances in Aqueous Zinc-Ion Batteries. *ACS Energy Lett.* **3**, 2480–2501 (2018).

172. Z. Hou & B. Zhang. Boosting Zn metal anode stability: from fundamental science to design principles. *EcoMat* **4**, e12265 (2022).

173. J. Hao, *et al.* An In-Depth Study of Zn Metal Surface Chemistry for Advanced Aqueous Zn-Ion Batteries. *Adv. Mater.* **32**, 2003021 (2020).

174. W.-G. Lim, X. Li & D. Reed. Understanding the Role of Zinc Hydroxide Sulfate and its Analogues in Mildly Acidic Aqueous Zinc Batteries: A Review. *Small Methods* **8**, 2300965 (2024).

175. M. Zhou, Y. Chen, G. Fang & S. Liang, Electrolyte/electrode interfacial electrochemical behaviors and optimization strategies in aqueous zinc-ion batteries. *Energy Storage Mater.* **45**, 618–646 (2022).

176. S. W. D. Gourley, R. Brown, B. D. Adams & D. Higgins. Zinc-ion batteries for stationary energy storage. *Joule* **7**, 1415–1436 (2023).

177. N. Dong, F. Zhang & H. Pan. Towards the practical application of Zn metal anodes for mild aqueous rechargeable Zn batteries. *Chem. Sci.* **13**, 8243–8252 (2022).

178. W. Shi, W. S. V. Lee & J. Xue. Recent Development of Mn-based Oxides as Zinc-Ion Battery Cathode. *ChemSusChem* **14**, 1634–1658 (2021).

179. Y. Zhao, Y. Zhu & X. Zhang. Challenges and perspectives for manganese-based oxides for advanced aqueous zinc-ion batteries. *InfoMat* **2**, 237–260 (2020).

180. T. Lv, *et al.* How About Vanadium-Based Compounds as Cathode Materials for Aqueous Zinc Ion Batteries? *Adv. Sci.* **10**, 2206907 (2023).

181. X. Chen, *et al.* Vanadium-based cathodes for aqueous zinc-ion batteries: Mechanism, design strategies and challenges. *Energy Storage Mater.* **50**, 21–46 (2022).

182. Y. Li, *et al.* Prussian blue analogs cathodes for aqueous zinc ion batteries. *Mater. Today Energy* **29**, 101095 (2022).

183. Q. Liu, *et al.* A polyaniline surface-modified Prussian blue analogue cathode for flexible aqueous Zn-ion batteries. *Chem. Commun.* **58**, 8226–8229 (2022).

184. Z. Tie & Z. Niu. Design Strategies for High-Performance Aqueous Zn/Organic Batteries. *Angew. Chem. Int. Ed.* **59**, 21293–21303 (2020).

185. J. Cui, *et al.* Organic Cathode Materials for Rechargeable Zinc Batteries: Mechanisms, Challenges, and Perspectives. *ChemSusChem* **13**, 2160–2185 (2020).

186. W. Du, *et al.* Challenges in the material and structural design of zinc anode towards high-performance aqueous zinc-ion batteries. *Energy Environ. Sci.* **13**, 3330–3360 (2020).

187. X. Yu, *et al.* Ten concerns of Zn metal anode for rechargeable aqueous zinc batteries. *Joule* **7**, 1145–1175 (2023).

188. Q. Yang, *et al.* Dendrites in Zn-Based Batteries. *Adv. Mater.* **32**, 2001854 (2020).

189. Q. Yang, *et al.* Do Zinc Dendrites Exist in Neutral Zinc Batteries: A Developed Electrohealing Strategy to In Situ Rescue In-Service Batteries. *Adv. Mater.* **31**, 1903778 (2019).

190. Z. Yi, *et al.* An Ultrahigh Rate and Stable Zinc Anode by Facet-Matching-Induced Dendrite Regulation. *Adv. Mater.* **34**, 2203835 (2022).

191. Z. Yang, *et al.* Revealing the Two-Dimensional Surface Diffusion Mechanism for Zinc Dendrite Formation on Zinc Anode. *Small* **18**, 2104148 (2022).

192. Q. Li, *et al.* Dendrites issues and advances in Zn anode for aqueous rechargeable Zn-based batteries. *EcoMat* **2**, e12035 (2020).

193. Y. Zhang, *et al.* Highly Strengthened and Toughened Zn–Li–Mn Alloys as Long-Cycling Life and Dendrite-Free Zn Anode for Aqueous Zinc-Ion Batteries. *Small* **18**, 2200787 (2022).

194. H. Shao, *et al.* Zincophilic Nanospheres Assembled as Solid-Electrolyte Interphase on Zn Metal Anodes for Reversible High-rate Zn-Ion Storage. *Small* **20**, 2403062 (2024).

195. Z. Zhang, *et al.* Dendrite suppression by anode polishing in zinc-ion batteries. *J. Mater. Chem. A* **9**, 15355–15362 (2021).

196. Y. Liang, M. Qiu, P. Sun & W. Mai. Comprehensive Review of Electrolyte Modification Strategies for Stabilizing Zn Metal Anodes. *Adv. Funct. Mater.* **33**, 2304878 (2023).

197. Y. Yang, H. Yang, R. Zhu & H. Zhou. High reversibility at high current density: the zinc electrodeposition principle behind the “trick”. *Energy Environ. Sci.* **16**, 2723–2731 (2023).

198. J. Su, *et al.* Temperature-Dependent Nucleation and Electrochemical Performance of Zn Metal Anodes. *Nano Lett.* **22**, 1549–1556 (2022).

199. D. Feng, *et al.* Immunizing Aqueous Zn Batteries against Dendrite Formation and Side Reactions at Various Temperatures via Electrolyte Additives. *Small* **17**, 2103195 (2021).

200. Z. Hu, *et al.* Highly Reversible Zn Metal Anodes Enabled by Increased Nucleation Overpotential. *Nano-Micro Lett.* **15**, 171 (2023).

201. Y. Li, *et al.* The Zn Deposition Mechanism and Pressure Effects for Aqueous Zn Batteries: A Combined Theoretical and Experimental Study. *Adv. Energy Mater.* **14**, 2303047 (2024).

202. M. Tribbia, G. Zampardi & F. La Mantia. Towards the commercialization of rechargeable aqueous zinc ion batteries: The challenge of the zinc electrodeposition at the anode. *Curr. Opin. Electrochem.* **38**, 101230 (2023).

203. Y. Shang & D. Kundu. Understanding and Performance of the Zinc Anode Cycling in Aqueous Zinc-Ion Batteries and a Roadmap for the Future. *Batter. Supercaps* **5**, e202100394 (2022).

204. C. W. Lee, S. W. Eom, K. Sathiyanarayanan & M. S. Yun. Preliminary comparative studies of zinc and zinc oxide electrodes on corrosion reaction and reversible reaction for zinc/air fuel cells. *Electrochimica Acta* **52**, 1588–1591 (2006).

205. L. Miao, Z. Guo & L. Jiao. Insights into the design of mildly acidic aqueous electrolytes for improved stability of Zn anode performance in zinc-ion batteries. *Energy Mater.* **3**, 300014 (2023).

206. M. Li, *et al.* Comprehensive understanding of the roles of water molecules in aqueous Zn-ion batteries: from electrolytes to electrode materials. *Energy Environ. Sci.* **14**, 3796–3839 (2021).

207. J. Hao, *et al.* Designing Dendrite-Free Zinc Anodes for Advanced Aqueous Zinc Batteries. *Adv. Funct. Mater.* **30**, 2001263 (2020).

208. J. Chen, *et al.* Challenges and perspectives of hydrogen evolution-free aqueous Zn-Ion batteries. *Energy Storage Mater.* **59**, 102767 (2023).

209. Z. Cai, *et al.* Chemically resistant Cu–Zn/Zn composite anode for long cycling aqueous batteries. *Energy Storage Mater.* **27**, 205–211 (2020).

210. S. D. Pu, *et al.* Decoupling, quantifying, and restoring aging-induced Zn-anode losses in rechargeable aqueous zinc batteries. *Joule* **7**, 366–379 (2023).

211. B. Li, *et al.* Interfacial Engineering Strategy for High-Performance Zn Metal Anodes. *Nano-Micro Lett.* **14**, 6 (2021).

212. G. Liang, *et al.* Gradient fluorinated alloy to enable highly reversible Zn-metal anode chemistry. *Energy Environ. Sci.* **15**, 1086–1096 (2022).

213. P. Samanta, *et al.* Recent Progress on the Performance of Zn-Ion Battery Using Various Electrolyte Salt and Solvent Concentrations. *ACS Appl. Electron. Mater.* **5**, 100–116 (2023).

214. Y. Du, *et al.* Electrolyte Salts and Additives Regulation Enables High Performance Aqueous Zinc Ion Batteries: A Mini Review. *Small* **18**, 2104640 (2022).

215. L. Zhang, *et al.* $ZnCl_2$ “Water-in-Salt” Electrolyte Transforms the Performance of Vanadium Oxide as a Zn Battery Cathode. *Adv. Funct. Mater.* **29**, 1902653 (2019).

216. S. Bai, *et al.* Electrolyte Additives for Stable Zn Anodes. *Adv. Sci.* **11**, 2304549 (2024).

217. L. Yu, *et al.* Ionic Liquid “Water Pocket” for Stable and Environment-Adaptable Aqueous Zinc Metal Batteries. *Adv. Mater.* **35**, 2210789 (2023).

218. L. Geng, *et al.* Eutectic Electrolyte with Unique Solvation Structure for High-Performance Zinc-Ion Batteries. *Angew. Chem. Int. Ed.* **61**, e202206717 (2022).

219. Y. Hao, *et al.* Gel Electrolyte Constructing Zn (002) Deposition Crystal Plane Toward Highly Stable Zn Anode. *Adv. Sci.* **9**, 2104832 (2022).

220. L. Ma, *et al.* Hydrogen-Free and Dendrite-Free All-Solid-State Zn-Ion Batteries. *Adv. Mater.* **32**, 1908121 (2020).

221. F. Ding, *et al.* Dendrite-Free Lithium Deposition via Self-Healing Electrostatic Shield Mechanism. *J. Am. Chem. Soc.* **135**, 4450–4456 (2013).

222. J. Xu, *et al.* Understanding the Electrical Mechanisms in Aqueous Zinc Metal Batteries: From Electrostatic Interactions to Electric Field Regulation. *Adv. Mater.* **36**, 2309726 (2024).

223. Z. Hu, *et al.* A Self-Regulated Electrostatic Shielding Layer toward Dendrite-Free Zn Batteries. *Adv. Mater.* **34**, 2203104 (2022).

224. X. Guo, *et al.* Alleviation of Dendrite Formation on Zinc Anodes via Electrolyte Additives. *ACS Energy Lett.* **6**, 395–403 (2021).

225. F. Wan, *et al.* Aqueous rechargeable zinc/sodium vanadate batteries with enhanced performance from simultaneous insertion of dual carriers. *Nat. Commun.* **9**, 1656 (2018).

226. X. Zhang, *et al.* Efficient Suppression of Dendrites and Side Reactions by Strong Electrostatic Shielding Effect via the Additive of Rb_2SO_4 for Anodes in Aqueous Zinc-Ion Batteries. *Small* **19**, 2303906 (2023).

227. P. Wang, *et al.* Mechanistic Insights of Mg^{2+}-Electrolyte Additive for High-Energy and Long-Life Zinc-Ion Hybrid Capacitors. *Adv. Energy Mater.* **11**, 2101158 (2021).

228. B. W. Olbasa, *et al.* High-Rate and Long-Cycle Stability with a Dendrite-Free Zinc Anode in an Aqueous Zn-Ion Battery Using Concentrated Electrolytes. *ACS Appl. Energy Mater.* **3**, 4499–4508 (2020).

229. Y. Mu, *et al.* Manipulating crystallographic growth orientation by cation-enhanced gel-polymer electrolytes toward reversible low-temperature zinc-ion batteries. *InfoMat* **6**, e12611 (2024).

230. R. Zhao, *et al.* Lanthanum nitrate as aqueous electrolyte additive for favourable zinc metal electrodeposition. *Nat. Commun.* **13**, 3252 (2022).

231. C. Chen, L. Li, Z. Long, E. H. Ang & Q. Liang. Enabling stable aqueous Zn metal anodes using scandium acetate electrolyte additives. *J. Mater. Chem. A* **12**, 18968–18976 (2024).

232. Y. Ding, *et al.* A dynamic electrostatic shielding layer toward highly reversible Zn metal anode. *Energy Storage Mater.* **62**, 102949 (2023).

233. Z. Hu, *et al.* Screening metal cation additives driven by differential capacitance for Zn batteries. *Energy Environ. Sci.* **17**, 4794–4802 (2024).

234. X. Xu, *et al.* Tailoring the solvation shells of dual metal ions for high-performance aqueous zinc ion batteries. *Chem. Eng. J.* **478**, 147313 (2023).

235. C. Lin, *et al.* High-Rate, Large Capacity, and Long Life Dendrite-Free Zn Metal Anode Enabled by Trifunctional Electrolyte Additive with a Wide Temperature Range. *Adv. Sci.* **9**, 2201433 (2022).

236. R. Chen, *et al.* Trace Amounts of Triple-Functional Additives Enable Reversible Aqueous Zinc-Ion Batteries from a Comprehensive Perspective. *Nano-Micro Lett.* **15**, 81 (2023).

237. A. Bayaguud, X. Luo, Y. Fu & C. Zhu. Cationic Surfactant-Type Electrolyte Additive Enables Three-Dimensional Dendrite-Free Zinc Anode for Stable Zinc-Ion Batteries. *ACS Energy Lett.* **5**, 3012–3020 (2020).

238. W. Xu, *et al.* Diethyl ether as self-healing electrolyte additive enabled long-life rechargeable aqueous zinc ion batteries. *Nano Energy* **62**, 275–281 (2019).

239. N. Hu, *et al.* A Double-Charged Organic Molecule Additive to Customize Electric Double Layer for Super-Stable and Deep-Rechargeable Zn Metal Pouch Batteries. *Adv. Funct. Mater.* **34**, 2311773 (2024).

240. L. Miao, *et al.* A Universal Descriptor in Determining H_2 Evolution Activity for Dilute Aqueous Zn Batteries. *Adv. Funct. Mater.* **33**, 2306952 (2023).

241. Q. Zhang, *et al.* Designing Anion-Type Water-Free Zn^{2+} Solvation Structure for Robust Zn Metal Anode. *Angew. Chem.* **133**, 23545–23552 (2021).

242. X. Li, X. Wang, L. Ma & W. Huang. Solvation Structures in Aqueous Metal-Ion Batteries. *Adv. Energy Mater.* **12**, 2202068 (2022).

243. L. Cao, *et al.* Solvation Structure Design for Aqueous Zn Metal Batteries. *J. Am. Chem. Soc.* **142**, 21404–21409 (2020).

244. T. Wei, *et al.* Reconstructing anode/electrolyte interface and solvation structure towards high stable zinc anode. *Chem. Eng. J.* **457**, 141272 (2023).

245. R. Qin, *et al.* Tuning Zn^{2+} coordination environment to suppress dendrite formation for high-performance Zn-ion batteries. *Nano Energy* **80**, 105478 (2021).

246. Q. Ma, *et al.* Regulation of Outer Solvation Shell Toward Superior Low-Temperature Aqueous Zinc-Ion Batteries. *Adv. Mater.* **34**, 2207344 (2022).

247. L. Miao, *et al.* Three-functional ether-based co-solvents for suppressing water-induced parasitic reactions in aqueous Zn-ion batteries. *Energy Storage Mater.* **49**, 445–453 (2022).

248. G. Ma, *et al.* Reshaping the electrolyte structure and interface chemistry for stable aqueous zinc batteries. *Energy Storage Mater.* **47**, 203–210 (2022).

249. W. He, *et al.* Decreasing Water Activity Using the Tetrahydrofuran Electrolyte Additive for Highly Reversible Aqueous Zinc Metal Batteries. *ACS Appl. Mater. Interfaces* **15**, 6647–6656 (2023).

250. C. You, *et al.* An inexpensive electrolyte with double-site hydrogen bonding and a regulated Zn^{2+} solvation structure for aqueous Zn-ion batteries capable of high-rate and ultra-long low-temperature operation. *Energy Environ. Sci.* **16**, 5096–5107 (2023).

251. Y. Dong, *et al.* Non-concentrated aqueous electrolytes with organic solvent additives for stable zinc batteries. *Chem. Sci.* **12**, 5843–5852 (2021).

252. H. Cao, *et al.* Unraveling the Solvation Structure and Electrolyte Interface through Carbonyl Chemistry for Durable and Dendrite-Free Zn Anode. *Adv. Funct. Mater.* **33**, 2305683 (2023).

253. T. C. Li, *et al.* A Universal Additive Strategy to Reshape Electrolyte Solvation Structure toward Reversible Zn Storage. *Adv. Energy Mater.* **12**, 2103231 (2022).

254. P. Sun, *et al.* Simultaneous Regulation on Solvation Shell and Electrode Interface for Dendrite-Free Zn Ion Batteries Achieved by a Low-Cost Glucose Additive. *Angew. Chem. Int. Ed.* **60**, 18247–18255 (2021).

255. J. Luo, *et al.* Regulating the Inner Helmholtz Plane with a High Donor Additive for Efficient Anode Reversibility in Aqueous Zn-Ion Batteries. *Angew. Chem.* **135**, e202302302 (2023).

256. D. Sheng, *et al.* Hydrogen Bond Network Regulation in Electrolyte Structure for Zn-based Aqueous Batteries. *Adv. Funct. Mater.* **34**, 2402014 (2024).

257. Z. Zhao, *et al.* End-capping of hydrogen bonds: A strategy for blocking the proton conduction pathway in aqueous electrolytes. *Energy Storage Mater.* **55**, 479–489 (2023).

258. K. Lu, *et al.* Versatile 1, 3-dimethyl-2-imidazolidinone electrolyte additive: Enables extremely long life zinc metal batteries with different substrates. *Chem. Eng. J.* **457**, 141287 (2023).

259. W. Deng, Z. Xu & X. Wang. High-donor electrolyte additive enabling stable aqueous zinc-ion batteries. *Energy Storage Mater.* **52**, 52–60 (2022).

260. Q. Meng, *et al.* Attenuating Water Activity Through Impeded Proton Transfer Resulting from Hydrogen Bond Enhancement Effect for Fast and Ultra-Stable Zn Metal Anode. *Adv. Energy Mater.* **13**, 2302828 (2023).

261. J. Hao, *et al.* Boosting Zinc Electrode Reversibility in Aqueous Electrolytes by Using Low-Cost Antisolvents. *Angew. Chem. Int. Ed.* **60**, 7366–7375 (2021).

262. M. Wang, *et al.* High-Capacity Zinc Anode with 96% Utilization Rate Enabled by Solvation Structure Design. *Angew. Chem. Int. Ed.* **62**, e202214966 (2023).

263. X. Shi, *et al.* Metallic Zinc Anode Working at 50 and 50 mAh cm^{-2} with High Depth of Discharge via Electrical Double Layer Reconstruction. *Adv. Funct. Mater.* **33**, 2211917 (2023).

264. J. Wei, *et al.* Supramolecule-Based Excluded-Volume Electrolytes and Conjugated Sulfonamide Cathodes for High-Voltage and Long-Cycling Aqueous Zinc-Ion Batteries. *ACS Energy Lett.* **8**, 762–771 (2023).

265. C. Tian, *et al.* Improved Interfacial Ion Migration and Deposition through the Chain-Liquid Synergistic Effect by a Carboxylated Hydrogel Electrolyte for Stable Zinc Metal Anodes. *Angew. Chem. Int. Ed.* **62**, e202310970 (2023).

266. W. Chen, *et al.* Hydrogen Bond-Functionalized Massive Solvation Modules Stabilizing Bilateral Interfaces. *Adv. Funct. Mater.* **32**, 2112609 (2022).

267. S. Ilic, *et al.* Effect of Antisolvent Additives in Aqueous Zinc Sulfate Electrolytes for Zinc Metal Anodes: The Case of Acetonitrile. *ACS Energy Lett.* **9**, 201–208 (2024).

268. D. Kang, M. Xiao & J. P. Lemmon. Artificial Solid-Electrolyte Interphase for Lithium Metal Batteries. *Batter. Supercaps* **4**, 445–455 (2021).

269. Y. Chu, *et al.* In situ built interphase with high interface energy and fast kinetics for high performance Zn metal anodes. *Energy Environ. Sci.* **14**, 3609–3620 (2021).

270. W. Xin, *et al.* Turning the Byproduct $Zn_4(OH)_6SO_4 \cdot xH_2O$ into a Uniform Solid Electrolyte Interphase to Stabilize Aqueous Zn Anode. *ACS Mater. Lett.* **3**, 1819–1825 (2021).

271. Y. Zhang, *et al.* Nonionic Surfactant-Assisted In Situ Generation of Stable Passivation Protective Layer for Highly Stable Aqueous Zn Metal Anodes. *Nano Lett.* **22**, 8574–8583 (2022).

272. D. Xie, *et al.* ZnF_2-Riched Inorganic/Organic Hybrid SEI: in situ-Chemical Construction and Performance-Improving Mechanism for Aqueous Zinc-ion Batteries. *Angew. Chem. Int. Ed.* **62**, e202216934 (2023).

273. H. Li, *et al.* Electrolyte Strategies Facilitating Anion-Derived Solid-Electrolyte Interphases for Aqueous Zinc–Metal Batteries. *Small Methods* **8**, 2300554 (2024).

274. C. Huang, *et al.* Stabilizing Zinc Anodes by Regulating the Electrical Double Layer with Saccharin Anions. *Adv. Mater.* **33**, 2100445 (2021).

275. C. Huang, *et al.* Selection criteria for electrical double layer structure regulators enabling stable Zn metal anodes. *Energy Environ. Sci.* **16**, 1721–1731 (2023).

276. D. Wang, *et al.* Solvation Modulation Enhances Anion-Derived Solid Electrolyte Interphase for Deep Cycling of Aqueous Zinc Metal Batteries. *Angew. Chem. Int. Ed.* **62**, e202310290 (2023).

277. Z. Deng, L. Ouyang, L. Ma, L. Yang & M. Zhu. From electrolyte to electrode interface: Understanding impacts of electrolyte additives for aqueous zinc-ion batteries. *Curr. Opin. Electrochem.* **45**, 101483 (2024).

278. X. Wang, C. Han, S. Dou & W. Li. The protective effect and its mechanism for electrolyte additives on the anode interface in aqueous zinc-based energy storage devices. *Nano Mater. Sci.* (2022).

279. H. Qiu, *et al.* Zinc anode-compatible in-situ solid electrolyte interphase via cation solvation modulation. *Nat. Commun.* **10**, 5374 (2019).

280. D. Wang, *et al.* Insight on Organic Molecules in Aqueous Zn-Ion Batteries with an Emphasis on the Zn Anode Regulation. *Adv. Energy Mater.* **12**, 2102707 (2022).

281. Z. Hou, *et al.* Surfactant widens the electrochemical window of an aqueous electrolyte for better rechargeable aqueous sodium/zinc battery. *J. Mater. Chem. A* **5**, 730–738 (2017).

282. J. Hao, *et al.* Toward High-Performance Hybrid Zn-Based Batteries via Deeply Understanding Their Mechanism and Using Electrolyte Additive. *Adv. Funct. Mater.* **29**, 1903605 (2019).

283. S.-J. Zhang, *et al.* Dual-Function Electrolyte Additive for Highly Reversible Zn Anode. *Adv. Energy Mater.* **11**, 2102010 (2021).

284. K. Guan, *et al.* Anti-Corrosion for Reversible Zinc Anode via a Hydrophobic Interface in Aqueous Zinc Batteries. *Adv. Energy Mater.* **12**, 2103557 (2022).

285. Y. Jin, *et al.* Stabilizing Zinc Anode Reactions by Polyethylene Oxide Polymer in Mild Aqueous Electrolytes. *Adv. Funct. Mater.* **30**, 2003932 (2020).

286. K. E. K. Sun, *et al.* Suppression of Dendrite Formation and Corrosion on Zinc Anode of Secondary Aqueous Batteries. *ACS Appl. Mater. Interfaces* **9**, 9681–9687 (2017).

287. C. Lin, *et al.* Regulating the plating process of zinc with highly efficient additive for long-life zinc anode. *J. Power Sources* **549**, 232078 (2022).

288. T. Zhou, *et al.* Toward stable zinc aqueous rechargeable batteries by anode morphology modulation via polyaspartic acid additive. *Energy Storage Mater.* **45**, 777–785 (2022).

289. M. Zhou, *et al.* Surface-Preferred Crystal Plane for a Stable and Reversible Zinc Anode. *Adv. Mater.* **33**, 2100187 (2021).

290. S. Guo, *et al.* Fundamentals and perspectives of electrolyte additives for aqueous zinc-ion batteries. *Energy Storage Mater.* **34**, 545–562 (2021).

291. Y. Liu, *et al.* Highly enhanced reversibility of a Zn anode by *in-situ* texturing. *Energy Storage Mater.* **47**, 98–104 (2022).

292. Y. Lin, *et al.* Dendrite-free Zn anode enabled by anionic surfactant-induced horizontal growth for highly-stable aqueous Zn-ion pouch cells. *Energy Environ. Sci.* **16**, 687–697 (2023).

293. T. Wei, *et al.* Addition of Dioxane in Electrolyte Promotes (002)-Textured Zinc Growth and Suppressed Side Reactions in Zinc-Ion Batteries. *ACS Nano* **17**, 3765–3775 (2023).

294. M. Chen, *et al.* Aqueous zinc-ion batteries at extreme temperature: Mechanisms, challenges, and strategies. *Energy Storage Mater.* **51**, 683–718 (2022).

295. J. Lu, T. Wu & K. Amine. State-of-the-art characterization techniques for advanced lithium-ion batteries. *Nat. Energy* **2**, 1–13 (2017).

296. M. F. Lagadec, R. Zahn & V. Wood. Characterization and performance evaluation of lithium-ion battery separators. *Nat. Energy* **4**, 16–25 (2019).

297. M. Xia, *et al.* Lab-Scale In Situ X-Ray Diffraction Technique for Different Battery Systems: Designs, Applications, and Perspectives. *Small Methods* **3**, 1900119 (2019).

298. S. Wi, *et al.* In situ x-ray photoelectron spectroscopy analysis of electrochemical interfaces in battery: Recent advances and remaining challenges. *J. Vac. Sci. Technol. A* **40**, 010808 (2022).

299. Z. Zhang, *et al.* Characterizing Batteries by In Situ Electrochemical Atomic Force Microscopy: A Critical Review. *Adv. Energy Mater.* **11**, 2101518 (2021).

300. Z. Ning, *et al.* Visualizing plating-induced cracking in lithium-anode solid-electrolyte cells. *Nat. Mater.* **20**, 1121–1129 (2021).

301. R. Bhattacharyya, *et al.* In situ NMR observation of the formation of metallic lithium microstructures in lithium batteries. *Nat. Mater.* **9**, 504–510 (2010).

302. H. Cheng, C. B. Zhu, M. Lu & Y. Yang. In situ micro-FTIR study of the solid–solid interface between lithium electrode and polymer electrolytes. *J. Power Sources* **174**, 1027–1031 (2007).

303. Q. Cheng, *et al.* Operando and three-dimensional visualization of anion depletion and lithium growth by stimulated Raman scattering microscopy. *Nat. Commun.* **9**, 2942 (2018).

304. C. Gong, *et al.* Revealing the Role of Fluoride-Rich Battery Electrode Interphases by Operando Transmission Electron Microscopy. *Adv. Energy Mater.* **11**, 2003118 (2021).

305. A. J. Merryweather, C. Schnedermann, Q. Jacquet, C. P. Grey & A. Rao. Operando optical tracking of single-particle ion dynamics in batteries. *Nature* **594**, 522–528 (2021).

306. R. Serra-Maia, *et al.* Nanoscale Chemical and Structural Analysis during In Situ Scanning/Transmission Electron Microscopy in Liquids. *ACS Nano* **15**, 10228–10240 (2021).

307. C. Zhang, *et al.* Recent Progress of In Situ Transmission Electron Microscopy for Energy Materials. *Adv. Mater.* **32**, 1904094 (2020).

308. S. Fahad, Z. Wei & A. Kushima. In-situ TEM observation of fast and stable reaction of lithium polysulfide infiltrated carbon composite and its application as a lithium sulfur battery electrode for improved cycle lifetime. *J. Power Sources* **506**, 230175 (2021).

309. W. Ye, *et al.* Superfast Mass Transport of Na/K Via Mesochannels for Dendrite-Free Metal Batteries. *Adv. Mater.* **35**, 2210447 (2023).

310. S. D. Pu, *et al.* Current-Density-Dependent Electroplating in Ca Electrolytes: From Globules to Dendrites. *ACS Energy Lett.* **5**, 2283–2290 (2020).

311. J. Park, *et al.* Graphene Liquid Cell Electron Microscopy: Progress, Applications, and Perspectives. *ACS Nano* **15**, 288–308 (2021).

312. Z. Zeng, *et al.* Visualization of Electrode–Electrolyte Interfaces in $LiPF_6$/EC/DEC Electrolyte for Lithium Ion Batteries via in Situ TEM. *Nano Lett.* **14**, 1745–1750 (2014).

313. R. L. Sacci, *et al.* Nanoscale Imaging of Fundamental Li Battery Chemistry: Solid-Electrolyte Interphase Formation and Preferential Growth of Lithium Metal Nanoclusters. *Nano Lett.* **15**, 2011–2018 (2015).

314. B. L. Mehdi, *et al.* Observation and Quantification of Nanoscale Processes in Lithium Batteries by Operando Electrochemical (S)TEM. *Nano Lett.* **15**, 2168–2173 (2015).

315. A. Kushima, *et al.* Liquid cell transmission electron microscopy observation of lithium metal growth and dissolution: Root growth, dead lithium and lithium flotsams. *Nano Energy* **32**, 271–279 (2017).

316. J. Zhao, *et al.* Surface Fluorination of Reactive Battery Anode Materials for Enhanced Stability. *J. Am. Chem. Soc.* **139**, 11550–11558 (2017).

317. S.-Y. Lee, *et al.* Unveiling the mechanisms of lithium dendrite suppression by cationic polymer film induced solid–electrolyte interphase modification. *Energy Environ. Sci.* **13**, 1832–1842 (2020).

318. M. Gu, *et al.* Demonstration of an Electrochemical Liquid Cell for Operando Transmission Electron Microscopy Observation of the Lithiation/Delithiation Behavior of Si Nanowire Battery Anodes. *Nano Lett.* **13**, 6106–6112 (2013).

319. Z. Zeng, *et al.* In Situ Study of Lithiation and Delithiation of MoS_2 Nanosheets Using Electrochemical Liquid Cell Transmission Electron Microscopy. *Nano Lett.* **15**, 5214–5220 (2015).

320. L. Sun, *et al.* Recent progress and future perspective on practical silicon anode-based lithium ion batteries. *Energy Storage Mater.* **46**, 482–502 (2022).

321. X. Liu, *et al.* Origin and regulation of oxygen redox instability in high-voltage battery cathodes. *Nat. Energy* **7**, 808–817 (2022).

322. J. H. Park, *et al.* Control of Growth Front Evolution by Bi Additives during ZnAu Electrodeposition. *Nano Lett.* **18**, 1093–1098 (2018).

323. Y. Sasaki, *et al. In situ* electron microscopy analysis of electrochemical Zn deposition onto an electrode. *J. Power Sources* **481**, 228831 (2021).

324. M. Li, L. Ran & R. Knibbe. Zn Electrodeposition by an In Situ Electrochemical Liquid Phase Transmission Electron Microscope. *J. Phys. Chem. Lett.* **12**, 913–918 (2021).

325. Y. Sasaki, K. Yoshida, A. Kuwabara & Y. Ikuhara. On-Chip Electrochemical Analysis Combined with Liquid-Phase Electron Microscopy of Zinc Deposition/Dissolution. *J. Electrochem. Soc.* **168**, 112511 (2021).

326. Y. Huang, *et al.* Unraveling dynamical behaviors of zinc metal electrodes in aqueous electrolytes through an operando study. *Energy Storage Mater.* **46**, 243–251 (2022).

327. Z. Zeng, *et al.* Electrode roughness dependent electrodeposition of sodium at the nanoscale. *Nano Energy* **72**, 104721 (2020).

328. C. Gong, *et al.* The role of an elastic interphase in suppressing gas evolution and promoting uniform electroplating in sodium metal anodes. *Energy Environ. Sci.* **16**, 535–545 (2023).

329. Y. A. Wu, *et al.* In-situ Multimodal Imaging and Spectroscopy of Mg Electrodeposition at Electrode-Electrolyte Interfaces. *Sci. Rep.* **7**, 42527 (2017).

330. A. Kushima, *et al.* Charging/Discharging Nanomorphology Asymmetry and Rate-Dependent Capacity Degradation in Li–Oxygen Battery. *Nano Lett.* **15**, 8260–8265 (2015).

331. S. Zhou, *et al.* Visualizing interfacial collective reaction behaviour of Li–S batteries. *Nature* **621**, 75–81 (2023).

332. H. Liu, *et al.* Recent advances in understanding dendrite growth on alkali metal anodes. *EnergyChem* **1**, 100003 (2019).

333. L. Li, Z. Chang & X.-B. Zhang. Recent Progress on the Development of Metal-Air Batteries. *Adv. Sustain. Syst.* **1**, 1700036 (2017).

334. T. Liu, *et al.* Current Challenges and Routes Forward for Nonaqueous Lithium–Air Batteries. *Chem. Rev.* **120**, 6558–6625 (2020).

335. Y. Wang & Y.-C. Lu. Nonaqueous Lithium–Oxygen batteries: Reaction mechanism and critical open questions. *Energy Storage Mater.* **28**, 235–246 (2020).

336. Z. Peng, *et al.* Oxygen Reactions in a Non-Aqueous Li^+ Electrolyte. *Angew. Chem. Int. Ed.* **50**, 6351–6355 (2011).

337. C. Batchelor-McAuley, *et al.* Recent Advances in Voltammetry. *ChemistryOpen* **4**, 224–260 (2015).

338. F. Mansfeld. Fundamental aspects of the polarization resistance technique—the early days. *J. Solid State Electrochem.* **13**, 515–520 (2009).

339. K. W. Pratt. Chronoamperometric determination of diffusion-layer thicknesses at hydrodynamic electrodes. *Anal. Chem.* **56**, 1967–1970 (1984).

340. M. Yang & Z. Hu. Electrodeposition of bismuth onto glassy carbon electrodes from nitrate solutions. *J. Electroanal. Chem.* **583**, 46–55 (2005).

341. S. Wang, *et al.* Electrochemical impedance spectroscopy. *Nat. Rev. Methods Primer* **1**, 1–21 (2021).

342. H. S. Magar, R. Y. A. Hassan & A. Mulchandani. Electrochemical Impedance Spectroscopy (EIS): Principles, Construction, and Biosensing Applications. *Sensors* **21**, 6578 (2021).

343. J. Huang, Z. Li, B. Y. Liaw & J. Zhang. Graphical analysis of electrochemical impedance spectroscopy data in Bode and Nyquist representations. *J. Power Sources* **309**, 82–98 (2016).

344. L. E. Franken, K. Grünewald, E. J. Boekema & M. C. A. Stuart. A Technical Introduction to Transmission Electron Microscopy for Soft-Matter: Imaging, Possibilities, Choices, and Technical Developments. *Small* **16**, 1906198 (2020).

345. N. de Jonge, L. Houben, R. E. Dunin-Borkowski & F. M. Ross. Resolution and aberration correction in liquid cell transmission electron microscopy. *Nat. Rev. Mater.* **4**, 61–78 (2019).

346. P. Abellan, *et al.* Probing the Degradation Mechanisms in Electrolyte Solutions for Li-Ion Batteries by in Situ Transmission Electron Microscopy. *Nano Lett.* **14**, 1293–1299 (2014).

347. J. M. Grogan, N. M. Schneider, F. M. Ross & H. H. Bau. Bubble and Pattern Formation in Liquid Induced by an Electron Beam. *Nano Lett.* **14**, 359–364 (2014).

348. S. Nasir, *et al.* Potential valorization of by-product materials from oil palm: A review of alternative and sustainable carbon sources for carbon-based nanomaterials synthesis. *BioResources* **14**, (2019).

349. T. W. Napporn, C. Canaff, E. Bere & V. Hacker. Chapter 8 - Characterization Methods for Components and Materials. *Fuel Cells and Hydrogen* **5**, 155–173 (2018).

350. M. Veerapandian & K. Yun. Study of Atomic Force Microscopy in Pharmaceutical and Biopharmaceutical Interactions - A Mini Review. *Current Pharmaceutical Analysis* **5**, 256–268 (2009).

351. P. Zimmermann, *et al.* Modern X-ray spectroscopy: XAS and XES in the laboratory. *Coord. Chem. Rev.* **423**, 213466 (2020).

352. D. K. Pandey, H. L. Kagdada, P. Sanchora & D. K. Singh. Overview of Raman Spectroscopy: Fundamental to Applications. *Modern Techniques of Spectroscopy: Basics, Instrumentation, and Applications*: 145–184 (2021).

353. N. Guo, *et al.* A Review on 3D Zinc Anodes for Zinc Ion Batteries. *Small Methods* **6**, 2200597 (2022).

354. M. Wen, C. Yang, Q. Liu, J. Qiu & L. Zang. Wide-Potential-Window Bimetallic Hydrated Eutectic Electrolytes with High-Temperature Resistance for Zinc-Ion Hybrid Capacitors. *Small* **19**, 2303348 (2023).

355. Q. Pang, *et al.* Understanding the mechanism of byproduct formation with in operando synchrotron techniques and its effects on the electrochemical performance of VO_2(B) nanoflakes in aqueous rechargeable zinc batteries. *J. Mater. Chem. A* **8**, 9567–9578 (2020).

356. Y.-H. Lee, *et al.* Byproduct reverse engineering to construct unusually enhanced protection layers for dendrite-free Zn anode. *Chem. Eng. J.* **464**, 142580 (2023).

357. Z. Cai, *et al.* Regulating the Zn Electrode/Electrolyte Interface Toward High Stability– Insights from the Resting Time Impact on Zn Electrode Performance. *Adv. Funct. Mater.* 2401367 (2024).

358. K. Haydarov. Analysis of Modern Corrosion Inhibitors. A Review. *Excell. Int. Multi-Discip. J. Educ. 2994-9521* **2**, 148–155 (2024).

359. Z. Liu, *et al.* Unraveling Paradoxical Effects of Large Current Density on Zn Deposition. *Adv. Mater.* **36**, 2404140 (2024).

360. D. Han, *et al.* A Self-Regulated Interface toward Highly Reversible Aqueous Zinc Batteries. *Adv. Energy Mater.* **12**, 2102982 (2022).

361. K. Ouyang, *et al.* Synergistic Modulation of In-Situ Hybrid Interface Construction and pH Buffering Enabled Ultra-Stable Zinc Anode at High Current Density and Areal Capacity. *Angew. Chem.* **135**, e202311988 (2023).

362. H. Li, *et al.* A Self-Regulated Interface Enabled by Multi-Functional pH Buffer for Reversible Zn Electrochemistry. *Adv. Funct. Mater.* **34**, 2313859 (2024).

363. M. Liu, *et al.* Strategies for pH regulation in aqueous zinc ion batteries. *Energy Storage Mater.* **67**, 103248 (2024).

364. L. Qian, *et al.* Ultralow-Salt-Concentration Electrolyte for High-Voltage Aqueous Zn Metal Batteries. *Adv. Funct. Mater.* **33**, 2301118 (2023).

365. Q. Nian, *et al.* Highly reversible zinc metal anode enabled by strong Brønsted acid and hydrophobic interfacial chemistry. *Nat. Commun.* **15**, 4303 (2024).

366. Z. Yi, G. Chen, F. Hou, L. Wang & J. Liang. Strategies for the Stabilization of Zn Metal Anodes for Zn-Ion Batteries. *Adv. Energy Mater.* **11**, 2003065 (2021).

367. J. Zheng, *et al.* Reversible epitaxial electrodeposition of metals in battery anodes. *Science* **366**, 645–648, (2019).

368. S. D. Pu, *et al.* Achieving Ultrahigh-Rate Planar and Dendrite-Free Zinc Electroplating for Aqueous Zinc Battery Anodes. *Adv. Mater.* **34**, 2202552 (2022).

369. Y. Zhang, *et al.* Manipulating the Zinc Deposition Behavior in Hexagonal Patterns at the Preferential Zn (100) Crystal Plane to Construct Surficial Dendrite-Free Zinc Metal Anode. *Small* **18**, 2105978 (2022).

370. T. Foroozan, *et al.* Non-Dendritic Zn Electrodeposition Enabled by Zincophilic Graphene Substrates. *ACS Appl. Mater. Interfaces* **11**, 44077–44089 (2019).

371. B.-S. Lee, *et al.* Dendrite Suppression Membranes for Rechargeable Zinc Batteries. *ACS Appl. Mater. Interfaces* **10**, 38928–38935 (2018).

372. L. Kang, *et al.* Nanoporous $CaCO_3$ Coatings Enabled Uniform Zn Stripping/Plating for Long-Life Zinc Rechargeable Aqueous Batteries. *Adv. Energy Mater.* **8**, 1801090 (2018).

373. J. P. Perdew, K. Burke & M. Ernzerhof. Generalized Gradient Approximation Made Simple. *Phys. Rev. Lett.* **78**, 1396–1396 (1997).

374. M. Schlipf & F. Gygi. Optimization algorithm for the generation of ONCV pseudopotentials. *Comput. Phys. Commun.* **196**, 36–44 (2015).

375. P. Zou, *et al.* Polymorph Evolution Mechanisms and Regulation Strategies of Lithium Metal Anode under Multiphysical Fields. *Chem. Rev.* **121**, 5986–6056 (2021).

376. K. S. Nagy, S. Kazemiabnavi, K. Thornton & D. J. Siegel. Thermodynamic Overpotentials and Nucleation Rates for Electrodeposition on Metal Anodes. *ACS Appl. Mater. Interfaces* **11**, 7954–7964 (2019).

377. X. Feng, *et al.* Enabling Highly Reversible Zn Anode by Multifunctional Synergistic Effects of Hybrid Solute Additives. *ACS Energy Lett.* **8**, 1192–1200 (2023).

378. J. Zheng, *et al.* Regulating electrodeposition morphology of lithium: towards commercially relevant secondary Li metal batteries. *Chem. Soc. Rev.* **49**, 2701–2750 (2020).

379. V. Jabbari, T. Foroozan & R. Shahbazian-Yassar. Dendritic Zn Deposition in Zinc-Metal Batteries and Mitigation Strategies. *Adv. Energy Sustain. Res.* **2**, 2000082 (2021).

380. W. Yuan, *et al.* Realizing Textured Zinc Metal Anodes through Regulating Electrodeposition Current for Aqueous Zinc Batteries. *Angew. Chem. Int. Ed.* **62**, e202218386 (2023).

381. G. Song, S. Li, G. Liu, Q. Fu & C. Pan. Influence of Graphene Oxide Content on the Zn-Gr Composite Layer Prepared by Pulse Reverse Electro-plating. *J. Electrochem. Soc.* **165**, D501 (2018).

382. A. A. Akl, S. A. Mahmoud, S. M. AL-Shomar & A. S. Hassanien. Improving microstructural properties and minimizing crystal imperfections of nanocrystalline Cu_2O thin films of different solution molarities for solar cell applications. *Mater. Sci. Semicond. Process.* **74**, 183–192 (2018).

383. R. Yao, *et al.* A Versatile Cation Additive Enabled Highly Reversible Zinc Metal Anode. *Adv. Energy Mater.* **12**, 2102780 (2022).

384. H. Yan, *et al.* Triggering Zn^{2+} Unsaturated Hydration Structure via Hydrated Salt Electrolyte for High Voltage and Cycling Stable Rechargeable Aqueous Zn Battery. *Adv. Energy Mater.* **12**, 2201599 (2022).

385. L. Cao, *et al.* Highly Reversible Aqueous Zinc Batteries enabled by Zincophilic–Zincophobic Interfacial Layers and Interrupted Hydrogen-Bond Electrolytes. *Angew. Chem. Int. Ed.* **60**, 18845–18851 (2021).

386. C. Zhang, *et al.* The electrolyte comprising more robust water and superhalides transforms Zn-metal anode reversibly and dendrite-free. *Carbon Energy* **3**, 339–348 (2021).

387. C. Zhang, *et al.* A $ZnCl_2$ water-in-salt electrolyte for a reversible Zn metal anode. *Chem. Commun.* **54**, 14097–14099 (2018).

388. C. Yang, *et al.* All-temperature zinc batteries with high-entropy aqueous electrolyte. *Nat. Sustain.* **6**, 325–335 (2023).

389. J. Cao, *et al.* Strategies of regulating Zn^{2+} solvation structures for dendrite-free and side reaction-suppressed zinc-ion batteries. *Energy Environ. Sci.* **15**, 499–528 (2022).

390. L. Yuan, *et al.* Regulation methods for the Zn/electrolyte interphase and the effectiveness evaluation in aqueous Zn-ion batteries. *Energy Environ. Sci.* **14**, 5669–5689 (2021).

391. Q. Zhang, *et al.* Chaotropic Anion and Fast-Kinetics Cathode Enabling Low-Temperature Aqueous Zn Batteries. *ACS Energy Lett.* **6**, 2704–2712 (2021).

392. K. W. Nam, H. Kim, J. H. Choi & J. W. Choi. Crystal water for high performance layered manganese oxide cathodes in aqueous rechargeable zinc batteries. *Energy Environ. Sci.* **12**, 1999–2009 (2019).

393. C. Wang, *et al.* Toward Flexible Zinc-Ion Hybrid Capacitors with Superhigh Energy Density and Ultralong Cycling Life: The Pivotal Role of $ZnCl_2$ Salt-Based Electrolytes. *Angew. Chem. Int. Ed.* **60**, 990–997 (2021).

394. X. Ji. A perspective of $ZnCl_2$ electrolytes: The physical and electrochemical properties. *eScience* **1**, 99–107 (2021).

395. H. Yang, *et al.* Constructing a Super-Saturated Electrolyte Front Surface for Stable Rechargeable Aqueous Zinc Batteries. *Angew. Chem. Int. Ed.* **59**, 9377–9381 (2020).

396. H. Li, *et al.* Zinc deposition characteristics on different substrates for aqueous zinc ion battery. *Appl. Surf. Sci.* **607**, 155111 (2023).

397. K. Bao, *et al.* Construction of low dielectric aqueous electrolyte with ethanol for highly stable Zn anode. *Nano Energy* **120**, 109089 (2024).

398. L. Hong, *et al.* An effective descriptor for the screening of electrolyte additives toward the stabilization of Zn metal anodes. *Energy Environ. Sci.* **17**, 3157–3167 (2024).

399. L. Gu, Y. Zhang, Q. Kong & C. Yang. Synchrotron X-ray Characterization Techniques for the Development of Aqueous Zinc Ion Batteries. *ChemElectroChem* **11**, e202300602 (2024).

400. D. Wang, *et al.* In Situ Formation of Nitrogen-Rich Solid Electrolyte Interphase and Simultaneous Regulating Solvation Structures for Advanced Zn Metal Batteries. *Angew. Chem. Int. Ed.* **61**, e202212839 (2022).

401. W. Zhang, *et al.* Self-repairing interphase reconstructed in each cycle for highly reversible aqueous zinc batteries. *Nat. Commun.* **13**, 5348 (2022).

402. J. Luo, *et al.* Stable zinc anode solid electrolyte interphase via inner Helmholtz plane engineering. *Nat. Commun.* **15**, 6471 (2024).

403. C. Li, *et al.* Highly reversible Zn anode with a practical areal capacity enabled by a sustainable electrolyte and superacid interfacial chemistry. *Joule* **6**, 1103–1120 (2022).

404. Y. Wang, *et al.* Enabling high-energy-density aqueous batteries with hydrogen bond-anchored electrolytes. *Matter* **5**, 162–179 (2022).

405. X. Luo, *et al.* Regulation of desolvation process and dense electrocrystalization behavior for stable Zn metal anode. *Energy Storage Mater.* **57**, 628–638 (2023).

406. Z. Hou, *et al.* Tailoring desolvation kinetics enables stable zinc metal anodes. *J. Mater. Chem. A* **8**, 19367–19374 (2020).

407. K. He, *et al.* Operando liquid cell electron microscopy of discharge and charge kinetics in lithium-oxygen batteries. *Nano Energy* **49**, 338–0345 (2018).